NOTICE

The quality of this microform is heavily dependent upon the quality of the original thesis submitted for microfilming. Every effort has been made to ensure the highest quality of reproduction possible.

If pages are missing, contact the university which granted the degree.

Some pages may have indistinct print especially if the original pages were typed with a poor typewriter ribbon or if the university sent us an inferior photocopy.

Reproduction in full or in part of this microform is governed by the Canadian Copyright Act, R.S.C. 1970, c. C-30, and subsequent amendments.

AVIS

La qualité de cette microforme dépend grandement de la qualité de la thèse soumise au microfilmage. Nous avons tout fait pour assurer une qualité supérieure de reproduction.

S'il manque des pages, veuillez communiquer avec l'université qui a conféré le grade.

La qualité d'impression de certaines pages peut laisser à désirer, surtout si les pages originales ont été dactylographiées à l'aide d'un ruban usé ou si l'université nous a fait parvenir une photocopie de qualité inférieure.

La reproduction, même partielle, de cette microforme est soumise à la Loi canadienne sur le droit d'auteur, SRC 1970, c. C-30, et ses amendements subséquents.

Experimental Identification of X-ray CT system characteristics for an improved understanding of image processing

Sylvie Doré

Mechanical Engineering
McGill University, Montréal

May, 1992

A thesis submitted to the Faculty of Graduate Studies and Research
in partial fulfillment of the requirements for the degree of
Doctor of Philosophy

ISBN 0-315-74836-9

À Pierreaudetdadugnepeterece,
agent secret

... ou au rêve et à l'imagination

ABSTRACT

The first goal of this study was to develop experimental tools to estimate the blur and noise characteristics of X-ray CT systems. We evaluated the noise power spectrum (NPS) using the averaged periodogram technique. As predicted by theory, varying the image reconstruction filter produced a shift in the frequency content while slice thickness only affected the amplitude of the noise.

In order to quantify the blur, we developed and evaluated two non-linear parametric models of the point spread function (PSF): the Gaussian and damped cosine models. We fitted these models to images of spatially distributed point sources and thus quantified the pattern of shift-variance. We found that the system produced a rotating blur and observed a loss of PSF radial symmetry as the input point source moved away from the center of the field of view. We validated the use of point sources by comparing non-parametric PSF estimates obtained with this input to those found using a correlation-based technique (Wiener-Hopf equation). We gained insight into the design of the input signal, which consisted of pseudo-randomly located holes, through an exhaustive simulation.

The second goal was to investigate how this information could be used to process CT images. We formulated and evaluated a coordinate transformation for shift-invariant restoration of CT images. We developed a simple evaluation procedure which proved beneficial in delimiting the usefulness and detecting limitations of the method. We also formulated a number of recommendations regarding the use of the threshold and Laplacian of a Gaussian segmentation operators taking the shape of the PSF and of the NPS into account.

RÉSUMÉ

Le premier objectif de ce travail était de développer des outils expérimentaux permettant d'estimer les propriétés de flou et de bruit de tomographes à rayons-X. Nous avons évalué le spectre de bruit en utilisant la technique du périodogramme moyen. Tel que prédit théoriquement, la variation du filtre de reconstruction a engendré une modification du contenu fréquentiel tandis que l'épaisseur des images n'a influencé que l'amplitude du bruit.

Afin de quantifier le flou, nous avons développé et évalué deux modèles paramétriques non-linéaires de la réponse impulsionnelle (RI): les modèles Gaussien et de cosinus amorti. Le patron d'anisotropie et de variation spatiale de la RI furent quantifiés en ajustant ces modèles à l'image de sources ponctuelles distribuées spatialement. Nous avons remarqué que le système produisait un flou rotatif et avons observé une perte de symmétrie radiale de la RI lorsque la source ponctuelle s'éloignait du centre du champ d'observation. Nous avons validé l'emploi de sources ponctuelles en comparant les estimés non-paramétriques obtenus avec ce type d'entrant à ceux issus d'une technique de corrélation (équation de Wiener-Hopf). Une simulation exhaustive nous a permis de concevoir un signal d'entré approprié qui consistait en une série de trous disposés pseudo-aléatoirement.

Le second but se voulait une réflexion sur la façon dont cette connaissance pourrait être utilisée pour traiter les images. Nous avons formulé une transformation de coordonnées permettant la restauration d'images non-stationnaires. Une procédure d'évaluation simple nous a permis de délimiter l'utilité et de détecter les limites de cette méthode. Finalement, des conseils portant sur l'utilisation de deux opérateurs de segmentation, le seuillage et le Laplacien d'une Gaussienne, ont été formulés en se basant sur la morphologie de la RI et du spectre de bruit.

ACKNOWLEDGEMENTS

This work would not have been possible without the help of many people. I wish to express my gratitude to the following:

- my supervisors, Dr. R.E. Kearney and Dr. J. De Guise, for their constant advice and support,
- Dr. R. Gariépy, for initiating this project,
- Dr. T. Peters for facilitating the access to the CT scanner located in the Centre de Recherch N-R Inc., and for opening the doors to his laboratory,
- Mr L. Botero, for his time and professionalism in acquiring the CT images,
- Mr T. Doukoglou who kindly shared his two-dimensional correlation-based identification programs with me,
- Mr R. Wagner, for helping me with programming IP and for accompanying me to Total Workouts (thanks also to Zoe and Shelly for their great routines and for keeping Ross' interest alive),
- all my friends at the Department of Biomedical Engineering, who had to put up with my constant remarks about lab cleanness (or lack of) and computer (up)grades,
- to my husband, family and friends for believing in me, even when I didn't.

I am also indebted towards l'Institut de Recherche en Santé et en Sécurité du Travail, McGill University, the Canadian Federation of University Women, and Pierrot for their financial support.

TABLE OF CONTENTS

Abstract iii
Résumé iv
Acknowledgements v
List of figures xi
List of tables xiii
List of abbreviations xiv

Chapter 1 Introduction

1.1 Context 1
1.2 Objectives 2
1.3 Outline 2

Chapter 2 Literature review

2.1 Introduction 5
2.2 Image formation 5
2.3 Artefacts 10
2.3.1 Partial volume effect 10
2.3.2 Exponential edge gradient effect 11
2.3.3 Beam hardening effect 11
2.3.4 Scatter 12
2.3.5 Aliasing 12
Number of projections 12
Number of rays per projection 12
Reconstruction grid 13
2.3.6 Justification of linear analysis 13
2.4 Identification of blur characteristics 13
2.4.1 Identification of general linear systems 14
2.4.2 Identification of the modulation transfer function of CT scanners 16
Impulse methods 16
Edge methods 17
Frequency methods 19
2.4.3 System shift-variance 20
2.4.4 Factors affecting blur 20
2.5 Noise in CT images 21
2.5.1 Photon statistics 21
2.5.2 Variance studies 22
2.5.3 Frequency structure studies 23
2.6 Conclusions 25

Chapter 3 Identification of noise characteristics

3.1 Introduction 27
3.2 Methods 27
3.3 Results 29
3.4 Conclusions 31

Chapter 4 Parametric modelling of the PSF

4.1 Introduction 32
4.2 Methods 32
4.2.1 Non-parametric identification 33
4.2.2 Parametric models for the point spread function 34
Gaussian model 34
Behavior of Gaussian model 35
Damped cosine model 36
4.2.3 Modulation transfer function 36
4.2.4 Resolution 37
Subjective technique 37
FWHM 37
HWZC 37
Inverse of the cut-off frequency 38
4.3 Results 38
4.3.1 Point spread function 39
Effects of scanning parameters 39
Repeatability of Gaussian parameters 41
Parameter B 43
4.3.2 Modulation transfer function 45
4.3.3 Resolution 47
4.4 Discussion 48
4.4.1 Parametric models 48
Importance of non-linear model 48
High resolution filter 49
Radial asymmetry 49
Effects of parameter B 50
4.4.2 Resolution 51
Effect of object shape 51
Differences between methods 54
Differences within the FWHM-based methods 55
Accuracy of measurement methods 55
4.5 Conclusions 55

Chapter 5 Experimental determination of CT point spread function anisotropy and shift-variance

5.1 Introduction 57
5.2 Method 58
5.2.1 Hardware 58
5.2.2 PSF shape descriptors 59
5.2.3 Coordinate systems 61
5.2.4 Statistical tests 64
5.3 Results 64
5.3.1 x-y coordinate system 67
5.3.1 s-t coordinate system 67
5.3.3 Effect of parameter B 70
5.3.4 Effect of scan time 73
5.3.5 Effect of image reconstruction filter 73
5.3.6 Radial symmetry 75
5.4 Discussion 76
5.4.1 Origin of shift-variance 76
5.4.2 Origin of rotating blur 79
5.4.3 Similarities with theoretical studies 79
5.4.4 Discrepancies with theoretical studies 80
5.4.5 Effect of scan time 81
5.4.6 Effect of image reconstruction filter 81
5.4.7 Effect of parameter B 83
5.5 Conclusions 83

Chapter 6 Correlation based non-parametric PSF identification

6.1 Introduction 85
6.2 Background 85
6.2.1 Theory 86
6.2.2 Implementation 87
6.3 Design of input signal 88
6.3.1 Choice of input sequence 88
6.3.2 Digitization of input sequence 89
6.4 Simulations 95
6.4.1 Method 95
6.4.2 Effect of hole size and separation 97
6.4.3 Effect of sequence length 98
6.4.4 Effect of pixel size 101
6.4.5 Effect of sub-pixel translation 101
6.4.6 Effect of rotation 105
6.4.7 Effect of cupping 105
6.4.8 Random .vs. PRLH input 107

Chapter 6 (continued)

6.5 Experimental identification 108
6.5.1 Description of phantom 108
6.5.2 Scanning parameters 111
6.5.3 Results 111
6.6 Discussion 114
6.6.1 Design of input sequence 114
6.6.2 Noise 115
6.6.3 Other factors affecting identification quality 118
6.6.4 Comparison with wire input 119
6.7 Conclusions 121

Chapter 7 Coordinate transformation for isoplanatic representation of shift-variant CT point spread function

7.1 Introduction 122
7.2 Restoration of shift-variant images 122
7.3 Proposed change of coordinates 125
7.3.1 Coordinate transformation 125
7.3.2 Requirements for correct mapping 130
7.3.3 Algorithm 131
7.4 Evaluation of proposed transformation 133
7.4.1 Simulated data 133
7.4.2 CT data 137
7.5 Discussion 138
7.5.1 Interpolation 138
7.5.2 Limitations 142
7.5.3 Usefulness of method 145
7.6 Conclusions 146

Chapter 8 Recommendations for segmentation

8.1 Introduction 147
8.2 Underlying principles 147
8.3 Thresholding 148
8.3.1 Background 148
Foundation 148
Thresholds for bone segmentation 149
Accuracy 149
8.3.2 Analysis 151
Theoretical relative threshold 151
2D edges 153
Edge interaction 154
8.3.3 Discussion 156

Chapter 8 (continued)

8.4 Laplacian of a Gaussian operator 157
8.4.1 Background 157
Regularization 157
Gradient 158
Laplacian of a Gaussian 158
Medical imaging literature 159
8.4.2 Discussion 160
8.5 Conclusions 162

Chapter 9 Conclusion

9.1 Summary 164
9.2 Original contributions 164
9.2.1 Parametric models 164
9.2.2 Shift-variant study 165
9.2.3 Correlation based non-parametric PSF identification 166
9.2.4 Coordinate transformation 166
9.2.5 Segmentation 167
9.2.6 General comments 167
9.3 Future work 168
9.3.1 Image processing 168
9.3.2 Reconstruction 169
9.3.3 Fabrication 171
9.3.4 Design evaluation 172

References 173

LIST OF FIGURES

1.1 Drawing of custom-fitted resurfacing articular implant 3

2.1 Data acquisition 6
2.2 Backprojection 7
2.3 Image of a point source 9
2.4 Fan-beam geometry 10

3.1 Image of section D of Philips performance phantom 28
3.2 1D noise power spectra 30

4.1 Image of section B of Philips performance phantom 33
4.2 Measured PSF 40
4.3 Effect of non-zero background on Gaussian model without parameter B 44
4.4 Modulation transfer function 46
4.5 Effect of object size and separation on resolvability 52
4.6 Creating a square wave by summing point sources 53

5.1 Custom shift-variant phantom 59
5.2 Relationship between coordinate systems 62
5.3 Estimating the Gaussian shape parameters in the s-t coordinate system from values defined in the x-y system 63
5.4 Variation of resolution along the x axis 68
5.5 Resolution along the x and y axes 68
5.6 Comparison of methods to obtain shape descriptors in s-t coordinate system 69
5.7 Average background as a function of radial distance 71
5.8 Effect of omitting parameter B from Gaussian model 72
5.9 Effect of scan time 74
5.10 Effect of image reconstruction filter 75
5.11 Strip integral kernel 78
5.12 Sinogram for parallel- and fan-beam geometry 82

6.1 Creation of input 90
6.2 Input sequence digitization algorithm 91
6.3 Geometry for input sequence digitization 92
6.4 Schematic diagram of simulation scheme 96
6.5 Effect of sequence length 100
6.6 Effect of pixel size 102
6.7 Effect of sub-pixel shift 104
6.8 Effect of rotation 106
6.9 Influence of type of input on MTF 109
6.10 Image of PRLH sequence phantom 110
6.11 Experimentally identified PSF without preprocessing 112
6.12 Experimentally identified PSF with preprocessing 113
6.13 Effect of pixel size on ACF of input signal 116

7.1 Principle of coordinate transformation restoration 124
7.2 Coordinate transformation for CT images 126
7.3 PSF shape in rotating cartesian (s-t) and polar (r-θ) coordinate frame 128
7.4 Creating values along the u axis 130
7.5 Flow chart of algorithm for coordinate transformation 132
7.6 Evaluation of coordinate transformation with simulated data 134
7.7 Evaluation of coordinate transformation with CT data 139
7.8 Effect of neglecting minimum mapping requirement 143
7.9 Mapping of PSF from polar (r-θ) to variably sampled polar (u-v) plane 144

8.1 Blurring of an isolated edge 152
8.2 Blurring of a double step edge 155
8.3 Comparison of noise power spectrum and frequency characteristics of LOG operator 161

9.1 Synopsis of long term project 169

LIST OF TABLES

2.1 Correspondence of functions used in general and imaging system identification 14

3.1 Estimates of NPS parameters 31

4.1 Gaussian model parameter estimates 39
4.2 Comparison of parameters for Gaussian and damped cosine models 42
4.3 Repeatability of Gaussian model parameters 42
4.4 Parameter estimates obtained with Gaussian model in absence of B and with non zero background level 43
4.5 Effect of region size and non zero background on Gaussian parameter estimates in absence of B 45
4.6 Comparison of resolution estimates 47

5.1 Summary of statistical tests 65
5.2 Statistics for points located at a radial distance of 51 mm 70

6.1 Effect of hole size and separation on identification quality 93
6.2 Effect of sequence length on identification quality 99
6.3 Effect of pixel size on identification quality 101
6.4 Effect of sub-pixel shift on identification quality 103
6.5 Effect of rotation on identification quality 107
6.6 Effect of cupping on identification quality 107
6.7 Identification quality for PRLH sequence and white input 108
6.8 Quality of experimental identification 112
6.9 Estimates of resolution for PRLH sequence and wire input 120

7.1 Data used for evaluation of coordinate transformation 136
7.2 Evaluation results for simulated data 137
7.3 Evaluation results for CT data 141

LIST OF ABBREVIATIONS

ACF auto-correlation function
BHE beam hardening effect
CT (X-ray) computerized tomography
EEGE exponential edge-gradient effect
ERF edge response function
FOV field of view
FWHM full width at half maximum
HWZC half width at firs zero crossing
IRF impulse response function
LSF line spread function
LOG Laplacian of a Gaussian
MTF modulation transfer function
NPS noise power spectrum
OTF optical transfer function
PRB pseudo-random binary (sequence or signal)
PRLH pseudo-randomly located holes
PTF phase transfer function
PVE partial volume effect
VAF variance accounted for

CHAPTER 1
INTRODUCTION

1.1 CONTEXT

The advent of computerized tomographic imaging opened a new window onto human morphological and functional anatomy. Not content with these two dimensional (2D) images, researchers soon began "stacking" these anatomical "slices" to form 3D images. This process is known today as 3D reconstruction from serial images.

Three dimensional reconstruction approaches belong to one of two classes: volume or surface rendering (Farrell and Zappulla, 1989; Udupa, 1990; Herman, 1990). In volume rendering, no assumption is made as to the contents of the volume. Each voxel, or volume element, is assigned a color and opacity depending on some physical property. The value of the pixel displayed on the computer screen is a function of the value and opacity of the voxels encountered by rays traversing the volume. These 3D images are qualitative in nature in the sense that a viewer can perceive the relative position of structures with respect to one another, but their exact position cannot be quantified. Although they can be quite impressive, they remain of limited use since capacities for mensuration are limited and interactive manipulation is difficult. They are helpful however when the surface of the object to be visualized is not well defined or when it not clear which surfaces within a body are of particular importance for the application at hand.

Applications such as radiation therapy, stereotactic and cranio-facial surgery planning as well as the design of custom orthopaedic implants, which require quantitative information, rely mostly on surface-based reconstruction. This method assumes that the volume of data contains specific structures that can be represented by their surfaces. Before being displayed, using depth-shading, hidden surface removal or other techniques, these surfaces must be isolated from their surroundings, i.e. they must be segmented. It is from this segmentation step that the quantitative structural information is obtained: knowing the position of the pixels forming the contours (or that of the voxels forming the surface) the position and size of the structures can be determined.

As the trend from qualitative to quantitative 3D reconstruction continues, the demands on accuracy increase. However, like any CAD/CAM system or finite element program, even the best reconstruction algorithm will give mediocre results if it is fed inaccurate data. It is surprising that compared to the amount of effort expanded in devising algorithms to three-dimensionally integrate the structural information, relatively little effort has been spent extracting the information from the series of 2D images. We share the

opinion of Stiehl (1990) and Robb and Barillot (1989) when they argue that segmentation is one of the areas requiring more research if accurate and reliable models are to be produced.

1.2 Objectives

Image processing tools are impressive in quantity and diversity. Nonetheless only the simplest of these techniques have been applied to process and extract information from medical images. More importantly, the limitations of the imaging device, such as blurring patterns, noise characteristics and artefact, have been largely ignored when applying these general techniques to medical images. Certain researchers advocate the use of more sophisticated tools (see Stiehl (1990) for example). However, we believe that by gaining a detailed knowledge of the characteristics of the imaging system, we will be in a better position to determine the limits of the image processing algorithms, even the simplest, and to improve their performance.

The first objective of this work was therefore to develop the experimental tools needed to characterize the imaging system. This goal was realized in the framework of linear systems theory. As such, the CT scanner was characterized in terms of its point spread function (PSF) - or its frequency domain representation, the modulation transfer function (MTF) - and its noise power spectrum (NPS). The PSF typifies the blur present in the images while the NPS describes the frequency distribution of the noise.

In the long term, we are interested in the design of custom-fitted resurfacing articular implants such as the one illustrated in figure 1.1. Because we will be required to reconstruct the geometry of bony articular surfaces, and these structures are best defined with x-ray CT, we will concentrate our study on this type of system. From this point on, when we refer to CT systems, we implicitly imply an x-ray energy source.

The second goal was to investigate how knowledge of the characteristics could be employed to process the images.

1.3 Outline

Principles underlying the formation of CT images are introduced in chapter 2 which also contains a review of the CT system identification literature.

The first goal of this work is realized in chapters 3 through 6. Results of NPS measurements are presented in chapter 3. In chapter 4, we develop and evaluate two parametric models of the PSF shape. Chapter 5 describes how these models were used to quantify the shift-variance and rotational asymmetry of the PSF. In both these chapters,

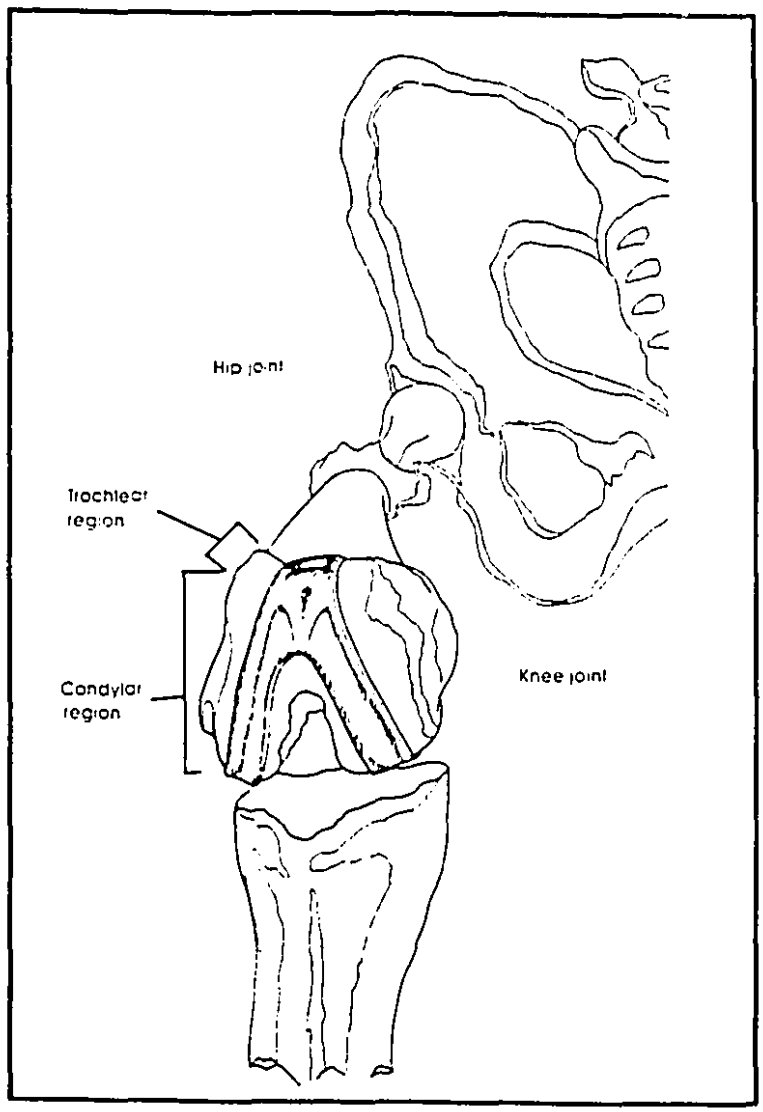

Figure 1.1 Drawing of custom-fitted resurfacing articular implant

images of thin metallic wires provided non-parametric PSF estimates to which the models were fitted. In order to validate these results, we compared these estimates with those obtained with a correlation-based identification method, the subject of chapter 6.

The next two chapters are devoted to the second objective. In chapter 7, we propose a coordinate transformation, based on the results of chapter 5, which can be used for shift-variant image restoration. We examine the performance of the threshold and Laplacian of a Gaussian segmentation operators based on the shape of the PSF and on the noise properties in chapter 8.

Chapter 9 concludes the thesis with a statement of original contributions and a discussion of topics considered for future work.

CHAPTER 2
LITERATURE REVIEW

2.1 Introduction

In order to limit the scope of this chapter, we will focus on the literature dealing with identification of the blur and noise characteristics of CT imaging systems. Topics concerning image restoration and segmentation will be reviewed in chapters 7 and 8 respectively.

Knowing how images are formed is important to understand how an imaging system behaves. We therefore felt justified in introducing the principles underlying the related topics, rather than only reviewing the literature. This approach seems appropriate since the field of 3D reconstruction attracts researchers from a number of different fields (medical physics, electrical and mechanical engineering, computer graphics ...) each with a strong comprehension of some aspect of the problem but with limited knowledge of some other. Nonetheless, the author assumes that the reader has a working knowledge of linear systems theory and Fourier analysis.

Consequently, this chapter serves a double purpose. The first goal is to introduce principles and the second is to review the literature concerning the topics related to image formation and system identification.

The ideal physical and mathematical principles of image formation are explained in section 2.2. Section 2.3 examines how deviations from ideal conditions give rise to artefacts. Sections 2.4 and 2.5 cover identification of blur and noise characteristics respectively. Finally, section 2.6 concludes the chapter.

2.2 Image formation

This section is a short synopsis of the physical laws describing the interaction of x-ray with matter under ideal conditions. It also describes the mathematical concepts underlying the formation of CT images. For a comprehensive discussion on these topics, the reader is invited to consult Kak and Slaney (1988) and chapter 7 of Barrett and Swindell (1981).

Tissue differentiation is made possible by the variation of the linear x-ray attenuation coefficient μ with factors such as density, mineral content, material thickness, and others. For a homogeneous medium of constant μ, irradiated with a mono-energetic x-ray beam, the relationship between emitted (I_0) and detected (I) intensity is given by Beer's law:

$$I(x_r) = I_O \, e^{-\int_{-\infty}^{\infty} \mu(r)\, dy_r} \qquad (2.1)$$

where x_r and y_r form a rotating cartesian system with the y_r axis pointing in the direction of the incident x-ray beam. Vector $r(x_r,y_r)$ represents the position of a point P. Figure 2.1(a) shows the orientation of the coordinate system.

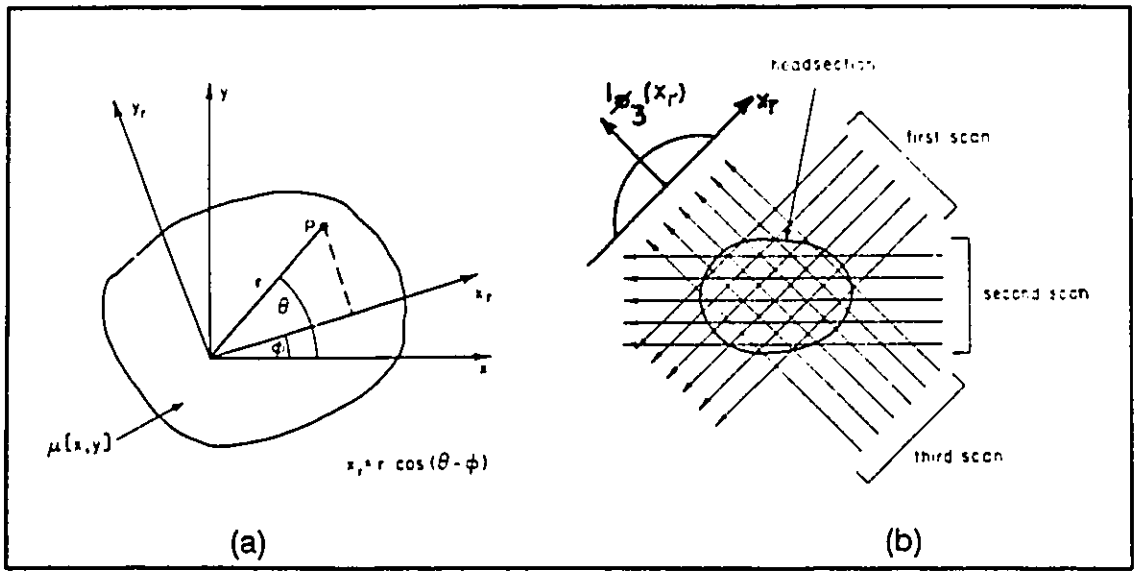

Figure 2.1 Data acquisition
(adapted from Barrett and Swindell, 1981; figures 7.1 and 7.2)

(a) Coordinate systems.The image plane is represented by a fixed cartesian coordinate system x-y. The x_r-y_r frame rotates with the source and detector assembly, with y_r pointing in the direction of the x-rays. Vector r represents the position of a point P. (b) With a first generation parallel-beam scanner, a single projection $I_\phi(x_r)$ is acquired by synchronously translating the source and detector assembly.The assembly is rotated a number of times to obtain the required set of projection data.

Unlike radiography which produces a two dimensional projection of volumetric data, the goal of CT imaging is to estimate the two dimensional spatial distribution of the linear attenuation coefficient μ contained within a "slice" of tissue. This problem is solved by techniques known as "image reconstruction from projections" (see also Herman, 1980 and Brooks and Di Chiro, 1971). The principle is illustrated in figure 2.1 for a first generation parallel beam scanner where a single detector moves synchronously with the source. The source-detector complex first sweeps in a translational movement to form a projection. By rotating the source and detector through an incremental angle and repeating the sweeping motion, a large number of projections, all lying in the image plane, are collected. A projection at given scan angle ϕ is described by linearizing equation (2.1):

$$l_\phi(x_r) = -\ln \frac{I_\phi(x_r)}{I_o} = \int_{-\infty}^{\infty} \mu(\mathbf{r})\, dy_r \tag{2.2}$$

A two-dimensional image is obtained by back-projecting the set of one dimensional projections. Although a number of methods have been devised for this purpose, most commercial scanners today (if not all) use a variation of back-projection. The concept is quite simple and is shown in figure 2.2. It consists of smearing each projection through the image plane along the y_r axis as expressed by the following expression:

$$g_\phi(x_r, y_r) = l_\phi(x_r) \tag{2.3}$$

and contributions corresponding to the various scan angles are summed up:

$$i(x_r, y_r) = \frac{1}{\pi} \int_o^\pi g_\phi(x_r, y_r)\, d\phi \tag{2.4}$$

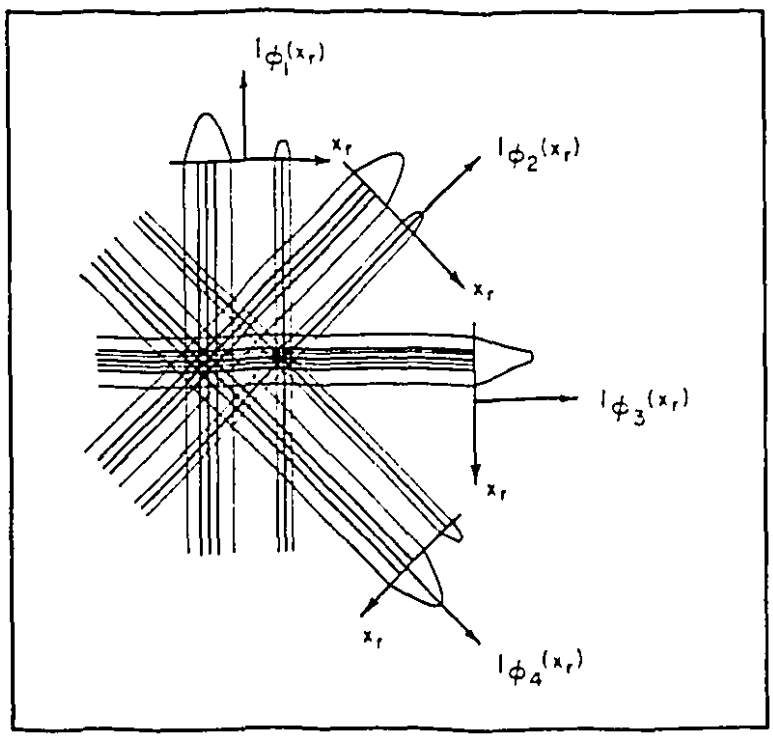

Figure 2.2 Backprojection
(adapted from Barrell and Swindell, 1981: figure 7.8)

The image is reconstructed by back-projecting or smearing the 1D projection back to the 2D image plane and adding all the contributions. The original object consists of two absorbing disks of different sizes.

Back-projection inherently blurs the reconstructed image. Figure 2.3 illustrates the image of a point source, or by definition, the point spread function. The increase in line density toward the center of the pattern, which characterizes the blur, is described by:

$$h_{bp}(\mathbf{r}) = \frac{1}{\pi\ r} \tag{2.5}$$

To rid the image of this intrinsic blur, a simple solution consists of convolving the image with πr. Alternatively, the image could be "rho-filtered", i.e. the Fourier transform of the image could be multiplied by $\pi\rho$ where ρ is spatial frequency. However, in order to limit high frequency noise, it is not desirable to extend the filter to infinitely high frequencies with ever increasing weight. Neither is it desirable to cut off the filter abruptly, a situation which would lead to excessive ringing or Gibb's phenomenon. Therefore, an apodizing function, a(r) is used to control the high frequency behavior of the rho-filter. The apodizing function can take a number of forms, resulting in slightly different images. Modern scanners offer a number of such filters: smoothing, normal, high resolution etc.

Therefore the final image is given by:

$$i(x_r, y_r) = a(r)\pi\ r * * \frac{1}{\pi}\int_0^{\infty} g_\phi(x_r, y_r)d\phi \tag{2.6}$$

$$= a(r)\pi r * * \frac{1}{\pi r} * * \mu(r)$$

$$= a(r) * * \mu(r)$$

Equation (2.6) states that the ideal filtered back-projected image is equal to the spatial distribution of x-ray attenuation coefficient convolved with the apodizing function. However, a few comments are in order:

1) The equations presented so far represent the ideal continuous case. But CT imaging is discrete and yields a two dimensional array of pixels or picture elements. This implies that the projections must be interpolated to obtain values corresponding to a given pixel. Interpolation, with its low pass filtering effect (Parker et al., 1983), also influences the blurring characteristics of the system. Furthermore, each pixel is assigned a CT number which represents the attenuation coefficient relative to water. In Hounsfield units, the relationship is:

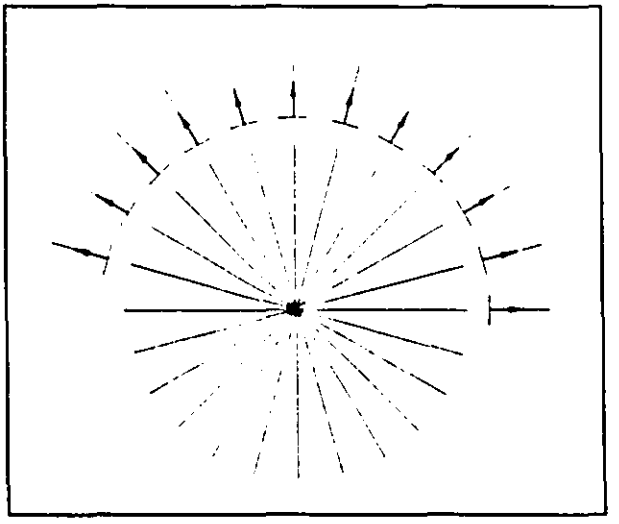

Figure 2.3 Image of a point source
(adapted from Barrett and Swindell, 1981; figure 7.20)

The image of a point source is a collection of radial lines. The line density, which characterizes the blur, is proportional to 1/r.

$$H = \frac{\mu(tissue) - \mu(water)}{\mu(water)} \; 1000 \qquad (2.7)$$

CT numbers are commonly quantitized to 12 bits, for a possibility of 4096 integer values. Air is at the low end of the scale with a typical value of -1000 H and bone at a higher level with +1000 H.

2)Modern scanners no longer rely on parallel-beam geometry, but rather on the fan-beam configuration. Figure 2.4 schematically describes the functioning of 3rd and 4th generation tomographs. The presence of a fan-beam permits many measurements to be taken simultaneously thus simplifying the hardware and reducing scanning time. Data collected with a fan-beam geometry are treated with special algorithms. Alternatively, data are interpolated to obtain a parallel ray arrangement and the principles presented above are applied, provided that the projections are collected over an angle of $\pi + \psi$, where ψ is the fan angle.

3)So far, the equations describing the formation of CT images are linear. However, the reconstruction procedure is based on the assumption that the projection data are line integrals of the attenuation coefficient along the x-ray beam path. In theory, this requires monoenergetic and infinitesimally thin x-ray photon-beams (Muller et al. 1985). Departures from this ideal situation, as well as other physical factors, will lead to artefacts.

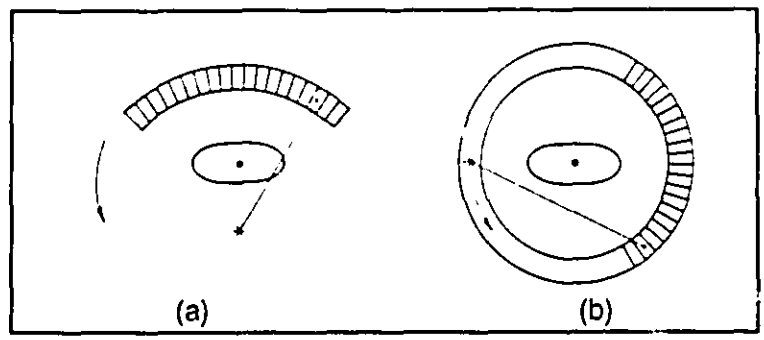

Figure 2.4 Fan-beam geometry

The translational movement of the source-detector assembly is not required since many measurements are taken simultaneously. (a) In third generation rotate-rotate scanners, both the source and detectors synchronously. (b) Fourth generation rotate-fixed scanners are equipped with a full ring of fixed detectors. In this design, only the source is mobile.

2.3 Artefacts

Artefacts manifest themselves as erroneous CT numbers, streaks and/or cupping, a phenomenon in which a homogeneous object appears darker in the middle than at the periphery. In this section, we will examine the different phenomena which give rise to these artefacts: partial volume and exponential edge-gradient effects caused by the finite beam size; beam hardening, a direct consequence of beam polychromacy; scatter and finally aliasing which results from improper sampling. Apart from their origin, we will discuss their effects and how they can be corrected or attenuated.

2.3.1 Partial volume effect (PVE)

Although a tomogram is two-dimensional, it results from the interaction between an x-ray beam of finite height and a three-dimensional object. Therefore the CT number at a given pixel is an axial average of the structures in the corresponding voxel, or volume element. During reconstruction, it is assumed that objects have constant attenuation characteristics in the direction perpendicular to the image plane. In practice, this is not always the case; there may be local variations in CT number within a given tissue or a voxel may be occupied by more than one structure.

According to Glover and Pelc (1980), PVE gives rise to cupping, streaks, and erroneous CT numbers especially at the boundary between two objects. Several algorithmic attempts by the same authors to correct PVE failed even with very simple models simulating the presence of two different tissues within the same pixel. They

attributed this failure to the lack of information necessary to estimate variation of x-ray attenuation in the axial direction. The authors suggested reducing slice thickness as the best way of correcting, or at least restraining, PVE.

2.3.2 Exponential edge-gradient effect (EEGE)

Joseph and Spital (1981) studied the effects of attenuation variations within the image plane. Because of the finite width of the detectors, discrete values representing the average intensity across the detector face are measured. When the finite beam width is taken into account during back-projection, averaging of the line integrals must also be performed. These two averages are often different, especially in the presence of strong spatial gradients. The error arising from this phenomenon is always negative. A slight cupping effect may be present but EEGE usually gives rise to the presence of streaks originating from long and strong edge gradients such as bone-air interfaces or straight metallic objects. These situations are rarely encountered in routine clinical situations but can become a problem with patients who have undergone reconstructive or corrective surgery involving metallic implants.

According to the same authors, the EEGE is inherent to the CT technique and can be present on all scanners. However, scanner geometry can reduce the extent of the artefact by limiting the width of the beam. Corrective algorithms can also attenuate the problem.

2.3.3 Beam hardening effect (BHE)

The attenuation capacities of tissues are strongly energy dependent since low energy x-rays are more easily absorbed than high energy ones. In the presence of a polychromatic source, the linear attenuation coefficient is not proportional to the thickness of the material and equation (2.1) no longer holds. In CT, two situations lead to beam hardening. The first is the presence of highly attenuating materials such as bone, resulting in depressed CT bone values and increased CT numbers in surrounding soft tissues. The second factor is unequal path lengths which results in cupping. In clinical situations, the two phenomena tend to cancel each other (Brooks and Di Chiro, 1976a).

These artefacts can be alleviated by increasing the homogeneity of the beam through prefiltering, by applying correction algorithms (Stonestrom et al. ,1981) and/or dual energy imaging (Coleman and Sinclair; 1985), Barrett and Swindell; 1981)).

2.3.4 Scatter

Compton scatter is due to the inelastic collision between an x-ray photon and an electron, which sends the photon off at a new angle with reduced energy. With the fan-beam configuration, it is inevitable that some photons hitting the detector will have been scattered one or more times. These photons are registered as false data. Scatter affects the image quality in two ways: increased noise and presence of systematic artefacts (Stonestrom and Macovski (1976). According to Kanamori et al. (1985) 3rd generation scanners exhibit cupping while edge round-off is emphasized for tomographs of the 4th generation. Stonestrom and Macovski studied the nature of scatter with a simple statistical model and showed that several schemes can be used for its correction.

2.3.5 Aliasing

Proper sampling requires that the sampling rate be at least twice the maximum frequency contained in the function being sampled. If this condition is not satisfied, frequencies above the Nyquist frequency are "folded back" and take on the identity of lower frequencies. The Nyquist frequency, which is equal to half the sampling frequency, represents the maximum frequency represented in the sampled signal. In CT, aliasing can arise from three different sources: insufficient number of projections, inadequate number of rays per projection, and deficient reconstruction grid.

Number of projections: Kak and Slaney (1988) associated the minimum number of projections M_{min} to the number of rays per projection N. They arrived at the conclusion that M_{min} must be approximately equal to 1.5N ($\pi N/2$) for an artefact free reconstruction. In their 1980 paper, Joseph and Shultz (1980) stated that N is not a relevant parameter to relate to M_{min}, and that ν_{max}, the maximum spatial frequency in the image should be used. In relating M_{min} to ν_{max} and to various machine parameters, they concluded that the number of projections influences the size of the error free reconstruction region. If the number of projections is smaller than M_{min}, streak artefacts appear within a circle of radius R. However even if this condition is not met, objects must be small with sharp edges and high attenuation to produce serious streaks. Even so, the streak intensity is small and narrow viewing windows are required to visualize the streaks.

Number of rays per projection: Joseph et al. (1980) studied the consequences of reconstructing images in which the spacing between ray samples is smaller that the width of the scanning beam. To avoid aliasing, at least two samples per beam width must be measured. If this requirement is not met, small narrow streaks appear. Furthermore, aliasing makes the PSF position dependent. They suggested averaging the output of

adjacent detectors to avoid aliasing artefacts. This is equivalent to expanding the detector size while maintaining the original inter-sample distance. Aliasing can thus be avoided at the expense of reduced spatial resolution.

Third generation scanners, in which each detector is associated with one ray measurement, are particularly susceptible to ray dependent aliasing since only one measurement is gathered per beam width. Peters and Lewitt (1979) suggested displacing the line between the center of the source and the center of rotation by 1/4 of the detector width with respect to the center of the detector face. This "quarter detector offset" geometry leads to interleaving of opposing views (θ and $\theta + 180°$) when data is collected over 360°. Although this simple stratagem may not quite double the sampling frequency, it nonetheless greatly improves aliasing related errors.

Reconstruction grid: The largest frequency to be represented by an N by N image is N/2 cycles per image width (or height). When the maximum frequency in the reconstructed image is larger than this number, Moire patterns appear. These artefacts can be reduced by using a back-projection filter tailored to match the image grid size (Kak and Slaney, 1988).

2.3.6 Justification of linear analysis

In theory, the principles of CT image formation are amenable to linear systems analysis. In reality however, the hypotheses on which the theory is based are not respected and this leads to linear as well as non-linear artefacts. Fortunately, most artefacts can be eliminated, or at least greatly attenuated, with appropriate corrective measures. Therefore, keeping these caveats in mind, it is justified to use linear systems theory to study real CT scanners.

CT systems are characterized by two properties: blur and noise. The following sections describe how these quantities can be estimated.

2.4 Identification of blur characteristics

We can qualify blur as a loss of sharpness associated with an attenuation of the high frequency terms present in a signal. The function which describes the magnitude of this attenuation as a function of frequency is the modulation transfer function (MTF).

We also saw, in the paragraph preceding equation 2.5, that the image of a point source, or the point spread function (PSF), characterizes the blur in the spatial domain. These two ways of considering blur are fully compatible since the PSF and the MTF are

related by the Fourier transform. Therefore, by measuring or identifying one of these entities, the other is automatically defined.

The goal of this section is to review the different methods that have been used to estimate either the PSF or the MTF, and to examine which factors affect blur.

2.4.1 Identification of general linear systems

This summary is based on textbooks by Bendat and Piersol(1980) and Norton (1986), as well as on the following articles: Rossman (1980), Metz and Doi (1979), Giger and Doi (1984), Sawaragi et al. (1985).

In classical system identification, the system is considered as a "black box" with the characteristics an unknown. By comparing the input and output signals, these characteristics can be deduced. The assumption of linearity allows one to find the response to any input by breaking this input into simple components and adding the contribution of each constituent. Therefore, by finding the response of the system to one of these simple inputs, the system is characterized. The appellation of various outputs, and their correspondence in general system and imaging system identification are summarized in Table 2.1.

GENERAL SYSTEMS		IMAGING SYSTEMS		DOMAIN
function name	symbol	function name	symbol	
impulse response	IRF	point spread	PSF	spatial
step response	SRF	edge response	ERF	spatial
		line spread	LSF	spatial
frequency response	FRF	optical transfer	OTF	frequency
gain		modulation transfer	MTF	frequency
phase		phase transfer	PTF	frequency

TABLE 2.1 Correspondence of functions used in general and imaging system identification

One of the simplest inputs is the impulse, whose associated output is called the impulse response function (IRF) in the general system identification literature and point spread function (PSF) when applied to imaging systems. The advantage of this input is that it directly describes the blurring characteristics. This must be weighted against the difficulty of producing an impulse, which, in theory, has no duration or spatial extent, and has infinite magnitude. The large input signal may also cause saturation and the appearance of non-linearities.

Some of these short-comings are alleviated with the use of a step function. The derivative of the system's reaction to this stimulus, the step response function (SRF), yields the IRF. The equivalence of the SRF in 2D is the edge response function (ERF) whose derivative is the line spread function (LSF). By definition, the LSF is the response to a line source of given orientation θ. It can also be thought of as the sum of a series of shifted PSF:

$$LSF_{\theta}(x_r) = \int_{-\infty}^{\infty} PSF(x_r, y_r)\, dy_r \tag{2.8}$$

Marchand (1964, 1965) and Roa and Jain (1967) have extensively studied the relationship between these two functions.

While a step function may be easier to produce than an impulse, it suffers from noise amplification produced during differentiation. Furthermore, the power of a step function is concentrated at low frequencies. With such an input signal, the attenuation characteristics at higher frequencies are not as reliable as if they had been obtained from a signal exhibiting a flat frequency spectrum.

The use of correlation methods can counteract the first of these objections. The methods are based on the Wiener-Hopf equation, which states that the input-output cross-correlation is equal to the convolution between the IRF and the input auto-correlation function:

$$C_{ab}(x, y) = h(x, y) ** C_{aa}(x, y) \tag{2.9}$$

where a and b: input and output signals
C_{aa}: input auto-correlation
C_{ab}: input-output cross-correlation

Correlation reduces the effects of noise through the summation of successively shifted terms. However, the method involves more computation than other methods since the IRF must be deconvolved. The stability of the numerical solution depends on the correlation properties of the input signal. Furthermore, the input must have sufficient power over all frequencies for proper identification.

We now turn our attention to identification based on frequency methods. If a 2D system is linear and shift-invariant, the output to a sinusoid is also a sinusoid of the same frequency and direction but with possibly a different amplitude and phase. The function describing these changes is the transfer function or optical transfer function (OTF) when applied to imaging systems. The magnitude of the OTF is the modulation transfer function (MTF). This last function describes the ratio of output to input modulation as a function of frequency, where modulation is defined as the ratio of amplitude to average value of a signal

(Barrett and Swindell, 1981). The phase transfer function (PTF) represents the phase lag as a function of frequency.

The OTF and PSF are Fourier transform pairs:

$$OTF(\nu_x, \nu_y) = \mathcal{F}\{PSF(x, y)\} \tag{2.10}$$

$$PSF(x, y) = \mathcal{F}^{-1}\{OTF(\nu_x, \nu_y)\}$$

where $\mathcal{F}$: Fourier transform

ν_x, ν_y: spatial frequency

When the PSF is symmetric, the PTF can only take on values 0 or π, and the MTF completely characterizes the blur in the frequency domain.

The advantage of using periodic signals as input is that the MTF can be obtained directly without Fourier transforming the data. However, measurements must be repeated at different frequencies and only discrete values of the MTF are obtained.

In the following section, we will see how these concepts have been used to identify the PSF or MTF of CT scanners.

2.4.2 Identification of the modulation transfer function of CT scanners

A few theoretical studies have been conducted to characterize the MTF (Glover and Einsner, 1979,1980; Glick et al. ,1989). These investigations are useful in relating the MTF to various design parameters such as detector size, sampling rate, focal spot size etc. However, these theoretical tools cannot be used to measure the MTF of any given unit, because the number of unknown parameters is too large. Therefore one must resort to experimental techniques.

Three types of inputs have been used to identify the MTF of CT scanners experimentally: impulses (or point sources) simulated by thin metallic wires, edges obtained by placing a straight edged object in water, and periodic signals such as star or bar patterns.

Impulse methods: Bishoff and Ehrhardt (1977) estimated the MTF by Fourier transforming the image of a 0.15 mm diameter steel wires placed in a water filled phantom. The estimates were corrected for finite wire size, non-zero mean value of the surrounding water and region size. By comparing the MTF in three different directions (horizontal, vertical and diagonal), they concluded that MTF was radially symmetric. They also determined that the system was shift-invariant, i.e. that the MTF (or PSF) was independent of position, by imaging the wires in three different positions.

Ehrhardt (1986) argued that if the image is off-centered or offset by a distance **d**, symmetry can be employed to double the sampling frequency by mirroring data from one side of the center line to the other. Simulations revealed that, in the presence of Poisson distributed noise, the error in computing the MTF was within reasonable range if the signal to noise ratio was high, the offset **d** in the range of 0.1-0.4 pixel width and the error in estimating the offset smaller than 2%-3% of pixel width. An error of 10% pixel width in estimating **d** leads to unacceptably large MTF errors (15% to 60%).

Nickoloff and Riley (1985) devised a simple identification technique applicable to most CT scanners via a modelling approach. Their analysis indicated that most PSFs could be described by a Gaussian function whose shape is described by a single parameter α related to the exponential rate of decay. This parameter is given by the slope of the linear regression between the square root of the natural logarithm of (1/PSF) and the radial distance from the point source. For all scanners tested, the linear correlation coefficient was greater than 0.99, indicating that the assumption of a Gaussian PSF was reasonable. The authors pointed out however that the method could cause problems with edge enhancement reconstruction filters. These apodizing functions introduce undershoots and the PSF can no longer be modelled as a Gaussian function.

A common objection to the use of a thin wire as input is that few points are available. This situation can lead to an ill-defined MTF due to aliasing (Ehrhardt, 1986; Nicholoff and Riley, 1985; Schnelders and Bushong, 1978). The method proposed by Ehrhardt (1986), and presented above, and/or reducing the pixel size can alleviate this shortcoming. Modelling can also be used to address this problem since the model can be digitized at any desired sampling rate. If the analytical function describing the PSF is not too complicated, the MTF can also be determined analytically.

The greatest advantage of this method is that the PSF is obtained directly with little or no data manipulation. Furthermore, a point source input provides a full two-dimensional description of the PSF. Being limited in size, it constitutes a good signal for the study of shift-variance.

Edge methods: The most popular method for measuring the MTF is via the edge response function (ERF):

$$MTF = \left| \mathcal{F}\left\{ \frac{d\ ERF(x)}{dx} \right\} \right| = \left| \mathcal{F}\{LSF(x)\} \right| \qquad (2.11)$$

Judy (1976) imaged 14 water-plexiglass interfaces in different orientations. The ERF demonstrated an undershoot on the side of the water and a consistently larger

overshoot near the plexiglass resulting in a non-symmetric LSF. Three arguments were offered to explain this phenomenon: scatter, a local change in the attenuation coefficient at the surface of the plastic through increased density due to machining and noise, which was identified as the primary source of variation in the estimates.

Logan and Hickey (1983) measured the LSF of a gamma camera in much the same way as Judy. The authors compared three methods of differentiation: three-point difference, five-point difference, and analytically differentiating a cubic spline function which had been previously fitted to the ERF. The third method proved to be the most accurate. This result is not surprising since fitting the spline function smooths the data thereby reducing the effects of noise.

To overcome the amplification of high frequency noise due to differentiation, Schneiders and Bushong (1978) proposed a method for obtaining the MTF directly from the ERF by integrating equation (2.11) by parts. This method was compared to Judy's in the presence of low and high noise. Both schemes were equivalent in the low noise case but the one step procedure proved superior when higher noise levels were involved. In a follow up article (Schneiders and Bushong (1980)), it was also compared to the impulse method. Prior to taking the Fourier transform, the PSF was manually smoothed (i.e. the user traced a smooth curve through the data according to his/her perception). The MTF derived with the wire technique showed slightly depressed values when compared to the other two. The authors offered two possible reasons. First, computation from the PSF was based on 18 points as compared to the ERF which counted 500 samples. Secondly, the wire was located further toward the periphery of the field of view, where it may actually be different than where the interface was located. Our own work presented in Chapter 5 supports this explanation.

Cunningham and Fenster (1987) noted that numerical differentiation differs from analytical differentiation and therefore introduces an error in the LSF and the MTF. The true MTF can be recovered from the sampled case by multiplication with a filter representing the frequency ratio of analytical versus finite element differentiation.

By placing an edge at a slight angle with the image raster, the sampling rate can be greatly increased, thereby circumventing the major objection to the use of point sources. However, this stratagem is valid only if the PSF is stationary or shift-invariant.

This method counts a number of disadvantages. It involves more data manipulation since the edge profiles must be differentiated to provide the LSF. Furthermore, the ERF must be smoothed or fitted with an analytical function prior to differentiation in order to attenuate the effects of noise. Alternatively, the method proposed by Schneiders and Bushong (1978) can be used for the same purpose. Another drawback is that the

procedure must be repeated at a number of edge orientations if a bi-dimensional description of the MTF is required. Furthermore, the energy of a step function is concentrated at low frequencies. With such an input signal, the attenuation characteristics at higher frequencies are not as reliable as if they had been obtained from a signal exhibiting a flat frequency spectrum.

Frequency methods: The MTF can be evaluated directly by measuring the response to periodic signals of different frequencies. To do so, McIntyre et al. (1976) used the sunburst phantom. Concentric circles drawn from the point of intersection of nylon tapered wedges placed in water create periodic signals whose frequency decreases with distance from the center. The authors expressed the MTF in terms of the ratio of output to input modulation:

$$MTF = \frac{(CT_{max} - CT_{min}) \;/\; (CT_{max} + CT_{min})}{(CT_{nylon} - CT_{water}) \;/\; (CT_{nylon} + CT_{water})} \qquad (2.12)$$

where CT_{min}, CT_{max}: minimum and maximum values of CT numbers along the circumference of a circle of given radius

CT_{nylon}, CT_{water}: average CT value of nylon and water measured in the bulk of the material

At high frequencies, near the center of the phantom, few points were available to determine CT_{min} and CT_{max}. As a consequence, the uncertainty in MTF estimates increased with frequency. The authors placed little credence in MTF values less than 0.15. Furthermore, because the input signal was a square wave as opposed to sine wave, and therefore contains high frequency harmonics, the MTF was overestimated.

Based on the Fourier series expansion of a square wave, and on the argument that the output of a square wave is a single sinusoid of the same frequency and reduced amplitude for frequencies greater than a third of the cut-off frequency, Droege and Morin (1982) derived a simple expression for the MTF. To circumvent the difficulty of estimating the maximum and minimum amplitudes in the presence of noise, they expressed the modulation in terms of signal variance, measured over a region within the image of bar patterns of discrete frequencies. The method was compared to the Fourier transform of a wire image. Both techniques yielded similar results for the mid-frequency range. However, the bar pattern method was not valid for very low frequencies since it is formulated for frequencies larger than a third of the cut-off frequency. Furthermore, uncertainty in the MTF values at high spatial frequencies made the determination of the cutoff frequency difficult. Advantages include simplicity, speed, and insensitivity to image noise as well as immunity to aliasing (Droege and Rzeszotarski (1985)).

2.4.3 System shift-variance

In the studies presented above, most authors assumed the system to be shift-invariant or isoplanatic, i.e. the shape and size of the PSF was invariant throughout the image plane. With real imaging systems, this hypothesis is a weak one (Goodenough (1977), Schneiders and Bushong (1980), Rossman (1961), Barrett and Swindell (1981)). Surprisingly only a few studies have been conducted on the subject. Bracewell (1977) and Verly and Bracewell (1979, 1980) showed that CT scanners are shift-variant due to finite x-ray beam width. Some of their conclusions regarding the change of PSF shape with position are:

1) Based on an analytical expression of the PSF as a function of radial and angular position, they determined that the PSF becomes progressively wider in both directions as distance from the center of the field of view increased.

2) The rate of change being different in the two directions, the rotational symmetry exhibited in the center is lost at the periphery of the field of view.

3) Scanners that collect data over 360° produce a rotating blur, i.e. the PSF is independent of angular position when expressed in a rotating coordinate system.

Joseph (1980) and Joseph et al. (1980) determined that aliasing can cause the PSF to change with position while Kijewski and Judy (1983) concluded that projection misregistration can have the same effect. Scanners with continuous detectors are particularly susceptible to registration errors.

2.4.4 Factors affecting blur

The PSF mathematically describes how the image is blurred. If a single measure were used to summarize this function, it would be the spatial resolution.

There is some controversy in the literature concerning the definition of resolution (Bassano, 1980; Boyd and Parker, 1983). Throughout this text, we refer to resolution as the smallest distance between point sources such that their images can be distinguished.

Because resolution is intimately related to the PSF, any factors affecting one will influence the other. The back-projecting procedure introduces a blur proportional to 1/r where r is the radial distance from the point source position. This inherent blur is corrected by the apodized rho-filter in such a way that the resulting ideal PSF due to filtered back-projection is the apodizing function, although the type of interpolation can also modify the PSF. The apodizing function is often referred to as the algorithmic contribution to the PSF as opposed to the hardware contributions which include: focal spot size, detector aperture size, sampling rate, as well as pixel size (Glover and Eisner (1979) and (1980), Citrin (1986)).

The focal spot and detectors are approximately rectangular. The Fourier transform of such a shape is a combination of sinc functions which lead to an attenuation of high frequencies and therefore to increased blur. The effect of pixel size is minimal until the pixel width becomes larger than the resolution due to other factors. When this situation arises, the resolution is said to be limited by pixel size. The sampling rate comes into effect when the signal is sub-sampled in which case aliasing can modify the PSF.

2.5 Noise in CT images

Noise limits the quantitative use of CT data as well as the capacity of an observer to detect low contrast objects. It may originate from a number of sources, photon statistics and electronic noise being the most important. Electronic noise arises in detector, amplifiers, analog to digital converters etc. This type of noise is not treated explicitly in the literature. However, Hanson (1979) notes that electronic noise is added to statistical noise in the projections and is subjected to the same reconstruction process.

We will therefore start by detailing the photon statistics before concentrating on the characteristics of the noise in CT images.

2.5.1 Photon statistics

This section is based on chapters 3 and 10 of Barrett and Swindell (1981) and chapter 5 of Kak and Slaney (1988). It first describes the amplitude structure of photon noise then examines how it affects the projection data and how it is propagated through the reconstruction process.

A photon must undergo a number of events before contributing to the projection values. It must be emitted, traverse a medium, and then be detected. These events are best described by a Poisson distribution:

$$Pr(N) = \frac{\overline{N}^N}{N!} e^{-\overline{N}} \tag{2.13}$$

where $\overline{N}$ is the mean number of photon counts in a given interval of time. The value of the measured projection at the i^{th} projection angle and j^{th} detector l_{ij}, affected by noise, becomes a random variable whose expected value is:

$$< l_{ij} > \approx -\ln \frac{\overline{N}_{ij}}{N_0} \tag{2.14}$$

where $\overline{N}_{ij}$ is the mean number of detected photons and N_0 the number of emitted photons. The variance of the measured projection is equal to:

$$\sigma^2_{I_{ij}} = \frac{1}{\bar{N}_{ij}} \tag{2.15}$$

With the assumption that all fluctuations in N_{ij} that have a significant probability of occurrence are much less than the mean, the expected value of the measured projection becomes the value of the noiseless projection (Kak and Slaney, 1988). Therefore, the expected value of the reconstructed image is that obtained in the noiseless case. However, its variance at point $(x_r,y_r) = (r,\theta)$ is a rather complicated expression:

$$\sigma^2_{\mu}(r,\theta) = \frac{M}{\pi} \int_0^{\pi} \left\{ \frac{1}{\bar{n}_{\phi}(x_i)} * a^2(x_i) \right\}_{x_r = r\cos(\theta-\phi)} d\phi \tag{2.16}$$

where $a(x_r)$: apodizing function,

M: number of projections,

$\bar{n}_{\Phi}(x_r)$: linear count density or number of detected photons per unit projection length.

Equation (2.16) demonstrates that image noise depends on the reconstruction filter (the algorithmic portion of the MTF). Furthermore, the shape of the source and detector have no bearing on the probability of emission or detection. This implies that noise is not blurred by the scanner aperture function as a signal is, and that the non-algorithmic or hardware portion of the MTF has no affect on noise (Kijewsky and Judy, 1987).

2.5.2 Variance studies

A number of studies have related the noise variance to various physical and geometrical factors. Brooks and Di Chiro (1976b) determined the following analytic relationship:

$$\sigma^2_{\mu} \propto \frac{1}{w^3\, h\, D} \tag{2.17}$$

where w: beam width,

h: beam height

D: dose.

The degree of beam collimation controls both the beam width and beam height, while the dose varies proportionally to tube current.

The predicted dependence of noise on slice thickness and dose agreed well with the experimental results of Goodenough at al. (1977). Similar relationships were reported by a number of authors (McCullough (1976), Chesler et al. (1977), Riederer et al. (1978), Hanson (1979)).

Equation (2.17) clearly brings out the relationship between noise and beam width which is intimately related to resolution. An increase in resolution will lead a cubic increase in noise. Furthermore, any attempt at reducing noise, by using a smoothing apodizing function as suggested by equation (2.16) for example, will lead to a deterioration in resolution. The only means of improving resolution without affecting noise is to increase the dose.

Goodenough et al. (1977) determined that the noise was stationary by measuring the variance of a water bath phantom at five different locations. In images of composite objects however, this conclusion does not hold because noise is signal dependent. Photons traversing tissues with high attenuation coefficients have a stronger probability of being delayed than those penetrating low attenuation tissues. Therefore, bone will generate more noise than soft tissue.

2.5.3 Frequency structure studies

Simple statistical parameters such as the variance describe only the amplitude structure of the noise. The noise power spectrum (NPS) is a measure of the frequency distribution of the mean square value of the data (Bendat and Piersol, 1980). It is mathematically defined as:

$$NPS(\nu_x,\nu_y) = \frac{1}{A} < \left| \int\int_A n(x,y)\, e^{-2\pi i(\nu_x x+\nu_y y)}\, dx\, dy \right|^2 > \qquad (2.18)$$

where n(x,y): reconstructed image containing only noise,

A: area of this image,

< >: expected value.

In order to estimate the NPS, a uniform object such as a water phantom is scanned. The central portion of the image is Fourier transformed and estimates of the NPS obtained by squaring the modulus of the transform (Hanson (1979), Borasi et al. (1984), Faulkner and Moores (1984), Kijewski and Judy (198⁻)). Usually a large number of spectra are averaged to obtain a smooth estimate. As many as 2000 images were used by Kijewski and Judy.

Although equation (2.18) is useful to experimentally measure the NPS, it does not reveal how the NPS is related to the image reconstruction process. To do so, a number of authors (Barrett and Swindell (1981), Faulker and Moores (1984), Kak and Slaney (1988), Riederer et al. (1978)) have used the relationship between the NPS and the autocorrelation function. Realizing that the autocorrelation function and NPS are Fourier transform pairs,

one can obtain the form of the NPS through the analysis of the autocorrelation function. This analysis leads to the following expression for the filtered back-projected NPS:

$$NPS(\varrho) = \frac{M}{\pi \bar{n}} \varrho \, |A(\varrho)|^2 \qquad (2.19)$$

where M: number of projections,

$\bar{n}$: average number of detected photons,

ρ: radial frequency,

A(ρ): apodizing function,

Here again the dependence of noise on the reconstruction filter is evident. Comparison of equations (2.16) and (2.19) shows that the variance can be obtained by integrating the NPS over frequency.

Equation (2.19) also shows that noise is spatially correlated and that the extent of correlation is governed by the apodisation function. The consequence of spatial correlation on the computation of the variance was investigated by Riederer et al. (1978) who concluded that the variance estimate computed over a region of given size, was a function of the region shape. For example, the variance computed over long narrow strips should be higher than for a square or circular region. This dependence on region shape was tested experimentally on a 4x64 and 16x16 pixel area. The variance for the rectangular region was 50% larger than for the square.

In a discrete formulation analysis of the NPS, Faulkner and Moores (1984), arrived at a formulation similar to equation (2.19). They pointed out, as did Wagner et al. (1979) that the NPS reveals the algorithmic portion of the MTF. Therefore the portion of the MTF due to hardware can be obtained by dividing the total MTF by the algorithmic contribution determined by the NPS.

Kijewski and Judy (1987, 1988) expanded Faulkner and Moores' study to consider interpolation and 2D sampling. They argued that, although the projections are discrete, their spectrum is continuous, with frequencies extending to infinity. This is due to interpolation: a continuous function must be formed for values to be available at the points where they are required. Because noise is not affected by aperture smoothing, the only mechanism for removing high frequencies, and thus limit aliasing, is interpolation, a low pass operation.

They concluded that aliasing can destroy the rotational symmetry of the NPS, an assumption which was used in the formulation of equation (2.19). They also showed that aliasing induces an increase in the low frequency components and can cause the DC term to be non-zero. Simulation studies demonstrated that aliasing effects were substantial for

nearest neighbor interpolation but minimal for linear interpolation. The measured NPS of a commercial scanner showed improved rotational symmetry over simulations. This discrepancy was explained by the use of stationary white noise and parallel-beam geometry in the formulation of the model. While these hypotheses simplified the model, they are not valid for real systems. Indeed, the noise is neither stationary, since it is correlated with the input, not is it white (see equation (2.19)). Furthermore, modern scanners are constructed according to a fan-beam geometry.

2.6 Conciusions

Although a great amount of research has been carried out to characterize X-ray scanners, we feel that these studied are inadequate for our needs. The goal of most of these studies was to provide a fast means of comparing different scanners or of monitoring a given scanner over time. This is quite different from our objective which is to use this information to process the images more effectively.

Theoretical studies are useful in establishing relationships between system characteristics and scanning parameters such as the apodizing function, beam width, beam height and so on. But they can only take a small number of factors into account. Because of this limitation, we chose to measure the system characteristics experimentally.

Both the variance of the noise and its frequency distribution are important in image processing. However, noise variance studies fail to reveal how the image reconstruction filter affects these characteristics. Furthermore, since each manufacturer implements differently a number of these filters, noise properties vary accordingly. Therefore, to study the influence of the image reconstruction filter on the amplitude as well as the frequency content of the noise, one must turn to frequency analysis techniques.

A number of comments can be made regarding the identification of blur:

1) Many of the non-parametric identification methods developed for general 1D systems (impulses, steps, wave patterns) were adapted to identify the PSF of X-ray CT scanners. However, correlation based methods, which are very popular in other fields, have never been used for this purpose.

2) It is generally assumed that CT scanners are shift-invariant. This hypothesis has been challenged by a small number of researchers who theoretically investigated the affect of aliasing, projection misregistration and finite beam width on the change of PSF shape with position. However, we found no evidence of an experimental protocol to measure shift-variance in the literature.

3) The absence of experimental shift-variant identification method may be explained by the lack of adequate parametric models describing the shape of the PSF. The

only efforts in this direction are due to Nickoloff and Riley (1985) who nonetheless assumed radial symmetry and linearized the proposed Gaussian model.

The first part of this thesis (Chapter 3-6) is committed to overcoming these deficiencies. In the following chapters (7 and 8) we will examine how the experimentally obtained system characteristics can be used in the context of image processing.

CHAPTER 3
IDENTIFICATION OF NOISE CHARACTERISTICS

3.1 Introduction

It is very common in image processing to assume the presence of Gaussian white noise with a given variance (Gonzalez and Wintz, 1987; Lunsher and Beddoes, 1986; Nalwa, 1987; Canny, 1986). Yet the outcome of many algorithms is influenced by the frequency structure of the noise, and deviation from the hypothesis of white noise can be detrimental. Therefore, before processing CT images, it is important to gain some knowledge of both the variance of the noise and its frequency distribution. Fortunately, the noise power spectrum (NPS) encompasses information about both these entities.

The goal of this chapter is therefore to estimate the NPS of a CT scanner, and to quantify the changes of noise properties due to image reconstruction filter and slice thickness. Section 3.2 describes the materials and methods used to achieve this goal. Results are presented and discussed in section 3.3 while section 3.4 concludes the chapter.

3.2 Methods

All data in this and subsequent chapters were generated with a Philips, third generation Tomoscan CX scanner. Scanning parameters included: 120 kV tube voltage, 200 mA current, and a 4.5 s scan time for 540 projections. A circular imaging field of view (FOV) of 200 mm in diameter was reconstructed onto a 320x320 image, providing square pixels of 0.625 mm in side. Smaller pixels were obtained by interpolating the projections prior to back-projection using the zoom option. This reduced the FOV by a factor equal to the zoom factor.

Figure 3.1 contains an image of section D of the Philips performance phantom. It consists of a plastic cylinder filled with water representing a homogeneous object. Images of the phantom were reconstructed with three different apodizing functions: head smoothing (0), head edge enhancement (1), and high resolution (4) in order to investigate the effect of the filtered back-projection algorithm on the NPS. The images were also produced with a slice thickness of 2, 5 and 10 mm.

A 128x128 pixel area in the center of the images provided the data required to estimate the NPS. The overlapped, averaged, periodogram technique was used for this purpose (Oppenheim and Schafer, 1975; and equation 2.18). The 128x128 region was

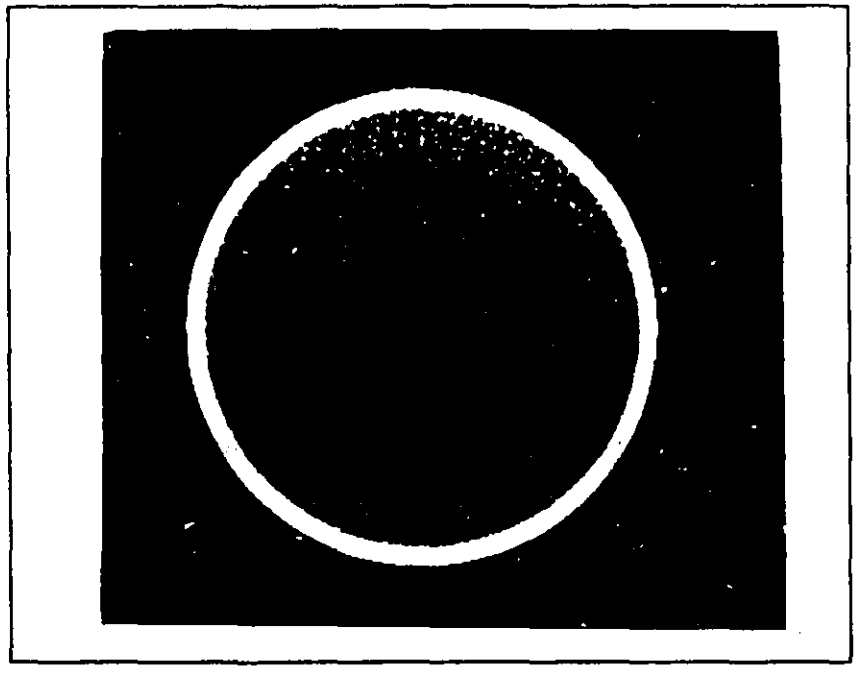

Figure 3.1 Image of section D of the Philips performance phantom

Section D of the phantom consists of a water filled plastic cylinder. A 128x128 pixel region in the center of the image was used for NPS computation.

subdivided into 32x32 pixel subregions overlapping by 24 pixels in both the row and column directions. The data in each subregion was Fourier transformed and averaged.

Due to the nature of the signal, it is very difficult to obtain a smooth estimate of the 2D NPS from a single image. One way of dealing with this problem is to average the estimates obtained from a large number of images. Kijewski and Judy (1987) opted for this alternative and used as many as 2000 images for a single estimate. We chose a second option which consisted of smoothing the NPS by averaging the power contained in concentric annuli centered on the DC term. A single image was necessary for each estimate thereby greatly reducing processing time compared to the previous method.

This method is based on the hypothesis that the spectra are radially symmetrical. We justify this assumption based on the results of Kijewski and Judy (1987, 1988). In a series of simulations, these authors determined that aliasing could destroy the rotational symmetry of the NPS. However, they observed that the degree of aliasing, which depends on the interpolation method, was minimal for linear interpolation. According to the information provided by the manufacturer (Philips, 1988), the Tomoscan CX uses such an interpolation mode. Furthermore, Kijewski and Judy observed that the NPS estimated with

data obtained from commercial scanners showed improved symmetry when compared to the results of the simulations. Under these circumstances we therefore felt justified to assume rotational symmetry.

The NPS was characterized in terms of total power, maximum power, the frequency corresponding to the maximum power, f_{max}, and the frequency below which 90% of the power was located, $f_{90\%}$.

3.3 Results

Due to the NPS smoothing technique, our results are presented in the form of 1D spectra. Figure 3.2(a) shows the NPS obtained using the three filters and a slice thickness of 10 mm. It is evident that there was substantially less noise at all frequencies with filter 0 than with filter 4, the smoothing and high resolution filters respectively. Table 3.1 shows that the total noise power obtained with filter 4 (291 205) was more than five times that exhibited by filter 0 (53 907). Furthermore, the noise was concentrated at lower spatial frequencies with filter 0 ($f_{max} = 0.25$ cycles/mm and $f_{90\%} = 0.60$ cycles/mm) than with filter 4 ($f_{max} = 0.50$ cycles/mm and $f_{90\%} = 0.95$ cycles/mm).

Figure 3.2(b) illustrates the NPS obtained with filter 0 and slice thickness of 2, 5 and 10 mm. The magnitude of the noise power decreased progressively with increasing slice thickness but there was no significant change in the frequency distribution, neither f_{max} nor $f_{90\%}$ changing. The other two filters behaved similarly.

Imaging mode and slice thickness both influence total noise power which is equal to the integral of the NPS. For a constant slice thickness, images produced with the high resolution filter (filter 4) were noisier than those created with the head edge enhancement or smoothing filters (filters 1 and 0 respectively). For any filter, noise power diminished with increasing slice thickness as predicted by equation 2.17,indicating that averaging is performed along the axis perpendicular to the plane of image formation.

Different combinations of image reconstruction filter and slice thickness may yield similar noise power levels. For example, filter 4 with a slice thickness of 10 mm and filter 1 with a slice thickness of 2 mm both generate total power of about 250 000 (see table 3.1). However, this does not guarantee that the output of an image processing algorithm would be the same when presented with images produced under these conditions. Indeed, many algorithms, as well as human perception, are sensitive to noise frequency distribution. Edge detectors are particularly affected by high frequency noise since edge information is present in the higher signal frequencies. This subject will be discussed at more length in Chapter 8.

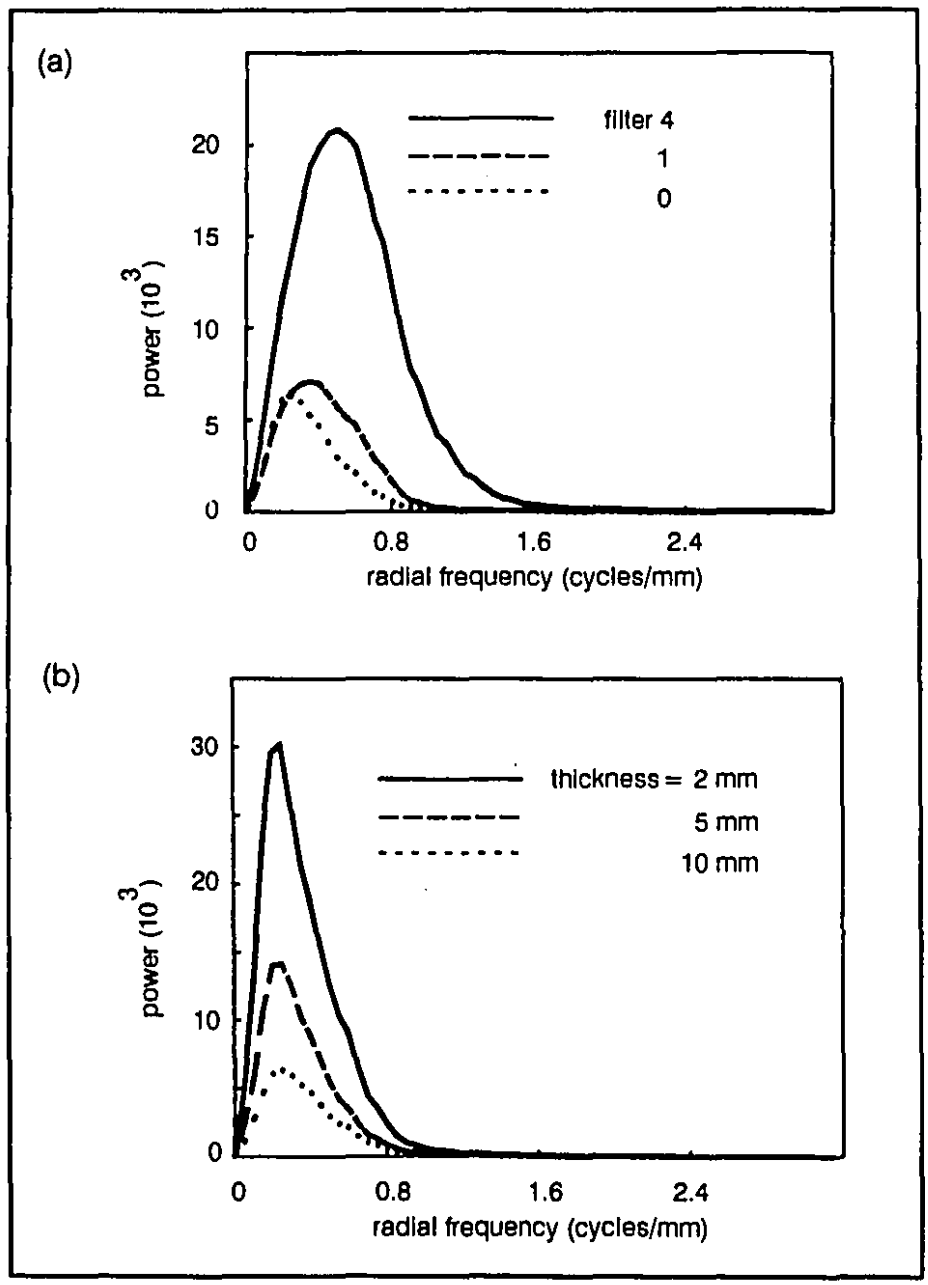

Figure 3.2 1D noise power spectra

The spectra were computed by averaging the values of 2D spectra contained in concentric rings centered on the DC term. (a) effect of reconstruction filter, the slice thickness for all filters was kept constant at 10 mm (b) effect of slice thickness for filter 0.

filter	thickness (mm)	$f_{max\ power}$ (cycles/mm)	max power	$f_{90\%\ power}$ (cycles/mm)	total power
4	10	0.50	20 804	0.95	291 205
1	10	0.35	7 063	0.70	77 476
0	10	0.25	6 331	0.60	53 907
0	5	0.25	14 152	0.60	108 116
0	2	0.25	30 148	0.60	239 110

TABLE 3.1 Estimates of NPS parameters

$f_{max\ power}$: frequency corresponding to maximum power
$f_{90\%\ power}$: frequency below which 90% of the power is contained
total power: sum of power terms contained at each frequency of full 2D NPS

3.4 Conclusions

The goal of this chapter was to quantitatively investigate the noise present in x-ray tomograms produced under different conditions of beam collimation, which defines the slice thickness, and image reconstruction filters.

The noise power spectrum analysis showed that both thickness and filter influence total noise power and hence the variance of the noise. The total power exhibited by the high resolution filter (filter 4) combined with a thickness of 10 mm was approximately five times greater than for the smoothing filter (filter 0). Furthermore, decreasing the slice thickness from 10 mm to 2 mm resulted in an almost fivefold increase in noise levels for filter 0.

The frequency structure was independent of slice thickness but greatly influenced by the reconstruction filter. The smoothing nature of filter 0 was emphasized not only by lower levels of maximum and total power for a given beam collimation, but by a concentration of power at lower frequencies as indicated by smaller values of f_{max} and $f_{90\%}$ when compared to the other filters.

CHAPTER 4
PARAMETRIC MODELLING OF THE PSF

4.1 Introduction

One of the hypotheses underlying many image restoration algorithms is that images are produced by a shift-invariant system. However, the theoretical work of Verly and Bracewell (1977, 1979, 1980) indicated that this assumption does not hold for real CT systems. Therefore, before restoring images from a given scanner, its shift-variance should be estimated.

In order to experimentally quantify the change in PSF shape with position, one must be able to parametrically describe this shape. However, a review of the CT system identification literature revealed a scarceness of parametric models of the PSF.

The first goal of this chapter is therefore to develop and evaluate non-linear, anisotropic models of the PSF. The second goal aims at simplifying model interpretation by relating the parameters to a simple physical quantity: resolution. The methodology is described in section 4.2 while the results are presented in section 4.3 and discussed in section 4.4. Finally section 4.5 concludes the chapter.

4.2 Methods

The use of a thin metallic wire as an input signal for non- parametric identification of the PSF presents a number of advantages:

1) it is localized and therefore constitutes a good signal for the analysis of shift-variance.

2) it is radially symmetric. Symmetry properties can be deduced from a single image as opposed to an edge whose orientation must be modified and many images analyzed to obtain this information.

For these reasons, images of the wire in the resolution section of a commercial phantom provided the data for the parametric models.

The Gaussian model has been suggested in the literature to describe the shape of the PSF. To our knowledge however, this model has not been thoroughly tested. Furthermore, certain features of the PSF produced with the high resolution filter cannot be represented by the Gaussian function. This encouraged us to generate a new model which we called the damped cosine function. Both models inherently assume a background level of 0 which is not always the case. A new parameter was therefore introduced to take this factor into account.

The blurring characteristics are best appreciated in the frequency domain. Parametric MTF were derived analytically for both models and compared to non-parametric estimates. The models also provided measures of resolution which were compared to non-parametric and subjective criteria.

4.2.1 Non-parametric identification

All data in this chapter were generated by imaging section B of the Philips performance phantom shown in Figure 4.1. Scanning parameters included a tube voltage of 120 kV, a current of 200 mA, and a scan time of 4.5 s necessary to gather 540 projections

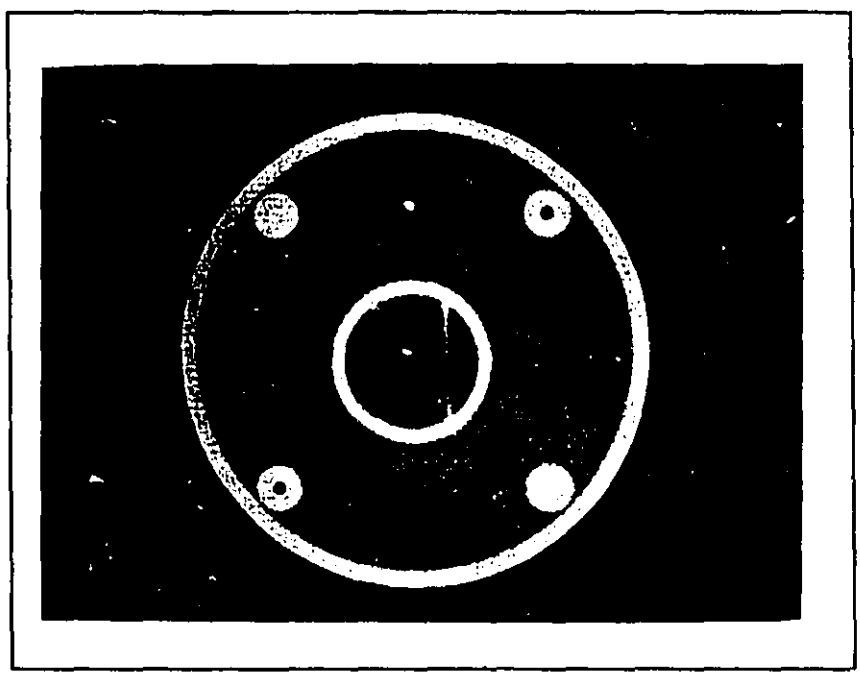

Figure 4.1 Image of section B of Philips performance phantom

Section B of the phantom was used for PSF and resolution analysis. The arrow, which has been added on the image of the phantom, points to the metallic wire simulating an impulse.

The effect of the apodizing function on the blurring characteristics was investigated by reconstructing the images with three filters: head smoothing (0), head edge enhancement (1) and general high resolution (4). The effect of noise on the parametric model fitting procedure was studied by producing images with a a slice thickness of 2, 5 and 10 mm.

Subjective measures of the system's spatial resolution were determined from images of periodic bar patterns found in the center of the phantom (see Figure 4.1). The

input for the non-parametric identification of the PSF consisted of a 0.35 mm diameter steel wire positioned above the bar patterns.

4.2.2 Parametric models for the point spread function

Gaussian model: A first parametric model of the scanner PSF was obtained by fitting a 2D Gaussian function to the data contained in a region surrounding the image of the wire. Regions of 16x16 and 64x64 pixels were used for the 200 mm and 50 mm field of view (FOV) respectively. The Gaussian model is given by:

$$PSF_g(x,y) = N\, e^{-p_x^2(x-t_x)^2}\, e^{-p_y^2(y-t_y)^2} + B \qquad (4.1)$$

where x row direction
y column direction
N maximum value of the function
t_x, t_y x and y coordinates of the maximum
p_x, p_y x and y direction shape parameter
B average background value.

The shape parameters, p_x and p_y, determine the rate of decay of the exponential. The higher the value of p, the faster the PSF decays, and the greater the resolution. The relationship between resolution and model parameters will be developed in more detail in section 4.2.4.

An iterative Gauss-Newton, nonlinear least-square fitting algorithm (NAG [1] subroutine e04fde) was employed to determine the model parameters providing the best fit to the wire image data. This algorithm required relatively good initial parameter estimates. These were obtained as follows:

1) The maximum value of the data was used as an estimate of N and the corresponding pixel location for t_x and t_y.

2) Model linearization and separation of variables then provided a means of estimating the shape parameters. This was achieved by scanning the data independently in the row and column direction passing through the maximum. Thus, when scanning in the column direction with $x = t_x$, the exponential term in x becomes 1 and equation (4.1) simplifies to:

$$PSF_g(t_x,y) = N\, e^{-p_y^2 y^2} \qquad (4.2)$$

1- NAG FORTRAN Library Mark 13, Numerical Algorithm Group, NAG Inc., 1101 31st Street, Suite 100, Downers Grove, Ill. 60515-1263, USA.

Taking the square root of the natural logarithm of equation (4.2) gives:

$$\sqrt{\ln\left[\frac{N}{PSF_y(t_x,y)}\right]} = p_y\, y \qquad (4.3)$$

The initial estimate of p_y was obtained from the slope of this linear relationship (NAG subroutine f04jge). Parameter p_x was estimated by scanning in the row direction passing through the maximum and applying a similar procedure.

The quality of fit was assessed in terms of the variance accounted for by the model:

$$VAF = 100\left[1 - \frac{\sum_{i=1}^{M}\sum_{j=1}^{N}\left(PSF_{obs}(i,j) - PSF_{par}(y_i,x_j)\right)^2}{\sum_{i=1}^{M}\sum_{j=1}^{N} PSF^2_{obs}(i,j)}\right]\% \qquad (4.4)$$

where
$PSF_{obs}(i,j)$	observed CT value at pixel location i,j
$PSF_{par}(y_i,x_j)$	CT value at y_i, x_j predicted by parametric model
i	pixel row index
j	pixel column index
x_j	x coordinate of pixel column j
y_i	y coordinate of pixel row i

Since the fitting procedure minimizes the residues, a large value of VAF is a sign of good fit.

Behavior of Gaussian model: Three tests were devised to establish how well the Gaussian model behaved under controlled conditions.

1) The repeatability of the Gaussian parameter estimates was evaluated by imaging the wire 16 times without changing the imaging modality (filter 0, thickness of 10 mm) nor the wire position.

2) The importance of parameter B and its influence on estimates of parameter N, p and t was verified by renewing the repeatability test and omitting parameter B from the Gaussian model.

Simulations were also carried out to study the effects of varying levels of background as well as the combined effect of non-zero background and varying region size. A series of PSFs of different area (16x16, 32x32, 48x48 pixels) were generated using results from the repeatability test as numerical values for N, p_x and p_y. The PSF were centered on the region thereby defining t_x and t_y according to region size. A background

value equal to ±30%, ±20%, ±10% of N was added to the simulated PSF prior to fitting the Gaussian model, with and without parameter B, to the data.

3) The accuracy of the estimates of t_x and t_y, the position of the maximum value of the PSF (not to be confused with the maximum value in the data) was also assessed. A precision micrometer attached to the phantom was employed to displace the steel wire in 16 different locations forming a 4 by 4 grid using an increment of 0.080 ± 0.005 mm in the row and column directions.

Damped cosine model: PSFs acquired with the high resolution filter (filter 4) exhibited negative tails which could not be represented by a simple Gaussian model. A more complex damped cosine model, however, does describe this feature:

$$PSF_{dc}(x,y) = N \quad e^{-p_x^2(x-t_x)^2}\cos(d_x(x-t_x)) \quad e^{-p_y^2(y-t_y)^2}\cos(d_y(x-t_y)) + B \tag{4.5}$$

where N, p, t, and B have the same significance as for the Gaussian model, and d_x and d_y are normalized spatial frequencies (radians/mm).

The fitting procedure was the same as for the Gaussian model with the addition that initial estimates of d_x and d_y were derived from the position of the first zero-crossing in the row and column directions respectively. The first zero-crossing corresponds to 1/4 of the cosine period.As with the Gaussian model, the VAF provided a measure of quality of fit.

4.2.3 Modulation transfer function

To provide further insight into the models, non-parametric estimates of the MTF were compared to parametric expressions.

The Fourier transform of the PSFs reconstructed onto a 50 mm field of view (FOV) provided non-parametric estimates of the MTF. These estimates were normalized with respect to maximum DC value since the volume under the curve of spatial distribution of CT numbers for the wire deviated from the ideal value of 1.

Parametric expressions for the MTF were derived by computing the analytical Fourier transform of the parametric models. For the Gaussian function, the expression is:

$$MTF_g(u,v) = e^{-(u\pi/p_x)^2} \; e^{-(v\pi/p_y)^2} \tag{4.6}$$

and for the damped cosine model:

$$MTF_{dc}(u,v) = \frac{\left[e^{-(\pi(u+d'_x)/p_x)^2} + e^{-(\pi(u-d'_x)/p_x)^2}\right]\left[e^{-(\pi(v+d'_y)/p_y)^2} + e^{-(\pi(v-d'_y)/p_y)^2}\right]}{4\, e^{-(\pi d'_x/p_x)^2}\, e^{-(\pi d'_y/p_y)^2}} \qquad (4.7)$$

where d'_x, d'_y spatial frequency (cycles/mm) in x and y directions.
u, v spatial frequency variables (cycles/mm) in x ands y directions

The parameters p_x, p_y, d_x, and d_y are the same as for the corresponding PSFs.

4.2.4 Resolution

We obtained and compared four different measures of resolution:

1. a subjective technique based on periodic bar patterns,
2. the full width at half maximum (FWHM) of the PSF,
3. the half width at first zero crossing (HWZC) of the PSF, and
4. the inverse of the MTF cut-off frequency ($1/f_c$).

Subjective technique: The manufacturer suggests a subjective procedure using the sets of periodic objects contained in Section B of the phantom. Each set consists of five pegs having sides of length L and the same edge-to-edge separation L; six sets of pegs (L = 1.25, 1.00, 0.85, 0.75, 0.65, 0.55 mm.) are scanned. The image is rendered binary by manipulating the CT number to grey scale mapping. The viewing window width is set to 1 and the window level is varied until 5 distinct peaks appear. The edge to edge distance of the most closely spaced set of pegs that can be resolved in this way provides a measure of resolution.

FWHM: Whereas the previous method is based on square periodic objects, the FWHM makes use of impulse like objects. The rationale is as follows. By definition, if the imaging system is linear, the output, or total image, will be the sum of the individual points or PSFs. When two point sources are far apart, the sum is two distinct functions, e.g. Gaussian. As the point sources are moved closer, the (Gaussian) functions merge (are summed) and the peaks become less distinct. When the distance separating the point sources is equal to the FWHM, resolution becomes marginal.

The FWHM can be measured directly from the CT image or derived from the Gaussian model parameter p. If the first option is chosen, a binary image of the wire is formed by selecting a viewing window width of 1 and a window level equal to half of the

difference between maximum and minimum CT number within the data set. The total width of the visible pixels constitutes the FWHM. When the FWHM is estimated from the Gaussian model parameter p, the following relationship is used:

$$FWHM = \frac{2(-ln\ 0.5)^{1/2}}{p} \tag{4.8}$$

HWZC: The argument behind the use of the HWZC as a measure of resolution is the same as for the FWHM. The PSF must however exhibit a zero crossing, i.e. it must take on both positive and negative values. It may be shown that for the damped cosine model, the HWZC is given by:

$$HWZC = \frac{2\pi}{4d} \tag{4.9}$$

Inverse of the cut-off frequency: The inverse of the MTF cut-off frequency, $1/f_c$., provides a frequency domain measure of resolution. In practice, f_c is defined as the frequency at which the MTF decreases to some arbitrarily small value, MTF_c, generally taken as 0.05 or 0.10. Estimates of f_c can be obtained directly from the non-p'.rametric MTF and from the Gaussian model using the relationship:

$$f_c = \frac{p(-\ln MTF_c)^{-1/2}}{\pi} \tag{4.10}$$

4.3 Results

The Gaussian function described the shape of the PSF extremely well as the model accounted for more than 99% of the variance in the data. The standard deviation of parameter estimates were very small further increasing our confidence in this model.

Based on the VAF, the Gaussian model seemed a reasonable choice to describe the high resolution PSF. However, a comparison of non- parametric and parametric MTF showed that the damped cosine model was more appropriate.

Omitting parameter B from either model hardly affected results since the average background value was close to the expected value of 0. Nonetheless, simulations showed that this omission can be detrimental as the average CT value of the material surrounding the wire differs from 0, especially in the presence of positive background values.

Measures of resolution varied greatly with results of the subjective method suggested by the manufactured clearly standing out. Variations within given methods could also be observed.

4.3.1 Point spread function

Effect of scanning parameters: We will first examine how the reconstruction filter and slice thickness affect the shape of the PSF and the model behavior.

Figure 4.2 depicts the non-parametric PSFs estimates obtained for the three filters with a slice thickness of 10 mm while table 4.1 summarizes the results of fitting the Gaussian model to these estimates and to those acquired with a slice thickness of 2 and 5 mm.

filter	thickness (mm)	N (CT number)	p_x (pixel^{-1})	(mm^{-1})	t_x (pixel)	p_y (pixel^{-1})	(mm^{-1})	t_y (pixel)	VAF (%)
0	2	1303	0.700	1.120	9.01	0.726	1.161	7.74	99.88
0	5	1325	0.706	1.130	9.03	0.725	1.159	7.75	99.91
0	10	1331	0.703	1.124	9.03	0.721	1.154	7.74	99.94
1	2	1810	0.805	1.288	9.02	0.848	1.357	7.76	99.65
1	5	1828	0.808	1.292	9.03	0.845	1.352	7.75	99.71
1	10	1835	0.806	1.290	9.03	0.842	1.347	7.76	99.75
4	2	2932	0.956	1.530	9.03	1.042	1.667	7.76	99.16
4	5	2979	0.961	1.537	9.03	1.046	1.673	7.76	99.25
4	10	did not converge							

TABLE 4.1 Gaussian model parameter estimates
(FOV = 200mm, 16x16 region)

The following comments can be made:

1) The shape of the PSF changed significantly with the reconstruction filter but was insensitive to the slice thickness. The PSF was broadest for the smoothing filter, filter 0, indicating that the reduction in the noise, described in the previous chapter, was achieved at the expense of increased blur.

2) Noise however, did seem to affect the quality of the fit. Indeed, the VAF obtained for a given reconstruction filter increased with increasing slice thickness, i.e. decreasing noise.

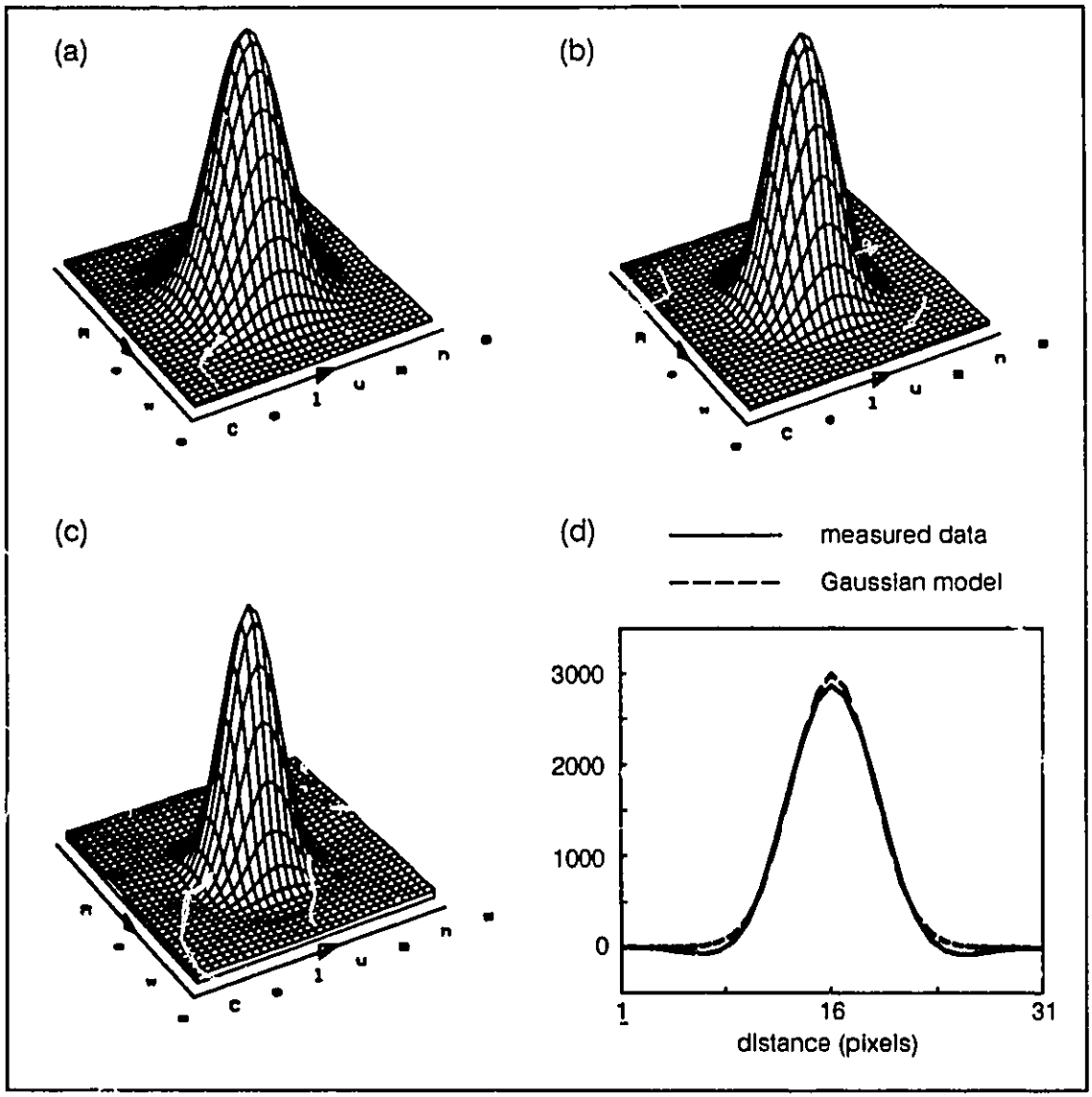

Figure 4.2 Measured PSF

Non-parametric point spread function obtained by imaging a thin steel wire with : (a) filter 0, (b) filter 1, and (c) filter 4. (d) Filter 4 exhibits negative tails as shown in the cross sectional view through the maximum. This undershoot cannot be accounted for by the Gaussian model.

3) As clearly seen in the cross-sectional view of the PSF shown in figure 4.2 (d), the Gaussian model failed to predict the negative values of the PSF obtained with the high resolution filter. This is also reflected in the slightly worse values of VAF compared to the other filters for a comparable slice thickness.

4) The Gaussian model failed to converge for filter 4 with a slice thickness of 10 mm and a FOV of 200 mm. It is possible that the undershoots were lost in noise for a thickness of 2 and 5 mm. However, for 10 mm, when less noise is present, the oscillation could be too strong and/or too few points are available for convergence to occur. This last supposition is supported by the fact that convergence did occur when the number of pixels was increased by a factor of 16 (reconstruction FOV = 50 mm).

5) Because the Gaussian function is inherently positive, it cannot model undershoots observed with the high resolution filter. In contrast, the damped cosine model is able to predict these negative values due to the presence of the cosine term.

Table 4.2 compares the parameter estimates obtained by fitting both models to the same high resolution PSF. Although the improvement in fit was only marginal with regard to the VAF (0.43%), it has very significant effects on estimates of the MTF and resolution, as will be discussed below.

It is important to note that that estimates of p_x and p_y obtained with the damped cosine model were lower than for the Gaussian model which implies a slower decay rate. This is due to the presence of the cosine term which acts concurrently with the exponential term to dampen the PSF.

6) Both models predicted the same position of the maximum, represented by parameters t_x and t_y. Furthermore, the results of the positional accuracy test, in which the wire was imaged at different locations, indicate that for a 200 mm FOV (pixel size of 0.625 mm), the difference between the measured and estimated wire position was no greater than 0.013 mm or about 2% of pixel width.

Repeatability of Gaussian parameters: Table 4.3 presents the results of the repeatability test, in which the wire was imaged 16 times under the same conditions.The standard deviations of all parameters were very small indicating that the parameter estimates were reliable. It should be noted that the values of p_x and p_y differed by a small but statistically significant amount (level of significance smaller that 0.01). This difference suggests that the PSF was slightly wider in the row direction than in the column direction at the given position of point source for which the data were collected, i.e. approximately 51.3 mm above the center of the FOV (see figure 4.1)

parameter	units	gaussian model	damped cosine model
N	(CT number)	2990	2886
p_x	($pixel^{-1}$)	0.246	0.174
	(mm^{-1})	1.577	1.116
t_x	(pixel)	16.09	16.09
d_x	(rad/pixel)	-	0.213
	(rad/mm)	-	1.364
p_y	($pixel^{-1}$)	0.256	0.187
	(mm^{-1})	1.638	1.197
t_y	(pixel)	16.05	16.05
d_y	(rad/pixel)	-	0.216
	(rad/mm)	-	1.384
VAF	(%)	99.45	99.88

TABLE 4.2 Comparison of parameters for Gaussian and damped cosine models
(filter 4, thickness = 10mm, FOV = 50mm, 31x31 region)

	N	p_x		t_x	p_y		t_y	B
	(CT number)	($pixel^{-1}$)	(mm^{-1})	(pixel)	($pixel^{-1}$)	(mm^{-1})	(pixel)	(CT number)
WITHOUT B								
mean	1319	0.7050	1.1280	8.2784	0.7178	1.1485	8.1336	-
standard deviation	3	0.0010	0.0016	0.0598	0.0009	0.0014	0.0218	-
WITH B								
mean	1319	0.7065	1.1304	8.2784	0.7186	1.1498	8.1336	1.4
standard deviation	3	0.0010	0.0016	0.0598	0.0012	0.0019	0.0282	0.2

TABLE 4.3 Repeatability of Gaussian model parameters
(filter 0, thickness = 10mm, FOV = 200mm, 16x16 region)

Parameter B: Table 4.3 also indicates that parameter B had little influence on the other parameters. There was no influence on the positional parameters at all and the difference in shape parameters was less than 0.2%. This behavior is not surprising since the average background value, 1.4 CT units or about 0.1% of N, was very close to 0.

However, simulations showed that parameter B becomes important as the average background value drifts away from 0. To study this effect, PSFs were generated using the average values of the repeatability test (parameter B included to the model).

Table 4.4 contains the estimates for the shape parameters in the case where B was omitted from the model for a region size of 32x32 pixels. The estimates deviated more and more strongly from actual figures as the average background value moved away from 0.

Background value		N	p_x	p_y
(%N)	(CT units)	(CT units)	(pixel^{-1})	(pixel^{-1})
-30	-396	933	.512	.499
-20	-264	1065	.474	.482
-10	-132	1197	.405	.410
+10	+132	482	.109	.109
+20	+264	384	.022	.022
+30	+396	515	.016	.108

TABLE 4.4 Parameter estimates obtained with Gaussian model in absence of B and with non zero background level
(Gaussian model parameters: N = 1319, p_x = 0.353 pixel-1, p_y = 0.359 pixel-1)
(FOV = 100mm, region size = 32x32 pixels)

For a given absolute deviation from zero background, estimates were much worse when the background was positive. This is also illustrated in figure 4.3 which illustrates a cross-section through the central portion of the PSF with a background of 132 and -132 CT units.

Furthermore, estimates were much more sensitive to region size in the presence of positive background as values in table 4.5 can attest. This table contains the shape parameters estimated under the same conditions as those described in table 4.4 but the absolute background deviation was kept constant and region size varied.

The reasons for greater sensitivity to positive background will be discussed in section 4.4.1.

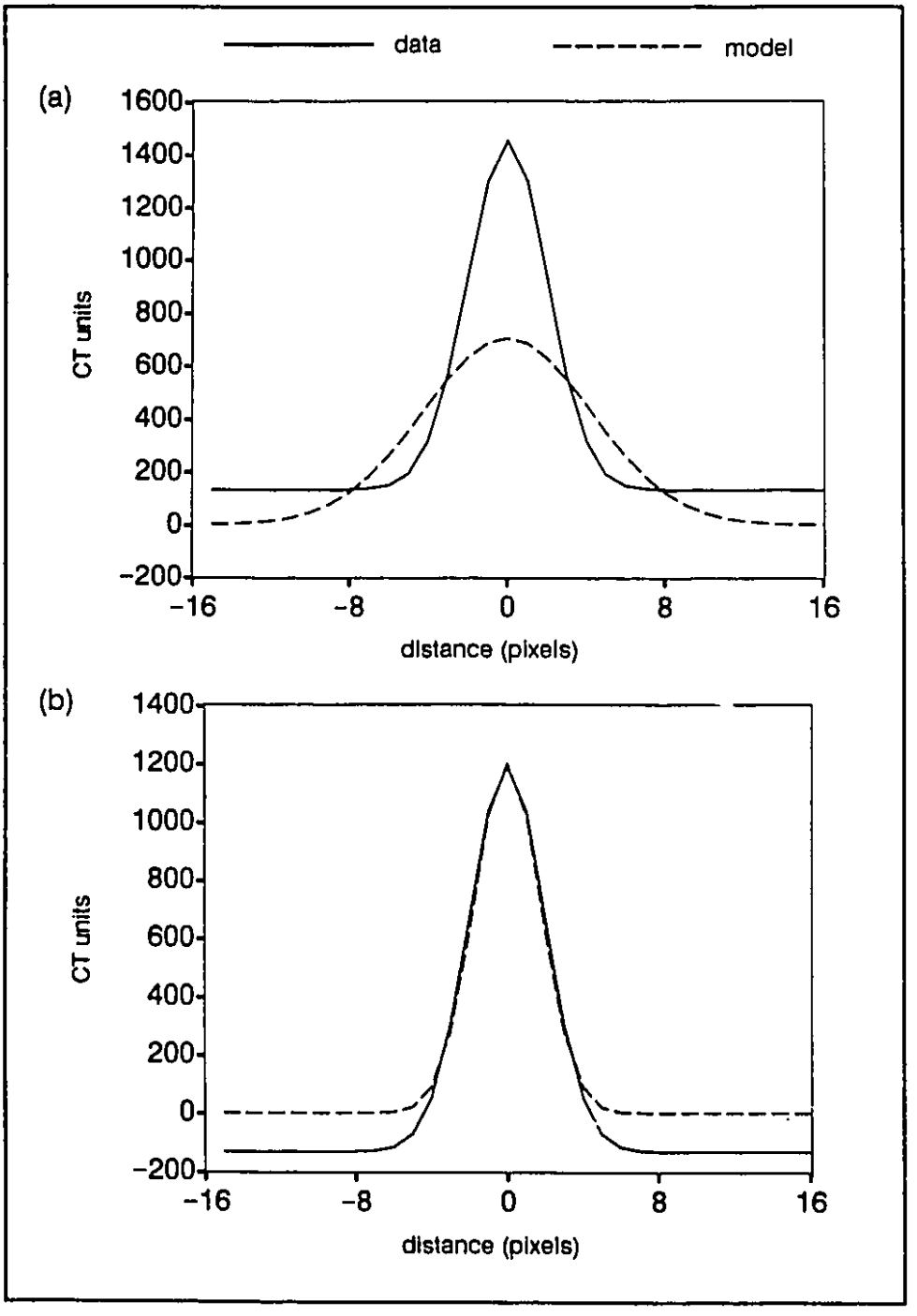

Figure 4.3 Effect of non-zero background on Gaussian model without parameter B
a) positive background level of 132 CT units b) negative background of -132 CT units

	B = -132 CT units			B = + 132 CT units		
size	N	p_x	p_y	N	p_x	p_y
(pixel^2)	(CT units)	(pixel^{-1})	(pixel^{-1})	(CT units)	(pixel^{-1})	(pixel^{-1})
16x16	1197	.409	.416	1234	.270	.274
32x32	1197	.405	.410	482	.109	.109
48x48	1197	.405	.410	464	.014	.015

TABLE 4.5 Effect of region size and non-zero background on Gaussian parameter estimates in absence of B

4.3.2 Modulation transfer function

The manner in which the reconstruction filter modifies an image is more easily interpreted from the MTF than from the PSF. Figure 4.4(a) shows the non-parametric MTFs, for positive frequencies in the row direction, corresponding to the PSFs in figure 4.2 . Filter 4, the high resolution filter, exhibited the highest cut-off frequency and will thus produce images with the sharpest edges but at the cost of increased noise, as noted in the previous chapter. In contrast, filter 0 had the lowest cut-off frequency and so will produce images having the most blur but least noise. Filter 1 provides a compromise between these two extremes.

The Gaussian parametric estimates of the MTF (equation (4.6)) for filters 0 and 1 were very similar to those obtained by Fourier transforming the PSF. The difference between parametric and non-parametric estimates was less than 0.01, or 1% of full scale. Parametric estimates of the MTFs for filters 0 and 1 are not shown in figure 4.4 since they cannot be distinguished from the nonparametric estimates.

The situation was somewhat different for filter 4. The parametric MTF obtained using the Gaussian model (equation (4.6)) was quite different from the nonparametric estimate as shown in figure 4.4(b); discrepancies as large as .12 (or 12% of full scale) were observed. The MTF estimate provided by the damped cosine model (equation (4.7)) was much closer to the nonparametric MTF with a maximum difference of 0.05 (or 5% of full scale).

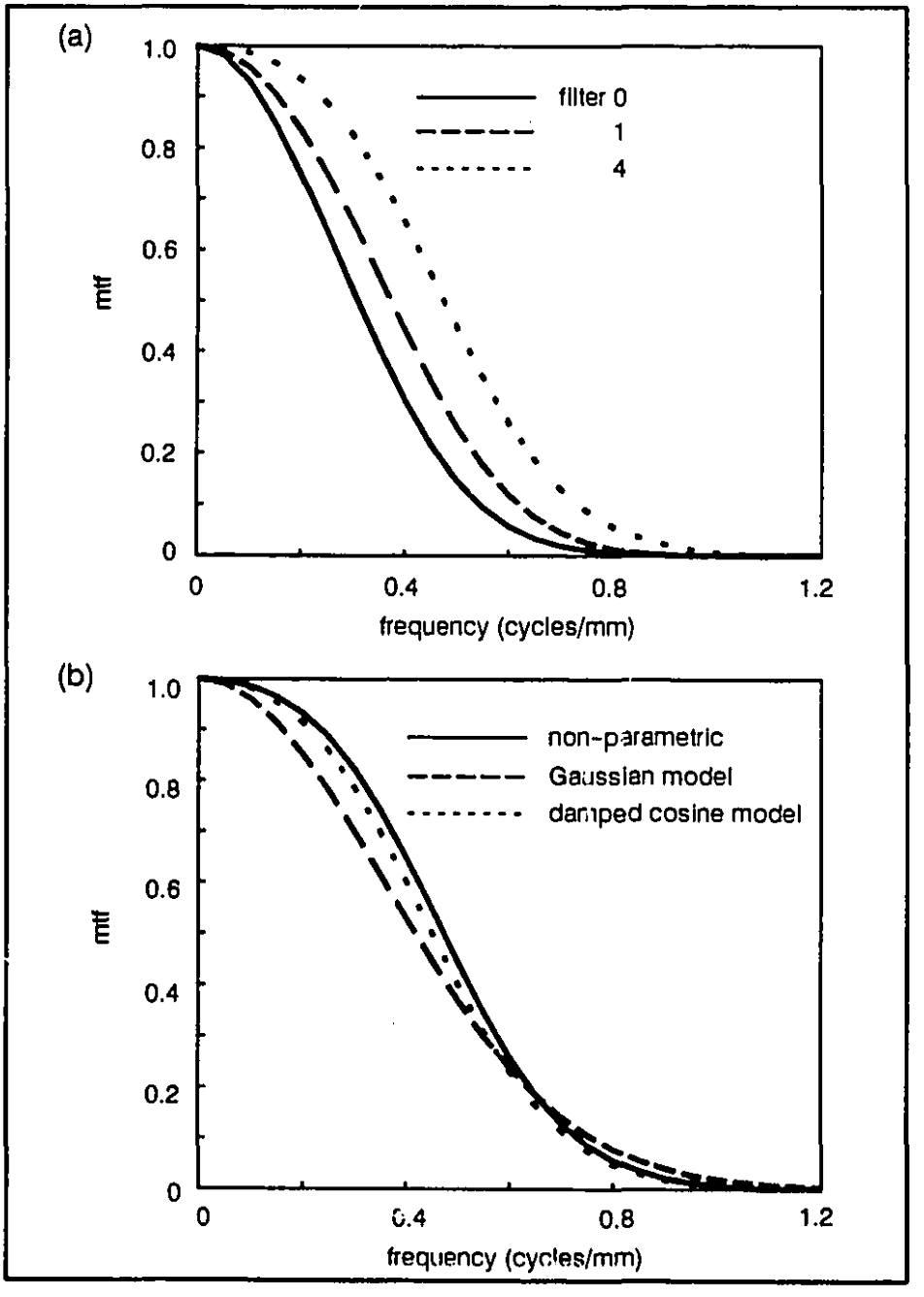

Figure 4.4 Modulation transfer functions

Modulation transfer functions along the positive frequency axis in the row direction. (a) non-parametric MTFs determined by computing the 2D Fourier transform of the wire imaged by all three filters (b) comparison of non-parametric MTF for filter 4 and analytically derived MTF for both the Gaussian and damped cosine models.

4.3.3 Resolution

Table 4.6 presents estimates of the scanner resolution obtained using the four methods described above and a variety of measurement conditions. The first five rows are based on the FWHM measured either directly from the image of the steel wire or by using equation (4.8) and the parameters of the Gaussian fit in the row direction found in table 4.3. The inverse of the cut-off frequency was obtained either from equation (4.10) based on the Gaussian model, or read directly off the non-parametric MTF. The HWZC was estimated for the high resolution filter with equation (4.9) derived from the damped cosine model. The last estimates were obtained using the subjective method suggested by the manufacturer. The wide discrepancies in estimates are the subject of discussion in section 4.4.2.

RESOLUTION (mm)			filter 0 $p_G = 1.13$	filter 4 $p_G = 1.60$
FWHM	gaussian model (equation (4.8))		1.48	1.04
	from image FOV = 200mm (pixel ~ 0.63 mm)	centered	1.88	0.63
		off-centered	1.25	1.25
	from image FOV = 50mm (pixel ~ 0.16mm)	centered	1.42	1.09
		off-centered	1.56	0.94
$1/f_c$	gaussian model MTF (equation (4.10))	$mtf_c = 0.1$	1.84	1.29
		$mtf_c = 0.05$	1.61	1.13
	non parametric MTF	$mtf_c = 0.1$	1.82	1.35
		$mtf_c = 0.05$	1.62	1.21
				d = 1.36
HWFZ	damped cosine model (equation (4.9))		-	1.15
	periodic objects		0.75	0.60

TABLE 4.6 Comparison of resolution estimates
p_G: parameter p from Gaussian model (mm^{-1})
d: parameter d from damped cosine model ($rad\ mm^{-1}$)
$1/f_c$: reciprocal of cut-off frequency (mm)

4.4 Discussion

The parametric models presented in this study differ from those proposed in the literature in a number of ways: they are non-linear in their parameters, they do not assume radial symmetry and they can account for non-zero background. Furthermore, our damped cosine function can model the shape of the MTF due to the high frequency filter throughout the whole frequency range better than the model proposed by Nickoloff and Riley (1985).

Differences in object shape can explain the discrepancies in resolution estimates obtained with the subjective method compared to the other criteria. The manner in which a method is implemented and its accuracy are also responsible for variations in the results.

4.4.1 Parametric models

We are not the first to propose parametric models to describe the shape of the PSF or MTF. Indeed, Nickoloff and Riley (1985) also proposed the Gaussian function for this purpose. However, our approach is novel in many aspects: it is non-linear in its parameters, it does not assume radial symmetry, and finally, a parameter taking the background value into account was added to the model. Furthermore, a new model, the damped cosine function, was created. These points will now be discussed in more detail.

Importance of non-linear model: The shape of the PSF for the smoothing and edge enhancement filters (filters 0 and 1), and that of the corresponding MTFs, is well described by the Gaussian model. Nickoloff and Riley (1985) also formulated a Gaussian model but they assumed radial symmetry and linearized their model, arguing that the shift parameter only affects the phase term of the Fourier transform and not its magnitude. Nickoloff and Riley proved this claim for the continuous case (see appendix in Nickoloff and Riley). We conducted a series of simulations to verify its validity for sampled data. We generated various PSF using the Gaussian model and shifted the position of the PSF by varying parameters t_x and t_y (position of the function maximum) in increments of 10% pixel width. For filter 0 and a simulated FOV of 200 mm, we found that parameters p_x and p_y were under-estimated by 13% when the wire was displaced by half a pixel.

Based on these simulations, we concluded that a linearized model can lead to negative biases in shape parameter estimates in the presence of sampled data. The bias increases as the center of the wire is moved away from the center of a pixel. This artefact is avoided by using a non-linear model formulation.

High resolution filter: Even if the Gaussian model explains over 99% of the variance of the PSF data obtained with the high resolution filter (filter 4), it fails to predict the negative values. Furthermore, examination of the MTF reveals that this model only accounts for part of its frequency response behavior. The shape of both the PSF and MTF produced by filter 4 are better represented by the damped cosine model.

The increase in MTF at higher frequencies exhibited by the high resolution filter can be explained as follows. Equation (4.7) tells us that the MTF is the sum of two shifted Gaussians which decay more rapidly than does the pure Gaussian model. Table 4.2 confirms this : values of the shape parameters p are smaller for the damped cosine model. One must keep in mind that, contrary to the PSF, a decrease in shape parameter causes a faster decay of the MTF (see equations (4.6) and (4.7)). In the low frequency range, the sum of the 2 Gaussians results in a larger MTF. However, the tail of the Gaussian centered in the negative portion of the spectrum has little effect on the sum in the high positive frequencies (and vice versa). Because these Gaussians decay more rapidly, the MTF is smaller at high frequencies.

The enhancement properties of the negative tails in the middle frequency range and damping of high frequencies were also noticed by Nickoloff and Riley (1985), who modelled the impulse response of the high resolution filter as a pure Gaussian PSF with a damped harmonic oscillation at its edge. Although their model explained the increased MTF in the mid frequency range, its high frequency behavior deviated from what could be expected. Our damped cosine model explains the shape of the MTF throughout the whole frequency range.

Radial asymmetry: We expected the PSF to demonstrate radial symmetry, or isotropy, and thus anticipated equal values for p_x and p_y. Despite this we found values of p_y to be consistently greater than p_x. In a theoretical study of the effect of finite X-ray beam size on the shift-variant nature of CT scanners, Verly and Bracewell (1979) showed that the radial symmetry, or isotropy, exhibited by the PSF in the center of the FOV was lost as the point source was moved outward. They also showed that the degree of anisotropy increased with the distance from the center of the FOV. Moreover, the PSF was wider in the angular than in the radial direction when the position of the point source was expressed in polar coordinates.

We believe our models to be sensitive enough to detect this anisotropy. In the tests outlined previously, the point source was placed directly above the center of the FOV (see figure 4.1). In such a configuration, the y and x axes correspond to radial and angular directions respectively. Thus a value of p_y greater than p_x indicates a PSF wider in the angular than in the radial direction, results consistent with the theoretical predictions of

Verly and Bracewell. Furthermore, one must bear in mind that anisotropy does not preclude axial symmetry: profiles taken through the center of the PSF along a diameter are symmetric about an axis located at the function's maximum, but these profiles change for different diameters.

Effect of parameter B: By definition, the CT value of water is zero. Therefore, at least in theory, parameter B could be omitted from the models (equations (1) and (4)) since the wire is surrounded by water. However, in third generation scanners, x-ray scatter produces cupping. Therefore, the average background value surrounding the wire could change depending on the position of the wire and the size of the FOV.

This situation can lead to erroneous MTF estimates as experienced by Bischof and Ehrhardt (1977). Their non-parametric MTF estimates rose significantly above the value of 1.0 at low spatial frequencies before regaining their expected values at higher frequencies. This was due to negative mean CT values for the water bath surrounding the point sources. Furthermore, they found that the magnitude of the error increased with size of the region surrounding the wire. Subtraction of the mean water bath CT level in the region surrounding the input resulted in proper estimates. The proper background CT level was chosen as the one which eliminated the dependency on array size. It was evaluated using a statistical convergence method.

Our own results indicated that the average CT value of the water surrounding the wire was 1.4 CT units based on estimates of parameter B. Being so close to 0, it had very little bearing on the other parameters. However, as with the experimental study by Bischof and Ehrhardt (1977), our simulations showed that neglecting the average background value can be detrimental and lead to meaningless results.

The simulations also showed that this trend is more sensitive to a positive than to a negative background level. In the case of least square fitting, two factors can explain this situation: firstly, all values of a Gaussian function are positive and secondly, the tails of the function tend to zero. In the case of a negative background, the model concentrates on the central, positive (and most significant) portion fo the data. Because the model discounts the negative values, and is therefore relatively insensitive to region size (see Table 4.5), it is able to track relatively accurately the central portion, while allowing its tails to fall to zero. However, the rate of decrease is greater for the modelled data, i.e. the modelled PSF is thinner. As a consequence, values for p_x and p_y raise as the background becomes increasingly negative.

When the background is positive, the model must contend with the positive tails which compete with the central portion. As a result, the modelled PSF broadens, i.e. values

of p decrease. This trend is accentuated not only with an increase in background level, but also with an elongation of the tails.

4.4.2 Resolution

Observation of table 4.6 reveals that estimates of resolution vary widely depending on how it is evaluated. Even with a given estimation method, FWHM based methods for example, large variations can arise depending on how the method is applied. However, the factor which seems to affect the results most is the shape of the objects on which the measurements were performed. Indeed, the first three methods (FWHM, HWZC, and $1/f_c$) are based on the approximation of an ideal impulse while the subjective method requires a set of periodic objects simulating square wave patterns. In the following paragraphs, we will explain the intra- and inter-method differences as well as discuss the accuracy of the different measurement approaches. However, we will start by discussing how object shape can influence results.

Effect of object shape: Although estimates vary widely, it is clear that the values obtained by imaging periodic patterns stand apart from the other measures derived from the point object. This discrepancy resides both in the nature of the method and of the objects being imaged. Figure 4.5 illustrates one dimensional objects of different size and separation along with their frequency content and their image produced by a low pass system. The square pegs of size L separated by L are represented by a square wave of period $T = 2L$ (figure 4.5(a)). Their frequency spectrum presents a peak at a frequency of $2p/T = p/L$ and every odd harmonic thereafter. As long as at least one of these peaks is located at a frequency below the imaging system's cutoff frequency, the objects will be resolvable in the image.

In figure 4.5(b), the object size is reduced to a point and separation distance kept at $L = T/2$. Because the frequency content is now shifted above the cut-off frequency, the images of the points merge. However, if the distance L is larger than the inverse of the cut-off frequency as in figure 4.5(c), they are resolvable.

A similar argument can be made in the space domain. Because the imaging system is considered linear, the image of a square wave pattern can be represented as a sum of point sources as illustrated in figure 4.6. An explanation of the object's resolution cannot be provided by simply adding contributions of individual points. Because the point corresponding to the falling edge of one period (point 3) and that of the leading edge of the next (point 1') (Figure 4.6(a)) are separated by less than the FWHM (or HWZC), their

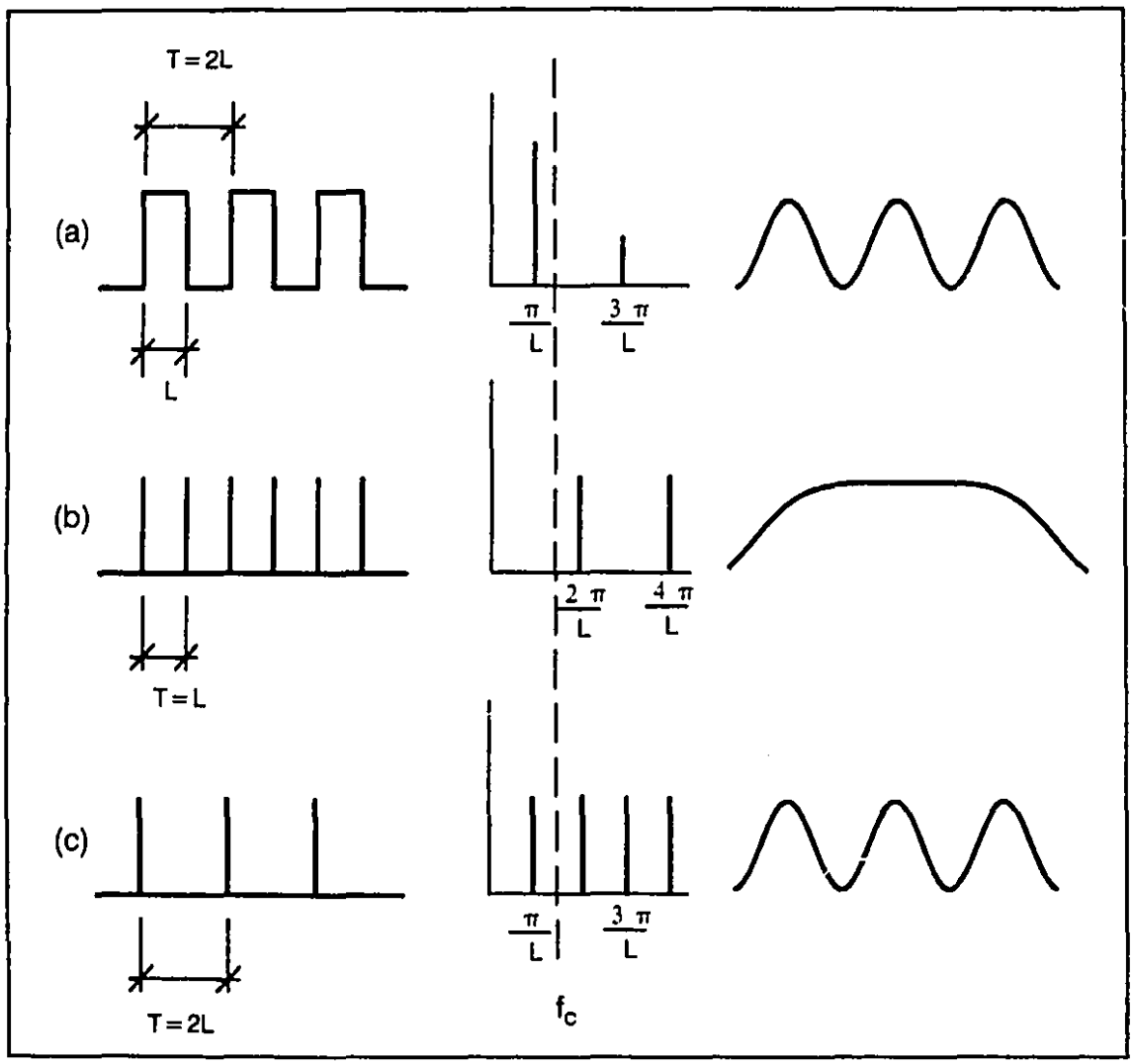

Figure 4.5 Effect of object size and separation on resolvability

As long as at least one of the frequency components is below the cut-off frequency f_c, the objects will appear separate when imaged. (a) Objects of size L separated by L forming a periodic signal of period T (b) points separated by period T = L (c) points separated by period T = 2L.

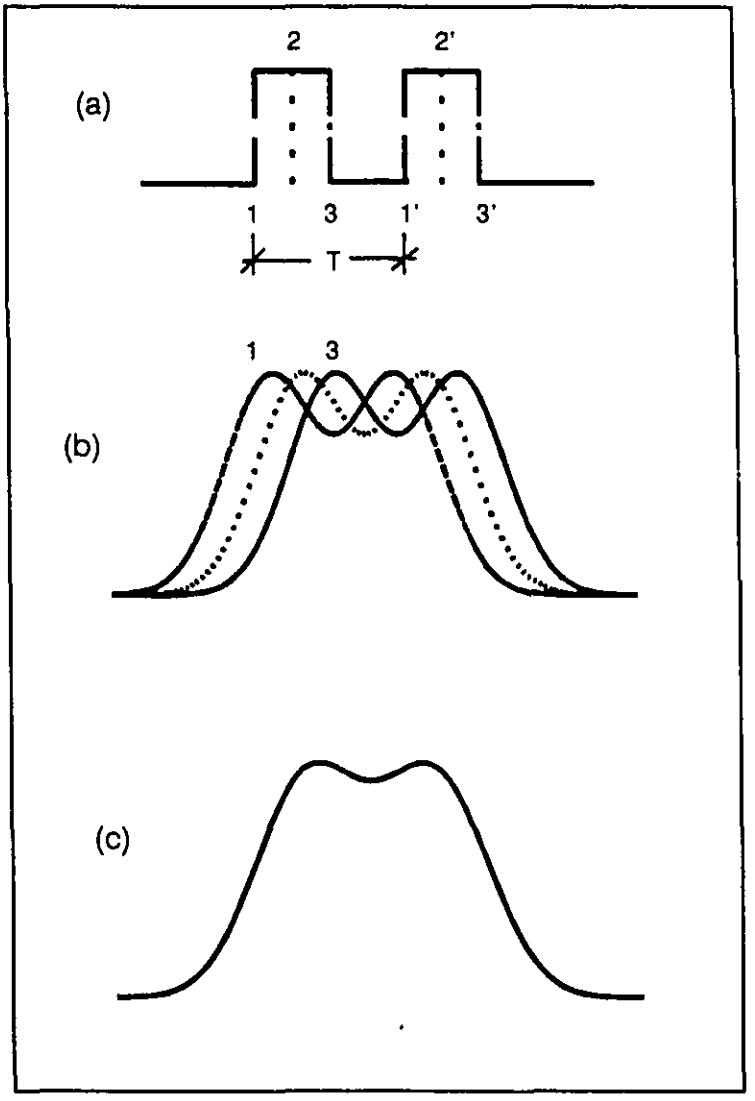

Figure 4.6 Creating a square wave by summing point sources

A square wave pattern is constructed by (a) adding pairs of points (1-1', 2-2', 3-3') separated by a distance equal to the period T (b) As long as the period is larger than the system resolution, the points within each imaged pair are resolvable. (c) The image of the square wave is the sum of images of pairs of points in (b)

Gaussian images would merge into a single peak. Therefore, the cyclic nature of the pattern must be explicitly recognized by adding pairs of points (1-1', 3-3') separated by period T (Figure 4.6(b)). The total contribution, or image, is then the sum of the contribution of pairs of points (Figure 4.6(c)). If T is larger than the FWHM (or HWZC), the objects are resolvable.

Differences between methods: Following this explanation, the estimates of resolution from the FWHM or HWZC and those determined from the periodic objects can be reconciled. For filter 0, FWHM is 1.48, approximately twice the manufactures claim of 0.75 mm. For filter 4, the measured HWZC is equal to 1.15 mm while the cyclic object separation is 0.6 mm. It should be noted that these figures of FWHM and HWZC are valid for point sources located 51 mm above the center of the FOV, and aligned in the row direction. Based on the same methods, the resolution in the column direction is 1.45 mm and 1.13 mm in the column direction for filters 0 and 4.

There is some controversy as to whether resolution should be evaluated as the reciprocal of the cut-off frequency or half of this value (Philips Medical Systems, 1988; Bushong, 1988; Bassano, 1983). The previous example also shows that it can be misleading to define resolution as half the inverse of the cut-off frequency determined from a series of periodic objects since the ability to distinguish the objects within the image depends not only on their separation but also on their shape and size. Because an impulse exhibits a flat spectrum, i.e. it contains all possible frequencies, it should be used as the reference. In this view, resolution should be defined as the minimum distance between point sources whereby they can still be discriminated when imaged.

The inverse of the cut-off frequency obtained from the Gaussian model, equation (4.10) and non-parametric MTF are very similar for filter 0 (1.84 and 1.82 for $MTF_c = 0.10$ and 1.61 and 1.62 for $MTF_c = 0.05$). However, because the Gaussian model overestimates the MTF in the high frequencies for filter 4 (see figure 4.4(b)), the cut-off frequency will be larger, hence the resolution poorer than if it were evaluated from the non-parametric MTF (1.29 vs 1.35 for $MTF_c = 0.10$ and 1.13 vs 1.21 for $MTF_c = 0.05$).

Measures of resolution based on the Gaussian model, i.e. equations (4.8) and (4.10) result in the lowest estimates for the high resolution filter (filter 4). The HWFZ, computed with equation (4.9) derived from the damped cosine model, and the entry from table 4.2 in the row direction, is more conservative as well as being closer to the inverse of the cut-off frequency evaluated with the non-parametric MTF. For these reasons, we recommend the HWZC over the FWHM as a measure of resolution for filters exhibiting negative tails.

Differences within the FWHM-based method: There is a considerable variation among values obtained with the FWHM methods although estimated from the Gaussian model fall within extreme values measured from the image both for a FOV of 200 and 50 mm. This results from problems associated with measuring the FWHM directly from the image. If the center of the wire is not aligned with the center of a pixel, the maximum CT number will not correspond to the PSF's maximum value. Consequently, the threshold value chosen to binarize the image will be incorrect, leading to an error in the estimate of the FWHM. Simulations of this situation were carried out by numerically generating several Gaussian functions and varying the peak position within a pixel by adjusting parameters t_x and t_y. The simulation showed that the FWHM could vary between 1.88 and 1.25 mm for a FOV of 200 mm, and 1.41 and 1.56 for a FOV of 50 mm depending on whether the wire was centered on a pixel or not.

Accuracy of measurement methods: The parametric and non-parametric FWHM approaches not only differ in the results they yield but also in accuracy. When the FWHM is evaluated from the image, accuracy is limited by pixel size since the measurement is performed on a finite number of pixels. For FOVs of 200 and 50 mm, the accuracy is therefore 0.625mm and 0.156 mm respectively. Therefore when using this method, it is important to use the smallest FOV possible.

On the other hand, the measure of FWHM obtained with equation (4.8) is limited by the precision with which parameter p can be determined and is thus more accurate. For example, using entries in table 4.3, a value of $p = 0.7065 \pm 0.0010$ pixel^{-1} (or 1.1304 ± 0.0016 mm^{-1}) translates into a value of $FWHM = 2.3568 \pm 0.0034$ pixels (or 1.4730 ± 0.0021 mm). The same level of accuracy is to be expected for the HWZC and the inverse of the cut-off frequency when determined from model parameters.

For its part, the accuracy of the method based on the periodic objects is limited by the discrete step between object size, 0.1 mm in this study.

4.5 Conclusions

This chapter represented efforts to develop and evaluate parametric models of the PSF. Rotational symmetry was not assumed thereby permitting a full bi-dimensional representation of the PSF. Non-linear numerical methods were used to estimate the parameters and the average background value was included in the models. These three aspects represent innovations compared to other models of the PSF presented in the literature. A variety of figures indicate that the proposed models are appropriate and adequate to represent the PSF.

These models represent the basis of the work presented in subsequent chapters. They will be used to:

- quantify shift-variance,

- compare non-parametric PSF estimates obtained with different identification methods,

- formulate a coordinate transformation for the shift-invariant representation of the PSF, and

-explain the behavior of the thresholding segmentation operator.

CHAPTER 5
EXPERIMENTAL DETERMINATION OF CT POINT SPREAD FUNCTION ANISOTROPICITY AND SHIFT-VARIANCE

5.1 Introduction

CT systems are neither strictly linear nor isoplanatic. Perhaps because the effects due to shift-variance are more subtle and less easily perceived than those arising from non-linearities (see sections 2.3 and 2.4.3), the issue of shift-variance has received comparatively little attention.

Nonetheless the variation of PSF shape with position has repercussions both on image restoration and segmentation. These issues will be covered in later chapters, but let us mention that most image restoration algorithms are developed for isoplanatic systems. Furthermore, the capability to distinguish, and properly segment neighboring edges, depends on the distance separating them as well as the width of the PSF. It is therefore important to identify trends in variation of PSF shape and to quantify these changes.

To our knowledge, only two groups have studied the position dependent nature of CT systems. Using a theoretical approach, Verly and Bracewell (1979) qualitatively characterized the change of PSF shape with position. Kijewski and Judy (1983) complemented an analytical analysis with a series of simulations using a method based on the edge response function (Judy, 1976). This method is time consuming since both the position and the orientation of the edge object must be modified to obtain a full two-dimensional description of the PSF.

The goal of this chapter was to experimentally measure the shift-variant as well as the PSF symmetry properties of a CT scanner. The experimental approach, which distinguishes this study from those previously mentioned, enabled us to take a large number of parameters, both hardware and software, into account. Furthermore, it permitted us to quantify the variations encountered.

In section 5.2 we propose a method, developed in chapter 4, based on the parametric identification of the PSF using a thin wire as input point source. The use of a wire directly supplies the two- dimensional information necessary to analyze the symmetry of the PSF, while the variation of model parameters with position provide the quantitative information sought. Section 5.3 presents the results which are discussed in section 5.4 and the conclusions are presented in section 5.5.

5.2 Method

The fabrication of a custom phantom was required since the phantom provided by the manufacturer was not suitable for the evaluation of shift-variance. Two simple measures characterizing the shape of the PSF were derived from the model parameters obtained by fitting the parametric models to the image of each wire in the phantom. These measures of shape were expressed in two different coordinate systems: a fixed orientation and rotating frame, in order to establish if the system produced a rotating blur. Furthermore, a number of statistical tests were performed on the data to verify if scanning variables and/or estimation methods significantly affected results.

5.2.1 Hardware

Figure 5.1 shows the custom phantom. It consisted of a 200 mm inside/ 216 mm outside diameter PVC tube and two plexiglass end plates. Enamel wires, 0.25 mm in diameter, were threaded through holes drilled in the end plates. They were put under tension before being glued with epoxy to the outside surface of the plates. The end plates were fastened to the tube with screws and a layer of silicon between the PVC/plexiglass surfaces assured a water tight seal. The phantom was suspended within the scanner gantry with the help of the standard Philips phantom attachment set. To this effect, a female adaptor was fastened to the end-plates of the custom phantom.

In order to avoid artefacts that could arise from an air/metal interface, the phantom was filled with distilled water. The water was poured through a hole drilled in the side of the tube while air was evacuated through a neighboring hole. Corks were used to seal the holes.

Sixty one wires, simulating impulses, were arranged in 5 concentric circles spaced approximately 17 mm apart. Along a given circle, a 22.5 degree angular increment separated each wire. Some of the wires in the innermost region were omitted in order to avoid interference between neighboring PSFs.

Images were produced with a Philips Tomoscan CX third generation scanner. Scanning parameters included a tube current of 200 mA, voltage of 120 kV, and a slice thickness of 2 mm.

Keeping these parameters constant, both the image reconstruction filter and the scan time were varied. Images were acquired with scan time settings of 4.5 s and 9.0 s making it possible to determine how the number of views, 540 in the first case and 1080 in the second, affected the shift-variance. The phantom was also imaged with the smoothing (filter 0) and high resolution (filter 4) filters.

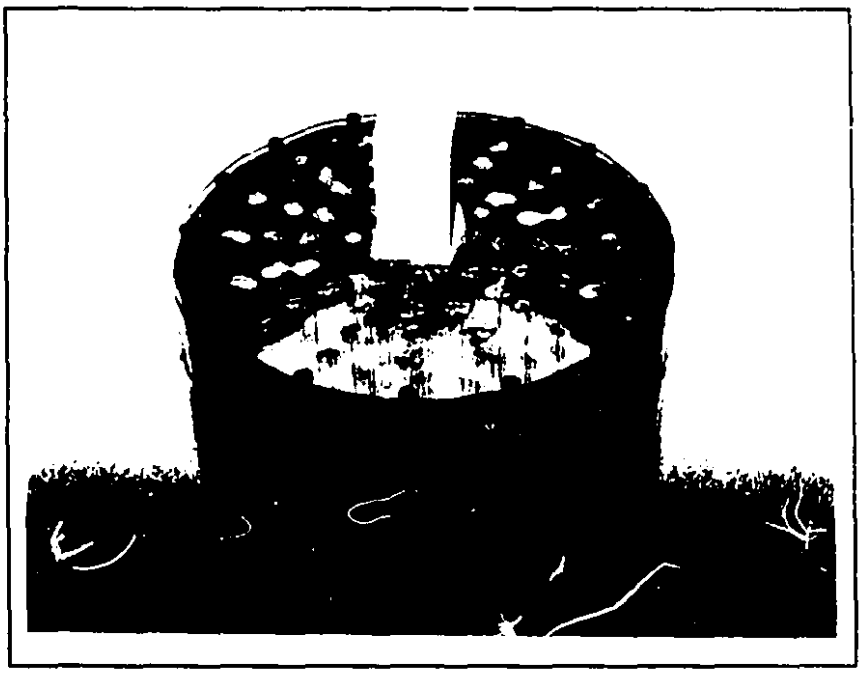

Figure 5.1 Custom shift-variant phantom

The phantom consists of a water filled PVC cylinder in which 61 wires arranged in 5 concentric circles simulate impulses.

The imaging field of view (FOV) was set to 250 mm, the smallest diameter containing the whole phantom. Each image was subdivided into 9 regions, and each region was reconstructed onto a 100 mm FOV with the zoom option. The reconstruction matrix being 320x320 pixels, the pixel size was thereby reduced from 0.78125 mm for the 250 mm FOV to 0.3125 mm.

5.2.2 PSF shape descriptors

The data contained in a 21x21 pixel region surrounding the image of each wire were fitted to a parametric model. We have previously shown (see chapter 4) that the Gaussian function and the damped cosine function are good models of the PSF produced by the smoothing (0) and high resolution (4) filters respectively. The models are repeated here for convenience. The Gaussian model is given by:

$$PSF_g(x,y) = N\, e^{-p_x^2 (x-t_x)^2}\, e^{-p_y^2 (y-t_y)^2} + B \qquad (1)$$

while the expression for the damped cosine model is:

$$PSF_{dc}(x,y) = N\, e^{-p_x^2 (x-t_x)^2} \cos(d_x\,(x-t_x))\; e^{-p_y^2 (y-t_y)^2} \cos(d_y\,(x-t_y)) + B \qquad (2)$$

where

x	= positive row direction;
y	= negative column direction;
N	= maximum value of the function;
t_x, t_y	= (x,y) coordinates of the maximum;
p_x, p_y	= shape parameters in x and y direction;
d_x, d_y	= normalized spatial frequencies in x and y direction (radians/mm)
B	= average background value.

From these two models, we extracted two simple measures characterizing the shape of the PSF: gain and resolution. Gain was computed by integrating the volume under the PSF. Its expression for the Gaussian model is:

$$G_g = \frac{N\ \pi}{p_x\ p_y} \tag{3}$$

and for the damped cosine model:

$$G_{dc} = \frac{N\ \pi}{p_x\ p_y}\ \ e^{\,-\,1/4\ [(d_x/p_x)^2\ +\ (d_y/p_y)^2]} \tag{4}$$

Resolution was expressed in terms of the full width at half maximum (FWHM) for the smoothing filter, and the half width at first zero crossing (HWZC) for the high resolution imaging mode.

Both the Gaussian and damped cosine functions are separable, i.e. they are the product of functions of independent variables, x or y. Resolution can therefore be defined in two orthogonal directions. The FWHM along the x axis is obtained from the Gaussian parameter p_x as follows:

$$FWHM_x\ =\ \frac{2(-\ln\ 0.5)^{1/2}}{p_x} \tag{5}$$

while the $HWZC_x$, expressed in terms of parameter d_x is given by:

$$HWZC_x = \frac{2\pi}{4d_x} \tag{6}$$

and similarly in the y direction.

5.2.3 Coordinate systems

We previously mentioned that model parameters were expressed in two different coordinate systems. Two other frames were necessary to complete the analysis, one to express the position of a pixel and the other the position of the input point sources. Figure 5.2 illustrates the relationships between these coordinate systems.

1) The position of a pixel in image space was given by its row and column indices (i,j). The origin lies in the upper left hand corner of the image with i increasing downwards and j to the right.

2) The position of the wires could have been obtained in the i-j frame, but because the acquisition system rotates about the center of the FOV, it was more natural to express wire position in a fixed polar coordinate system (R,θ). The origin of this reference frame coincides with the center of the imaging FOV.

3) Model parameters were presented in a local, fixed orientation cartesian system (x,y). The x axis corresponds to a constant row (j) while y points in the negative constant column direction (-i). There exist one local coordinate system for each input point source.

4) The model parameters were also expressed in a local, rotating cartesian frame s-t, where s is oriented in the radial direction and t, tangentially. As we will see in sections 5.3.1 and 5.3.2, the comparison of parameter behavior in the x-y and s-t frames enabled us to verify if the system produced a rotating blur, as predicted by Verly and Bracewell (1979).

While computing the model parameters in the x-y system was trivial since the axes align with the row and column directions, determining their values in the s-t system required more effort. Three methods were used to determine the model parameters in the s-t coordinate system:

1) Ellipse method. If the PSF exhibits radial symmetry, its cross-section is circular and the resolution along the x, y, s and t axes is equal. However, if the PSF possesses an axis of symmetry without being isotropic, the PSF cross-section is elliptical with the minor and major axes corresponding to the s and t axes respectively. The length of these axes can be deduced from the length of an arbitrary set of axes. Therefore, given $FWHM_x$, $FWHM_y$ and the angle between x-y and s-t coordinate systems, $FWHM_s$ and $FWHM_t$ (or HWZC) can easily be determined. Figure 5.3 illustrates the principle.

The length of the axis ρ, rotated from the major axis a by angle α is given by:

$$\rho^2 = \frac{t^2 s^2}{t^2 \sin^2 \alpha + s^2 \cos^2 \alpha} \qquad (7)$$

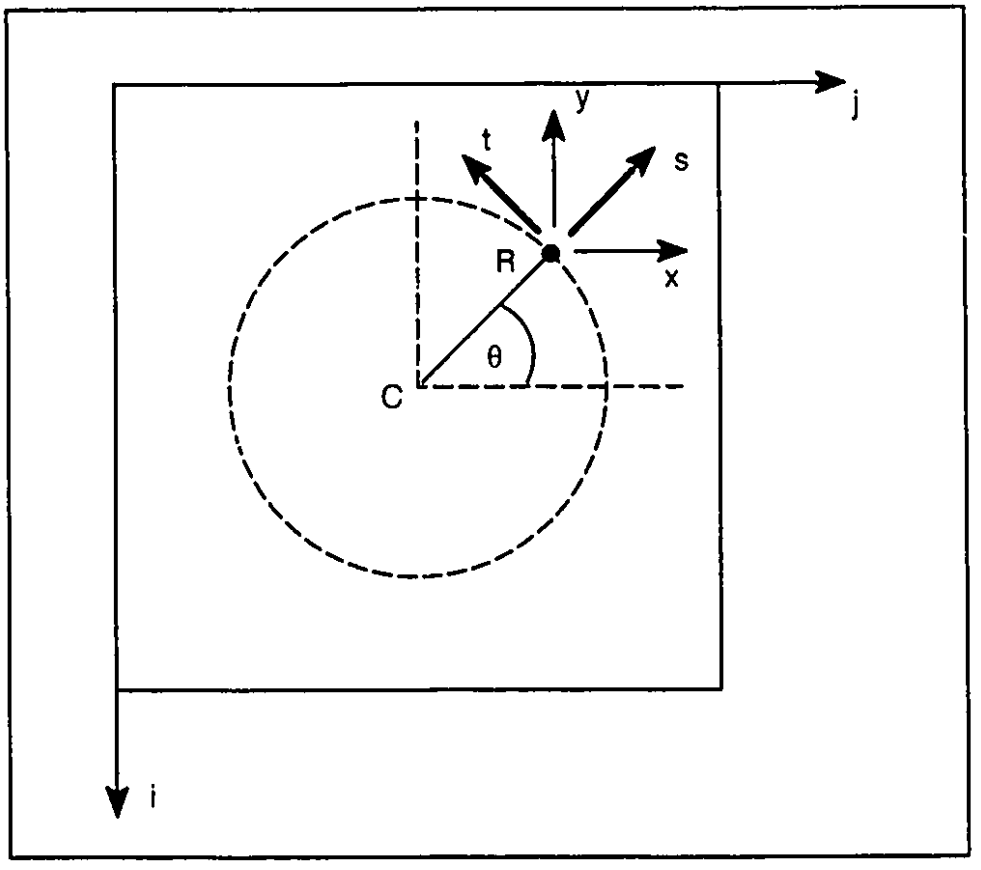

Figure 5.2 Relationship between coordinate systems

The position of an input point source is defined in polar coordinates (R,θ) whose origin is fixed in the center (C) of the image. Model parameters are given either in a local rotating (s-t) or local fixed orientation frame (x-y). Row and column indices (i-j) define the position of a pixel in image space.

By definition, the angle between the x and s axes is θ, the angular position of the input point source. Therefore, the angle between the t and x axes is $\alpha_x = \pi/2 - \theta$, and between t and y, $\alpha_y = \pi - \theta$. Replacing these values in equation (7), and making use of the reduction formulae for circular functions, gives:

$$FWHM_x^{\,2} = \frac{FWHM_s^{\,2}\, FWHM_t^{\,2}}{FWHM_s^{\,2}\sin^2(\theta) + FWHM_t^{\,2}\cos^2(\theta)} \tag{8}$$

$$FWHM_y^{\,2} = \frac{FWHM_s^{\,2}\, FWHM_t^{\,2}}{FWHM_s^{\,2}\cos^2(\theta) + FWHM_t^{\,2}\sin^2(\theta)} \tag{9}$$

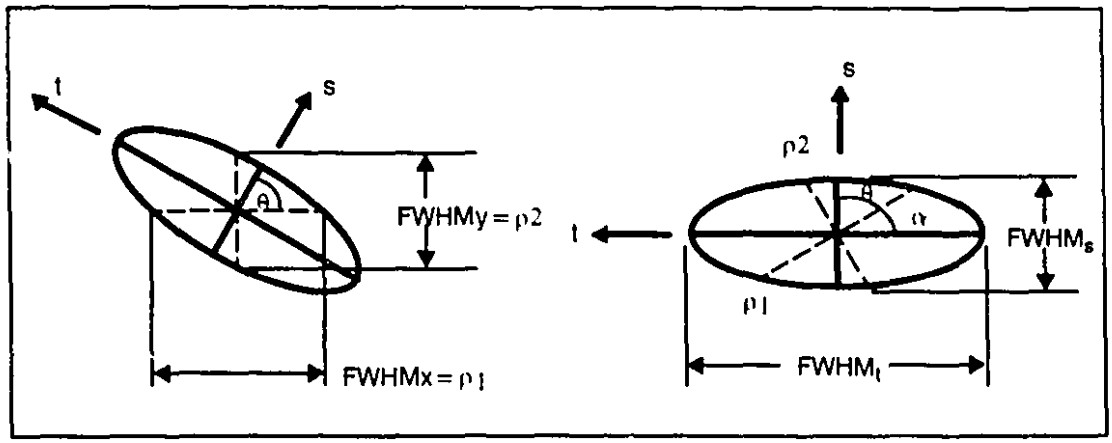

Figure 5.3 Estimating the Gaussian shape parameters in the s-t coordinate system from values defined in the x-y system

The shape of an ellipse is defined by the length of minor and major axes (FWHMs, FWHMt). Given these dimensions, the length of a set of normal axes (FWHMx, FWHMy) can be determined, and vice versa, if the orientation (θ) between them is known.

From these two equations, $FWHM_s$ and $FWHM_t$ are isolated:

$$FWHM_s^2 = \frac{FWHM_x^2 FWHM_y^2 [\cos^4(\theta) \sin^4(\theta)]}{FWHM_x^2 \sin^2(\theta) - FWHM_y^2 \cos^2(\theta)} \quad (10)$$

$$FWHM_t^2 = \frac{FWHM_x^2 FWHM_y^2 \sin^2(\theta)}{FWHM_x^2 - FWHM_y^2 \cos(\theta)} \quad (11)$$

This approach is not valid for points with an angular position $\theta = (2n + 1)\pi/4$, $n = 0,1,2,\ldots$ Noticing that $\sin^2((2n + 1)\pi/4) = \cos^2((2n + 1)\pi/4)$, equations (8) and (9) clearly show that the length of the axes in the x and y directions are equal. Therefore the solution collapses since the denominator of equation (10) becomes 0.

2) Image rotation. By rotating the image, the s and t axes can be made to coincide with the column and row directions respectively. However, if the rotation angle θ is not a multiple of $\pi/2$ radians, the image must be resampled since the new coordinates along the s-t axes do not necessarily fall on the original x-y pixel grid (Parker et al., 1983). Although implemented in one step, resampling involves two processes: interpolation (to form a continuous image from the discrete one) and sampling (the continuous image to obtain a new discrete representation). Two interpolation functions were evaluated: nearest neighbor and high resolution cubic splines. Spline interpolation was implemented using the algorithm in Keys (1981).

3) Change of model coordinates. This method consists of replacing the x and y variables in equations (1) and (2) by s and t. This requires that the pixel position be recomputed along the s-t coordinate system according to:

$$s = (j - j_p)\cos\theta + (i_p - i)\sin\theta \qquad (12)$$
$$t = -(j - j_p)\sin\theta + (i_p - i)\cos\theta$$

where (i_p, j_p) are the row and column coordinates of the upper left hand corner of the 21x21 region surrounding the image of the wire.

5.2.4 Statistical tests

A statistical test was performed to determine if the methods of estimating the model parameters in the s-t coordinate system were equivalent. The same approach was taken to verify if variables such as scan time and reconstruction filter significantly affected the shape of the PSF.

A t-test was performed when values were compared two by two. If the quantities were positively correlated, the data were paired, thereby increasing the effectiveness of the experimental design. When the experiment involved more than two samples, a one-way layout F-test, or analysis of variance, was used.

In all cases, the assumption that a given treatment or variable had no effect on the quantity tested constituted the null hypothesis H_o. Depending on whether it was assumed that the treatment yielded different, smaller or larger results, a two-sided test, in the first case, or one-sided test, as with the last two alternatives, was required. Unless indicated, the level of significance α was set at 0.01, which means that the probability of rejecting H_o even though it was true is equal to 0.01.

Except for the paired test, data were assumed independent. Furthermore, the random errors corrupting the data were expected to be normally distributed, with zero mean and constant variance. The assumption of normality can be relaxed without strongly affecting the test. For more details, the reader is invited to consult Freund (1981) and Rice (1988).

5.3 Results

Our results show that the pattern of shift-variance is greatly simplified when expressed in the rotating s-t compared to the fixed orientation x-y coordinate system. They also demonstrate that the system does produce a rotating blur. Furthermore, a comparison of the resolution along the radial and tangential axes of the rotating frame indicate that the PSF is not radially symmetric throughout most of the FOV. Table 5.1, to which we will refer throughout this section, summarizes the results of the statistical tests.

quantity tested	variable	type of test	alternative hypothesis	conclusion
radial symmetry	direction (resolution along s axis .vs. t axis)	two sided t-test	$FWHM_s(R_i) = FWHM_t(R_i)$ similarly for HWZC	$51 < R_c < 68$ mm [1,3] $34 < R_c < 51$ mm [2] $17 < R_c < 34$ mm [4]
	methods to obtain model parameters in s-t system	two-sided F-test across methods	methods yield different results	all methods are equivalent
	presence of absence of parameter B	unpaired one-sided t-test	$FWHM_{+B}(R_i) < FWHM_{-B}(R_i)$	$68 < R_c < 85$ mm [1] $51 < R_c < 68$ mm [2]
resolution	scan time	paired two-sided t-test for s direction	$FWHM_{s,4.5}(R_i) = FWHM_{s,9.0}(R_i)$	no effect in s direction
		paired one-sided t-test for t direction	$FWHM_{t,4.5}(R_i) > FWHM_{t,9.0}(R_i)$ similarly for HWZC	$51 < R_c < 68$ mm in t direction
	filter	unpaired one sided t-test	$FWHM(R_i) > HWZC(R_i)$	Ho rejected throughout most of the FOV

TABLE 5.1 Summary of statistical tests

quantity tested	variable	type of test	alternative hypothesis	conclusion
Gain	presence of absence of parameter B	unpaired one-sided t-test	$Gain_{+B}(R_i) < Gain_{-B}(R_i)$	$51 < R_c < 68$ mm [1,2]
	scan time	unpaired two-sided t-test	$Gain_{4.5}(R_i) = Gain_{9.0}(R_i)$	no clear pattern
	filter	unpaired one-sided t-test	$Gain_0(R_i) < Gain_4(R_i)$	Ho reject throughout the field of view
	radial distance	two-sided F-test across radial distance	$Gain(Ri) = Gain(Rj)$ $i = j$	no definitive trend

TABLE 5.1 Summary of statistical tests (continued)

R_c: critical distance; for $R < Rc$, accept Ho, for $R > Rc$, reject Ho
(1) filter 0, scan time of 4.5 s; (2) filter 0, scan time of 9.0 s
(3) filter 4, scan time 4.5 s; (4) filter 4, scan time of 9.0 s

5.3.1 X-Y coordinate system

Figure 5.4 illustrates the variation of FWHM in the row direction within the FOV. These curves are valid for the smoothing filter, a scan time of 4.5 s and parameter B absent from the Gaussian model. Moving from the center outward, resolution, which is inversely proportional to the FWHM, decreases. One can also distinguish an increasing fluctuation with angular position as the radial distance increases.

The relationship between FWHM along rows and columns for points located on the outermost circle is presented in Figure 5.5. The scanning and modelling conditions are the same as those for the data shown in the previous figure. These quantities are 180 degrees out of phase, indicating that resolution is different in the row and column directions in most of the image. Furthermore, it demonstrates that the PSF is radially asymmetric, since isotropy requires that p_x and p_y, hence $FWHM_x$ and $FWHM_y$, be equal.

Based on the previous argument, it would seem that the PSF is radially symmetric for $\theta = (2n+1)\pi/4$, $n = 0,1,2...$ since the two curves intersect at these points. It was previously shown however, that if the cross-section of the PSF is elliptical, the length of orthogonal axes angularly displaced by $(2n+1)\pi/4$ with respect to the major-minor axes are always equal, given any ratio of minor to major axis length.

5.3.2 S-T coordinate system

The values of resolution in Figure 5.5 were used as data to evaluate the different transformation methods: ellipse geometry, image rotation with nearest neighbor and high resolution spline interpolation, and change of model coordinates. As shown in figure 5.6 (a) and (b), the methods appear similar on a qualitative basis. A two-sided F-test, presented in table 5.1 under the topic of resolution, confirms this claim. Although these methods are statistically equivalent, the ease of implementation and the time required to perform the transformation varies greatly. The method based on the change of model coordinates, being the simplest and quickest, was applied to all further analysis.

Figure 5.6 (c) illustrates the FWHM in the s-t coordinate system obtained using the change of model coordinates method. The cyclic dependance of the FWHM on angular position is no longer observable, suggesting that the imaging system does produce a rotating blur. To further verify this possibility, the basic statistics (mean and standard variation) of 16 wires arranged in a circle were compared to those obtained by imaging a wire in a constant position 16 times. The single wire in section B of the Philips performance phantom (see figure 3.1) provided the data for the former test. Since this wire was located 51.3 mm directly above the center of the FOV, the 16 wires located at a radial distance of

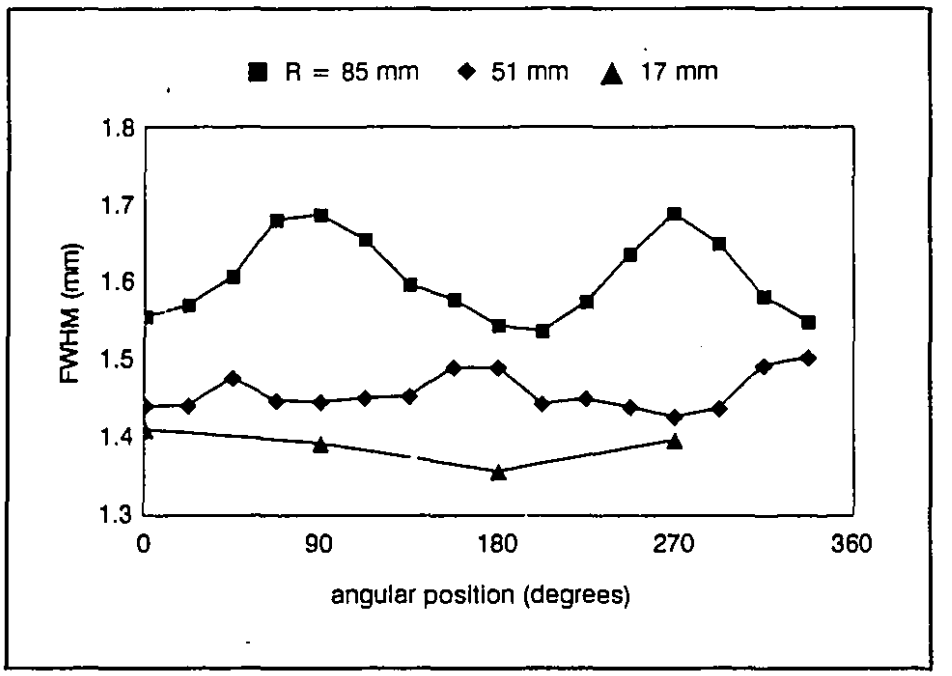

Figure 5.4 Variation of resolution along the x axis
(filter 0, 4.5 s, parameter B absent from Gaussian model)

The resolution in the row direction varies sinusoidally with angular position. As the position of the input point moves closer to the center of the field of view, the amplitude of the variation decreases.

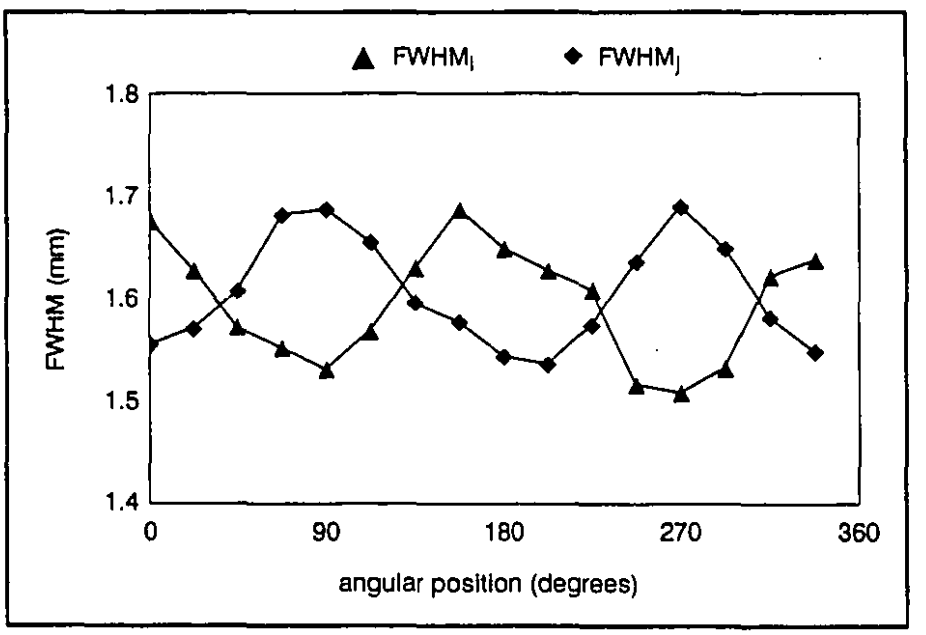

Figure 5.5 Resolution along the (a) x and y axis and (b) s and t axis for points located at a radial distance R=85 mm (filter 0, 4.5 s, parameter B absent from Gaussian model)

The resolution in the row and column directions are both sinusoidal, coupled and 180° out of phase.

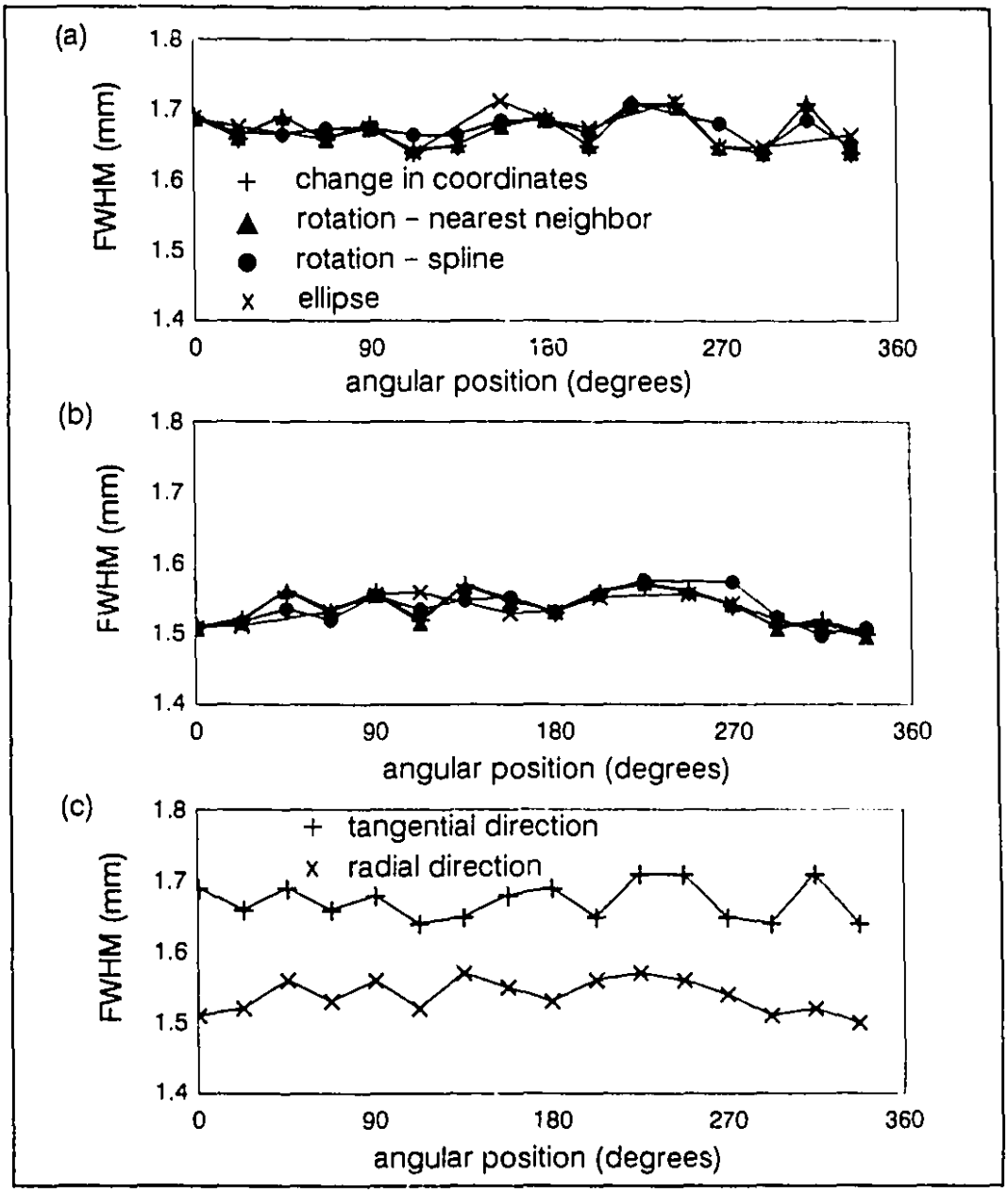

Figure 5.6 Comparison of methods to obtain shape descriptors is s-t coordinate system (filter 0, 4.5 s, parameter B absent from Gaussian model)

The four methods used to obtain the model parameters in the local rotating frame are statistically equivalent for (a) radial direction (s axis), and (b) tangential direction (t axis). (c) results for change of coordinates method. Expressing the model parameters in a local rotating coordinate system decouples the resolution estimated in two perpendicular directions. Furthermore, resolution is no longer a function of angular position.

51 mm in the shift-variance phantom were used in the other case. The results are compared in table 5.2. Although there is more variation for the data coming from the shift-variant phantom, an unpaired two-sided t-test concluded that there is no statistical difference in the mean values between the two experimental designs.

test	radial direction		tangential direction	
	mean	standard deviation	mean	standard deviation
same wire imaged 16 times	1.451	0.002	1.476	0.002
16 wires arranged in a circle in same image	1.439	0.017	1.476	0.028

Table 5.2 Statistics for points located at a radial distance of 51 mm

5.3.3 Effect of parameter B

Because the wires were placed in water, the CT number of the pixels surrounding the PSF should average 0. However, the cupping artefact due to x-ray scatter, causes a depression of CT values in the center of the FOV, while inflating values at its periphery.

In Figure 5.7, the average background value surrounding the points forming a circle is plotted against radial distance. The four curves represent different combinations of image reconstruction filter and scan time. In all cases, the background values increases slightly moving from the center of the FOV outward.

Figure 5.8 (a) compares the FWHM obtained when adding or omitting parameter B from the Gaussian model for a scan time of 4.5 s. Parameter B seems to have no effect in the center of the field of view, but as radial distance increases, the values obtained with parameter B appear lower.

In a paired t-test, the null hypothesis, which states that the expected value of FWHM computed in the presence or absence of B are equivalent, was tested against the alternative hypothesis of the FWHM computed in presence of parameter B being smaller. The results reveal that values of FWHM computed with parameter B added to the model are indeed lower but only for points located beyond a critical distance R_c. At the 0.01 level of significance, the critical distance is located between 51 and 68 mm for a scan time of 9.0, and between 68 and 85 mm when the number of views is halved. However, if the level of significance is relaxed to 0.03, $51 < Rc \leq 85$ mm irrespective of scan time.

The effect of parameter B on gain is illustrated in figure 5.8 (b). The omission of parameter B results in an increase of the gain estimates with radial distance past Rc, $51 < Rc \leq 85$ mm, confirmed by a one-way layout F-test across the radial distance (level of significance = 0.01). This statement is valid both for a scan time of 4.5 and 9.0 s.

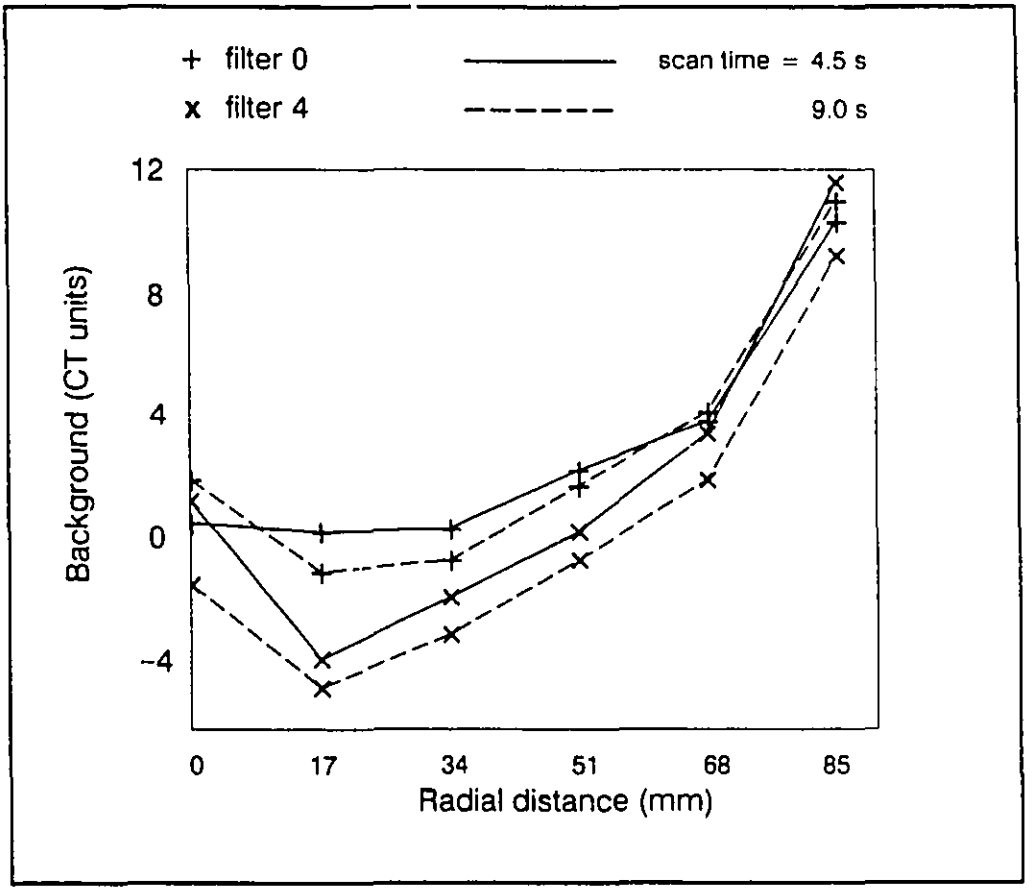

Figure 5.7 average background as a function of radial distance

In third generation scanners, X-ray scatter produces an artefact known as cupping. The CT values in the center of the FOV are depressed, while those in the outlying regions are overestimated.

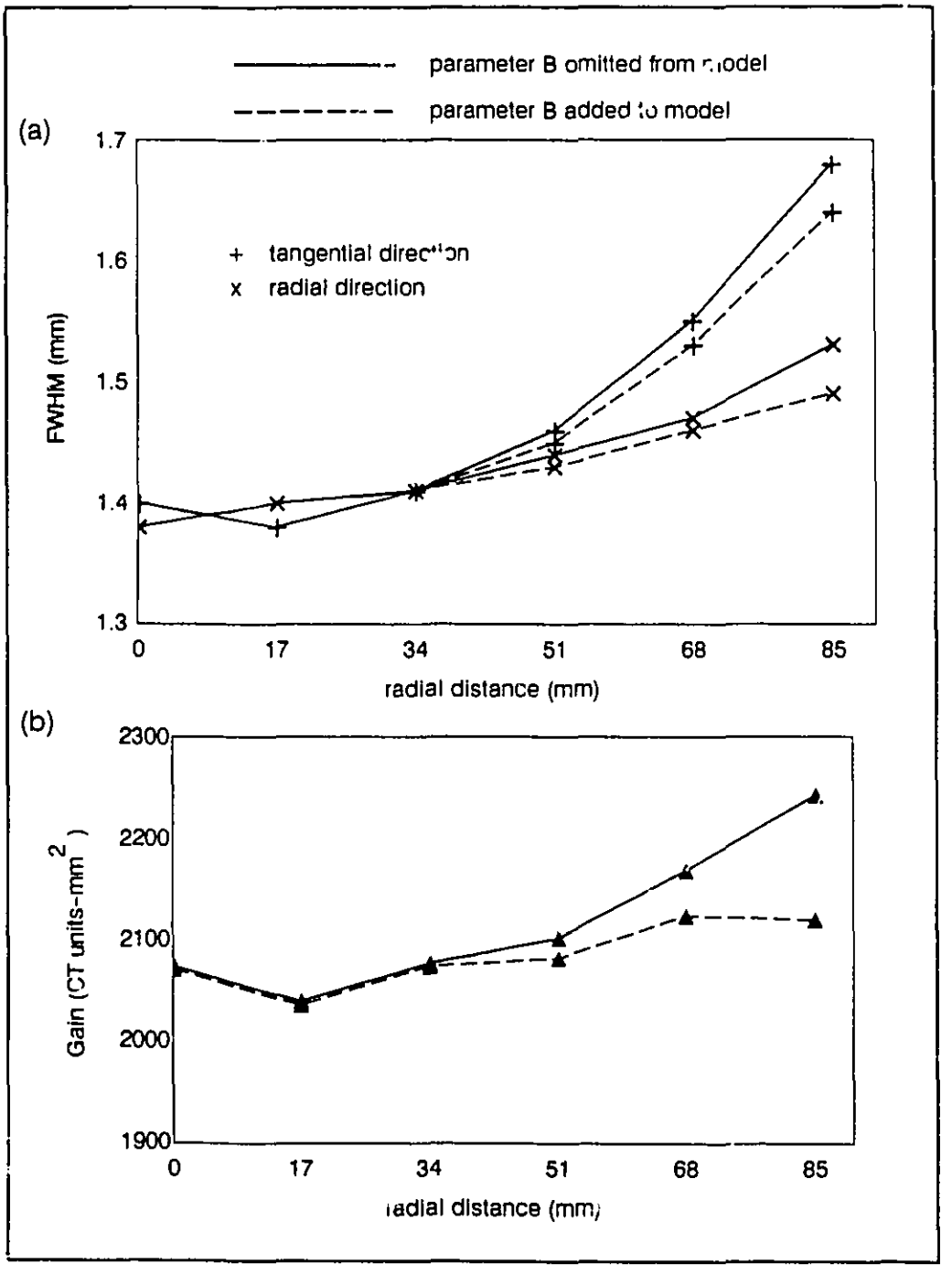

Figure 5.8 Effect of omitting parameter B from Gaussian model on (a) resolution and (b) gain estimates (filter 0, scan time of 4.5 s, parameter B added to model)

Past a critical distance Rc, estimates of gain and FWHM both increase as a result of omitting parameter B from the Gaussian model. For a level of significance $\alpha = 0.03$, $51 < Rc < 68$.

5.3.4 Effect of scan time

Figure 5.9 (a) illustrates the effect of doubling the scan time on the estimates of resolution. The estimates of FWHM and HWZC are barely affected in the radial direction, but increasing the number of views results in a large improvement in resolution in the tangential direction.

These qualitative observations are confirmed by a paired t-test performed at discrete values of radial distance. In the case of resolution estimated along the s axis (radial), the null hypothesis is tested against the values being different. However, for the t axis (tangential), the alternative hypothesis consists of verifying if values of FWHM or HWZC are greater for a scan time of 4.5. The level of significance is again set at 0.01. The statistical tests show that changing the scan time has no bearing on resolution in the radial direction either for the smoothing nor the high resolution filter. However, as shown in Figure 5.9 (a), the resolution in the tangential direction improves with a larger number of views past a certain critical radius R_c located between 34 and 51 mm ($R > R_c$, $34 < R_c \leq 51$ mm). The increase is as large as 0.21 and 0.28 mm for the smoothing and high resolution filters respectively for a radial distance of 85 mm.

No clear pattern emerges when gain is considered. Estimates of gain for both filters and the two scan times are compared in Figure 5.9 (b). A t-test reveals that, for the smoothing filter, the estimates of gain are significantly different only for distances of 68 and 85 mm, while for the high resolution filter, only the values at 68 mm are affected.

5.3.5 Effect of image reconstruction filter

Of all the factors examined so far, the image reconstruction filter has the strongest influence on resolution. Figure 5.10 shows the estimates of resolution as a function of radial distance for both filters considered. The trends are similar irrespective of the filter used to create the image. However, the values of FWHM obtained with the smoothing filter are substantially larger than those of HWZC obtained with the high resolution filter, confirmed by a t-test with level of significance of 0.01.

The influence of omitting parameter B from the models and of scan time are felt past a given radial distance. However, when the reconstruction filter is considered, the difference in mean values between the two filters remains constant throughout the range of distance examined. For a scan time of 4.5 s, the difference in resolution averaged over radial distance is about .31 mm both for radial and tangential directions. However, for a scan time of 9.0, the difference is larger in the tangential than in the radial direction with values of .35 mm and .29 mm respectively.

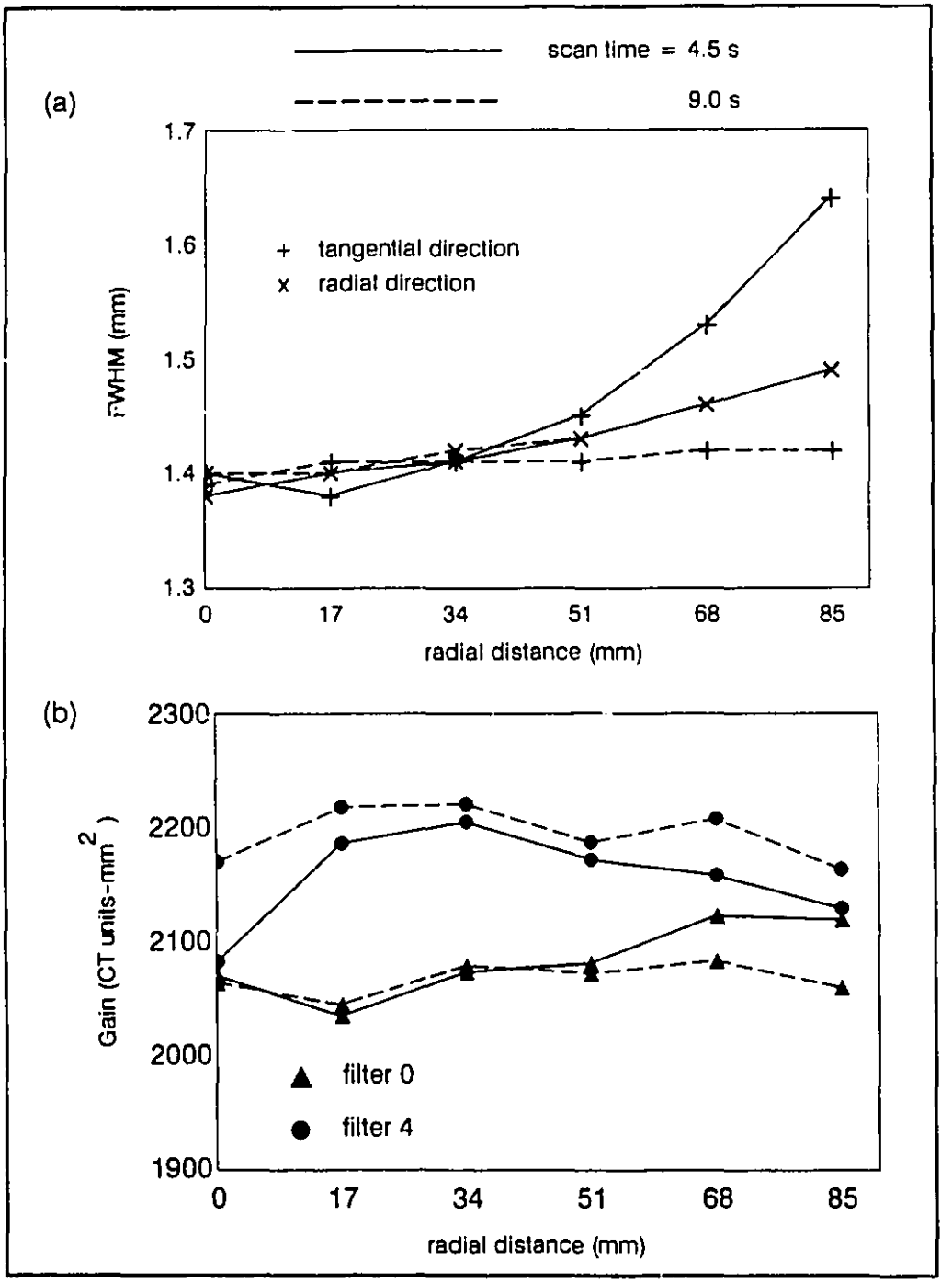

Figure 5.9 Effect of scan time on (a) resolution (filter 0) and (b) gain estimates (filters 0 and 4)

Doubling the number of views significantly improves the resolution in the tangential resolution past a critical radial distance Rc, $51 < Rc < 68$. Resolution in the radial direction is not affected by this parameter. No clear pattern emerges for the gain.

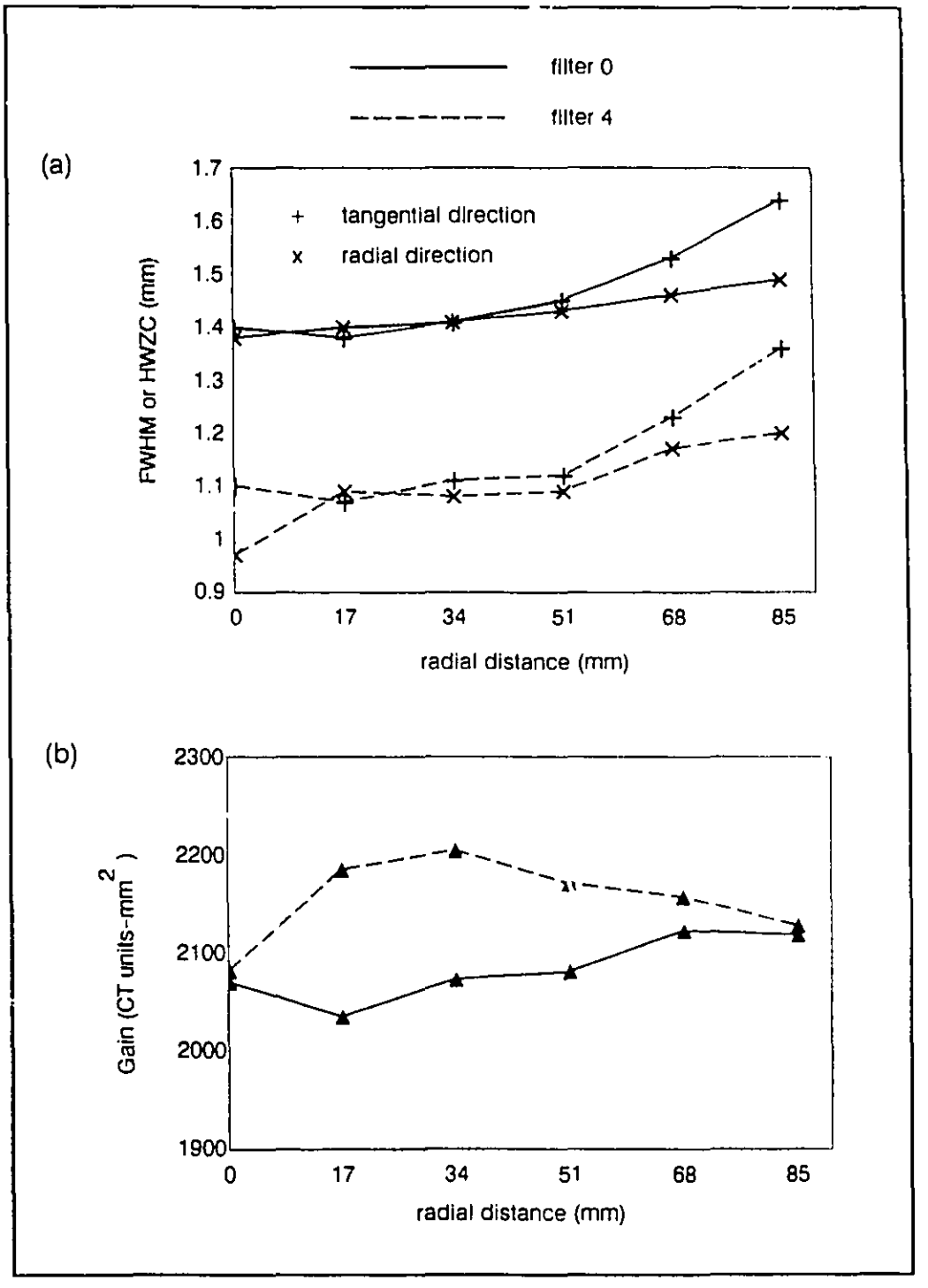

Figure 5.10 Effect of image reconstruction filter on (a) resolution and (b) gain (scan time of 4.5 s)

While the image reconstruction filter is the parameter which affects the amount of blur the most, it has no bearing on shift-variance.

Figure 5.10 (b) compares estimates of gain for the two filters. As with resolution, changing the reconstruction filter significantly affects the gain. A one-sided t-test, where the null hypothesis is tested against the gain of filter 4 being larger than that of filter 0, reveals that the gain produced by the high resolution filter is indeed significantly larger over the whole FOV ($\alpha = 0.01$). However, reserve must be expressed for data obtained with a scan time of 4.5 and in the vicinity of 85 mm, since the level of significance must be increased to 0.25 to arrive at the same conclusion.

5.3.6 Radial symmetry

A PSF produced by the smoothing filter and modelled by a Gaussian function is radially symmetric if the parameters p measured along two perpendicular axes are equal. Because the FWHM is directly related to parameter p, equal values of FWHM in the radial and tangential directions indicate the presence of a radially symmetric PSF. The same argument is valid for the high resolution filter based on the HWZC.

Observing figures 5.9 (a) and 5.10 (a), one notices that estimates of resolution along the s and t axis are similar in the center of the FOV. However, past a critical radial distance, the values diverge. Based on a t-test with a level of significance of 0.01, Rc varies largely with the filter and number of views used to create the image:

$51 < R_c \leq 68$ for filters 0 and 4 and a scan time of 4.5 s,

$34 < R_c \leq 51$ for filter 0 and a scan time of 9.0 s,

$17 < R_c \leq 34$ for filter 4 and a scan time of 9.0 s.

However, if the level of significance is relaxed to 0.05, we observed a value of $34 < R_c \leq 51$ for a scan time of 4.5 s irrespective of the filter used.

5.4 Discussion

We will open the discussion by explaining the origin of shift-variance and of the rotating blur. This will bring us to compare our results with those of the theoretical studies. The effects of scanning variables and of the model parameter B will close the section.

5.4.1 Origin of shift-variance

Various authors have identified a number of factors which can cause the PSF to become shift-variant: projection misregistration, aliasing and x-ray beam sensitivity.

Kijewski and Judy (1983) determined that the misregistration of projections leads to anisotropy and position dependence of the PSF. They mentioned that scanners most

susceptible to this type of error were those with continuous detectors, SPECT scanners with gamma cameras as detectors for example. In such systems, the positional information is determined by electronic means. X-ray CT scanners on the other hand depend on the physical positions of discrete detectors and are therefore much less prone to misregistration.

Joseph et al. (1980) considered the effect of varying the number of samples per beam width on the shape of the PSF. They showed that the PSF would be isoplanatic if it were possible to image structures with infinitely thin x-rays. However, projections being acquired with detectors of finite width and due to the digital nature of the data, projections must be resampled. This can lead to the introduction of supra-Nyquist frequencies (Parker et al., (1983)) and to aliasing.

One of the effects of aliasing, apart from systematic artefacts, is to make the PSF shift-variant. The extent of aliasing depends on the distance between ray samples: decreasing the distance, or increasing the number of rays per beam width, reduces aliasing. Unless designed with a 1/4 detector offset, Joseph (1980) warns that third generation scanners are particularly susceptible to aliasing since they collect only one sample per detector.

Although not mentioned by the authors, the type of interpolation function can also control the extent of aliasing. Using a function with smaller side-lobes, for example linear interpolation rather than nearest neighbor, limits the amount of aliasing.

Unfortunately, Joseph et al. did not investigate how aliasing affects the variation of PSF shape with position. From two illustrated simulations carried out by Joseph (1980), it appears that aliasing destroys the radial and axial symmetry of the PSF. The presence of "streaming tails" can also be observed.

An important consequence of a finite beam width which was not taken into account in the previous study is that projections can no longer be represented as line integrals of the linear attenuation coefficients. Instead, projections should be represented by strip integrals defined by the source and detector collimators. Bracewell (1977) and Verly and Bracewell (1979) showed that the detector response to a point source depends on the position of that source within the strip. They characterized the variation by a strip integral kernel $K_0(x,y,R,\phi)$, also known as the spatial response or the profile of the x-ray beam. Figure 5.11 illustrates the beam spatial response in the case of non-zero eccentricity, i.e. when the midpoint of the strip does not coincide with center of the FOV. The PSF of a point located at (x_0,y_0) is given by the integral over rotation angle ϕ of $K_0(x_0,y_0,R,\phi)$ convolved by the appropriate apodized rho-filter.

Numerical integration of the strip integral kernel for the condition of equal source and detector width and of rectangular shape revealed that the PSF, expressed in a rotating frame s-t, exhibited the following features:

1) the presence of a cratered cone radially symmetric PSF in the center of the FOV. This is also known as the volcano effect (Joseph et al. (1980)).

2) the emergence of infinite peaks along the t axis whose separation is proportional to radial distance. In the presence of non-zero eccentricity, the infinite peaks are transformed into depressions.

3) the response was strictly limited to a circle of radius equal to half the beam width.

Although the authors did not discuss the issue of radial symmetry, this simulation clearly showed that the increasing separation of the peaks along the t-axis destroyed the radial symmetry that the PSF exhibited in the center of the FOV.

Verly and Bracewell also mentioned that the cross section of $K_0(x,y,R,\phi)$ perpendicular to the y axis is composed of trapezoids of equal area. Since the PSF is built up from a large number of these cross-sections, their constant weight assures that the volume, or gain, of the PSF is the same at every point, even if the PSF is shift-variant.

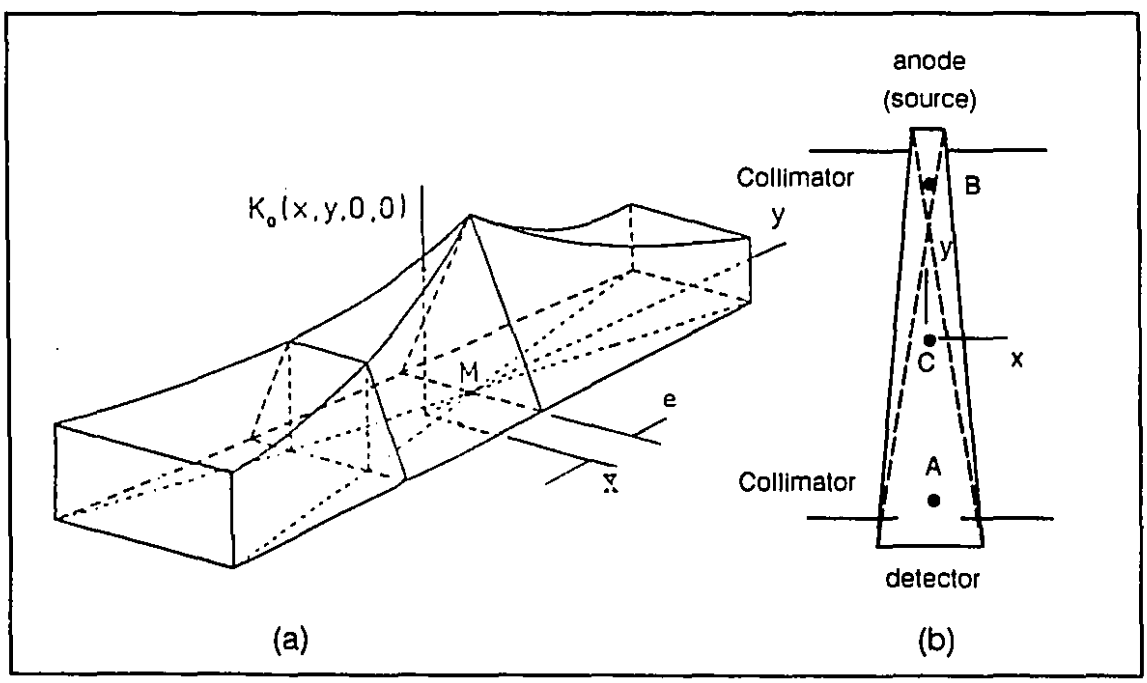

Figure 5.11 Strip integral kernel (a) perspective plot for non-zero eccentricity (Verly and Bracewell (1979) , (b) beam profile in x-y plane

Two points A and B equidistant from the center of the field of view C will create different responses due to beam profile inhomogeneity. For a 360 acquisition mode the responses average out since both points are imaged once near the source and once near the detector, thus resulting in rotating blur.

5.4.2 Origin of rotating blur

To understand the origin of rotating blur for a 360° reconstruction, let us consider two points A and B in figure 5.11 (b). These points are equidistant from the center C of the FOV. For a scan angle of 0 degrees, A is located closer to the detector and B near the source. These two points generate different detector responses due to the inhomogeneity of the beam profile. If data are acquired in a 180° mode, points A and B are measured only once for a given (R,ϕ), and the resulting PSFs will be different. However, with a 360° acquisition mode, each point is measured twice, once near the source and once near the detector. Because the responses are averaged, the image of the two points, and of all points located at the same radial distance, will be the same.

5.4.3 Similarities with theoretical studies

Our experimental results confirm many theoretical findings. They lead to the same conclusions regarding rotating blur, radial symmetry and the general shape of the PSF.

1) Several experimental results lead to the conclusion that the CT system produces a rotating blur. Firstly, the sinusoidal dependance of FWHM on angular position when expressed in a local fixed orientation (x-y) coordinate system disappears when the shape of the PSF is described in a local rotating frame (s-t).

Secondly, the mean value of resolution for 16 wires arranged in a concentric circle is statistically equivalent to imaging a single wire in a constant position 16 times , as shown in Table 5.2. The larger variance for the former case can be explained as follows. Due to variations in radial and angular wire positions in the shift-variance phantom, it is improbable that the input point sources occupy the same position within the beam profiles. Because of beam non-homogeneity, small changes in position lead to slightly different responses. This also explains why the variance in the tangential direction is larger than for the radial orientation. As seen in figure 5.10, the slope of the FWHM as a function of radial distance is larger in the tangential direction for a scan time of 4.5 s. Hence, for a given change in position, the variation in FWHM will be greater. On the other hand, unless the scanner does not realign itself properly, the position of the single wire with respect to the beam profile should remain constant. The variance seen in this case is largely due to noise in the data.

2)The PSF looses its radially symmetry as the excitation moves away from the center of the FOV. A direct consequence of anisotropicity is that resolution not only depends on position, due to the shift-variance of the PSF, but it is also a function of orientation. Fortunately, this effect becomes significant only at a certain critical distance

from the center of the image. The largest difference in resolution along perpendicular axes is estimated at 0.15 mm. This figure is valid for structures located at a radial distance of 85 mm in an image reconstructed with the smoothing filter and produced with a scan time of 4.5 s.

3)The stretching of the PSF along the t axis predicted by Verly and Bracewell is also observed for data acquired over 4.5 s.

5.4.4 Discrepancies with theoretical studies

Despite the similarities described above, our results differ from those of the theoretical studies in a number of points, principally where discontinuities in the PSF and its extent are concerned.

The theoretical studies and the experimental approach presented above share many similar results

1) In contrast to Verly and Bracewell, we observed no discontinuities in the PSF (see Figure 4.2). Several factors can explain this discrepancy. These authors attribute the presence of discontinuities to the breakpoints in the trapezoidal profiles along the beam spatial response. The cross-sectional shape of $K_0(x,y,R,\phi)$ largely depends on the focal spot, or source, intensity distribution and the detection sensitivity distribution. While it is reasonable to assume a uniform distribution for the detector, the hypothesis of uniform photon emission has been challenged by a number of authors (Prasad (1979), Joseph et al. (1980), Verly (1980)). There is no doubt that a Gaussian source distribution (Rathee et al. (1990)) would lead to a smoother PSF. Bracewell (1977) also concedes that features such as the volcano effect may not be revealed due to limited pixel size or because of the computing procedure. Furthermore, Joseph et al. showed that a finite sampling rate across the beam width tends to fill the central depression and produce a smoother PSF.

2) Verly and Bracewell pointed out that the PSF was limited to a circle of radius equal to half the beam width, a feature that we did not observe. Finite ray sampling is certainly a key factor in explaining this discrepancy. Apart from lessening the volcano effect, Joseph et al. showed that finite ray sampling also extends the range of the PSF beyond the beam width. Furthermore, in their formulation, Verly and Bracewell did not consider the effect of the apodizing function. This factor is known to greatly affect the shape of the PSF and could also be at play here.

5.4.5 Effect of scan time

By considering the angular position ϕ as a continuous variable, Verly and Bracewell and Joseph et al. greatly simplified their analysis. However, by doing so, they neglected to consider the effect of finite view sampling. Joseph et al. justified their choice by arguing that the effects of ray sampling and view sampling are entirely distinct. Finite view sampling affects the radius of an error free reconstruction for a given spatial resolution (Joseph and Schultz (1980)).

Our results showed that the shape of the PSF along the s axis was not affected by increasing the number of views. However, the resolution in the tangential direction significantly improved past a critical radial distance. The critical distance was estimated to lie between 51 mm and 68 mm. For points in the outlying regions, changing the scan time produced a change in resolution almost as large as that produced by reconstructing the image with a different filter.

It is tempting to argue that increasing the number of views improves sampling in the angular or tangential direction only, and it is therefore normal to see an improvement only along the t axis. This argument would be valid for a parallel ray geometry but does not hold for a fan-beam configuration. The effect of scanner geometry is best appreciated in sinogram space as illustrated in figure 5.12. For both constructions, the sinogram is filled up by a series of parallel lines, each line representing a view or projection. For a parallel beam scanner, views are parallel to the line $\phi = 0$ and an increase in view density only decreases intersample distance in the angular direction.

However, for a fan-beam geometry, the views fill up the sinogram as a series of parallel lines oriented at an angle ψ, where ψ is the fan angle. Because the position of a point in a given projection is now a function of both scan angle and radial position, increasing the sampling rate of either one of these variables decreases the intersample distance of the other. Hence, for a fan-beam geometry, one could improve the radial, as well as the tangential resolution by doubling the scan time. However, taking advantage of the new data requires an increase in processing time and storage space. It is possible that the manufacturer, satisfied with the relatively little variation of resolution in the radial direction compared to the angular orientation, chose only to improve the latter. Despite repeated requests addressed to the manufacturer, we were unable to confirm this hypothesis.

5.4.6 Effect of image reconstruction filter

The theoretical studies failed to take the apodizing function into account in their formulation. Verly and Bracewell argued that its action can be considered and added at

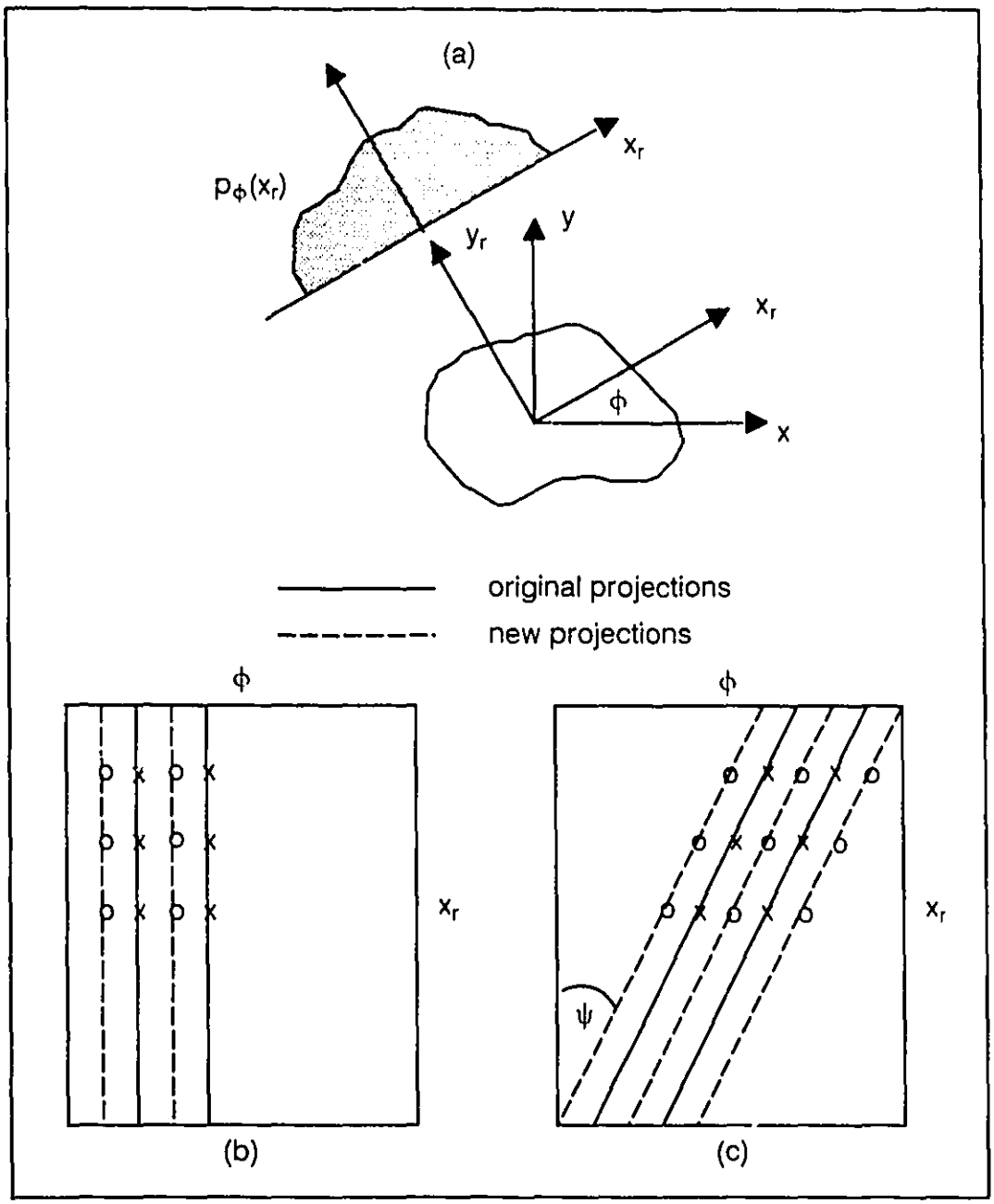

Figure 5.12 Sinogram for parallel- and fan-beam geometry

(a) A projection, or view, is composed of a series of line integrals of attenuation coefficient in the direction of the x-ray beam. For parallel-beam scanners, projections show up as lines parallel to $\phi = 0$. The introduction of new views increases the number of samples in the angular direction but does not affect radial inter-sample distance. Projections are oriented at an angle ψ for fan-beam geometry. As a result, increasing the number of views also increases the sampling rate radially.

anytime on the basis of linearity, but that its effect can be neglected without loss of generality.

Our experimental results show that their approach was justified. Changing the reconstruction filter did not affect patterns of shift-variance. The difference in resolution remained constant as radial distance was increased and estimates of gain were consistently larger for the high resolution filter. This is not to say that the effect of the apodizing filter is negligible. Of all the parameters considered in this study, reconstruction filter is the one that affected the amount of blur the most. However, this effect did not depend upon the position of the input point source.

5.4.7 Effect of parameter B

Simulations have shown (see section 4.4.2) that a positive background introduces a negative bias to the shape parameters p_x and p_y of the Gaussian model while a negative background produces a positively biased estimate. In both cases, the normalizing parameter N is underestimated.

Experimental results show that the effect of omitting parameter B is felt past a critical radial distance R_c. For the smoothing filter, the critical distance is estimated to be located between 51 and 68 mm. At this point, the average background is about 3 CT units.

One could be tempted to use the variation of parameter B with radial distance to quantify the cupping artefact. However, one must keep in mind that the amount of scatter, and the extent of cupping, depends on the object composition and its size, or more specifically on the portion of the imaging FOV occupied by the object. Therefore, the results presented in this work should only be used for similar scanning conditions.

5.5 Conclusions

Using a parametric system identification approach, we have successfully characterized and quantified the shift-variant as well as anisotropic properties of an x-ray CT scanner. We also investigated the effect of image reconstruction filter and finite number of views, parameters which had not been considered in previous studies.

When the position of the input point source is represented in polar coordinates, the shape of the identified PSF, expressed in a local fixed-orientation coordinate system x-y, is a function of both angular and radial coordinates. The variation with angle is sinusoidal and the amplitude increases with radial distance. However, because the system produces a rotating blur, the positional dependence is only a function of radial distance when the PSF

is represented in a local rotating frame s-t. The s and t axes correspond to the radial and tangential directions respectively.

Increasing the number of views greatly improves the resolution in the tangential direction in the outer regions of the FOV. The only other parameter considered in this study to have a greater effect is the image reconstruction filter. This result is not surprising since the apodizing function completely modifies the characteristics of the PSF. However, because the changes are constant throughout the FOV, the apodizing function does not affect patterns of shift-variance.

The radial symmetry that the PSF exhibits in the center of the FOV is progressively lost as the input source moves toward the periphery. As a consequence, the capacity to distinguish closely spaced objects is not only a function of their position but also of their orientation. This is particularly true of low scan times where the difference in resolution in the radial and tangential axes of the rotating frame are greater than for the case where a large number of projections are collected.

CHAPTER 6
CORRELATION BASED NON-PARAMETRIC PSF IDENTIFICATION

6.1 Introduction

The use of a thin wire as input for the non-parametric identification of the PSF has often been criticized in the literature (Judy, 1976; Droege and Morin, 1982; Nickoloff and Riley, 1985; Ehrhadt, 1986). Since the results of the previous chapters are based on this input, it became important to verify if these estimates were valid.

One possibility would have been to estimate the PSF with the edge method (Judy, 1976). However, a large number of edge orientations would be necessary to generate a two-dimensional estimate. Furthermore, to take advantage of the method, the edge must be relatively long and the issue of shift-variance can become a problem.

For these reasons, we preferred the correlation-based method. Furthermore, this method has never been applied to medical imaging systems. This study presents a good opportunity to introduce this tool to the imaging community.

The first goal of this chapter was therefore to estimate the PSF from the input/output correlation relationship known as the Wiener-Hopf equation. The second objective was to compare the non-parametric PSF estimates obtained with this method with those generated with the wire input.

The following section is devoted to the origin of the Wiener-Hopf equation and to its implementation in two dimensions. Section 6.3 contains a detailed description of the design of the input signal. Section 6.4 explores how a number of factors affect the identification quality through a series of simulations. Knowledge gained from these simulations is then applied to the experimental identification in section 6.5, followed by a discussion in section 6.6. Section 6.7 finally concludes the chapter.

6.2 Background

Correlation methods have been successfully used to identify the system characteristics in a wide variety of engineering fields ranging from nuclear power plants (Godfrey, 1969) to linear (Hunter and Kearney, 1983; Kearney and Hunter, 1990) and non-linear physiological structures (Marmarelis and Marmarelis, 1978). The underlying principles are explained in a concise manner by Godfrey (1980) while a more detailed account can be found in Bendat and Piersol (1986) and Marmarelis and Marmarelis (1978).

In this section, we will introduce the reader unfamiliar with this approach to the Wiener-Hopf equation. We will also elaborate on how the equation is solved using a matrix formulation. Throughout the text, special emphasis is placed on the 2D discrete nature of the CT imaging device.

6.2.1 Theory

In absence of noise, the relationship between the output and the input for a linear, stationary, shift-invariant system is given by the convolution integral:

$$b(x,y) = \int_{-\infty}^{\infty}\int_{-\infty}^{\infty} h(\chi,\gamma)\ a(x-\chi,\ y-\gamma)\ d\chi\ d\gamma \tag{6.1}$$

where x, y, χ, γ: independent and continuous spatial variables,
h(x,y): system impulse response or point spread function (PSF),
a(x,y): input and
b(x,y): output.

In terms of an imaging system, h(x,y) represents the point spread function (PSF), while a(x,y) and b(x,y) are the object under observation and its image respectively. In a two sided, discrete version, equation (6.1) becomes:

$$b(u,v) = \Delta\mu\Delta\nu \sum_{\mu=-I}^{I}\sum_{\nu=-J}^{J} h(\mu,\nu)\ a(u-\mu, v-\nu) \tag{6.2}$$

where u, v,, μ, ν are independent, discrete, spatial variable. The object and image are of size K by L pixels and the PSF is assumed to be of finite size M by N pixels where $M = 2I + 1$ and $N = 2J + 1$. Changing the variable u to $u+i$ and v to $v+j$, multiplying both sides by a(u,v) and summing yields:

$$\sum_{u=-I}^{I}\sum_{v=-J}^{J} a(u,v)\ b(u+i, v+j) = \Delta\mu\Delta\nu \sum_{\mu=-I}^{I}\sum_{\nu=-J}^{J} h(\mu,\nu) \sum_{u=-I}^{I}\sum_{v=-J}^{J} a(u,v)\ a(u+i-\mu, v+j-\nu) \tag{6.3}$$

A biased estimator for the autocorrelation and cross-correlation functions for zero-mean input and output signals is:

$$C_{aa}(u,v) = \frac{1}{MN}\sum_{u=-I}^{I}\sum_{v=-J}^{J} a(u,v)\ \ a(u+\mu, v+\nu) \tag{6.4}$$

$$C_{ab}(u,v) = \frac{1}{MN}\sum_{u=-I}^{I}\sum_{v=-J}^{J} a(u,v)\ \ b(u+\mu, v+\nu) \tag{6.5}$$

Incorporating equations (6.4) and (6.5) into (6.3) yields:

$$c_{ab}(i,j) = \Delta u \Delta v \sum_{\mu=-I}^{I} \sum_{\nu=-J}^{J} h(\mu,\nu)\ c_{aa}(i-\mu, j-\nu) \tag{6.6}$$

where i,j : independent discrete spatial variables,
c_{ab}: input-output cross-correlation function, and
c_{aa}: input auto-correlation function.

Equation (6.6) is known as the Wiener-Hopf equation. It states that the cross-correlation function (CCF) between the object and its image is equal to the convolution of the PSF with the object auto-correlation function (ACF). To avoid edge effects during convolution, $c_{aa}(i,j)$ must be twice the size of the PSF, which implies that:

$i = -M+1, -M+2 \ldots 0 \ldots M-2, M-1 = -2I, -2I+1 \ldots 0 \ldots 2I-1, 2I$

$j = -N+1, -N+2 \ldots 0 \ldots N-2, N-1 = -2J, -2J+1 \ldots 0 \ldots 2J-1, 2J$

whereas c_{ab} and h are arrays of size M by N and therefore:

$i = -I, -I+1 \ldots 0 \ldots I-1, I$

$j = -J, -J+1 \ldots 0 \ldots J-1, J$

6.2.2 Implementation

Unless the input signal has an extremely simple ACF, a subject which will be discussed later, the estimate of the PSF must be obtained through deconvolution of equation (6.6) (Sawaragi et al., 1985). This can be done by expressing this equation in matrix form:

$$\mathbf{C_{AB}} = \mathbf{C_{AA}}\ \mathbf{H} \tag{6.7}$$

where $\mathbf{C_{AB}}$: vector containing elements of the cross-correlation function $c_{ab}(i,j)$
$\mathbf{H}$: vector containing elements of the point spread function h (i,j)
$\mathbf{C_{AA}}$: square matrix containing elements of the auto-correlation function $c_{aa}(i,j)$

In the equations above, the terms $\Delta u \Delta v$ were incorporated into matrix $\mathbf{C_{AA}}$. The solution for H is readily obtained by pre-multiplying both sides of (6.7) by the inverse of $\mathbf{C_{AA}}$.

$$\mathbf{H} = \mathbf{C_{AA}}^{-1}\ \mathbf{C_{AB}} \tag{6.8}$$

The main difficulty in estimating the filter is computing the inverse of the matrix containing elements of the auto-correlation function. The size and contents of the vectors $\mathbf{H}$, $\mathbf{C_{AB}}$ and matrix $\mathbf{C_{AA}}$ depend on the method chosen to do so.

The system of equation (6.7) can be set up so that $\mathbf{C_{AA}}$ is a symmetric Toeplitz matrix. The methods of solution using this property are fast and require modest amounts of memory but are unstable (Doukoglou, 1989). Because of its robustness, we adopted singular value decomposition (SVD) as a mean of inverting $\mathbf{C_{AA}}$. Using this approach, the arrays **H**, $\mathbf{C_{AB}}$, and $\mathbf{C_{AA}}$ are built up as follows:

1. **H**, and $\mathbf{C_{AB}}$ are (one-dimensional) vectors MxN elements long constructed by reading the rows of h(i,j) and c_{ab}(i,j) sequentially.

$$\mathbf{H} = [h(-I,-I),\ h(-I,-I+1)\ \ldots\ h(-I,0)\ \ldots\ h(-I,I),\ h(-I+1,-I)\ \ldots\ h(I,I-1),\ h(I,I)\ ] \tag{6.9}$$

and similarly for $\mathbf{C_{AB}}$.

2. $\mathbf{C_{AA}}$ is a (MxN) by (MxN) square matrix of the form:

$$\mathbf{C_{AA}} = \begin{bmatrix} \mathbf{C_{AA}}^{0} & \mathbf{C_{AA}}^{1} & \ldots & \mathbf{C_{AA}}^{M-1} \\ \mathbf{C_{AA}}^{-1} & \mathbf{C_{AA}}^{0} & \ldots & \mathbf{C_{AA}}^{M-2} \\ \ldots & \ldots & \ldots & \ldots \\ \mathbf{C_{AA}}^{-M+1} & \mathbf{C_{AA}}^{-M+2} & \ldots & \mathbf{C_{AA}}^{0} \end{bmatrix} \tag{6.10}$$

where the element $\mathbf{C_{AA}}^{I}$ is itself a N by N square matrix formed with elements of the i^{th} row of the auto-correlation function c_{aa}(i,j):

$$\mathbf{C_{AA}}^{I} = \begin{bmatrix} c_{aa}(i,0) & c_{aa}(i,1) & \ldots & c_{aa}(i,N-1) \\ c_{aa}(i,-1) & c_{aa}(i,0) & \ldots & c_{aa}(i,N-2) \\ \ldots & \ldots & \ldots & \ldots \\ c_{aa}(i,-N+1) & c_{aa}(i,-N+2) & \ldots & c_{aa}(i,0) \end{bmatrix} \tag{6.11}$$

The proof that this matrix arrangement corresponds to the convolution of equation (6.6) can be found in Doukoglou (1989).

6.3 Design of input signal

The quality of the estimation and the robustness of the numerical solution method largely depend on the input signal auto-correlation function. Ideally, the ACF should be as simple as possible. However classical signals proved to difficult to generate. We therefore had to design a new signal as well as an algorithm to obtain its digital representation.

6.3.1 Choice of input sequence

The first signal to consider as a choice for the input signal is white noise. Indeed, the auto-correlation function for this type of signal is equal to 0 except for element c_{aa}(0,0) which is equal to the mean square value of the signal ψ^2. Inspection of equation (6.6) shows that the PSF is simply the cross-correlation function c_{ab} itself divided by ψ^2.

If white noise cannot be generated, a suitable alternative is the pseudo-random binary (PRB) sequence. This sequence assumes one of two values, and the switch from one level to the other occurs only at particular, pseudo-random, intervals. There exists two major differences between the PRB sequence and white noise. In the former, the occurrence of change is predetermined and therefore true randomness is not achieved. Secondly, the PRB sequence is periodic. For example, a PRB sequence generated with an n-stage shift register, has a length equal to $N=2^n-1$ and a period of $N\Delta d$ (Godfrey, 1969). The digit interval Δd is the physical distance separating two events within the sequence. Nonetheless, the ACF of the PRB sequence closely resembles that of white noise since it consists of triangular spikes of width $2\Delta d$ repeated at every period T.

Making a phantom based on either of these signals would have proven a formidable task. A white noise phantom required a large number of materials exhibiting different x-ray attenuation properties. Furthermore, the exact spatial variation of attenuation would have had to be known in order to compute the correlation functions.

Only two materials were necessary for the PRB sequence, thereby simplifying the construction of the phantom. However, the neighboring cells, each cell representing an event, were required to be square and with an area equal to the image pixel size. Indeed, to preserve the binary character of the signal, every pixel had to contain only one type of material. If this condition was not respected, averaging occurred with a corresponding pixel CT value anywhere between the two extremes representing a purely binary signal.

These difficulties prompted us to design our own input signal, based on a PRB sequence. It consists of a series of pseudo-randomly located holes (PRLH) drilled in radiopaque material. The position of the holes correspond to 0's in a two-dimensional (2D) PRB sequence. This 2D sequence was formed by stacking NROW groups of NCOL consecutive elements of a 1D sequence as illustrated in figure 6.1. The 1D sequence was itself generated by the NEXUS operator PRBS based on the n-stage shift-register algorithm.

6.3.2 Digitization of input sequence

In order to compute the input-output cross-correlation function, the input signal had to be digitized since the output image was available only in this form. A digital representation of the PRLH signal is obtained by laying a digitizing grid of square pixels upon the sequence of holes of known size and position.

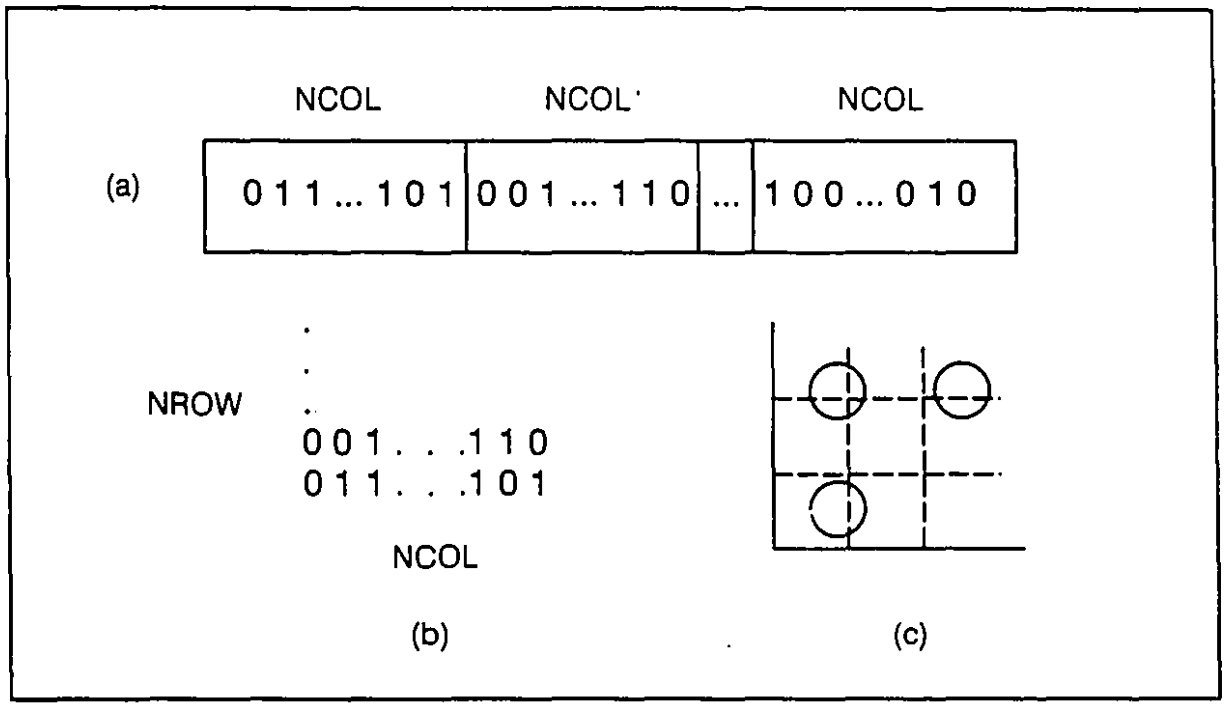

Figure 6.1 Creation of Input

(a) Elements of a 1D PRB sequence are assembled into NROW groups of NCOL elements to form a 2D sequence shown in (b). (c) The zeros in the sequence represent holes drilled in a radiopaque material

The digitization process is conceptually simple: it requires computing the area of a pixel covered by a hole, or a portion of it. The object being binary, the remaining pixel surface is occupied by the solid radiopaque material. The digitized object fits into a grid of K rows and L columns where each grid element, or pixel, is assumed square and of user defined area A. The upper limit on the diameter of the hole is set to twice the pixel width or $2\sqrt{A}$.

The digitization process counts 6 steps, described in the rectangular boxes in figure 6.2. Figure 6.3 defines the geometry and the symbols used in the subsequent equations.

1- *Initialization.* The object is assumed to be a homogeneous block of plastic. Therefore, the pixel area covered by a hole A_H is initialized to 0 for every grid element:

$$A_H(i,j) = 0, \quad i = 0, K-1; \; j = 0, L-1 \tag{6.12}$$

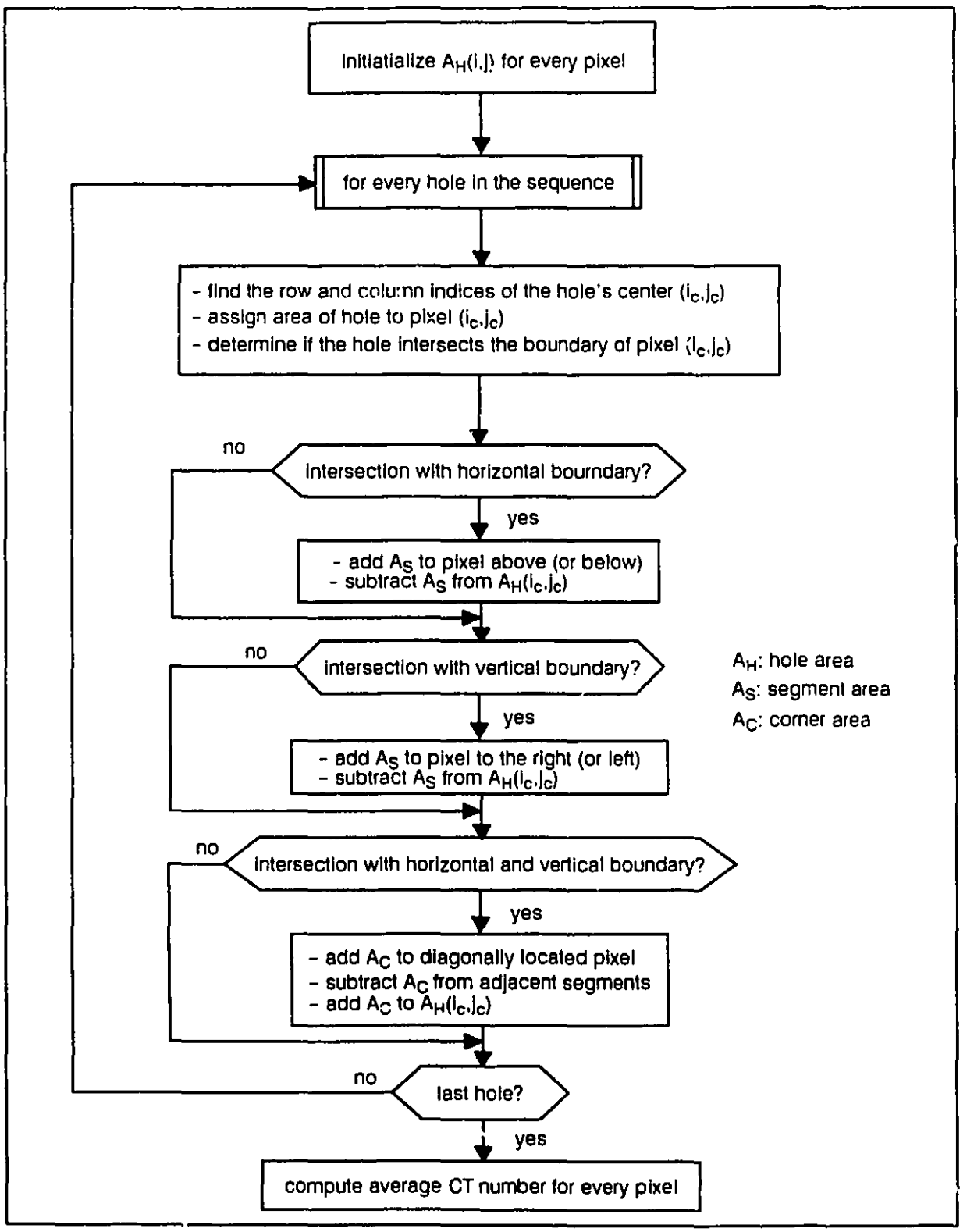

Figure 6.2 Input sequence digitization algorithm

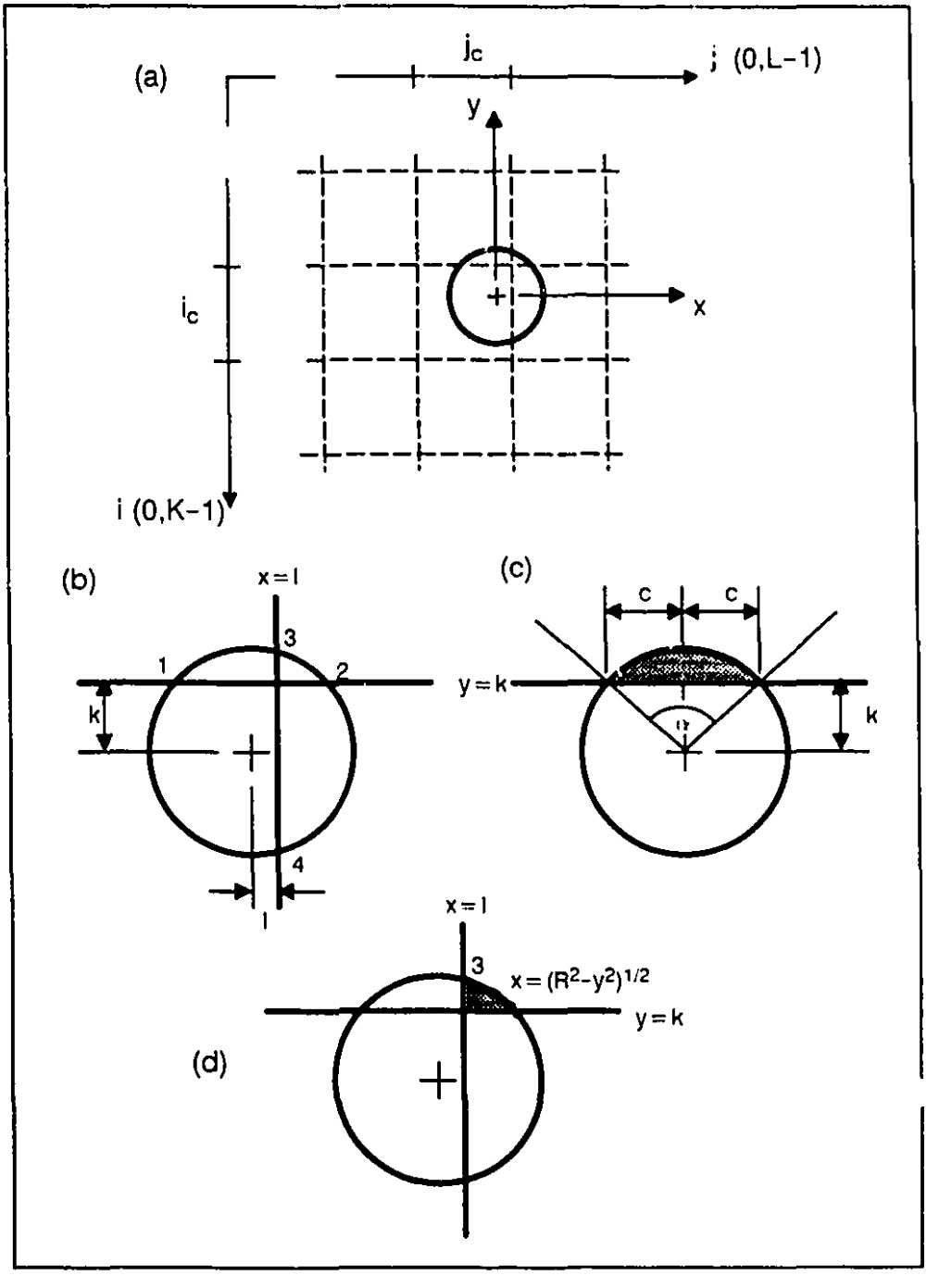

Figure 6.3 Geometry for input sequence digitization

(a) the algorithm first determines the pixel containing the center of a hole and determines which pixels within a possible 9 contain a portion of the hole. (b) It then computes the intersection points (if any) between the grid lines and the hole. (c) the area of the segment A_S beyond the horizontal and vertical (not shown) grid lines. (d) and the corner area Ac if the hole intersects both a horizontal and vertical line.

2- *Position of hole and intersection with pixel boundaries.* The second step is depicted in figure 6.3 (a). It consists of finding the row and column indices (i_c,j_c) of the pixel over which a given hole is centered. The equation of the grid lines defining the boundaries of pixel (i_c,j_c) are expressed in a local coordinate system (x,y) whose origin coincides with the center of the hole.

When the diameter of the hole is limited to twice the width of a pixel, a maximum of 4 neighboring pixels are affected by a given hole. However, depending on the subpixel location of the hole's center within pixel (i_c,j_c), any of its 8 neighbors can contain a portion of it. Not knowing at this stage how many pixels are involved, the total area of the hole is assigned to central pixel:

$$A_H(i_c,j_c) = \pi R^2 \tag{6.13}$$

At this stage, the algorithm also determines if the hole intersects the boundaries of pixel (i_c,j_c) (see figure 6.3 (b)). In the general case, a line $y = ax + b$ intersects a circle $x^2+y^2=R^2$ if $D \geq 0$ (Tuma, 1987) where D:

$$D = R^2 + R^2a^2 - b^2 \tag{6.14}$$

More specifically, if $D>0$, the line intersects the circle at two points the coordinates of which are:

$$x_{1,2} = \frac{-ab \pm \sqrt{D}}{1 + a^2} \tag{6.15}$$

$$y_{1,2} = \frac{b \pm a\sqrt{D}}{1 + a^2} \tag{6.16}$$

If $D=0$, the line is tangent to the circle and $x_1=x_2$, $y_1=y_2$. Finally, when $D<0$, the line and circle do not intersect. For a horizontal line, equations (6.14) to (6.16) simplifies to:

$$y_1 = y_2 = k \quad D = R^2 - k^2 \quad x_{1,2} = \pm \sqrt{D} \tag{6.17}$$

and for a vertical line:

$$x_3 = x_4 = l \quad D = R^2 - l^2 \quad y_{3,4} = \pm \sqrt{D} \tag{6.18}$$

3- *Intersection with horizontal boundary.* If the hole has been found to intersect a horizontal boundary, the area of the sector As located above or below pixel (i_c,j_c) is computed. This surface is shown as the shaded area in figure 6.3 (c), and is given by:

$$A_s = \frac{R^2}{2}(\alpha - \sin\alpha) \tag{6.19}$$

where α is the angle sub-tending the sector:

$$\alpha = 2\ \tan^{-1}\left(\frac{c}{k}\right) = 2\ \tan^{-1}\left(\frac{|x_2 - x_1|/2}{k}\right) \tag{6.20}$$

Having been assigned to pixel (i_c,j_c) in step 2, As must be subtracted from $A_H(i_c,j_c)$ and assigned to the pixel above (i_c-1,j_c) or below (i_c+1,j_c).

4- *Intersection with vertical boundary.* If the hole intersects a vertical boundary, the segment area A_s located to the right or left of pixel (i_c,j_c) is computed. Equation (6.19) still applies but α is now given by:

$$\alpha = 2\ \tan^{-1}\left(\frac{|y_3 - y_4|/2}{l}\right) \tag{6.21}$$

As in step 3, A_s is subtracted from $A_H(i_c,j_c)$ but added to $A_H(i_c,j_c-1)$ or $A_H(i_c,j_c+1)$.

5- *Intersection with horizontal and vertical boundary.* A corner, covering the surface A_c, is formed when the hole intersects both a vertical and horizontal boundary. In general terms, A_c, depicted as the shaded area in figure 6.3 (d), is given by:

$$A_c = \int_y \int_x dx\ dy \tag{6.22}$$

The integration limits vary depending on where the corner is located. For the upper right pixel (i_c-1,j_c+1) the limits are:

$$\begin{aligned} k < x < \sqrt{R^2 - y^2} \\ l < y < y_3 \end{aligned} \tag{6.23}$$

and

$$A_c = \left[\frac{y}{2}\sqrt{R^2 - y^2} + \frac{R^2}{2}\sin^{-1}\left(\frac{y}{R}\right) - l\ y\right]_l^{y_3} \tag{6.24}$$

A_s is added to the proper diagonally located pixel $(i_c \pm 1,j_c \pm 1)$ and subtracted from the pixels affected in steps 3 and 4. Finally, it must be added to $A_H(i_c,j_c)$.

6- *Average pixel value.* After steps 2 through 5 have been repeated for every hole in the sequence, the CT number of each pixel is computed by weighing the CT number of the radiopaque and the material filling the holes with the area they respectively occupy:

$$CT(i,j) = \frac{CT_{radiopaque}(i,j)\ (A - A_H(i,j)) + CT_H(i,j)\ A_H(i,j)}{A} \tag{6.25}$$

6.4 Simulations

A series of simulations were carried out to fine tune the design of the phantom and to investigate the effect of different imaging situations. More specifically, we examined the influence of the following factors on identification quality: the size of the holes and their separation, the length of the PRB sequence, misregistration in the form of relative shift and rotation between the input and output signals and cupping. In the last simulation, the performance of our input signal was compared to a white noise input.

6.4.1 Method

Figure 6.4 schematically describes how the simulations were performed. The object a(i,j) was generated using the method presented in section 6.3. In all cases, the CT number of the radiopaque material was set to 200 and the material filling the holes was assumed to be air with a CT number of -1000. The PSF to be identified h(i,j) was modelled as a Gaussian function (see equation 3.1). The parameters N, p_x and p_y were taken from table 3.2 thereby simulating images reconstructed with the smoothing filter (filter 0). In the remainder of the section, h(i,j) is called the actual PSF. Convolution of the object with the actual PSF yielded a simulated image b(i,j). Using the identification method outlined in section 6.2, with a(i,j) as input and b(i,j) as output, an estimate of the actual PSF $\underline{h}(i,j)$ was obtained. Finally, the input a(i,j) was convolved with $\underline{h}(i,j)$ to generate an estimated image $\underline{b}(i,j)$.

The quality of the identification procedure was established using three quantitative measures. The first is based on the variance accounted for (VAF) between the output b(i,j) and the estimated output $\underline{b}(i,j)$:

$$VAF_{out} = \left[1 - \frac{\sum_{i=-I}^{I} \sum_{j=-J}^{J} (\ \underline{b}(i,j) - b(i,j)\ )^2}{\sum_{i=-I}^{I} \sum_{j=-J}^{J} b^2(i,j)} \right] x\ 100$$

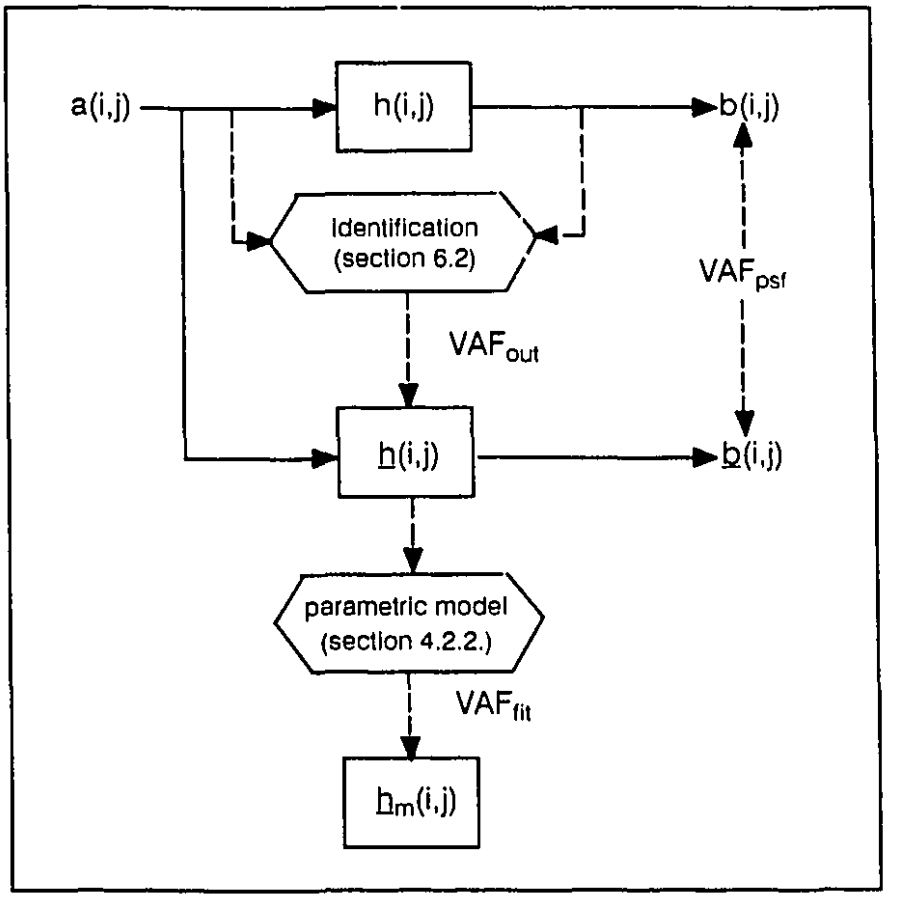

Figure 6.4 Schematic diagram of simulation scheme

Three measures of identification quality are based on a comparison between the actual PSF h(i,j) and its estimated non-parametric version $\underline{h}(i,j)$ (VAF_{psf}), between the image b(i,j) and its estimate $\underline{b}(i,j)$ (VAF_{out}), and between the non-parametric h(i,j) and parametric estimate of the PSF $\underline{h}_m(i,j)$ (VAF_{fit}) .

The second measure accounts for variations between the actual PSF h(i,j) and its estimate $\underline{h}(i,j)$:

$$VAF_{psf} = \left[1 - \frac{\sum_{i=-I}^{I} \sum_{j=-J}^{J} (\underline{h}(i,j) - h(i,j))^2}{\sum_{i=-I}^{I} \sum_{j=-J}^{J} h^2(i,j)} \right] x\ 100$$

Finally, the Gaussian model was fitted to $\underline{h}(i,j)$ using the procedure outlined in section 3.2.2, resulting in an estimated modelled filter $\underline{h}_m(i,j)$ and the following measure:

$$VAF_{flt} = \left[1 - \frac{\sum_{i=-I}^{I} \sum_{j=-J}^{J} (\underline{h}(i,j) - \underline{h}_m(i,j))^2}{\sum_{i=-I}^{I} \sum_{j=-J}^{J} \underline{h}_m{}^2(i,j)} \right] x\ 100$$

6.4.2 Effect of hole size and separation

For the PSF to be accurately identified, the input object must contain power over the range of frequencies covered by the system's modulation transfer function. This is controlled by the size of the holes drilled in the solid material as well as the distance separating the holes. For example, the larger the holes and the greater the gap between them, the more the power is concentrated in the lower end of the spectrum.

During this simulation, a diameter range from 0.2 mm to 0.8 mm in steps of 0.2 mm was investigated. The holes were not allowed to overlap and the minimum separation was set to 100% of the diameter. This limit reflects a practical consideration: the drill bit must be surrounded by a thin wall of material. Without this support the drill wobbles and can easily break.

All 2D sequences were formed from the same 1D sequence and digitized onto a 49x49 pixel grid. With a pixel width of 0.4 mm, the signals covered a 19.6 mm x19.6 mm region.

Table 6.1 contains the results of this simulation. With values greater than 99% over the range studied, VAF_{out} was not a good discriminator in this case and the choice of a hole size must be based on the other two measures. The insensitivity of VAF_{out} was probably due to relatively small error between the output and the simulated output when compared to the overall signal intensity. Values of VAF_{psf} and VAF_{flt} were at their worst for a hole diameter of 0.2 mm and peaked for objects created with a hole size of 0.6 mm. Table 6.1 also shows that for this diameter, identification quality was relatively insensitive to the separation between the holes. However, over the range studied, the best identification occurred when the inter-hole distance was about 150% of the diameter.

For this reason, a #73 drill bit with a diameter of 0.61 mm, the closest to 0.6 mm, was selected to generate the holes. Although table 6.1 indicates optimal results for a hole separation of 1.0 mm, we nonetheless chose a value of 0.9 mm, creating a signal with a slightly higher frequency content. We thereby hoped to generate a single input signal

diameter (mm)	separation (mm)	VAF_{out}	VAF_{psf}	VAF_{fit}
0.2	0.2	99.52	63.02	83.00
	0.3	99.65	89.64	93.53
	0.4	99.43	75.27	89.61
	0.5	99.43	75.27	89.61
0.4	0.4	99.63	83.16	90.26
	0.5	99.88	99.55	99.73
	0.6	99.71	99.45	99.56
	0.7	99.42	98.51	99.55
	0.8	99.93	95.50	95.63
0.6	0.7	99.85	99.07	99.25
	0.8	99.58	99.46	99.17
	0.9	99.40	99.24	99.74
	1.0	99.22	99.88	99.76
	1.1	99.65	98.99	99.48
0.8	1.0	99.77	98.93	99.28
	1.1	99.56	98.65	99.13
	1.2	99.45	97.99	99.18
	1.3	99.73	98.94	99.18
	1.4	99.58	98.31	98.75

TABLE 6.1 Effect of hole size and separation on identification quality

adequate to identify the PSF of the smoothing and high resolution image reconstruction filters, the latter exhibiting a slightly higher cut-off frequency.

A hole size of 0.61 mm and separation of 0.9 mm were used in all of the following simulations.

6.4.3 Effect of sequence length

The length of the PRB sequence, or the number of holes, regulates the size of the object. It must be larger than the settling distance of the PSF but, on the other hand, it must be contained within a region where the hypothesis of shift-variance remains plausible.

The performance of object created from a sequence length of 8x8 to 64x64 elements, covering a region of 8.8x8.8 to 59.5x59.2 mm^2 is found in table 6.2. In all cases,the pixel width was equal to 0.4 mm. Results show that increasing input size lead to an improved estimate.

sequence length (elements^2)	object size (mm^2)	VAF_{out}	VAF_{psf}	VAF_{fit}
8x8	8.8x8.8	80.10	87.83	96.84
16x16	16.0x16.0	90.76	89.69	98.90
24x24	23.2x23.2	96.56	95.91	99.33
32x32	30.4x30.4	98.89	98.47	99.59
64x64	59.2x59.2	99.60	99.37	99.75

TABLE 6.2 Effect of sequence length on identification quality

However, as figure 6.5 depicts, this improvement was due to a reduction in the amplitude of the ripples surrounding the central peak as the object grew in size. The central portion was not affected by sequence length. These ripples strongly affected the blurring pattern, explaining the the large improvements in VAF_{out} with sequence length. On the other hand these ripples had little influence when the Gaussian model was fitted to the PSF, hence the large values of VAF_{fit}. Their effect appeared moderate when the estimated PSF was compared to the actual PSF as the variation of VAF_{psf} attest. Nonetheless, these three measures show that it became increasingly difficult to improve the quality of identification as the object size became larger.

We established in the previous chapter that the PSF was isotropic and shift-invariant within a circular region centered within the field of view. The critical radius R_C was evaluated at $34 < R_C \leq 51$ mm for the smoothing apodizing function and $17 < R_C \leq 34$ mm for the high resolution filter. These figures are valid for a scan time of 9.0 s. A signal based on a 32x32 sequence, even off-centered, therefore fits within a region where shift-variance is respected. And with all measures of identification quality greater than 98%, such a sequence is adequate for our purposes.

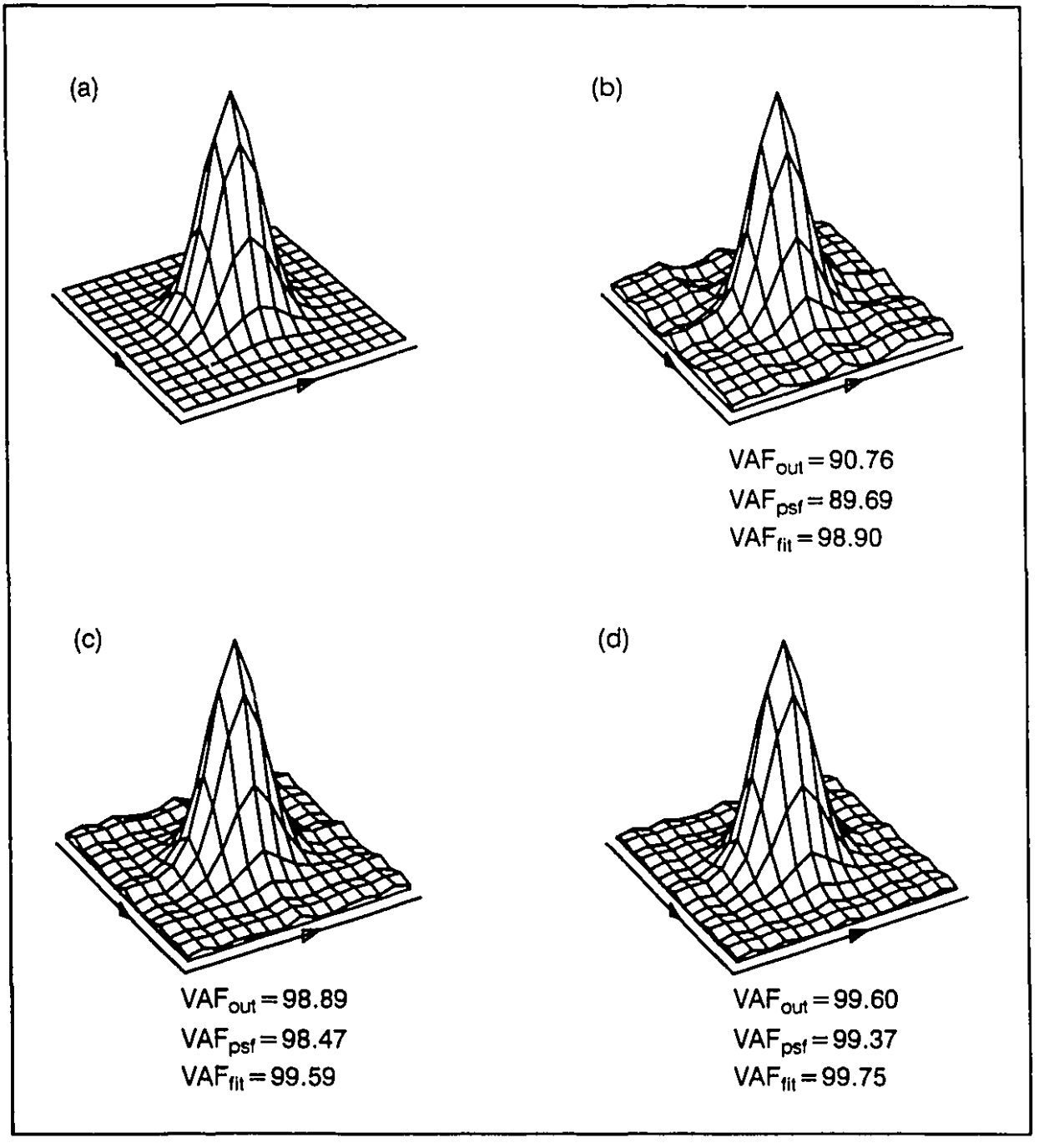

Figure 6.5 Effect of sequence length

(a) PSF to be identified; estimated PSF when the obeject is created from a (b) 16x16, (c) 32x32, and (d) 64x64 pseudo-random binary sequence

6.4.4 Effect of pixel size

During experimental identification, the image can easily be reconstructed with pixels of different sizes using the scanner's zoom option. To simulate the effect of this imaging parameter, the object created from a 32x32 sequence with holes of 0.61 mm in diameter separated by 0.9 mm was digitized onto a series of grids with a pixel width varying between 0.305 mm and 0.5 mm (0.305 mm represents the smallest pixel size that the digitization algorithm can handle for a hole diameter of 0.61 mm).

As shown in figure 6.6, increasing the pixel size had a smoothing effect: the amplitude as well as the frequency of the ripples surrounding the central peak of the PSF decreased as the pixel was larger.

In principle, this should guarantee an improvement in identification quality. However, the PSF is also increasingly blurred and small details can be lost. Furthermore, the PSF is represented by an ever decreasing number of pixels. As a result of these conflicting effects, the measures of identification quality found in table 6.3 reveal no pattern. Fortunately, with all values greater than 98.5%, it can be said that pixel size is not a critical parameter.

pixel width (mm)	VAF_{out}	VAF_{psf}	VAF_{fit}
.305	99.80	99.27	99.47
.350	99.53	99.13	99.58
.400	99.68	99.44	99.73
.450	99.17	99.15	99.77
.500	98.99	98.66	99.67

TABLE 6.3 Effect of pixel size on identification quality

6.4.5 Effect of sub-pixel translation

Proper identification procedure requires that the input and output be aligned. Both translation and rotation can be responsible for misregistration. In this simulation, we investigated how the shape of the estimated PSF is affected by subpixel shift between the object and its image.

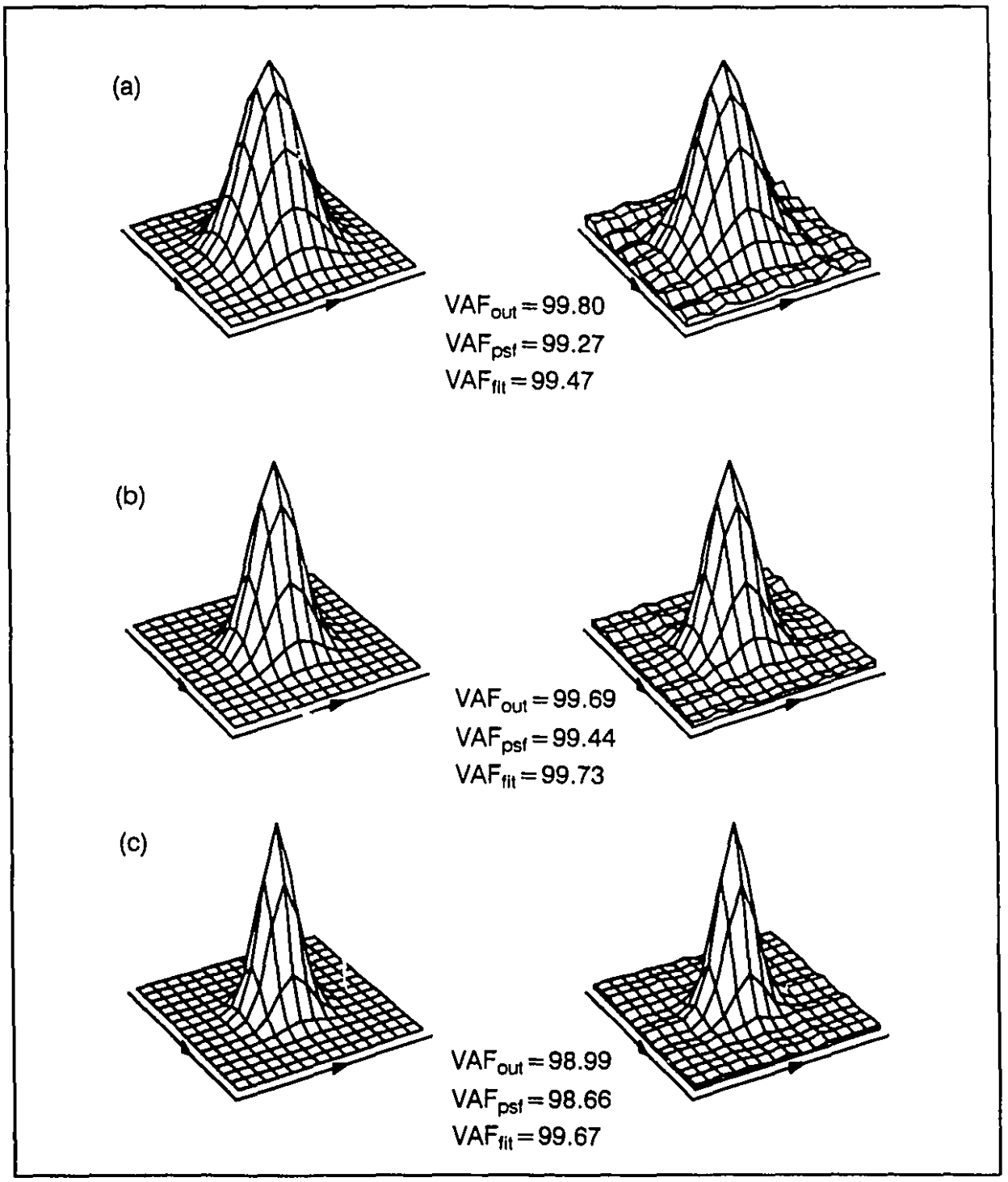

Figure 6.6 Effect of pixel size

The PSF in the right hand column are estimates of those in the left when both the object and the image are digitized into a grid with a pixel width of (a) 0.305 mm, (b) 0.400 mm and (c) 0.500 mm

A reference object, used as input, was created by digitizing a 32x32 sequence onto a 0.4 mm pixel grid. As with the previous simulations, the diameter of the holes was set to 0.61 mm and their separation to 0.9 mm. Various amounts of shift were introduced independently in the x and y direction to this reference object which was then convolved with h(i,j) to create the shifted images.

According to the values in table 6.4, the identification appeared to be at its worst when the image was shifted by half a pixel in one direction and 30% in another. The resulting estimated PSF is compared in figure 6.7 to the actual PSF and the one identified when the signals were properly registered.

shift (% of pixel width)		VAF_{out}	VAF_{psf}	VAF_{fit}	p_x (pixel^{-1})	p_y (pixel^{-1})	t_x (pixel)	t_y (pixel)
0.0	0.0	99.68	99.44	99.73	0.4596	0.4721	7.9993	7.9997
0.1	0.1	99.64	99.00	99.72	0.4591	0.4725	7.8988	8.0947
0.2	0.2	99.57	97.70	99.73	0.4589	0.4739	7.7984	7.1919
0.3	0.3	99.18	87.08	99.66	0.4611	0.4713	7.6996	7.3310
0.4	0.4	99.23	88.50	99.68	0.4596	0.4740	7.6035	7.4281
0.5	0.5	99.28	89.09	99.69	0.4587	0.4762	7.5080	7.5249
0.5	0.4	99.18	86.65	99.67	0.4587	0.4752	7.5084	7.4279
0.5	0.3	99.08	83.80	99.63	0.4591	0.4741	7.5085	7.3307
0.5	0.2	99.44	93.41	99.71	0.4557	0.4782	7.5094	8.1905
0.5	0.1	99.48	94.03	99.70	0.4553	0.4783	7.5089	8.0935
0.5	0.0	99.51	94.03	99.70	0.4553	0.4783	7.5083	7.9994
				mean	0.4583	0.4749		
				standard deviation	0.0019	0.0025		

TABLE 6.4 Effect of subpixel shift on identification quality

Values varying between 99.68 and 99.08 establish the relative insensitivity of VAF_{out} to subpixel misregistration. This can be explained by the fact that, with a resolution of about 1.5 mm, or 3.75 pixels, structures were blurred over a large distance compared to the amount of shift. Small shifts did not affect the average CT value of a pixel.

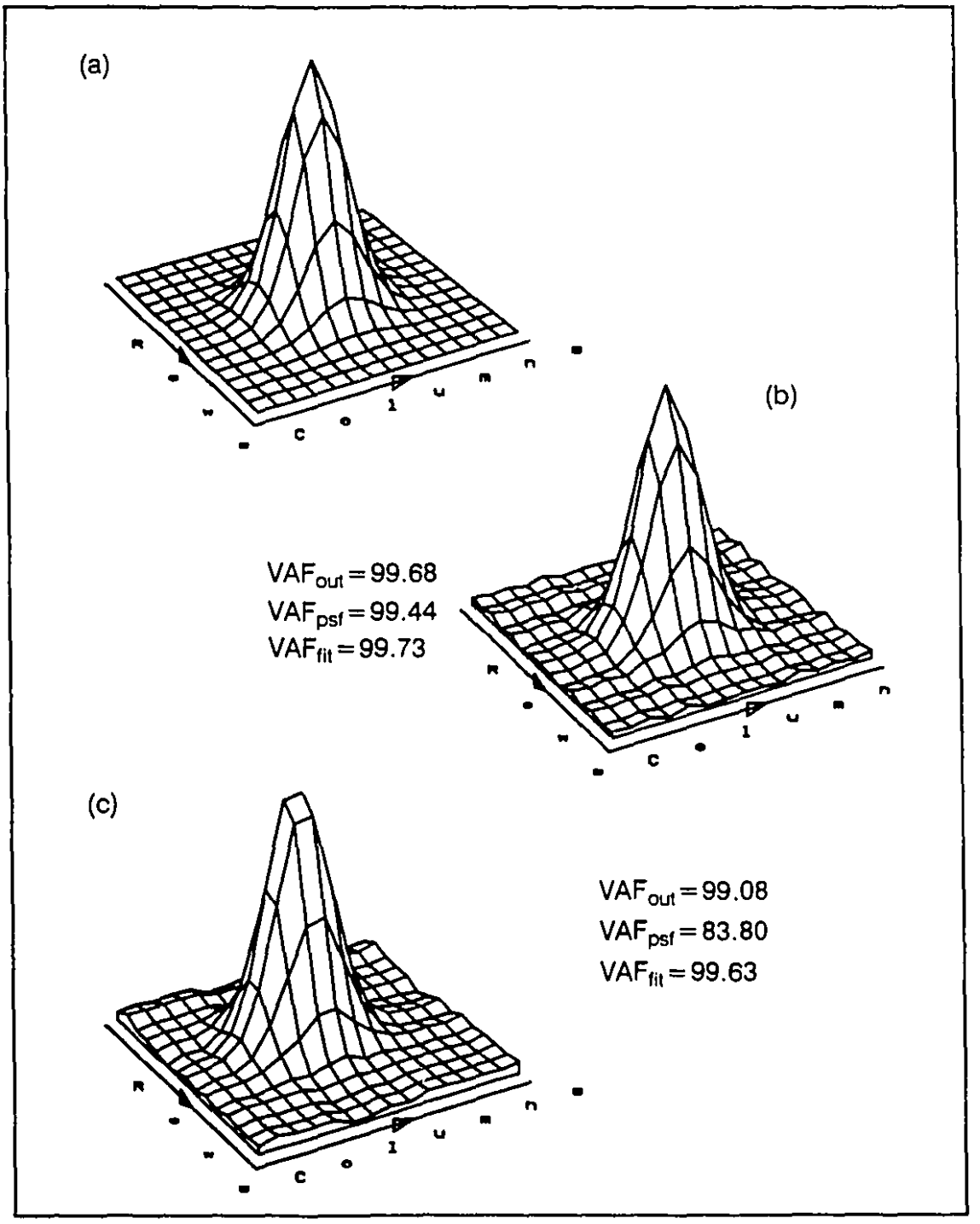

Figure 6.7 Effect of sub-pixel shift

(a) PSF to be identified (b) estimated PSF under ideal conditions (c) estimated PSF with 50% pixel shift in x (column) and 30% in y (row) direction

With values between 99.63 and 99.73, VAF_{flt} is even less sensitive. This resulted from the ability of the Gaussian model to estimate the position of the peak value even at subpixel level (see section 4.3.2). Table 6.4 also shows that the amount of shift can be estimated to within 3% of pixel width. The small variations of parameter p_x and p_y indicate that the shape of the underlying Gaussian function was not modified. The apparent loss of symmetry shown in figure 6.7(c) was simply due to a shift of the estimated PSF with respect to its own grid by the same amount between the input and output. As a consequence, when the true and estimated PSF are compared, values of VAF_{psf} fall off with the amount of shift.

6.4.6 Effect of rotation

The second factor responsible for misregistration is rotation. To investigate this parameter, various amounts of rotation were substituted in the procedure described above. The rotation was applied about the upper left corner of the object and ranged from 0.5 to 5.0 degrees.

Even modest amounts of rotations have a much more severe effect than sub-pixel misregistration as a comparison of tables 6.4 and 6.5 discloses. The diminishing values of p_x and p_y with increasing amounts of rotation indicate that the estimated PSF progressively broadened. Furthermore, only the upper left corner of the object and image was properly aligned. All the other points were translated by an increasing amount as the distance from that corner and the amount of rotation increased. The variation of parameters t_x and t_y reflects this translation which can also be observed in figure 6.8. Rotation also introduced ripples of increasing amplitude. These ripples decrease the ability of the fitting procedure to recognize a Gaussian function and explain the decrease in VAF_{flt}. This factor, compounded by the previous two, is also responsible for the rapid fall of VAF_{out} and VAF_{psf}.

6.4.7 Effect of cupping

Cupping invalidates the assumption of stationarity necessary for the application of equation (6.6). The effect of cupping was simulated by adding the equation of a plane to the output. In table 6.6, the plane is represented by values added to the lower left (LL), lower right (LR) and upper left (UL) corner of the image.

Adding a certain amount of drift in the image while it is absent from its estimated version will caused a drop in VAF_{out} proportional to the severity of the cupping. A slight decrease in the other two measures of identification quality can also be observed. However with all values of VAF greater than 98%, this artefact did not have a large effect on identification quality.

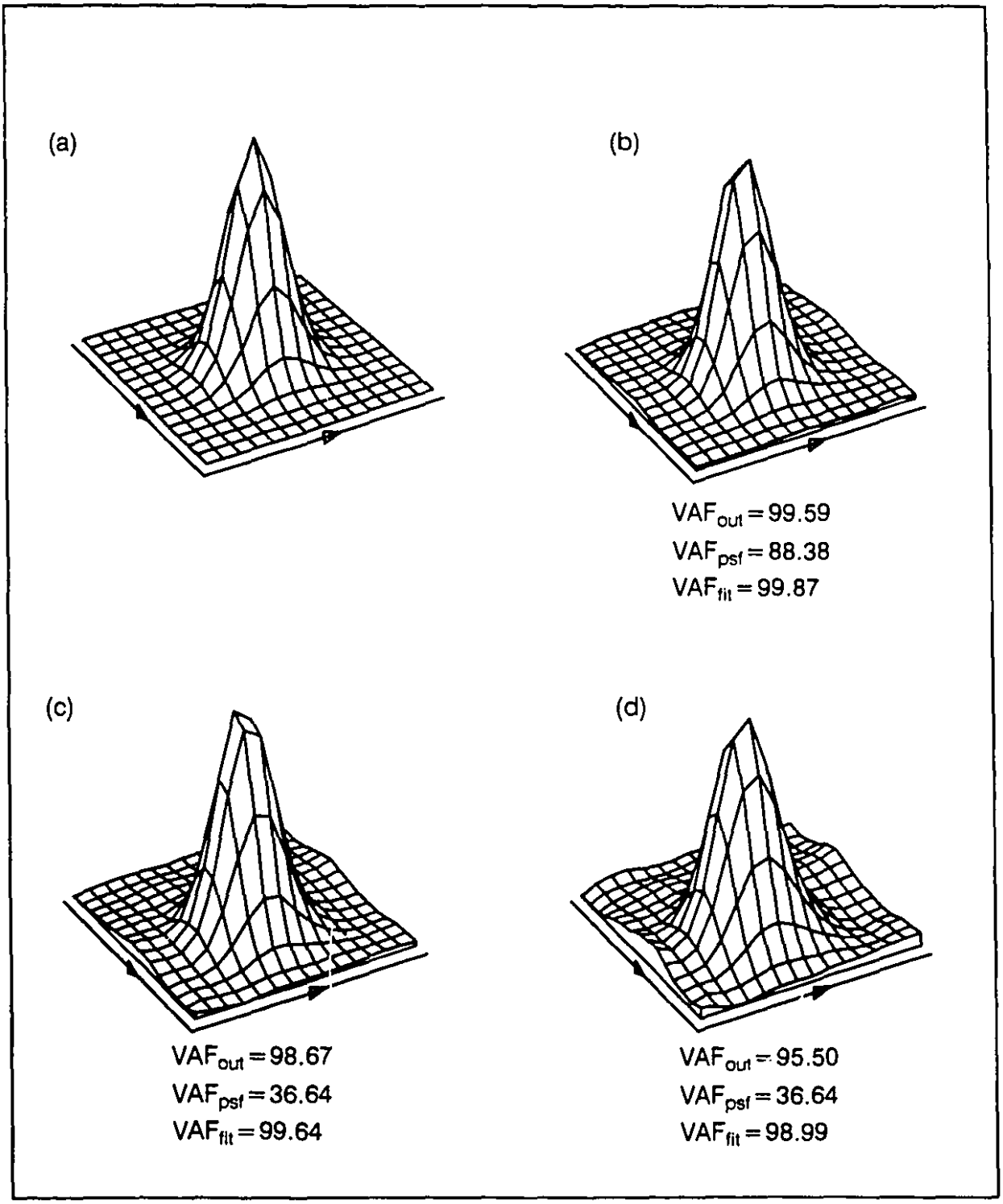

Figure 6.8 Effect of rotation

(a) PSF to be identified, estimated PSF when the object and its image are rotated by (b) 0.5 °, (c) 1 °, and (d) 2° with respect to one another

rotation (degrees)	VAF_{out}	VAF_{psf}	VAF_{fit}	p_x (pixel^{-1})	p_y (pixel^{-1})	t_x (pixel)	t_y (pixel
0.0	99.68	99.44	99.73	.4596	.4721	7.9993	7.9997
0.5	99.59	88.34	99.87	.4458	.4499	7.6979	8.6741
1.0	98.67	59.64	99.64	.4373	.4400	7.4020	9.3502
2.0	95.50	36.64	98.99	.4006	.4034	6.8217	9.7332
3.0	91.54	21.11	98.09	.3515	.3588	6.2439	10.0906
4.0	87.52	14.36	97.17	.3079	.3157	5.6872	10.4417
5.0	83.94	11.42	95.77	.2584	.2745	5.0408	10.8054

TABLE 6.5 Effect of rotation on identification quality

CT number added to corner					
LL	LR	UL	VAF_{out}	VAF_{psf}	VAF_{fit}
0	5	0	99.94	99.88	99.99
0	5	10	99.67	99.87	99.98
0	5	20	99.12	99.83	99.97
0	5	30	98.28	99.76	99.96

TABLE 6.6 Effect of cupping on identification quality

6.4.8 Random vs. PRLH sequence input

In this simulation, we wished to compare the performance of our input design strategy with a white noise input. Two objects were generated, the first from a 32x32 PRB sequence, with holes 0.61 mm in diameter spaced 0.9 mm apart, and the other consisting of zero-mean Gaussian white noise with a standard deviation of 1 CT number. Both objects were represented with pixels 0.4 mm in width and covered an area of 75x75 pixels.

Table 6.7 compares the quality of identification for both inputs and contains the parameters of the Gaussian fit to the identified PSF as well as those of the actual PSF we are trying to identify. All values of VAF were lower for the PRLH object than for the white noise input. With larger values for parameters p_x and p_y, the PSF identified with the PRLH object estimated a narrower PSF, or overestimated the modulation transfer function (MTF).

Input	VAF_{out}	VAF_{psf}	VAF_{fit}	p_x (pixel-1)	p_y (pixel-1)
actual				.4522	.4599
PRLH signal	99.68	99.44	99.73	.4596	.4721
white	99.97	99.96	99.98	.4568	.4593

TABLE 6.7 Identification quality for PRLH sequence and white input

Figure 6.9 shows the non-parametric MTF, obtained by Fourier transforming the non-parametric PSF. The largest difference between the actual MTF and the one estimated from the PRLH object in 2.4% and 3.7% in the row and column directions respectively. For the white input, the values drop to 1.5% and -1.9%. As a consequence of overestimating the MTF, the resolution evaluated with this method will be slightly lower than if they had been estimated from a white noise input. The small peaks observed near the frequency of 1 cycle/mm are due to a large increase of power in the PRLH signal at a frequency of 1.1 cycles/mm, the reciprocal of the distance separating the hole.

6.5 Experimental identification

The previous simulations provided useful insight into the design of the input signal and into the results we can expect from this technique. In this section we will see how this knowledge was used to fabricate the phantom and to maximize, in the informal sense, the identification.

6.5.1 Description of the phantom

Figure 6.10 shows the image of the 150 mm diameter phantom. Ease of machinability and homogeneity motivated the choice of delrin as the plastic support for the phantom. The position of the holes, totalling 501 in number, was generated with a 32 by 32 element PRB sequence using a 10 stage shift register algorithm (NEXUS operator PRBS). A #73 drill was used to produce holes 0.61 mm in diameter to a depth of approximately 6 mm. A center to center separation of 0.9 mm between holes guaranteed structural support to the drill bit while providing an adequate signal for identification purposes. The input signal covered a region of 28.2 mm x 28.2 mm with the lower left hand corner corresponding to the center of the phantom.

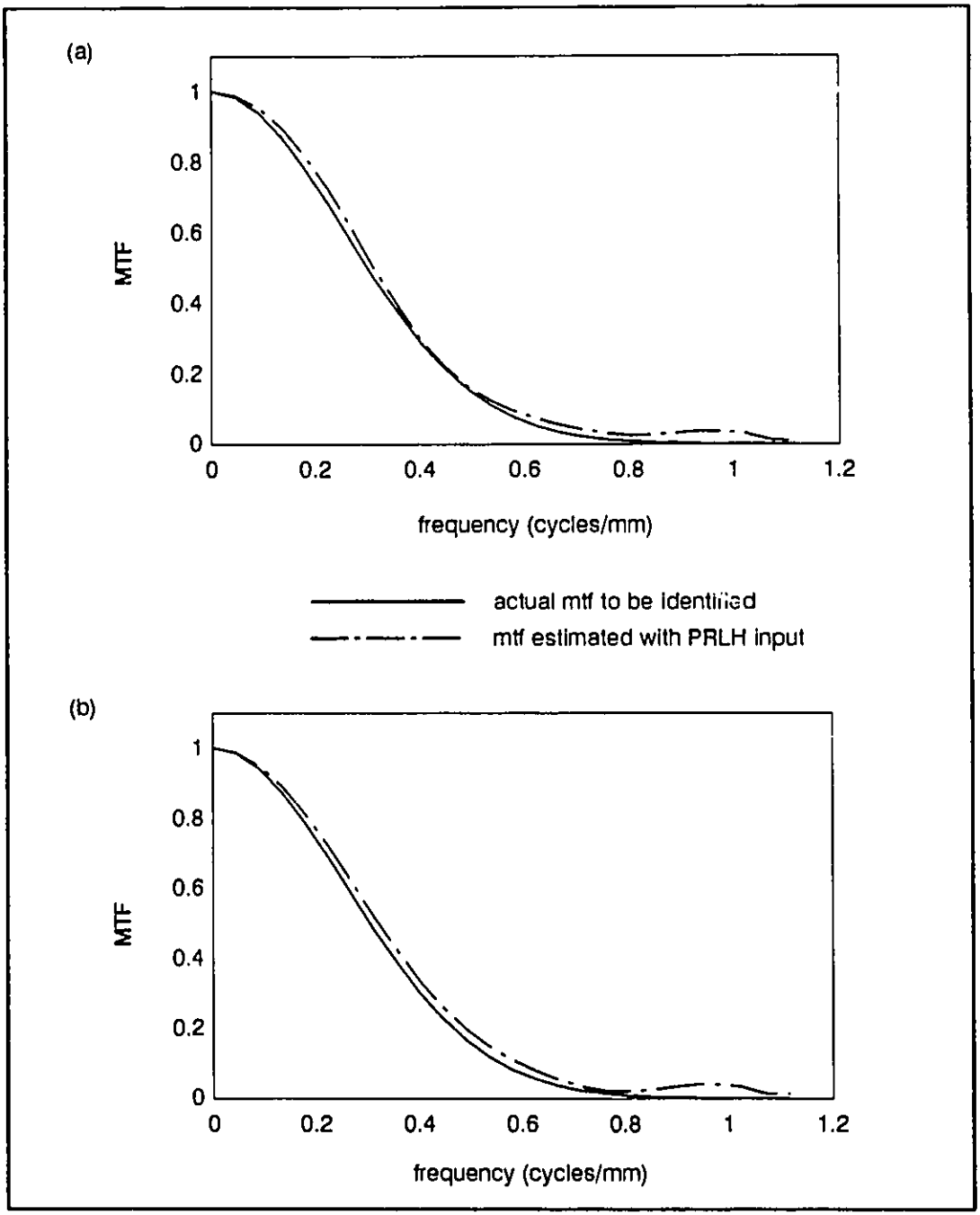

Figure 6.9 Influence of type of input on MTF

Cross-sections taken through the center of non-parametric MTFs (a) in the row and (b) column directions. Non-parametric MTFs are obtained by computing the Fourier transform of the non-parametric PSFs. The signal based on the PRB sequence slightly overestimates the actual MTF we are trying to identify. Estimates obtained with the white noise input are indistinguishable from the actual MTF and is therefore not shown.

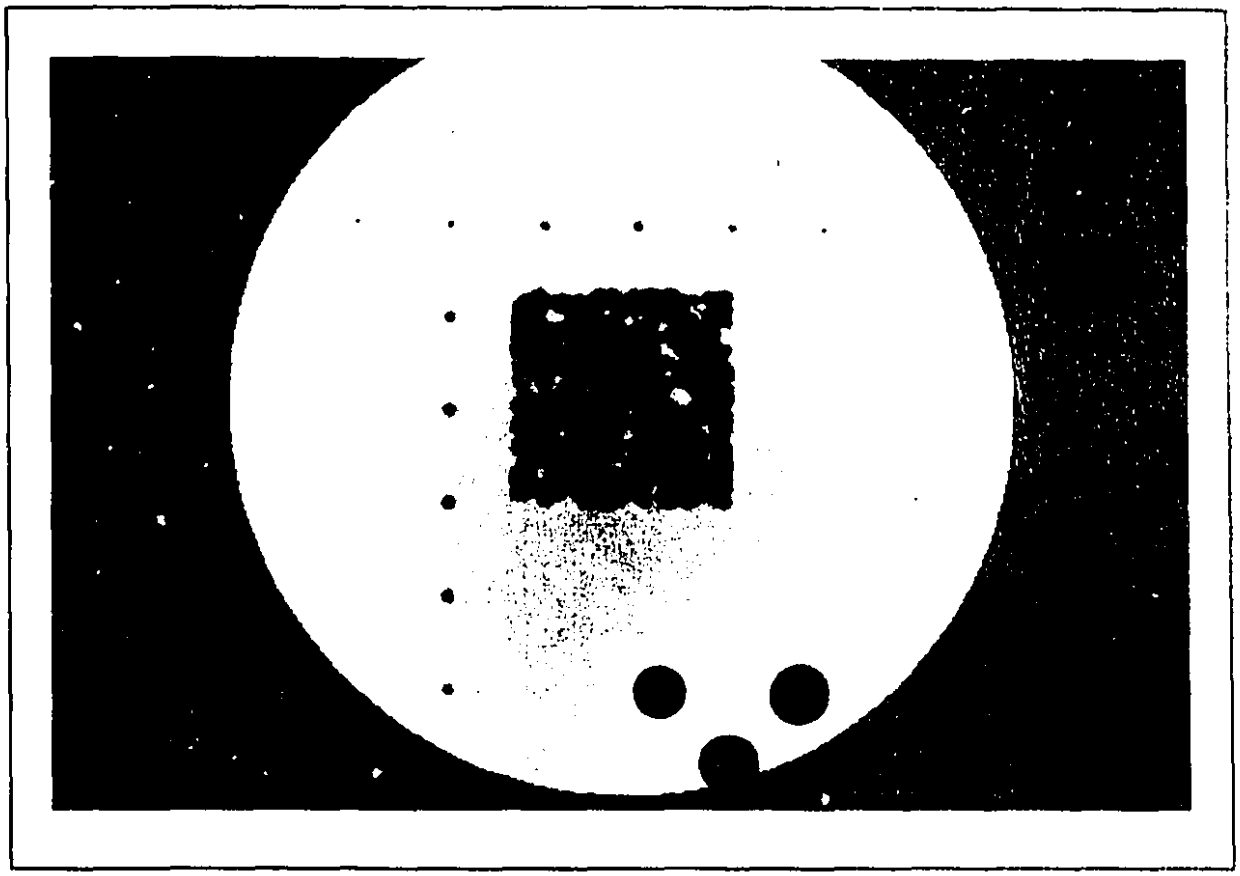

Figure 6.10 Image of PRLH sequence phantom

Apart from the signal itself, the phantom contains a set of alignment axes created by drilling a series of holes parallel to the top and to one of the sides of the signal. The phantom coupled to the scanner attachment set via a custom adaptor. This adaptor is mounted onto the phantom with 5 nylon screws inserted through the large holes seen at the bottom.

A series of seven holes, also 0.61 mm in diameter but spaced 12.7 mm apart were drilled parallel to the top edge of the signal. These holes together with a second series, parallel to one of the sides, formed a set of perpendicular axes providing a mean of rotationally aligning the object with its image.

The holes forming the signal itself as well as the alignment axes were drilled with an Excello numerically controlled milling machine with a positional accuracy of 0.001 in or 25 microns.

Finally, the phantom was mounted onto a custom adaptor with the use of 5 nylon screws passing through holes located below the signal.

6.5.2 Scanning parameters

The phantom was mounted to the scanner phantom attachment set via the custom adaptor and was centered within the gantry. The scanning parameters included a tube current and voltage of 200mA and 120 kV. In order to minimize noise, the slice thickness should be as large as possible. However, because of the shallowness of the holes, this parameter was set to 2 mm. Shift- variance was minimized by using a scan time of 9.0 s corresponding to 1080 views per image.

Keeping the above parameters constant, the image of the phantom was reconstructed with the smoothing (filter 0) and high resolution (filter 4) reconstruction filters. The phantom was imaged with the smallest FOV compatible with its size, namely 160 mm. A pixel width of 0.334375 mm was obtained by reconstructing the image onto a 107 mm FOV using the zoom option.

6.5.3 Results

Figure 6.11 shows the PSF estimated without any processing of the output images. Values of VAF_{out} equal to 96.77 and 93.93 and VAF_{flt} of 99.15 and 98.97 were obtained for images reconstructed with the smoothing and high resolution filters respectively.

VAF_{out} was computed by comparing the real CT images on a pixel by pixel basis to the simulated version generated by convolving the input with the estimated PSF. Similarly, the appropriate model, either Gaussian for the smoothing filter and damped cosine in the case of the high resolution filter, was fitted to the estimated PSF resulting in VAF_{flt}. However because the PSF was not known "a priori", VAF_{psf} could not be evaluated.

Simulations showed that better results could be achieved by removing cupping and by properly aligning the image with the input object. Due to the restricted area within which the signal was concentrated, cupping was modelled as a bi-linear variation in CT numbers. The equation of a plane, estimated from the CT numbers of the plastic material surrounding the output signal was added to the input, thereby cancelling this artefact.

The amount of rotation was evaluated as follows. The Gaussian model was fitted to the image of each hole forming the alignment axes thereby providing their subpixel location. The inverse tangent of the slope of these lines, obtained through linear regression, provided an estimate of the angle between the lines and the digitization grid. A value of 0.58 and 0.68 for the horizontal and vertical directions respectively averaged 0.63.

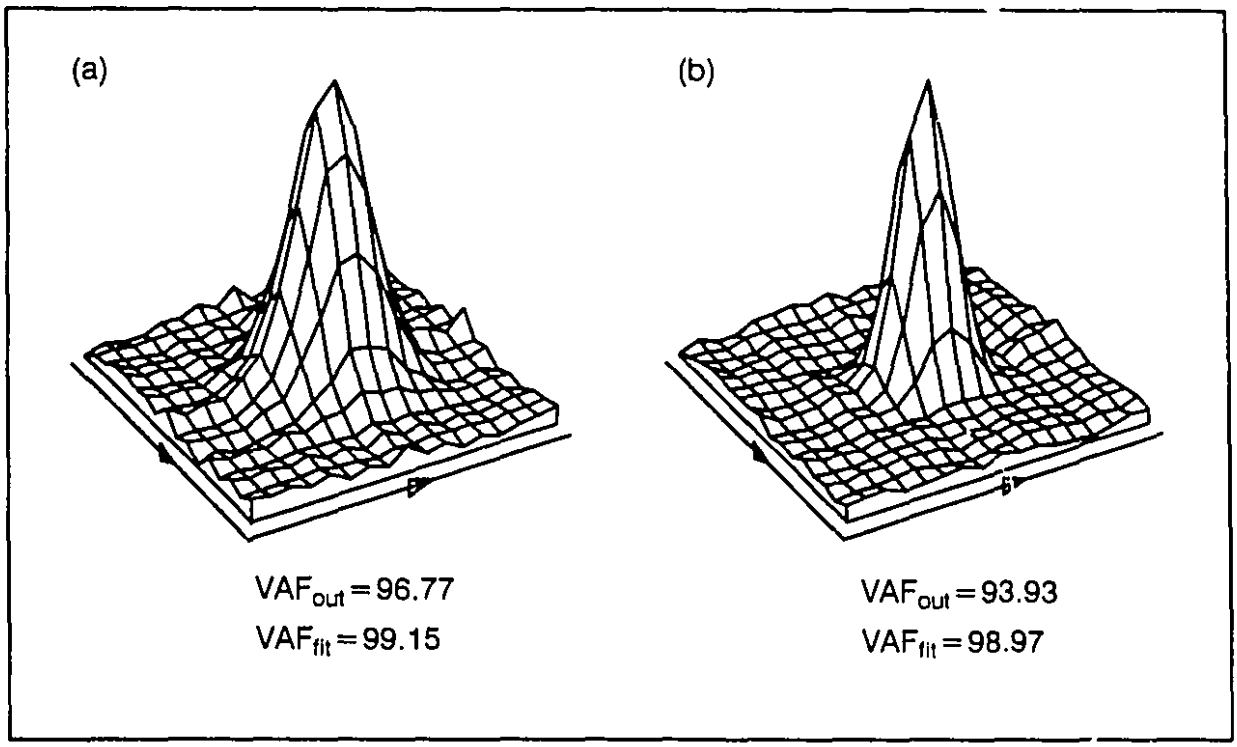

Figure 6.11 Experimentally identified PSF without preprocessing

Experimentally estimated PSF for (a) smoothing and (b) high resolution filter. These estimates were obtained without properly registering the input and output signals and neglecting the cupping artefact.

Fitting the Gaussian model to the PSF produced with the smoothing filter (figure 6.11 (a)), revealed that the output was shifted by 28% and 30% of pixel width in the x and y directions respectively with respect to the input.

Figure 6.12 shows the identified PSF obtained after the images had been properly processed. Table 6.8 contains measures of identification quality as well as model shape parameters. The values of VAF$_{out}$ increased to 98.79 and 97.95 for filters 0 and 4 while VAF$_{fit}$ rose to 99.29 and 99.39.

filter	VAF$_{out}$ (%)	VAF$_{fit}$ (%)	p_x mm^{-1}	d_x cycle mm^{-1}	p_y mm^{-1}	d_y cycle mm^{-1}
smoothing	98.79	99.29	1.1867	-	1.2025	-
high resolution	97.95	99.39	1.2650	0.2344	1.2495	0.2430

TABLE 6.8 Quality of experimental identification

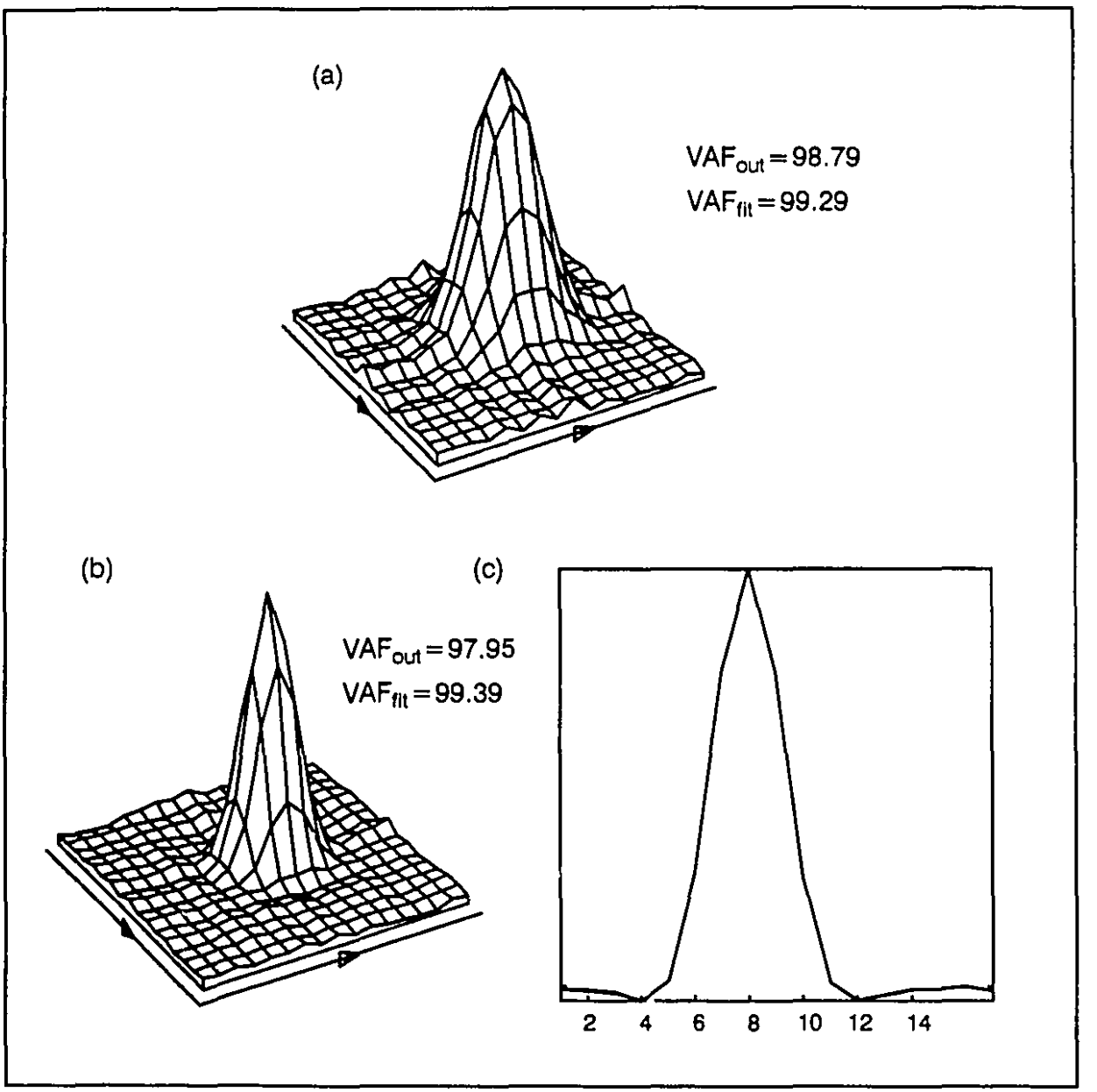

Figure 6.12 Experimentally identified PSFs with preprocessing

PSF obtained for (a) smoothing and (b) high resolution image reconstruction filter. (c) cross section in the column direction taken through the center of the PSF in (b) showing negative tails characteristics of this filter. The input signal was processed to match the cupping characteristics of the image, as well as its orientation and sub-pixel location.

6.6 Discussion

Many factors influence the quality of identification. In this section we will consider the influence of the design of the input signal, noise, non-stationarity and misregistration. We will also discuss how PSFs estimated with the correlation method compare with those evaluated from the wire input.

6.6.1 Design of the input sequence

When white noise cannot be employed as an input, many authors suggest using a PRB sequence. If the fabrication of a white noise phantom seemed insurmountable, the creation of a pure PRB signal would also have proven very difficult. We therefore chose to build a phantom by drilling holes, the position of which was based on a PRB sequence.

When designing a PRB sequence, three parameters must be fixed: the signal amplitude, the digit interval and the period (Godfrey, 1969). To complete the design of our input signal, two additional factors had to be considered: the size of the holes and of the pixels.

Signal amplitude The amplitude is governed by the choice of materials composing the phantom. The radiopaque material was chosen for its ease of machinability and homogeneity. Delrin, whose CT number averaged 200, fulfilled both requirements. In order to avoid x-ray scatter, test signals are usually imaged in water. However we feared the formation of air bubbles within the holes if the phantom had been immersed. We therefore simply imaged the phantom in air whose CT number is very low with a value of -1000.

Digit interval The digit interval, or the distance between adjacent sequence elements was set to 0.9 mm, the minimum distance between neighboring holes. The period was equal to the product of the digit interval and the sequence length $N = 2^n - 1$ where n is the number of stages in the shift register. The signal represented a full cycle of a 32x32 element sequence generated with 10 stages. With a digit interval of 0.9 mm, the period was therefore equal to 28.8 mm.

Period Norton (1985) and Godfrey (1969) suggest using several short sequences, each with a period slightly larger than the settling time of the PSF, rather than one long sequence. In the former case, several estimates can be averaged since the computation of the correlation functions in done over one period. Using this strategy, useful estimates can still be obtained in the advent of a breakdown of the experiment.

We were not concerned with this type of problem: if a portion of the image is unusable, the scanner must be serviced. Furthermore, a foreseeable problem with the

approach is that the correlation estimates corresponding to each period must be properly registered prior to averaging. For the estimates to occupy the same location within the pixel grid, the period must be an integer multiple of the pixel size. Our simulations (section 6.4.3) showed that excellent results could be obtained with one large sequence. The determining factor in this case was the overall size of the object. For these reasons, we preferred using one large period.

Hole size For proper identification, it is important that the input signal contain sufficient power at the frequencies over which the system operates. The size of the holes and the distance between them control the frequency content of the signal. Simulations in section 6.4.2 showed that the best identification for the smoothing filter occurred when the holes were approximately 0.6 mm in diameter. Within the range studied, the separation between the holes did not have much influence for this size of hole.

Pixel size The most serious drawback with our input design is that the signal was not binary. The CT value of a given pixel varied depending on the portion occupied by holes, which in turn was a function of the position of the holes and of the size of the pixel relative to the holes. If the pixel width was smaller than $\phi/\sqrt{2}$ where ϕ is the hole diameter, the surface occupied by the hole ranged from 0% if the pixel fell between holes, to 100 % since the pixel may be inscribed within a hole. When the pixel size increased past $\phi/\sqrt{2}$, the upper limit decreased and the probability distribution more closely approximate the distribution of a real PRB sequence. As shown in figure 6.13, with a decrease of the ripples with respect to the central peak, the ACF also became closer to that of a PRB sequence. Identification should therefore improve by increasing the pixel size. But this must be weighted against the fact that the PSF will be represented by an ever decreasing number of pixels as illustrated in figure 6.6. Unfortunately, there is no clear rule governing the choice of pixel size.

6.6.2 Noise

One of the factors explaining the better results obtained for the smoothing filter is that the phantom was tuned to maximize results for this apodizing function. The second factor is noise.

Supposing that both the input and output are corrupted with additive noise (the pixel coordinates have been dropped for ease of notation):

$$a_m = a + m \tag{6.26}$$

$$b_n = b + n \tag{6.27}$$

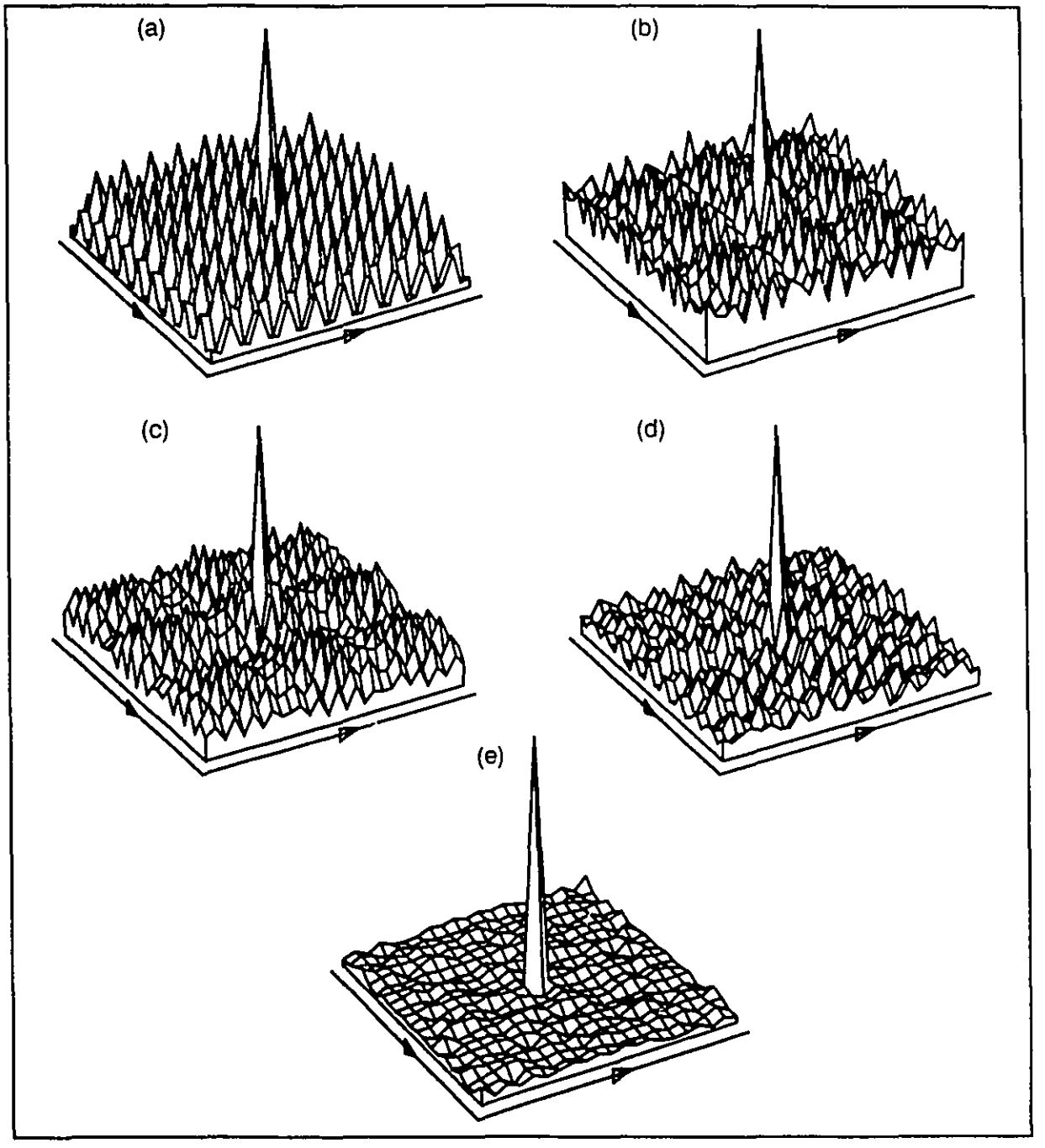

Figure 6.13 Effect of pixel size on ACF of input signal

ACF of signal consisting of holes 0.61 mm in diameter separated by 0.9 mm for pixel width of (a) 0.305 mm, (b) 0.4 mm, (c) 0.5 mm and (d) 0.6 mm. The position of the holes is based on a 32x32 PRB sequence. (e) ACF of a real PRB sequence for a pixel size of 0.4 mm.

where a_m: noisy input
m: input noise
b_n: noise output
n: output noise.

the auto- and cross-correlation functions become:

$$c_{a_m\, a_m} = c_{aa} + c_{am} + c_{ma} + c_{mm} \tag{6.28}$$

$$c_{a_m\, b_n} = c_{ab} + c_{an} + c_{bm} + c_{mn} \tag{6.29}$$

It is usually assumed that there is no noise at the input of the system. However in our case, such noise will arise from errors in digitizing the input. The derivation of analytical expressions for computing the portion of a pixel occupied by holes and the use of an N/C machine to fabricate the phantom have contributed to keeping input noise low. Input noise being so intimately related to the design of the input signal, the terms to the right of c_{aa} in equation (6.26), although small, are not equal to 0.

Output noise is due to a variety of factors resulting from the interaction of x-ray photons with matter as well as electronic noise at the detectors, analog-to-digital converters etc. Section 2.3 covers this topic in more depth. It is generally assumed that output noise is uncorrelated to the input signal, but this is not true of x-ray CT. As a general rule, the larger the x-ray attenuation of a tissue, the higher the level of noise. Furthermore, with input noise related to the input signal, and output a function of the input, the input noise should also be correlated to the output signal. Therefore, the only term in equation (6.29) equal to 0 is c_{mn}, inasmuch as it reasonable to assume that the input and output noise are unrelated, arising from completely different phenomena.

Input noise is very critical to the deconvolution of the PSF. Errors in the input, along with the complicated form of the ACF, bring about difficulties during the inversion of matrix $\mathbf{C_{AA}}$, requiring a robust matrix inversion technique. Furthermore, input noise also appears in the cross-correlation matrix. On the other hand, output noise only shows up in matrix $\mathbf{C_{AB}}$, which is multiplied by the inverse of $\mathbf{C_{AA}}$ to provide the PSF. As a consequence, the method can tolerate higher levels of output noise more easily than input noise.

Godfrey (1969) suggests two methods to reduce the effect of output noise. the first is to increase the amplitude of the signal. Neglecting input noise and assuming that the output noise is uncorrelated to the input, he argues that an increase of the input signal by a factor α increases the terms c_{ab} and c_{an} in equation (6.29) by α^2 and α respectively, thereby resulting in a relative decrease of noise with respect to the signal. Unfortunately this manner of reducing noise cannot be transposed directly to x-ray CT since output noise is correlated to the input. Consequently, for a given signal amplitude, it is best to use materials at the low end of the x-ray attenuation scale than those at the high end.

The second means by which noise can be reduced is by increasing the length of the input signal. The correlation evaluated at lag (i,j) is the sum, over a given length, of the product of two functions, one of which has been delayed by (i,j). The summing portion of this operation amounts to averaging. By increasing the length over which the correlation is computed, more noise is averaged out of the correlation function being computed. This is the main reason why deconvolution of equation (6.6) yields much better results than if the PSF had been evaluated from equation (6.1) directly.

It is interesting to note that only output noise is influenced by the choice of image reconstruction filter. For a given slice thickness, the level of noise in images produced with the high resolution apodizing function is approximately 5 times larger than in images reconstructed with the smoothing filter. This higher output noise level incurred when imaging the input with the former filter accounts, together with the design of the input, for the lower identification quality. The fact that a fivefold increase in noise produces only modest changes in identification quality demonstrates the method's relative immunity to output noise.

6.6.3 Other factors affecting identification quality

A considerable amount of cupping was present in the images. Two factors contributed to this artefact. Firstly, the phantom could not be immersed in water for fear of air bubble formation within the holes. It was therefore imaged in air. Secondly, the shallowness of the holes required that the images be taken very close (about 2 mm) to the surface of the phantom. Both factors were responsible for an unusual amount of x-ray scatter leading to cupping.

Godfrey (1969) defined drift as a slow change of the output of a process from its desired operating point. In x-ray CT, cupping produces such a variation in mean value with position. This type of non-stationarity can be modelled by adding a deterministic function d(i,j) to the output. If the variation of d(i,j) is slow , then it can be separated from the signal. Bendat and Piersol (1986) propose 3 methods to do so:

1- digital low pass filtering
2- polynomial curve fitting and trend removal
3- short averaging operations.

We chose the second option. Cupping was modelled as a bi-linear variation of CT numbers with position. Its effect was reduced by subtracting the equation of a plane from the output image. The parameters of this equation were estimated from the CT numbers of the plastic material surrounding the signal. However, our simulations showed that even in the presence of quite severe cupping, the implication on identification was minimal.

Much more important than cupping is the effect of input-output signal misregistration. Incorrect alignment between the two signals can be due to relative shift and/or rotation. Of these two causes, relative shift is the most benign. The amount of shift can easily be estimated since the identified PSF is shifted by the same amount with respect to its own digitization grid. Furthermore, its shape is undistorted.

The effect of rotation is much more severe. Not only does the estimate of the PSF broaden with increasing rotation, but it is also progressively shifted. Furthermore, it introduces side lobes of growing amplitude. Unfortunately the amount of rotation cannot be easily evaluated from the identified PSF itself as is the case with pure translation. When the output is shifted with respect to the input, all points within the signal move by the same amount and therefore affect the identification in the same way. However, when rotation occurs, the relative displacement changes from point to point and influences the estimation procedure differently. It is therefore important to provide a means exterior to the signal to assess how much the image is rotated with respect to the object. We did so by drilling a series of holes parallel to the top and one of the sides of the signal thus forming a set of perpendicular alignment axes.

6.6.4 Comparison with wire input

Up until now, we have dwelt on issues concerning the correlation method itself and have completed the first goal stated at the beginning of this chapter. The high values of identification quality are encouraging indicators as to the success of the method. However, before making such a statement, results obtained with the PRLH must be compared with those of the wire input.

We therefore fitted the parametric models (chapter 4) to the non-parametric estimates obtained in this chapter and those of the wire input. The estimates for the wire input are those corresponding to points located at 17 mm from the center of the shift-variant phantom (see section 5.4.1). These wires are the closest to the center of the PRLH signal which was located at a radial distance of 20 mm from the center of the field of view.

Instead of basing the comparison on the model shape parameters, we decided to use a more easily interpreted physical quantity: resolution. Estimates for the smoothing filter were based on the full width at half maximum (FWHM) of the Gaussian model (equation 4.8) while the damped cosine model's half width at first zero crossing (HWZC) (equation 4.9) was used for the high resolution filter. Both these estimates are derived from model parameters. These parameters were taken from table 6.8 for the PRLH phantom.

Although not tabulated, measures of resolution for the wire input are illustrated in figures 5.9 and 5.10.

Table 6.9 shows that the estimates derived from the PRLH signal are lower than those of the wire.

	smoothing		high resolution	
	x	y	x	y
PRLH signal	1.403	1.385	1.067	1.029
wire	1.407 ± 0.004	1.395 ± 0.011	1.099 ± 0.036	1.048 ± 0.019

TABLE 6.9 Estimates of resolution for PRLH sequence and wire input

It should be noted that the estimates derived from the PRLH signal are lower than those of the wire. This is compatible with the fact that the PRLH object slightly overestimates the MTF of the system (see section 6.4.8) or that the PSF derived from this input is narrower that the actual system filter.

Nonetheless, all estimates for the PRLH signal fall within a two-sided confidence interval of at least 90% built around the mean values obtained for the wire input. This implies that the two methods are equivalent at a level of significance α of 5%, or that the probability of rejecting this hypothesis even if it is true is 5%. (As a general rule, the narrower the interval, or the higher the level of confidence, the more powerful the test, i.e. the lower the probability of accepting the hypothesis when it is false.)

Therefore, either both type of inputs identify a narrower PSF or the difference between the actual PSF and the one estimated with the PRLH sequence input falls within experimental error encountered with the wire input. The first explanation is highly improbable. A wire of finite size is only an approximation of an impulse and larger estimates of resolution should be expected. While the frequency spectrum of an impulse is flat, that of a circular object is equal to $2J_1(\pi\nu d)/\pi\nu d$ where d is the diameter of the wire, J_1 the first order Bessel function and ν radial frequency. As the diameter increases, the signal is progressively deprived of power at higher frequencies. As a consequence, the MTF obtained from a wire can only be underestimated, and the PSF derived from this input is wider than the true PSF.

If the estimates produced by these two inputs are biased in different directions, but that they are statistically equivalent, we must conclude that these biases are very small and fall within experimental error. The estimates obtained from the correlation based method therefore validate the results yielded from the wire input.

6.7 Conclusions

We have successfully applied the Wiener-Hopf equation to identify the PSF of an x-ray CT scanner. The input consisted of a series of holes 0.61 mm in diameter and spaced at least 0.9 mm apart. The position of the holes was based on a 32x32 element PRB sequence generated with a 10 stage shift-register algorithm. Once the design of the signal was finalized, the single most important factor affecting the identification quality was the proper rotational alignment of the object and its image.

Identification was slightly better for the smoothing image reconstruction filter compared to the high resolution filter. Two factor are responsible for this difference. Firstly, the frequency content of the input was tuned for the former apodizing function, and secondly the output noise was five times lower for this filter. Input noise, which complicates the inversion of the auto-correlation matrix, was the same in both cases.

Measures of resolution were obtained by fitting appropriate models to the non-parametric PSF estimated with the PRLH and wire input. The two sets of estimates were found to be statistically equivalent at a 95% confidence interval thereby validating the results of the previous chapters.

The correlation based method is more computationally involved than other non-parametric estimation methods. It also requires a more complicated input. However, once the algorithm is programmed, and an appropriate phantom built, the estimation procedure is very simple.

Like the wire input, and in contrast to the edge method, a bi-dimensional estimate is acquired from a single image. To get the same information, an edge would have to be positioned in a number of different orientations, with one image to process per orientation, thereby increasing the processing time.

Another advantage of the method is its relative immunity to output noise. While this may not appear a great benefit for X-ray CT scanners, it could prove helpful for nuclear medicine imaging techniques (SPECT, PET) for which the signal to noise ratio is much lower.

CHAPTER 7

COORDINATE TRANSFORMATION FOR ISOPLANATIC REPRESENTATION OF SHIFT-VARIANT CT POINT SPREAD FUNCTION

7.1 Introduction

The imaging process introduces noise, blur and artefacts which limit the precision with which edges can be localized. Some of these effects can be counteracted through image restoration whose goal is to estimate the underlying object from its image. Image restoration could therefore be used as a pre-processing step prior to segmentation.

The vast majority of linear as well as non-linear restoration schemes are designed for isoplanatic imaging systems. We have shown however, that CT systems, like most real systems, are shift-variant. A number of strategies have been developed for dealing with this issue. The most common approach has been to simply ignore the problem. Others discount its importance, using the hypothesis that the change in PSF properties are small enough to be ignored or by arguing that the region of interest is small. These arguments are often put forward without even measuring the spatial variation of the PSF.

Yet there exist methods for handling shift-variance explicitly. Of these methods, a technique known as coordinate transformation restoration is quite promising and will be investigated herein. Therefore the first goal of this chapter was to develop a coordinate transformation suited to the behavior of a CT scanner presented in chapter 5 while the second was to evaluate this method.

The chapter is organized as follows. In section 7.2, different methods for dealing with shift-variance are reviewed. Section 7.3 presents the proposed change of coordinates both conceptually and in detail. The method is evaluated in section 7.4, which is followed by a short discussion and a conclusion in sections 7.5 and 7.6 respectively.

7.2 Restoration of shift-variant images

The fact that most real imaging systems are shift-variant is rarely acknowledged when restoring images thus violating one of the hypothesis on which most of the restoration schemes are based. Two notable exceptions in the medical imaging literature are Peters (1980) and Hon et al. (1989) who recognized the shift-variant nature of the imaging system. Nonetheless, in order to simplify the restoration task, they assumed that the region of interest was relatively small compared to the image and that shift-invariance could be

assumed within that region. However, there are a number of methods for dealing with shift-variance explicitly and we now present four different methods.

1- The first method is called **mosaic formation** by Bates and McDonnell (1989). It consists of dividing the image into zones and considering the image shift-invariant within each zone. The zones are usually rectangular in shape and their area is determined by the size of the error one is willing to tolerate and how fast the PSF changes.

2- Andrew proposed a **matrix formulation** of the type:

$$I_{MN,1} = H_{MN\,MN}\ O_{MN,1} \tag{7.1}$$

where I, H and O are matrices composed of elements of the image, point spread function and object respectively. The image (and object) are considered to be of size M by N pixels. Shift-variance can easily be taken into account since the matrix H is composed of sub-matrices describing the local blurring structure for every point in the image. This method requires huge amounts of memory: matrix H counts 65536 rows and columns or over 4295 million elements for a 256 by 256 image.

3- **Kalman filtering** is also a candidate for shift-variant restoration provided that changes in PSF shape are relatively slow. The Kalman filter, like the Wiener filter, is also a solution to the minimum mean square error problem. It is formulated as a recursive spatial domain algorithm which is applied point by point or at best row by row. It requires a priori knowledge of the image in the form of an autoregressive model, and of the blurring characteristics of the imaging system (Biemond, 1990). Though it has been successfully applied to 1D problems, its extension to 2D is not trivial. One of the major problems associated with this method is the difficulty of formulating a suitable 2D recursive model compatible with reasonable computational load. Computation time is generally 10 to 20 times greater than with other linear methods using quadratic distances (Demoment, 1989).

4- The fourth method is referred to as **rectification** by Bates and McDonnell (1989) and **coordinate transformation restoration** by Sawchuk (1974). Compared to the methods presented above, this technique requires only a limited amount of memory and is fast. The approach, illustrated in Figure 7.1 , consists of transforming the x-y image into a shift- invariant one represented in a coordinate system u-v through a change of variables $u=u(x,y)$, $v=v(x,y)$. Classic shift-invariant restoration methods, such as Wiener filtering (Peters, 1980; Dhawan, 1985; Hon et al. 1989; Madsen, 1990; Penney et al. 1990), are then used to estimate

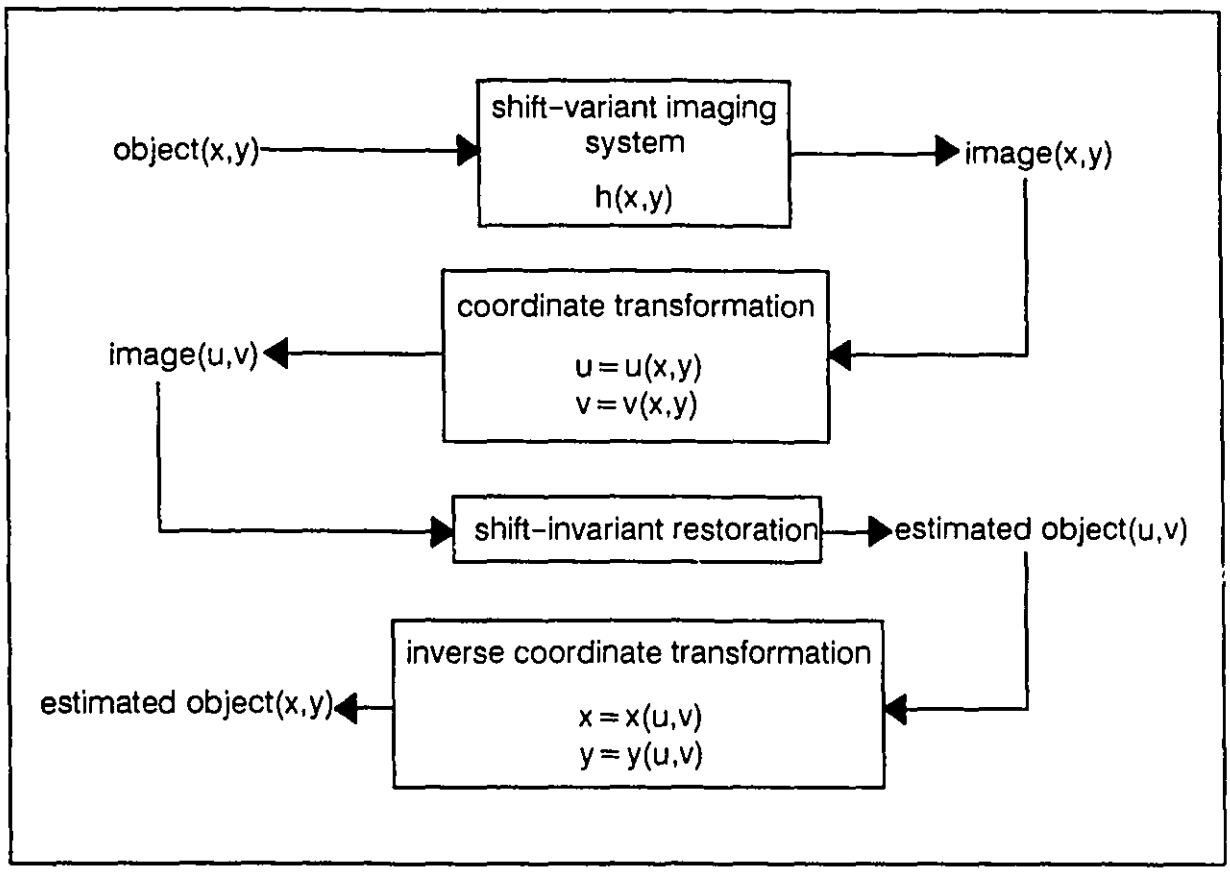

Figure 7.1 Principle of coordinate transformation restoration

An image produced with a shift-variant system, is made shift-invariant by an appropriate coordinate transformation. A classic linear shift-invariant restoration method is used to obtain an estimate of the object in the transformed space. The inverse coordinate transformation is applied, yielding the estimated object in the original coordinate system.

the object in the transformed coordinate system u-v. The deblurred image is finally returned to the original image coordinates by applying the inverse coordinate transformation.

This method has been used to restore optical images distorted by shift-variant degradations such as coma aberration (Robbins, 1970; Robbins and Huang, 1972), linear and rotational motion blur (Sawchuk, 1972 and 1974) along with astigmatism and curvature of field (Sawchuk and Peyrovian, 1975).

The shift-variance due to these optical degradations can be expressed as relatively simple equations. The coordinate transformation can therefore be handled with elegant

analytical tools such as the Mellin transform, a close relative of the Fourier transform (Sawchuk, 1974; Robbins and Huang, 1972; Bracewell, 1986).

For CT systems, the spatial variation in PSF shape is very similar to the changes seen with a combination of astigmatism and curvature of field. Both exhibit a rotating blur, and in both cases, the isotropicity of the PSF is destroyed as the distance from the center of the field of view increases since the PSF stretches more rapidly along the tangential than the radial axis. Consequently, coordinate transformation, which has been successfully applied to these optical degradations, seems very promising for shift-variant restoration of CT images.

However, the analytical coordinate transformations developed for the optical degradations cannot be transposed directly to CT for two reasons. Firstly, the analytical expression for the shift-variant CT PSF is so complex it must be evaluated numerically (Verly and Bracewell, 1979). Secondly, this expression does not take sampling, which strongly affects the pattern of shift-variance, into account. Both these difficulties prompted us to develop a new algorithm, presented in the next section.

7.3 Proposed change of coordinates

The proper change of variables is dictated by the nature of the shift-variance. In this section, we will propose a coordinate transformation based on the experimental results obtained in chapter 5. We will then state the conditions that must be respected for a proper mapping from one image space to the other.

7.3.1 Coordinate transformation

Before going into the mathematical details of the transformation, it is worthwhile explaining the concepts. The PSF maintains the same basic shape throughout the FOV but this shape is progressively stretched at a different rate along two perpendicular axes as the distance from the FOV increases. The basic principle underlying the coordinate transformation is that the cross-section at some non-zero value of the PSF, say half its maximum, should be represented by the same number of samples irrespective of the position of the input point source.

We will now show that the PSF is represented by an equal number of samples when it is represented in a variably sampled polar coordinate system. The upper left hand portion of figure 7.2 represents a cross-section taken through the PSF measured at different positions within the FOV in the original (x,y) image plane. The position of the input source is defined in a polar coordinate system (r,θ) whose origin corresponds to the center of

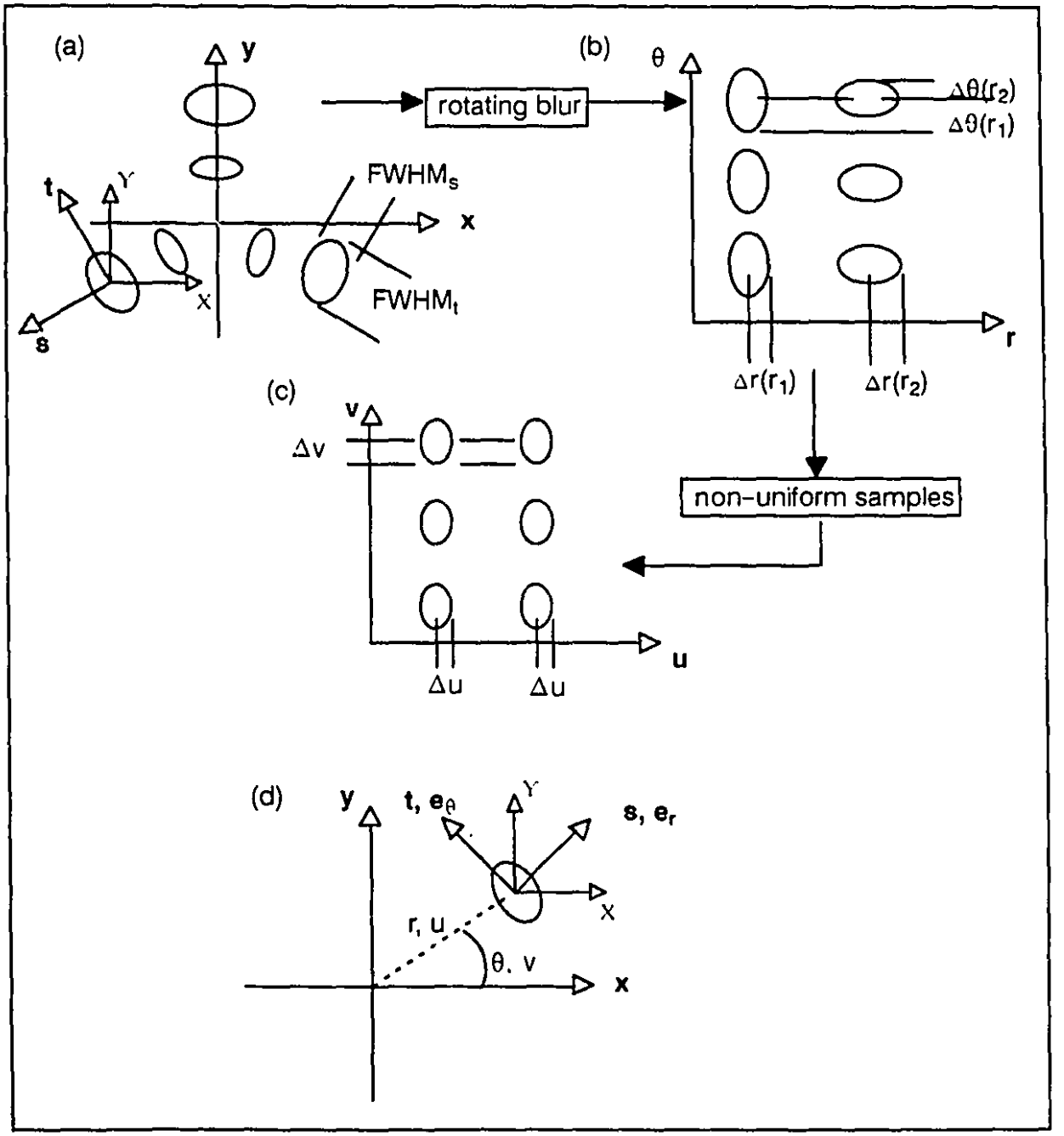

Figure 7.2 Coordinate transformation for CT images

(a)-(c) The rotating blur exhibited by CT scanners suggests a transformation from a Cartesian to polar coordinates. The variation in PSF width thus becomes a function of a single variable: the radial distance. By varying the sampling increment in the angular and radial directions as a function of radial distance, the PSF can be represented by an equal number of samples, thus obtaining a shift-invariant representation. (d) Relative orientation of coordinate systems.

the FOV. The shape of the PSF is given either in a fixed orientation (X,Y) or a local rotating frame (s,t). The unit vectors s and t point in the radial and tangential directions respectively. As shown in chapter 5, the shape of the PSF varies both with radial and angular position of the input point when expressed in the (X,Y) coordinate system. More specifically, this variation is sinusoidal with angular position for input sources located at a fixed radial distance (see figures 5.4, and 5.5). However, because the system exhibits a rotating blur, the dependence on the angular position disappears when the PSF is expressed in the s-t rotating frame (figure 5.6). From radially symmetric in the center of the FOV, the PSF becomes progressively wider in both the radial (s) and tangential (t) directions. However, because the rate of change in the two directions is different, the cross-section changes from circular in the center of the FOV, to elliptical as the input source moves outward.

The rotating blur suggests that the relationship between shape and position would be simplified by a polar coordinate transformation as shown in Figure 7.2 (b). The shape of the PSF is now a function of radial distance only. The final transformation plane (u,v), shown in Figure 7.2 (c), is obtained by varying the sampling increment in the angular and radial directions as a function of radial distance r. The PSF is thus represented by an equal number of samples in the (u,v) coordinate system satisfying the requirement for isoplanicity. It is clearly seen from this explanation that the (u,v) plane is a variably sampled polar coordinate system with the **u** axis corresponding to the radial direction and and **v** to the angular orientation.

Conceptually, the process is therefore divided in three steps:

1) The first step consists of describing the shape of the PSF in the local rotating frame s-t. As in previous chapters, we summarize the shape of the PSF by using measures of resolution. For example, a PSF modelled by a 2D Gaussian function is fully characterized by the full width at half maximum (FWHM) in two orthogonal directions. In Chapter 5, we experimentally estimated the relationship of $FWHM_s(r)$ and $FWHM_t(r)$ for a variety of imaging conditions. Typical curves, obtained with the smoothing image reconstruction filter and a scan time of 4.5 s, are shown in Figure 7.3 (a) and (b).

2) To take advantage of the rotating blur, the relationship between shape and position must now be expressed in polar coordinates. Since the s axis corresponds to the r axis (both $\mathbf{s}$ and $\mathbf{e}_r$ represent distances and have the same orientation):

$$FWHM_r(r) = FWHM_s(r) \tag{7.2}$$

The correspondence between angular ($\mathbf{e}_\theta$) and tangential (t) variables is not as simple. Even if the axes have the same orientation, the former represents angular increments while the later measures distances. However, the expression for the

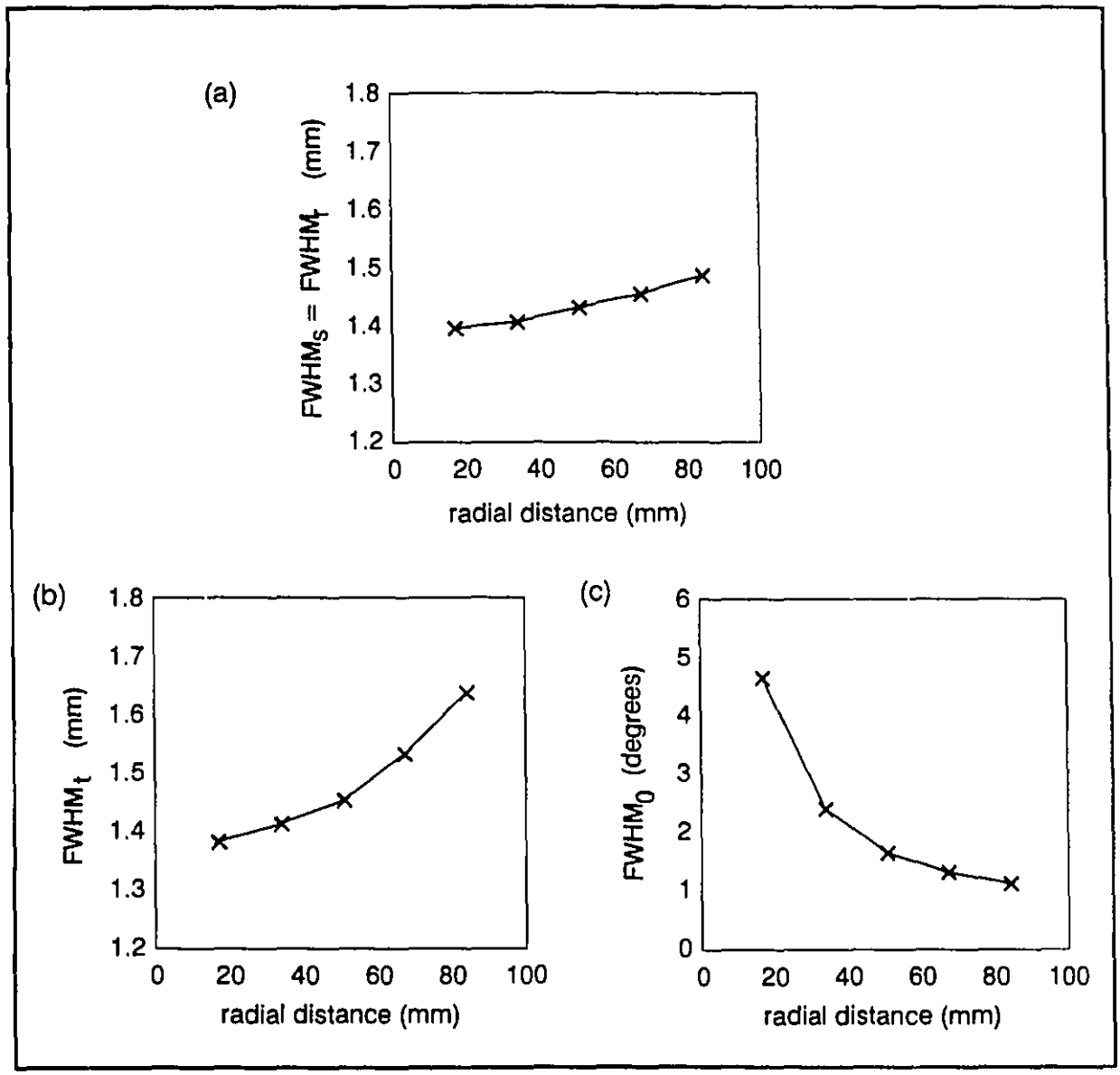

Figure 7.3 PSF shape in rotating cartesian (s-t) and polar (r-θ) coordinate frames

(a) Since the $\mathbf{s}$ and $\mathbf{e}_r$ axes are equivalent, the relationships $FWHM_s(r)$ and $FWHM_r(r)$ are the same. However, even if the $\mathbf{t}$ and $\mathbf{e}_\theta$ axes have the same orientation, the difference in units requires that (b) $FWHM_t(r)$ be manipulated to obtain (c) $FWHM_\theta(r)$

FWHM in the angular direction corresponds to the angle subtending the PSF in the tangential direction. From simple geometry, we deduce:

$$FWHM_\theta(r) = 2 \tan^{-1}\frac{FWHM_t(r)}{2r} \tag{7.3}$$

Figure 7.3 (c) illustrates this new relationship. The decrease of $FWHM_\theta(r)$ simply indicates that the angle subtending the width of the PSF in the tangential direction decreases with radial distance even though the linear width increases.

3) The final (u,v) plane is obtained by variably sampling the polar plane defined above. We first start with the **u** axis which corresponds to a variably sampled $\mathbf{e}_r$ axis. The problem now becomes one of selecting the proper increments, and the solution is contained in the relationship $FWHM_r(r)$ as shown in Figure 7.4. We wish to represent the PSF with a constant number of samples k across $FWHM_r$. Because the PSF is narrower in the central region than a the edges of the FOV, the intersample distance Δr must increase with radial position if the PSF is to be shift-invariant along the u axis. The increment Δr is given by:

$$\Delta r(r) = \frac{FWHM_r(r)}{k} \tag{7.4}$$

Given the initial conditions:

$$n = 0 \tag{7.5}$$

$$u_n = 0 \tag{7.6}$$

the function u(r) is constructed iteratively as follows:

$$\Delta r(u_n) = \frac{FWHM_r(u_n)}{k} \tag{7.7}$$

$$u_{n+1} = u_n + \Delta r(u_n) \tag{7.8}$$

The relationship between the v, or variably sampled angular, axis and radial distance is obtained directly from $FWHM_\theta(r)$. If the PSF is represented by an equal number of samples l across $FWHM_\theta$:

$$\Delta\theta(u_n) = \frac{FWHM_\theta(u_n)}{l} \tag{7.9}$$

$$v_m = m\ \Delta\theta(u_n) \tag{7.10}$$

subject to the initial conditions:

$$m = 0 \tag{7.11}$$

$$v_m = 0 \tag{7.12}$$

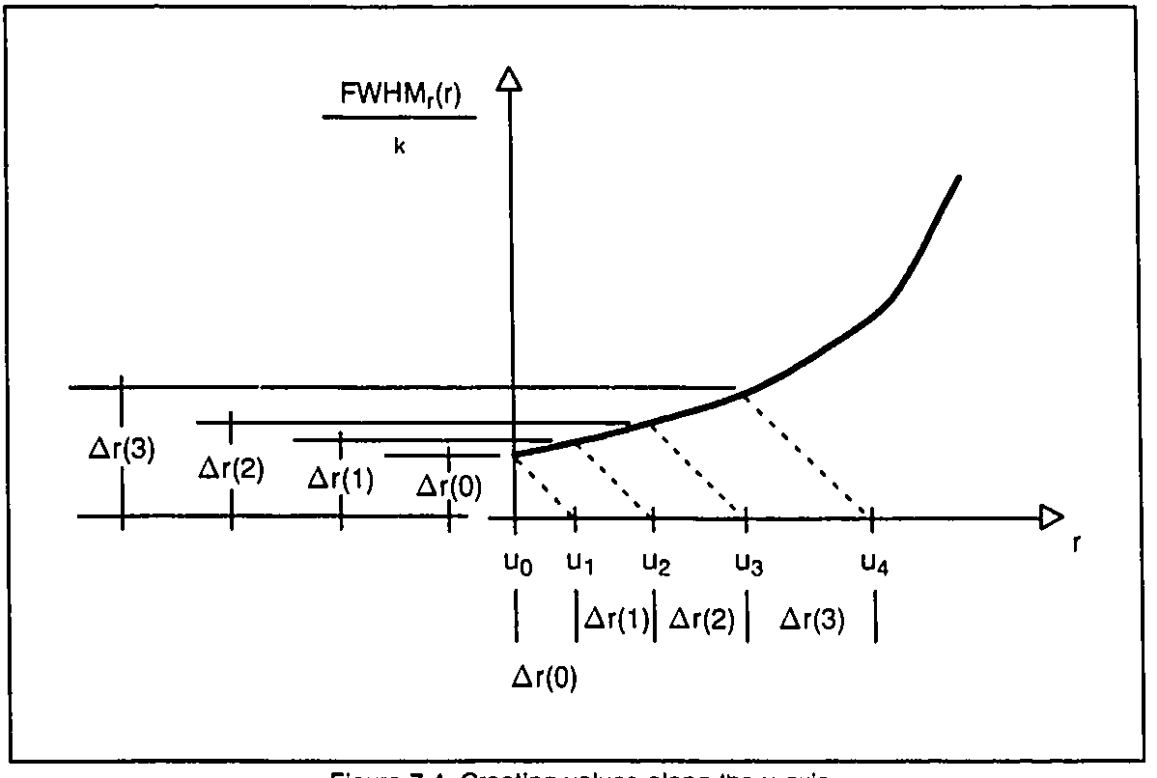

Figure 7.4 Creating values along the u axis

Values of u are found iteratively by adding an increment $\Delta r(u_n)$ - equal to the FWHM in the radial direction divided by the number of samples k - to the previous value of u .

7.3.2 Requirements for correct mapping

The number of samples k and l across the width of the PSF influences the quality of the transformation. For an image to be unaffected by the cascade of forward and inverse transformations, every pixel of the (x,y) image must be mapped into the (u,v) plane. Therefore, the maximum radial increment Δr must be no larger than 1 pixel. Since the largest increment occurs at the outer edge of the region of interest, the value of k is found by replacing $\Delta r(r) = \Delta r(r_{max}) \leq 1$ in equation (7.4):

$$k \geq FWHM_r(r_{max}) \tag{7.13}$$

The PSF is also at its widest in the tangential direction at $r = r_{max}$. Therefore, the value of l is found by equating the chord length at distance r_{max} subtended by $\Delta\theta$ to a value smaller or equal to 1. This implies that:

$$\Delta\theta \leq 2 \tan^{-1}(1/2r_{max}) \tag{7.14}$$

Combining equations (7.3), (7.9) and (7.14):

$$l \geq \frac{\tan^{-1} FWHM_t(r_{max})/2r_{max})}{\tan^{-1}(1/2r_{max})} \tag{7.15}$$

If r_{max} is much larger than $FWHM_t(r_{max})$, the previous equation simplifies to:

$$l \geq FWHM_t(r_{max}) \tag{7.16}$$

7.3.3 Algorithm

We now have all the equations to establish the algorithm which is described as a flow-chart in figure 7.5. The user starts by selecting proper values for the number of samples across the PSF, k and l, according to equations (7.13) and (7.16). He/she must also fix the maximum radial distance, r_{max}, thereby defining a circular region of interest fitting within the original image. After initializing variables in the u direction, the program fills the u-v plane column by column until the value r_{max} is reached.

Filling any given column proceeds as follows. The v variables are first initialized according to equations (7.11) and (7.12). The x-y coordinate corresponding to pixel (u_n,v_m) is then found, given the following relationship:

$$x = u_n \cos v_m \tag{7.17}$$

$$y = u_n \sin v_m \tag{7.18}$$

The CT number corresponding to this (x,y) pixel is assigned to the pixel (u_n,v_m). Values are updated (equations (7.9) and (7.10)) until they reach a value of 2π. Before proceeding tc the next column, the values of n and u_n are updated (equations (7.5) and (7.8)).

The size of the transformed image is determined by the functions $FWHM_r(r)$ and $FWHM_\theta(r)$ as well as the number of samples taken across the width of the PSF. Because the relationship between the r and u axes is iterative, the number of samples N_u along the u axis cannot be determined in closed form. Rather, it is found by adding the Δr terms until r_{max} is obtained:

$$r_{max} = \sum_{i=0}^{N-1} \Delta r_i(r(u_i)) \tag{7.19}$$

$$r_{max} = \sum_{i=0}^{N-1} \frac{FWHM_r(r(u_n))}{k} \tag{7.20}$$

The total number of samples M along the θ axis is given by:

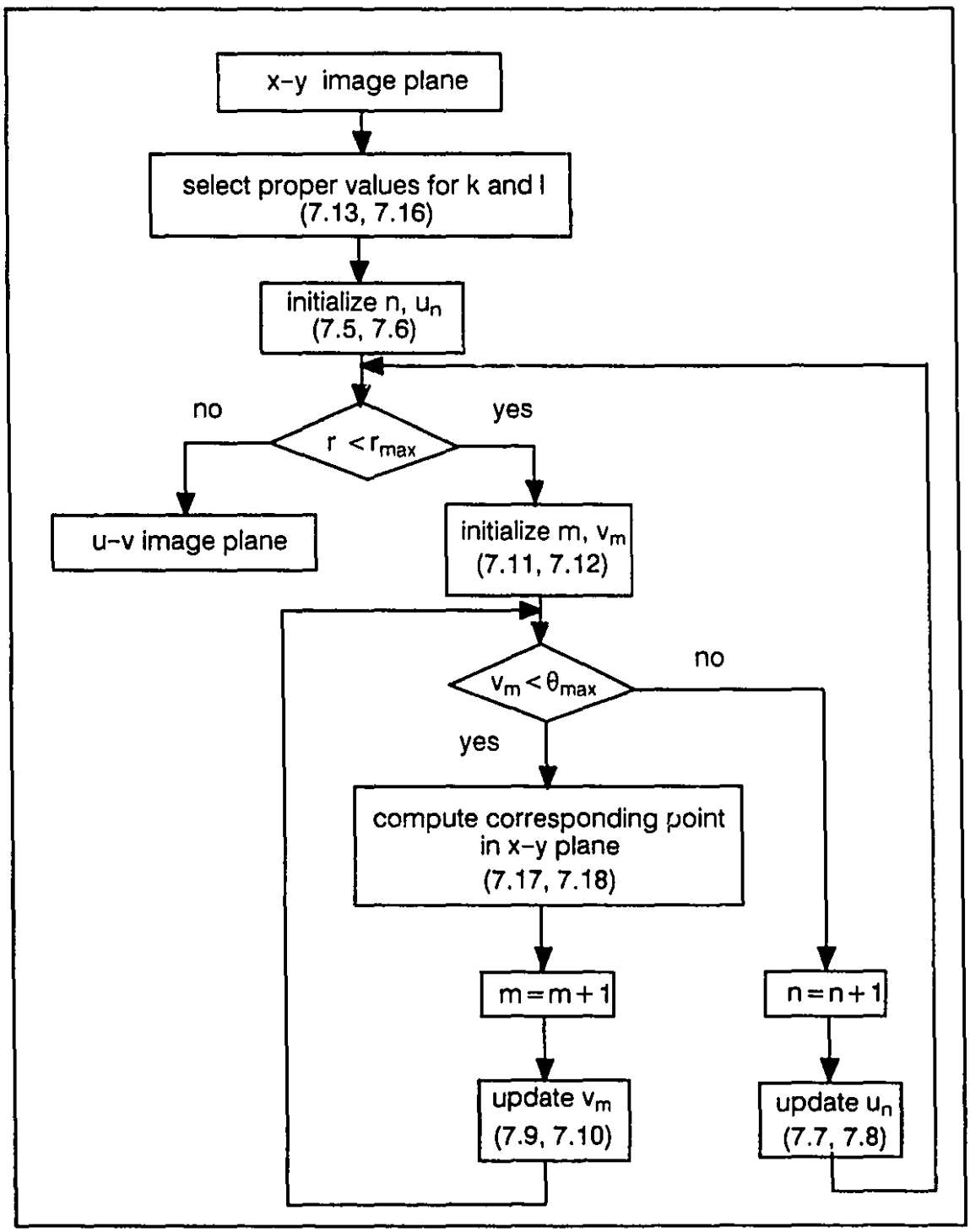

Figure 7.5 Flow chart of algorithm for coordinate transformation

(The numbers in parentheses correspond to equations)

$$M = \frac{2\pi}{\Delta\theta_{min}} \tag{7.21}$$

$$= \frac{2\pi l}{FWHM_\theta(r(u_N))} \tag{7.22}$$

It should be mentioned that the functions $FWHM_r(r)$, $FWHM_\theta(r)$ and $FWHM_t(r)$ should be specified in pixels in equations (7.13) through (7.22).

7.4 Evaluation of proposed transformation

This method has been applied to a variety of optically degraded images. Like most image processing techniques, it was evaluated with images representing a real scene. While these images give some information as to the usefulness of a given method, they do not provide much insight into the method itself. Furthermore, the evaluation is often qualitative: a method is judged according to the appearance and pleasantness of the processed image.

We developed a rather different approach with the goal of quantifying the evaluation as well as gaining a better understanding of the method. The evaluation was based on two criteria:

1- the PSF must be shift-invariant in the (u,v) plane

2- the original image must not be affected by the forward-inverse transformation.

7.4.1 Simulated data

Instead of working with real images, we synthesized the image found in figure 7.6 (a). It consisted of a number of Gaussian PSFs located along 3 radial spokes. The spokes were oriented at 22.5°, 45° and 67.5° with respect to a horizontal (x) axis. Although the pattern of shift-variance was similar to CT data, the changes in shape with radial distance were much larger than those observed with the Philips Tomoscan CX unit (the ratio of inner to outer FWHM was about three times larger). The variation in shape is quantified in the left hand portion of table 7.1. Because the system exhibits a rotating blur and the data are expressed in a rotating frame, the values in Table 7.1 represent variations in PSF width with radial distance along any given spoke.

We used such large variations for two reasons:

1- If the method can handle large changes in PSF shape, it will be applicable to smaller variations.

2- Any error will be amplified and more easily detected.

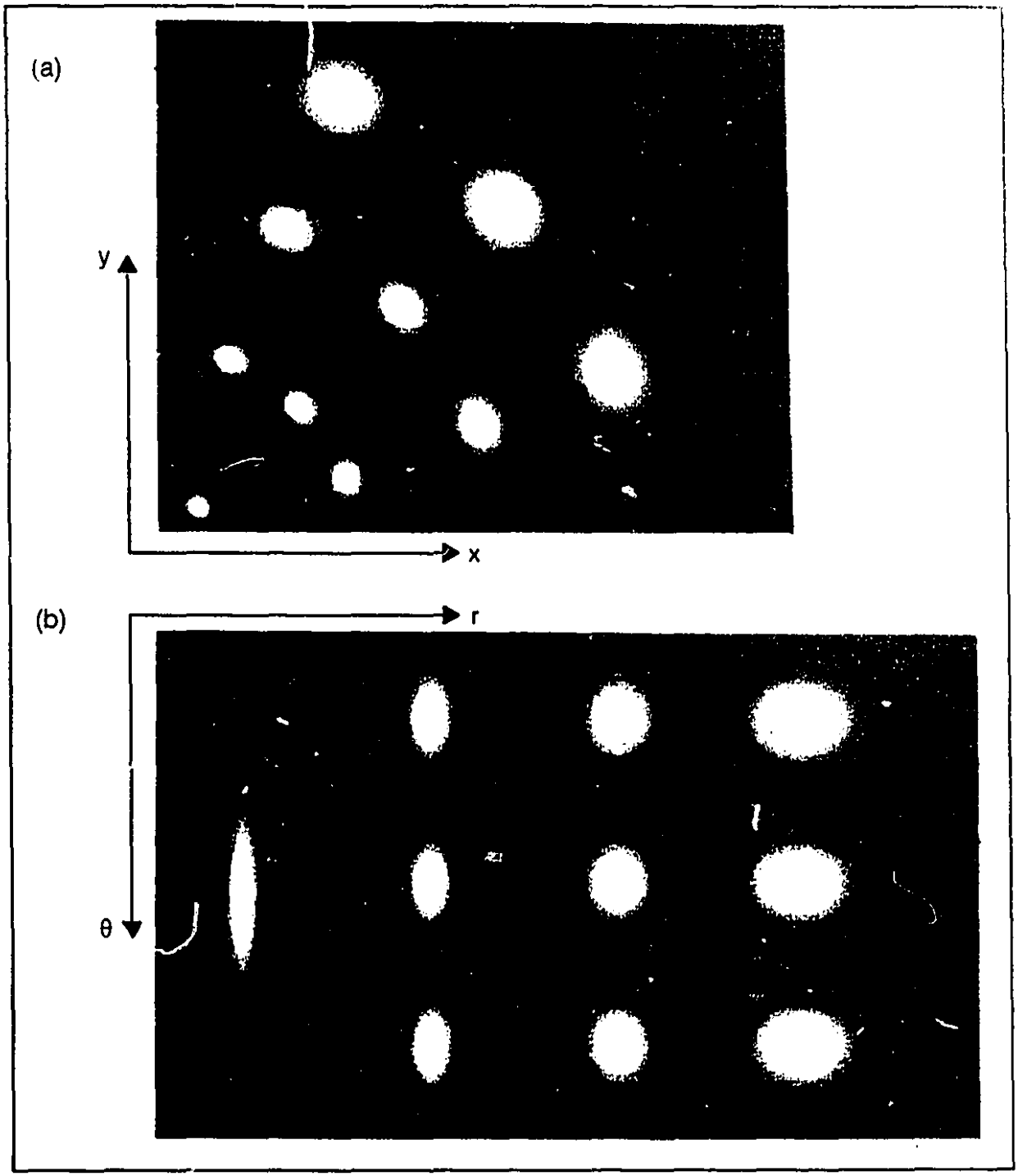

Figure 7.6 Evaluation of coordinate transformation with simulated data
(a) original data in x-y frame , (b) after polar coordinate transformation, (c) in variably sampled polar coordinate u-v when FWHMθ(r) is piecewise linear, (d) in u-v frame when FWHMθ(r) is piecewise constant (the origin of the polar and u-v planes is the upper left corner).

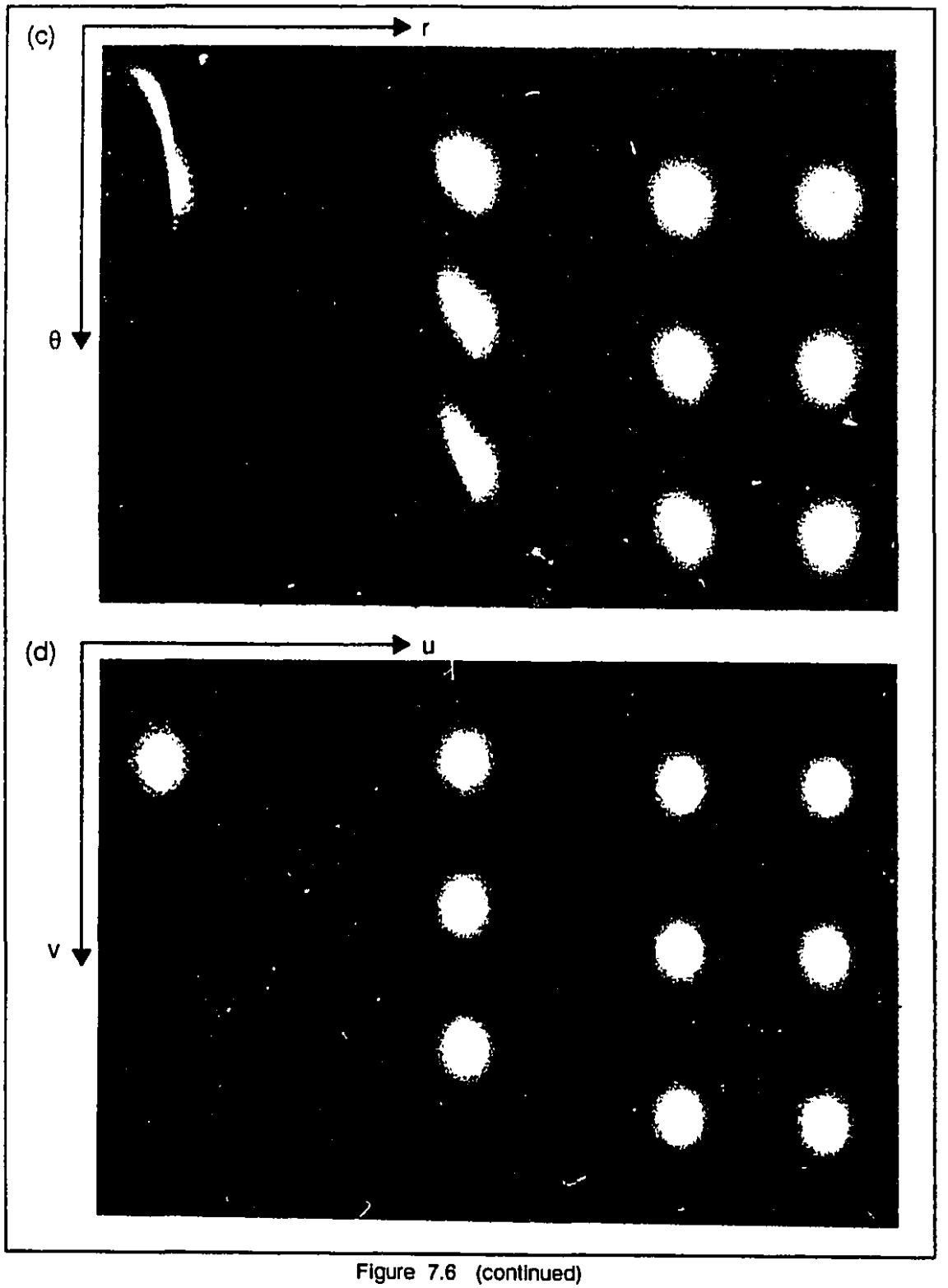

Figure 7.6 (continued)

simulated data (pixels)			CT data (mm)			CT data (pixels)		
R	$FWHM_s$	$FWHM_t$	R	$FWHM_s$	$FWHM_t$	R	$FWHM_s$	$FWHM_t$
25	5	6	17.0	1.396	1.381	72.7	5.96	5.89
75	7	9	33.9	1.407	1.412	144.5	6.00	6.02
125	10	13	50.8	1.532	1.453	213.3	6.11	6.20
175	15	18	67.4	1.456	1.532	287.5	6.21	6.54
			84.4	1.488	1.636	359.9	6.35	6.98

TABLE 7.1 Data used for evaluation of coordinate transformation

We were able to quantify the evaluation criteria by fitting the Gaussian model (see section 4.2.2) to the various PSFs in the original (x-y) and transformed (u-v) planes. As in previous chapters, we derived the FWHM from the model parameters. By comparing the variation of the PSF width with radial distance, we were able to verify if the PSF was indeed shift-invariant in the u-v plane and thereby substantiate the first criterion. The second standard,which states that the original image must not be affected by the forward-inverse transformation, was quantified by comparing the change of FWHM of every PSF within the (x-y) plane before and after the cascade of forward-inverse transformation.

The results are illustrated in figure 7.6. Section (b) shows the PSF in the polar (r-θ) coordinate plane and demonstrates the rotating blur very well: for a given radial distance, the PSFs are independent of the angular variable. Figure 7.6(c) shows the image in the (u-v) plane when the function $FWHM_\theta(r)$ is allowed to vary linearly with radial distance. Even by visual inspection, it can be seen that the PSF are non isoplanatic, contrary to what could be expected. This situation can be rectified, and the anticipated results obtained, by allowing the function $FWHM_\theta(r)$ to vary in a piecewise constant manner. This situation is shown in figure 7.6(d).

This phenomenon, which has never been reported in the literature, constitutes a limitation of the method and will be discussed in more depth in section 7.5.

Table 7.2 presents quantitative results obtained with a piecewise constant $FWHM_\theta(r)$. As with Table 7.1, these values are valid for any given spoke. Application of the coordinate transformation for the simulated data resulted in a large improvement in shift-variance. The FWHM varied by as much as 10 pixels and 13 pixels in the radial and

tangential directions in the original (x-y) plane. These variations were reduced to 0.24 and 1.18 pixels respectively. This improvement shows that the first criteria is satisfied, and that the proposed coordinate transformation does produce a shift-invariant image. Differences between the PSF width in the original plane, and after both forward and inverse transformation were applied to the image, are no more than 0.08 and 0.12 pixel for the radial and tangential directions respectively. These small numbers indicate that the method also complies with the second criteria.

	XY	UV	UV^{-1}	criterion 2 (2)
RADIAL	5.00	15.4	5.00	0.00
	7.00	15.19	7.00	0.00
	10.00	15.16	9.97	0.03
	15.00	15.28	15.08	-0.08
criterion 1 (1)	10.00	0.24		
TANGENTIAL	6.00	19.32	6.00	0.00
	9.00	18.54	9.00	0.00
	13.00	18.34	13.00	0.00
	18.00	18.14	17.88	0.12
criterion 1 (1)	13.00	1.18		

TABLE 7.2 Evaluation results for simulated data

Values in this table represent FWHM in the radial and tangential directions for radial distances given in Table 7.1. (1) maximum difference within the column (2) column XY - column UV^{-1} .

7.4.2 CT data

Although the coordinate transformation has been proposed in the literature for the restoration of nuclear medical images (Hon et al. , 1989) the technique has never been evaluated either for this type of images nor for X-ray CT. We therefore evaluated the

method, using the same procedure outlined above, on a second set of data representing the variation in PSF for a real system. The values found in the right hand side of table 7.1 correspond to the changes observed with the Philips Tomoscan CX for the smoothing filter and a scan time of 4.5 s (see chapter 5). A pixel size corresponding to a FOV of 75 mm (75 mm / 320 pixels) was used to transform distances and lengths from millimeter to pixel.

The results in Table 7.3 and figure 7.7 are valid for a piecewise constant $FWHM_\theta(r)$. They show, for this particular case, that the improvement in shift-invariance was quite small. The change in PSF width with radial distance stayed approximately the same in the (x-y) and (u-v) planes for the radial direction with values of 0.38 and 0.37 pixel respectively. Meanwhile, there was a slight improvement in the tangential direction: the maximum variation in FWHM changed from 1.09 pixel in the (x-y) plane to 0.22 pixel in the (u-v) plane. As with the previous data set, the forward-inverse transformation did not affect the data. Maximum deviations were evaluated at 0.08 pixels and 0.01 pixels in the radial and tangential directions respectively.

7.5 Discussion

The quantitative evaluation procedure was helpful in two ways. We were able to find a limitation of the coordinate transformation method which had not been reported in the literature. It also gave us the opportunity to establish the usefulness of the method without having to perform an actual restoration. However, before discussing these subjects, we would like to bring up the issue of interpolation.

7.5.1 Interpolation

It is highly improbable, during the forward transformation, that a given pixel in the (u-v) plane corresponds to an integer pixel value along the x and/or y axes and vice versa during the inverse transformation. Image values must therefore be interpolated.

Interpolation has a low pass filtering effect which can be explained as follows. When interpolating, one conceptually produces a continuous version of the discrete signal in order to be able to evaluate the function at any point. The frequency spectrum of the (infinite) continuous function is band-limited. On the other hand, the spectrum of the discrete signal is repeated at multiples of $2\pi f_s$, where f_s is the sampling frequency, and is therefore non band-limited. In order to remove the replicates of the frequency spectrum introduced by sampling, i.e. to reproduce a band-limited function from a set of samples, the interpolation function must have low pass filtering characteristics (Parker et al., 1983).

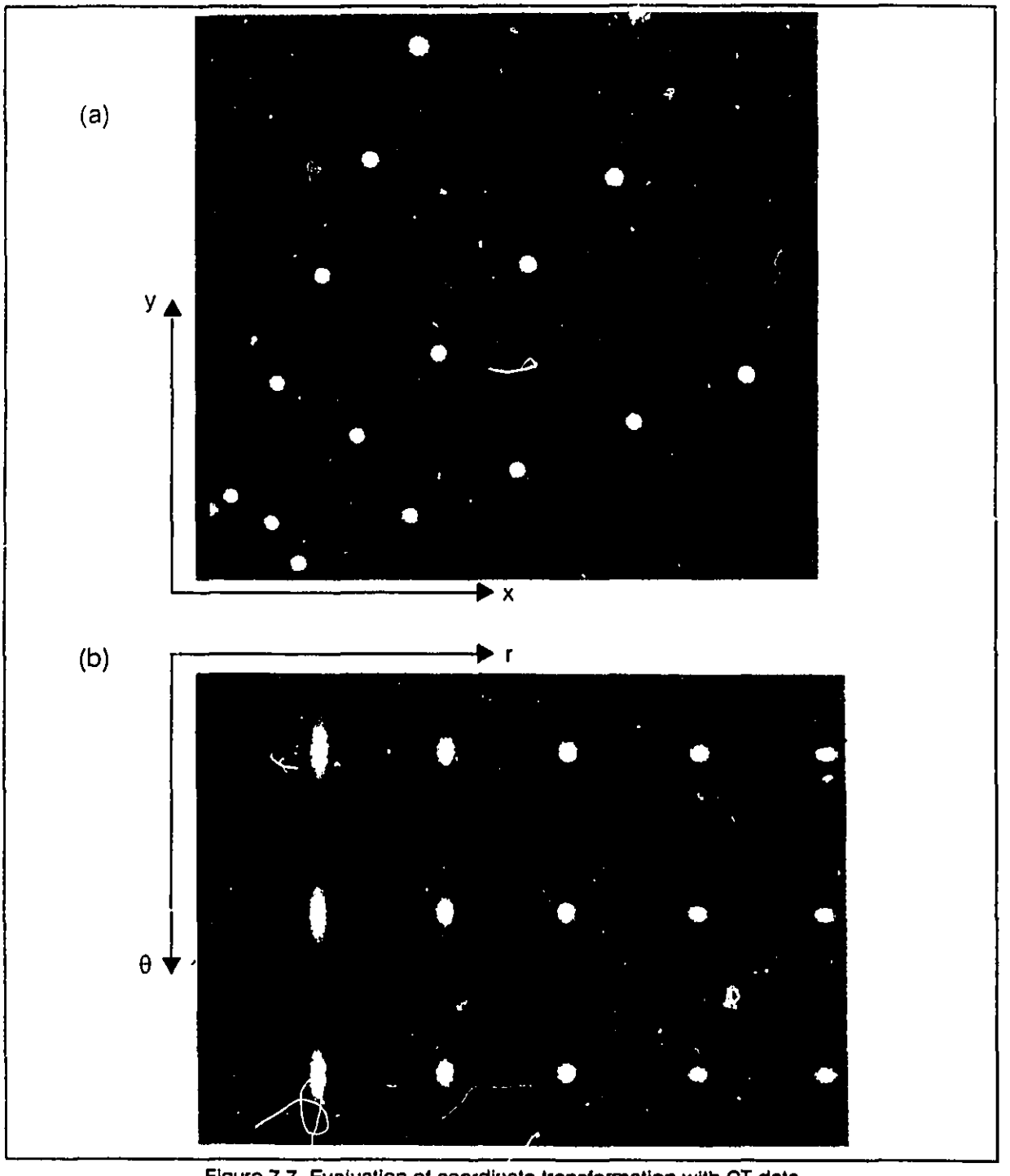

Figure 7.7 Evaluation of coordinate transformation with CT data

(a) original data in x-y frame, (b) after polar coordinate transformation, (c) in u-v frame when FWHMθ(r) is piecewise constant.

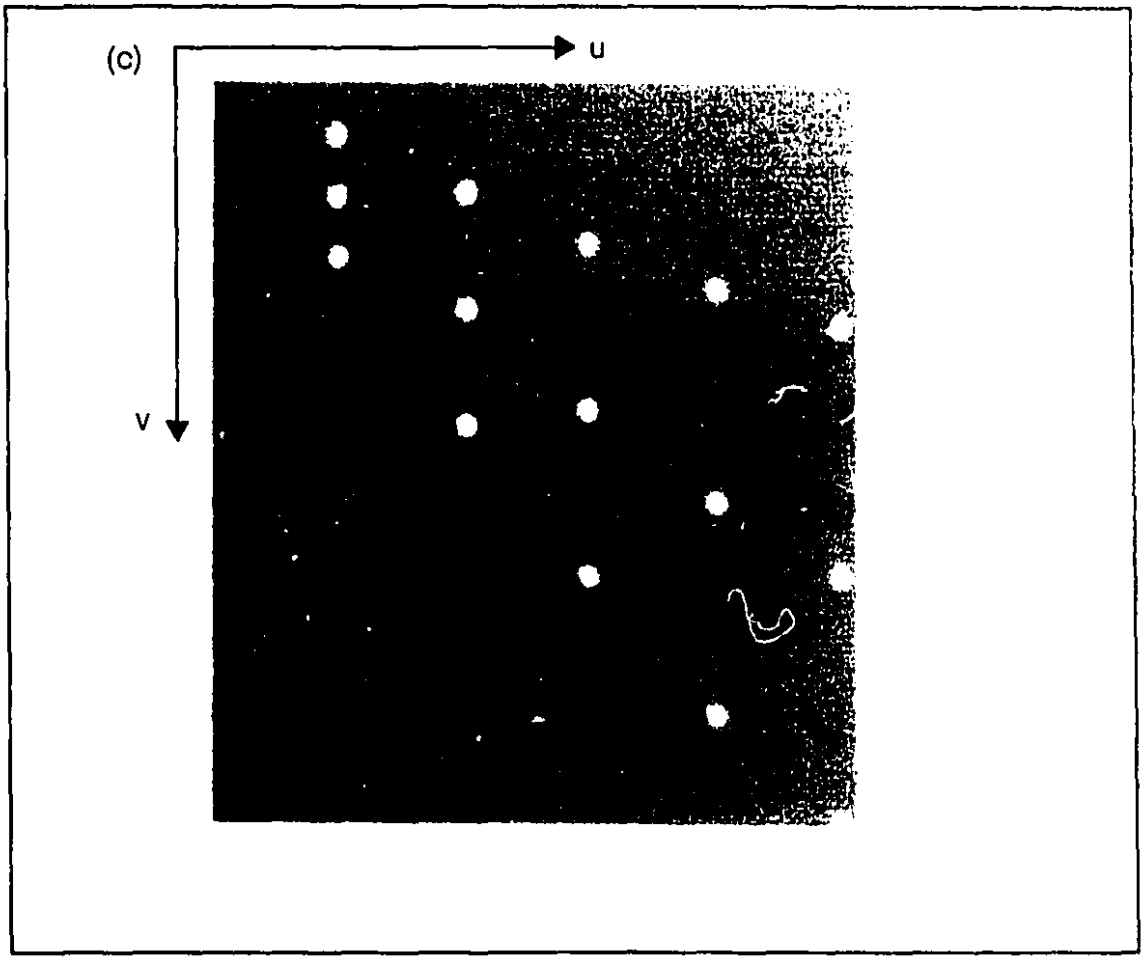

Figure 7.7 (continued)

	XY	UV	UV^{-1}	criterion 2 (2)
RADIAL	5.96	6.69	5.96	0.00
	6.00	7.01	5.98	0.02
	6.11	7.01	6.14	-0.03
	6.21	7.05	6.21	0.00
	6.34	7.06	6.42	0.08
criterion 1 (1)	0.38	0.37		
TANGENTIAL	5.89	8.23	5.89	0.00
	6.02	8.01	6.02	0.00
	6.20	8.23	6.21	-0.01
	6.54	8.07	6.55	0.01
	6.98	8.07	6.98	0.00
criterion 1 (1)	1.09	0.22		

TABLE 7.3 Evaluation results for CT data

Values in this table represent FWHM in the radial and tangential directions for radial distances given in Table 7.1. (1) maximum difference within the column (2) column XY - column UV^{-1} .

This low pass filtering effect will add to the blur already present in the image. In theory therefore, the PSF should be broader after the cascade of forward-inverse transformation than in the original image plane. The simulation results helped us quantify this effect. The last column in Tables 7.2 and 7.3 express the variation in FWHM before and after the double transformation. These differences are very small even if a nearest neighbor interpolation scheme, the worst case possible as blur is concerned, had been adopted. The values are even negative in some instances which could, but should not, be interpreted as a narrowing of the PSF as a result of the transformation! These discrepancies are probably due to numerical round-off and to residual errors in fitting the Gaussian model.

The negligible blurring effect due to interpolation was possible because great care was taken to make sure that every pixel in the original image was mapped at least once

in the transformed image. In the evaluation procedure, we minimally satisfied this requirement, governed by equations (7.13) and (7.16), by taking 15 and 18 samples across the FWHM in the radial and tangential directions for the simulated data set and 6 and 7 samples for the CT data. Indeed these values characterize the shape of the PSF in the outer limits of the region of interest. It is interesting to note that these are the values for the FWHM found in the u-v plane (see tables 7.2 and 7.3). However, this is not be surprising, and only confirms that the PSF is represented by an equal number of samples in the u-v plane.

Figure 7.8 demonstrates that failure to satisfy the mapping requirements leads to the formation of artefacts. These show up as a roughening of the edges and a circular blurring pattern.

7.5.2 Limitations

The evaluation with the simulated data showed that the proposed change of variables can be used to transform a shift-variant rotating blur system into a isoplanatic one. We saw however, that the function $FWHM_\theta(r)$, which describes the variation of the PSF width in the angular or tangential direction, had to be defined as piecewise constant. Figure 7.9 explains why this is so.

Let us consider the position of the endpoints along an axis parallel to the radial direction in the polar and (u-v) planes. These points are labelled a-d in Figure 7.9. Points with a given value of r map into constant u as with points a-c or b-d. The position along the v axis depends on the angular position of the point as well as the angular increment associated with its radial position:

$$v = \theta/\Delta\theta(r) \tag{7.23}$$

Since $\Delta\theta(r_1) > \Delta\theta(r_2)$, the angular increment decreases with radial distance (see Figure 7.3 and equation (7.4)), and the distance between points a and c along the v axis will be smaller than the interval separating points b-d. Consequently, the PSF in the (u-v) plane, which should be shift-invariant, is stretched towards the positive v axis. As can be seen in figure 7.6(b), the phenomenon is worst near the origin of the (u-v) plane (or at the center of the imaging FOV) since the variation of $FWHM_\theta(r)$ is greatest in that region (see figure 7.3).

However, if the increment $\Delta\theta$ is kept constant over a certain region, or if the function $FWHM_\theta(r)$ is piecewise constant, the method yields an isoplanatic transformation. This corresponds to dividing the polar plane into strips parallel to the v axis. Within each strip, the sampling increment is kept constant in the v direction but allowed to vary in the u

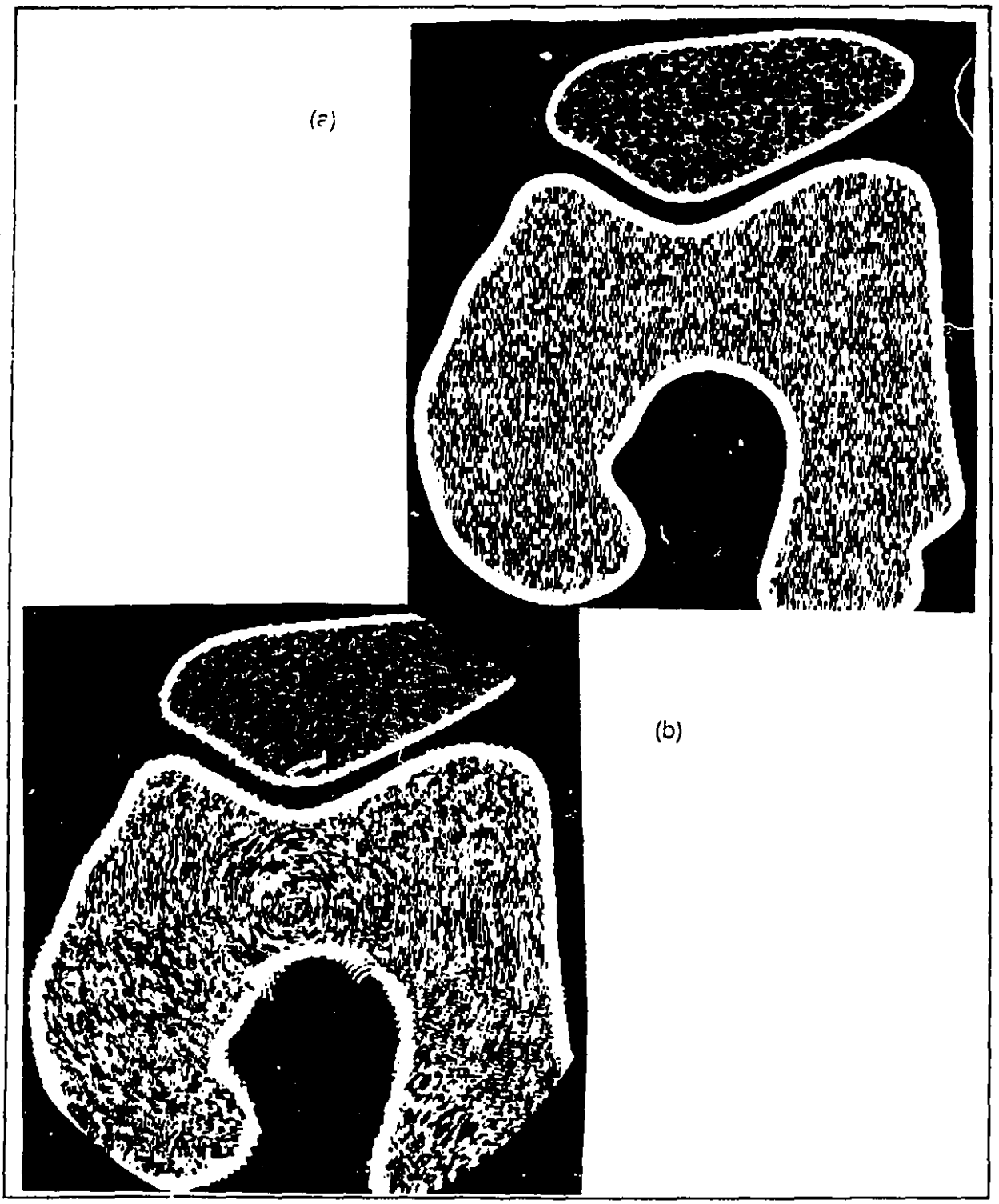

Figure 7.8 Effect of neglecting minimum mapping requirement

Simulated image of a femur in (a) original x-y frame (b) after forward-inverse transformation. Failure to meet the minimum mapping requirements results in a rotational blurring pattern. (Only the pixels within a circular region inscribed within the image are manipulated which explains why the image in (b) is clipped)

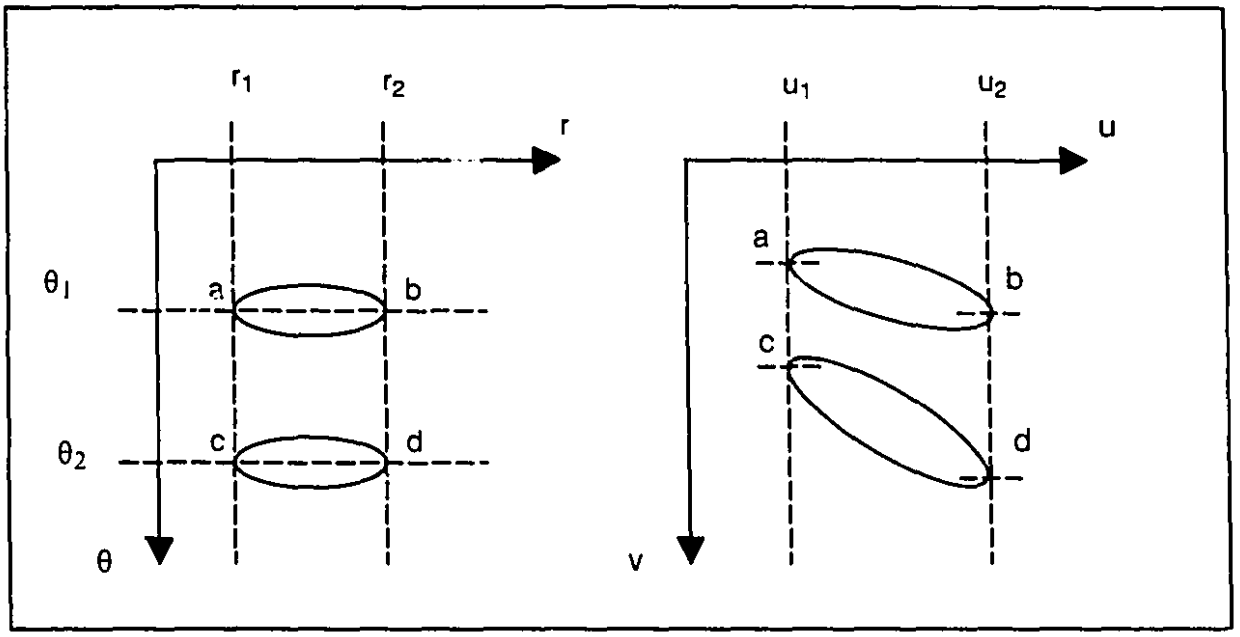

Figure 7.9 Mapping of PSF from polar (r-θ) to variably sampled polar (u-v) plane
The position of a point on the v axis is inversely proportional to the angular increment $\Delta\theta$ associated with a given radial distance. Because $\Delta\theta(r_1) > (r_2)$ when the function $FWHM_\theta(r)$ varies piecewise linearly, the distance between points a-c is smaller than points b-d. The PSF appear progressively stretched in the positive v axis.

direction. It is also equivalent to dividing the original image plane (x-y) into concentric circles. Within each circular band, the sampling increment is constant along the t axis but can change in the s direction.

Under these circumstances, the method becomes very similar to the technique of **mosaic formation**. With this last approach however, the image is usually divided into rectangular patches and the PSF assumed constant within each sub-region. We saw in Chapter 5 that the pattern of shift-variance is quite complex when expressed in a fixed orientation cartesian coordinate system. By taking advantage of the rotating blur, and dividing the image into concentric circles, it becomes easier to model the change of PSF shape with position. But most image processing algorithms are defined over rectangular domains. One solution for overcoming this limitation is to represent the image in a polar coordinate system since circular regions in the original image space are mapped into rectangular ones. The shift-variance is further reduced by adding variable sampling along the radial (r or u) axis.

The size of the region within which $\Delta\theta$ is kept constant depends largely on the error in approximating the true PSF shape in the tangential direction that one is willing to accept.

It is also a function of the rate of change in PSF shape. This method will run into serious problems if the shape changes appreciably over the width of the PSF. The same comment applies to mosaic formation.

The coordinate transformation is greatly simplified when the width of the PSF in the tangential direction varies linearly with distance from the center of the FOV. Under such conditions, the angle subtending the PSF along the **t** axis remains constant and the PSF is automatically shift-invariant in the angular direction. Variable sampling is needed only in the radial direction (**r** or **u** axes).

7.5.3 Usefulness of method

The usefulness of the method for real systems depends largely on the pixel size, the amount of variation in shape over the distance covered and the application.

The evaluation with the CT data showed that not much improvement in shift-variance is to be expected with this method especially if the variation in resolution is in the order of one pixel or less. However, as the pixels become smaller for a given region of interest, the benefits become more apparent. We also showed that the spatial variation in FWHM could be improved to a sub-pixel level. This may not be important if the application does not require this level of precision. An example would be to consider the restoration as a pre-processing step for a segmentation scheme with pixel accuracy, such as thresholding (Weszka, 1973). However, it might prove useful with sub-pixel edge detectors such as the Nalwa-Binford (Nalwa and Binford; 1987) or Laplacian of a Gaussian operators (Huertas and Medioni, 1986).

We showed in chapter 5, that of the factors considered, scanning time, or the number of projections, affected shift-variance the most. The proposed method might therefore also prove useful for the restoration of images reconstructed with missing or a limited number of views.

A limitation of the present study is that we did not demonstrate that the coordinate transformation can improve the restoration itself. For example, the Wiener filter kernel is a function of object and noise power spectra as well as the imaging system's modulation transfer function. Application of the coordinate transformation will surely modify the frequency content of these entities. It is possible therefore that the performance of the restoration operator could be affected accordingly. The manner in which the coordinate transformation affects any given restoration procedure merits further attention and is considered for future work. However, the study presented here showed that, under the circumstances mentioned in the previous paragraphs, it is an endeavor worth pursuing.

Furthermore, the fact that the method has been successfully applied to optical degradations is encouraging.

7.6 Conclusions

We adapted a coordinate transformation method, originally developed for optical systems, for an isoplanatic representation of systems exhibiting a shift-variant pattern similar to 3rd generation CT scanners. The technique calls for a variable sampling of the original image in the angular and radial directions. The functions describing the variable increment size were expressed in terms of the spatial variation of the system's resolution, a characteristic which can be easily estimated.

We also developed a new evaluation procedure capable of quantifying the improvement in shift-variance. A substantial amelioration can be expected provided that the change in angular increment be piecewise constant and the variation in PSF be larger than the pixel size. The simulation also brought out a limitation of the method which had never been reported in the literature. In order for the PSF to be isoplanatic in the transformed plane, the sampling rate in the tangential direction must be defined in a piecewise constant manner.

Another point which had not received any attention in the literature is the issue of interpolation. We noticed that the blurring associated with interpolation can be kept very small if a simple mapping requirement is respected: every point in the original image must be represented at least once in the transformed plane. We mathematically formulated this requirement with two simple criteria. Failure to meet these criteria results in a rotational blurring pattern and a roughening of the edges.

The evaluation procedure was used on real CT data and showed that changes in PSF width are small and improvements marginal if one wishes to manipulate the image only at the pixel level. However, if sub- pixel image processing techniques are envisioned, this method can be used to improve shift-variance from the order to the pixel to sub-pixel levels. Nonetheless, the evaluation procedure outlined in this chapter allows the user to quantify the improvement and assists him/her in deciding if it is worthwhile applying a coordinate transformation to improve isoplanicity.

To simplify the restoration algorithm, it is common either to ignore the problem of shift-variance, or to claim that the changes in PSF shape are small enough to be ignored. However, before making such a hypothesis, the user should quantitatively evaluate the shift-variance and use a procedure such as the one presented here to substantiate his/her claims.

CHAPTER 8
RECOMMENDATIONS FOR SEGMENTATION

8.1 Introduction

Before a 3D surface model can be constructed, pertinent information must be extracted from the images, i.e. images must be segmented. Even though accurate segmentation is paramount to the elaboration of a good 3D model, very little effort has been devoted to this task. It is not uncommon to find articles on 3D reconstruction that do not even mention how the geometric input information was obtained.

The threshold and Laplacian of a Gaussian (LOG) operators are two popular segmentation schemes, used both in the context of general and medical imaging. The goal of this chapter was to explore the limits of these techniques, based on the shape of the PSF and on the noise properties of CT scanners. We also theoretically justified certain experimental results obtained with the threshold operator.

General segmentation principles are introduced in section 8.2. Sections 8.3 and 8.4 are devoted to thresholding and LOG filtering respectively. The major results are summarized in section 8.5.

8.2 Underlying principles

In mathematical terms, segmentation can be viewed as a procedure that divides an image R into subregions R_1, ... R_n such that (Fu and Mui, 1981):

1) $\bigcup_{i=1}^{n} R_i = R$ (segmentation must be complete)

2) R_i is a connected region (a region must be composed of contiguous points)

3) $R_i \bigcap R_j = \varnothing \quad \forall\, i,j \;\; i \neq j$ (regions must be disjoint)

4) $P(R_i) = True \;\; i = 1,n$ (points within a region share a common property)

5) $P(R_i \bigcup R_j) = False \quad i \neq j$ (separate regions have different properties)

One can see from this definition that properties must be clearly defined if a segmentation approach is to be successful. These properties can have a purely mathematical formulation but are often complemented by heuristic criteria. A priori knowledge can also be used to assist the segmentation process.

Underlying most segmentation schemes, although seldom mentioned, is a model of the edge. A common model is the step edge: adjacent objects are characterized by an abrupt change in grey level. This model is well suited to the study of the muscolo-skeletal system with CT scanners since adjacent tissues are characterized by distinct x-ray attenuation values.

8.3 Thresholding

According to Gonzalez and Wintz (1987), thresholding is one of the most important techniques of image segmentation in general. Its popularity has been transposed to medical images. Indeed, this method is by far the most common to extract bony structures from X- ray CT images. Furthermore, many region growing (Rhodes, 1979) and region splitting or octree encoding algorithms (Meagher, 1982; Koltai and Wood, 1986) rely on binary images. This makes us believe that thresholding is also used as a pre-processing step for these segmentation algorithms although the authors did not mention so explicitly.

The accuracy with which a detected edge is localized is highly depended on the value of the threshold, system's blurring characteristics and the spacing between neighboring edges. These issues will be discussed after the principles underlying the threshold operator have been presented.

8.3.1 Background

Foundation: The method's appeal resides in its simplicity: all pixels with a grey level or CT number above a certain threshold are assumed to belong to a given object. All the pixels below the threshold are required to represent the background or another object. More often than not, the resulting image is binary, i.e. the segmented pixels can only assume a value of 1 if they are assigned to the object or 0 otherwise.

Most efforts have been directed to select thresholds in an unsupervised fashion (Weszka, 1978; Clos and Sarieh, 1990). Most methods make use of the grey level histogram or graph of the number of pixels versus grey level. It is assumed that grey levels related to different objects are concentrated about a mean value and form distinctive peaks or modes. The problem thus becomes one of choosing a threshold that will separate the different modes. As a general rule, the threshold is chosen in the valleys, between the peaks. This approach minimizes the probability of misclassifying a pixel since the grey levels in these areas are relatively unpopulated (Fu and Mui 1981).

Apart from it's ease of implementation, once the threshold has been identified, the greatest benefit of thresholding is its relative immunity to noise when compared to edge

detectors. (As we will see in section 8.4, edge detectors rely on derivative operators. These act as high pass filters and therefore amplify noise).

There are a number of disadvantages however. Assumptions must be made regarding the statistical distribution of the grey level histogram as well as the number of nodes. Secondly, no spatial information is used to select to threshold. As a result, there is no guarantee that the segmented regions are contiguous. Furthermore, features other than grey level are image dependent and can be difficult to identify. Finally, threshold selection is difficult in the presence of flat broad valley. This situation is common in X-ray CT images of the musculo-skeletal system since the X-ray attenuation coefficient of bone is much larger than the surrounding tissues. Weszka et al. (1974, 1975) and Rosenfeld and Davis (1977) proposed different methods to sharpen the valleys.

Thresholds for bone segmentation: Different thresholds, either global or local, have been proposed in the medical imaging literature to separate bone from other tissues. A threshold is global if its selection depends on the grey level distribution of the entire image. However, if some property in the neighborhood of the pixel is involved, the average for example, the threshold is said to be local.

Vannier et al. (1983) and Artzy et al. (1981) selected a global threshold equal to the average CT number of bone. This is equivalent to placing the threshold at the center of a peak in the histogram (assuming the peaks are symmetric). We will show in section 8.3.2 that this leads to a bias in the true edge position and is therefore not recommended. More recently, Toennies et al. (1990) claimed than any threshold less than the minimum attenuation coefficient of bone and higher than the coefficient of neighboring tissue is acceptable. This is to say than the threshold can be selected anywhere within the valley. While this is preferable to choosing the central peak value, the bias in edge position will vary depending on where the threshold is chosen within the valley.

An alternative approach consists of defining a local relative threshold equal to a percentage of the difference between the maximum and minimum values in the local edge profile. Based on a study by Rothuizen et al. (1987), which will be discussed in more depth in the next two sections, Tümmler et al. (1989) used a relative threshold of 50% to 55%. For their part, Klotz et al. (1989) empirically chose a value of 60% because, according to the authors, it best matched visual perception of the edge position.

Accuracy: Fu and Mui mentioned in 1981 that evaluating any segmentation algorithm is difficult because of a lack of criteria for defining success apart from the percentage of misclassified pixels. Not much progress has been made since then, but we have found two studies concentrating on the accuracy of the relative threshold operator.

Using the high resolution algorithm on a Siemen Somaton DR3 scanner, Rothuizen et al. (1987) assessed the accuracy of global and local relative thresholding methods. In a phantom study, PVC tubes of known thickness were scanned in air. One of the tubes was filled with calcium chloride to simulate trabecular bone. They encountered larger errors in average tube diameter estimates with the global threshold especially when the concentration of calcium chloride was varied. A 45 % relative criteria which the authors found "approximately optimal" for tubes with a wall thickness of 9 mm underestimated the average tube diameter for a wall thickness of 2 mm. For thin walled tubes, a 60% criteria provided better results.

In the same study, a proximal femur was imaged in a variety of media and later sectioned at the corresponding locations. They found that the accuracy of the global criterion was markedly affected by the bone environment, region of scanning and the type of contour to be detected (inner or outer). Errors in outer diameter as large as 3.9 mm and 1.6 mm were encountered for the diaphysis (shaft) and metaphysis (wider part at the end of the shaft) respectively and 3.6 mm and 5.8 mm for the inner diameter. The optimal relative threshold level, i.e. the one for which the error was minimal, corresponded to 45% and 50% for the diaphysis and metaphysis respectively. Relative thresholds resulted in better or similar results when compared to the global criterion except for the inner contours in the metaphyseal region where both approaches yielded disappointing results. The authors did not provide any reasons to explain this observation nor did they theoretically justify their results.

In a more recent but similar study, Sumner et al. (1989) found that the optimum local absolute threshold varied substantially for the periosteal (outer) and endosteal (inner) contours and depending on the environment surrounding the bone. The authors mention that the absolute thresholds roughly correspond to a 50% criteria. They also estimated that the use of an incorrect threshold for both surfaces can lead to errors of cortical bone thickness in the order of 30%.

From this short literature review, we conclude that the value of a global threshold changes depending on the material surrounding an object and that selecting an incorrect threshold can lead to large errors in edge position. A relative threshold of about 50% appears optimal but this criteria is affected by the size of the object.

These results are exclusively founded on experimental observations. In the next section, we will show why and under which circumstances the 50% relative threshold is optimal. We will also interpret some of these experimental results in terms of the characteristics of the PSF and the noise properties in section 8.3.3.

8.3.2 Analysis

Theoretical relative threshold: We will start by finding the optimal theoretical relative threshold, i.e. the one corresponding to the edge position. Figure 8.1 illustrates the edge profile of a 1D isolated step edge blurred by a Gaussian PSF. For a linear system and in the absence of noise, the relationship is given by:

$$I_b(x) = I(x) * G(x) \tag{8.1}$$

where I(x): unit step edge located at $x_0 = 0$
$I_b(x)$: imaged and blurred step edge
G(x): Gaussian PSF of standard deviation σ.

Expanding, we find:

$$I_b(x) = \frac{1}{\sigma\sqrt{2\pi}} \int_{\infty}^{-\infty} I(x)\, e^{\frac{-(x-u)^2}{2\sigma^2}}\, du \tag{8.2}$$

$$I_b(x) = \frac{1}{\sigma\sqrt{2\pi}} \int_{0}^{\infty} e^{-\frac{u^2 - 2ux + x^2}{2\sigma^2}}\, du \tag{8.3}$$

Since:

$$\int_{0}^{\infty} e^{-(ax^2 + bx + c)} dx = \frac{1}{2}\sqrt{\frac{\pi}{a}}\, e^{\frac{b^2 - 4ac}{4a}}\, erf\frac{b}{2\sqrt{a}} \tag{8.4}$$

equation (8.3) simplifies to:

$$I_b(x) = \frac{1}{2}\left[1 + erf\left(\frac{x}{\sigma\sqrt{2}}\right)\right] \tag{8.5}$$

where erf(x): error function of x.

The right hand term of equation (8.5) is the expression for the cumulative distribution function (CDF) of a Gaussian random variable of zero mean and standard deviation σ, i.e. $\phi(x/\sigma)$. In terms of parameter p or the FWHM used in the previous chapters to define the Gaussian function, equation (8.5) becomes:

$$I_b(x) = \frac{1}{2}\left[1 + erf\,(px)\right] \tag{8.6}$$

$$I_b(x) = \frac{1}{2}\left[1 + erf\left(\frac{2\sqrt{-\ln(1/2)}\,x}{FWHM}\right)\right] \tag{8.7}$$

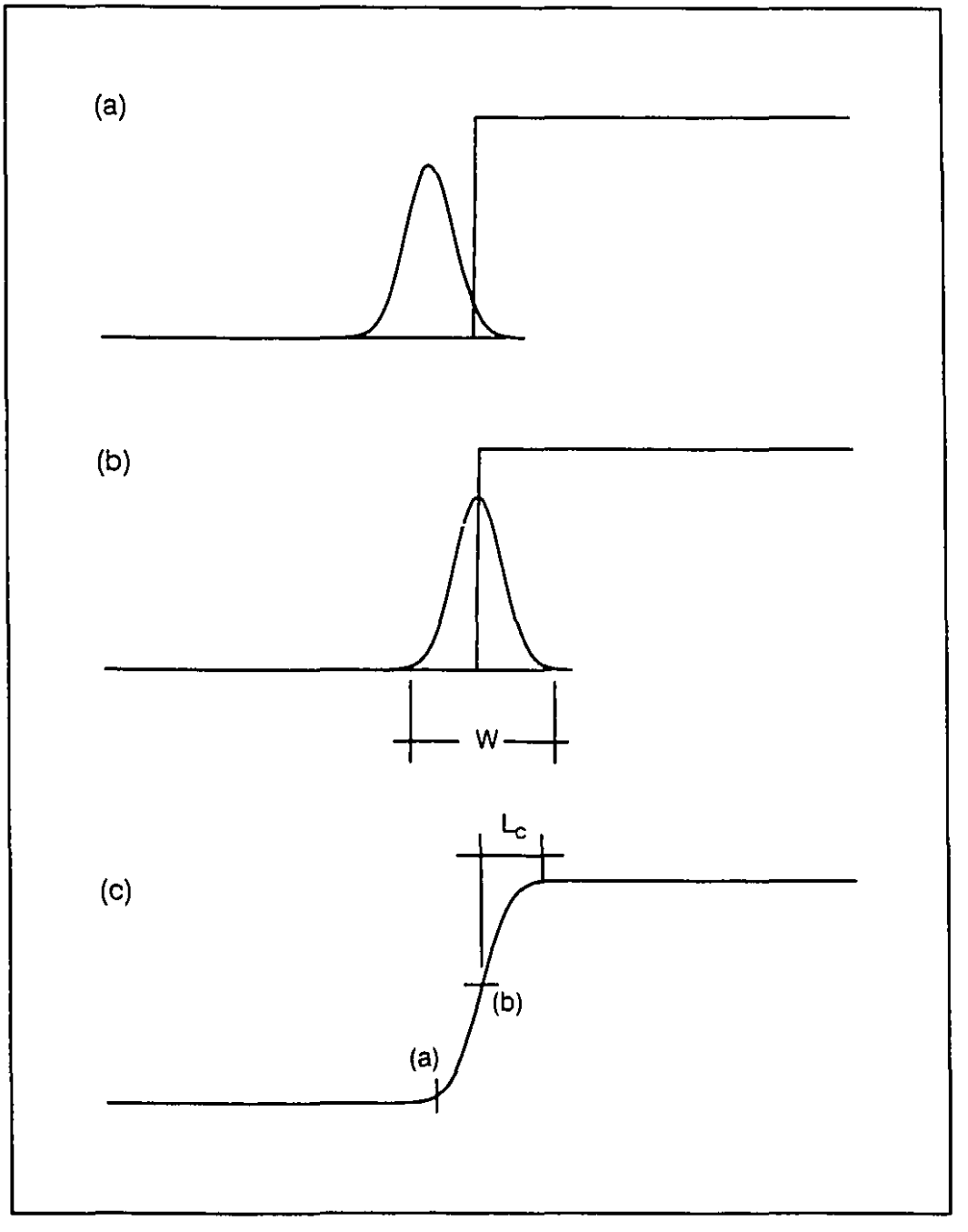

Figure 8.1 Blurring of an isolated edge

An interface between adjacent tissues is modelled by a step edge. The noiseless image is given by the convolution of the step edge with the PSF as shown in (a) and (b). The value of the edge profile at a given position is proportional to the area of the PSF under the step (c). The length L_c over which the edge is blurred to one side is equal to half the width (W) of the PSF

By consulting tables of the CDF for a Gaussian distribution, one easily verifies that $I_b(0) = 0.5$ and conclude that the optimal relative threshold is 50%.

This is readily visualized in Figure 8.1. The value of the blurred edge profile at a given position x is proportional to the area of the PSF centered at x which falls under the step. At the position $x = 0$, half the PSF is under the step. This is true for any symmetric PSF.

From this analysis, we conclude that the 50% relative threshold criterion is optimal for an isolated 1D step edge blurred by any axially symmetric PSF.

2D edges: Until now, we have only considered 1D edges. We now ask ourselves if the above statement is also valid for 2D edges? We could turn the question around and ask if there are any situations where 2D edges behave like 1D edges? To answer this question, let us consider a straight 2D edge $e(x,y)$. Without loss of generality, let us also orient the edge vertically, i.e. $e(x,y) = e(x,0)$. Neglecting noise, the image of the edge will be given by the convolution of the edge with a (2D) PSF:

$$e(x,0) ** PSF(x,y) = \int_{-\infty}^{\infty} \int_{-\infty}^{\infty} e(X,0)\ PSF(x-X, y-Y)\ dX\ dY \tag{8.8}$$

Since the limits of integration are independent:

$$= \int_{-\infty}^{\infty} e(X,0) \left[\int_{-\infty}^{\infty} PSF(x-X, y-Y)\ dY \right] dX \tag{8.9}$$

$$= \int_{-\infty}^{\infty} e(X,0)\ LSF(x-X)\ dX \tag{8.10}$$

$$= e(x,0) * LSF(x) \tag{8.11}$$

$$= e(x) * LSF(x) \tag{8.12}$$

Equation (8.12) tells us that the image of the edge could also have been obtained by convolving a 1D edge, having the same profile as the 2D edge, with the line spread function (LSF). Or in other words, that a straight 2D edge behaves like a 1D edge.

We could also consider a straight 2D edge as one having an infinite radius of curvature. It is therefore reasonable to assume that a curved 2D edge could also be considered a 1D edge as long as its radius of curvature was (much) larger that the extent of the PSF. More work is required to determine limits on edge curvature with respect to the size of the PSF. Research in this direction could be guided by the work of Berzins (1984)

who studied the interaction between the Laplacian of a Gaussian (LOG) operator and edge geometry (see also section 8.4.1).

Edge interaction: As shown in figure 8.1 (c), the distance L_c over which the edge is blurred to one side is theoretically infinite since the area under the normalized Gaussian curve is equal to 1 only for infinite values of x. However, in a noisy and quantitized environment, the cumulative distribution function rapidly reaches a value which can be considered equal to 1. The value of L_c is found by looking up the argument of the CDF corresponding to a value close to 1. For example, given a Gaussian PSF, if a 1% error in step size can be tolerated:

$$If \quad I_h\left(\frac{2\sqrt{-\ln(1/2)}\ L_c}{FWHM}\right) = 0.99 \tag{8.13}$$

$$then \quad \frac{2\sqrt{-\ln(1/2)}\ L_c}{FWHM} = 2.33 \tag{8.14}$$

For a FWHM of 1.20 mm and 1.50 mm, Lc is equal to 1.19 mm and 1.48mm respectively. Graphically, as shown in figure 8.1, we can see that L_c is equal to half the width of the PSF, where the PSF width (W) is defined as the distance necessary for the area under the PSF curve to be (almost) equal to 1. In the case of the Gaussian function, W/2 is almost equal to FWHM , and to the HWZC for the damped cosine function. Therefore, as a rule of thumb, we can conclude that the distance over which an isolated edge is blurred to one side is close to the resolution of the imaging system. We defined resolution earlier as the minimum distance separating two point sources such that they can be distinguished when imaged.

Since edges are blurred over a certain (finite) distance, closely spaced edges will interact with one another. We now ask ourselves how closely two step edges can be located before the 50% criteria fails. Figure 8.2 illustrates the graphic convolution between double step edges of varying width D with a normalized symmetrical PSF of width W.

1) $D < W$: In the case where the PSF extent is larger or equal to the step width (see figure 8.2 a and b), the whole PSF fits under the step, and the maximum in the blurred edge profile is equal to the height H of the step edge. At the true edge position ($x = 0$; $x = D$), the value of the blurred edge is equal to half the step height H/2. Because the maximum value in the blurred edge profile is a good estimator of the (unblurred) step height, the 50% criteria is respected.

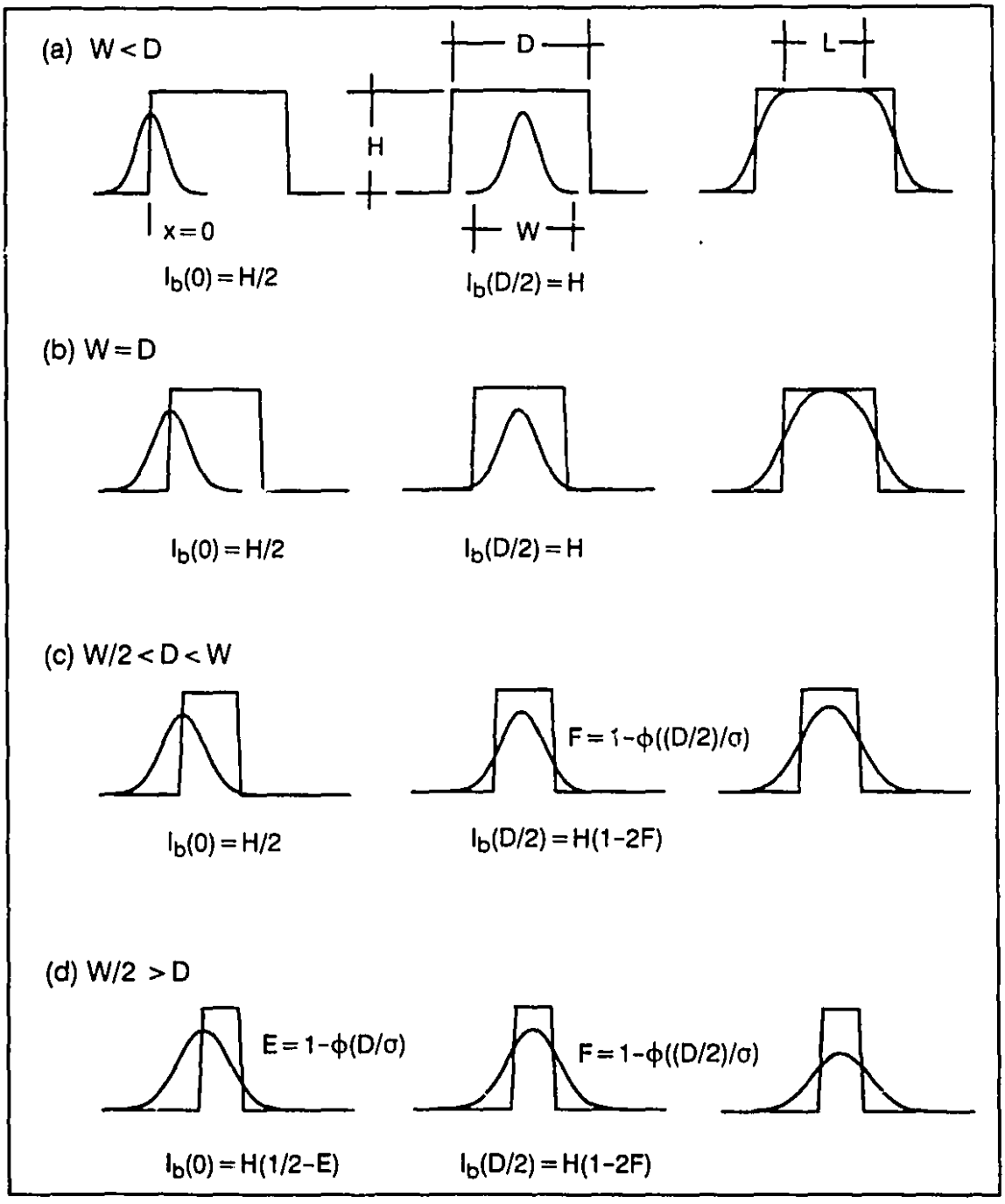

Figure 8.2 Blurring of a double step edge

(a) and (b):When the extent of the PSF (W) is smaller than the double step width (D), the value of the blurred edge profile at the true edge position is equal to half the step height (H). Furthermore, the maximum in the blurred edge profile is a good estimator of H and the 50% relative threshold criterion is respected. When W > D, either the second (c) or both of these conditions (d) are invalidated, and the 50% criterion no longer holds.

2) $W/2 < D < W$: Figure 8.2 (c) illustrates the situation where the width of the step edge is larger than half the PSF width but smaller that its full width, as shown in figure 8.2 (c). The blurred edge profile at the true edge position is also equal to half the (unblurred) step height. However, because the PSF no longer fits completely under the step, the blurred profile maximum is smaller than the step height. Application of the 50% criteria on the blurred edge will result in a wider step estimate since the corresponding selected absolute threshold will be lower than H/2.

3) $D > W$: When the step width is smaller than half the PSF width (see figure 8.2 d), the situation degenerates even more since the value of the blurred edge profile at the true edge position is no longer equal to half the step height.

8.3.3 Discussion

One of the implications of the 50% criteria is that the absolute threshold level will vary depending on the objects in contact. For example, the absolute threshold for a bone/fat interface will be different than a bone/muscle interface: to respect the 50% relative criteria, the absolute threshold will be lower for the fat since the CT number of fat is lower than muscle. This explains why the optimum absolute threshold varied depending on the scanning environment in both experimental studies presented above. Furthermore, using a global threshold will lead to erroneous edge location if a giving object is in contact with more than one tissue type. Local variations in bone density, mineral content etc. could further compound errors for a given interface.

Another consequence is that selecting the average CT value of bone as the global threshold, as suggested by Artzy et al. (1981) and Vannier et al. (1983), results in a detected edge displaced towards to bone side of the interface by an amount comparable to the system's resolution. Furthermore, because the system is shift-variant, the bias will depend on the position and orientation of the edge.

We suspect that deviation from theory obtained by Rothuizen et al. (1989) in the diaphyseal region (45%) might have been due to the choice of high resolution filter as a means of forming the images. The higher noise values as well as the over- and under-shoots produced by the negative tails usually associated with this type of filter both hinder the estimation of the minimum and maximum values in the edge profile. A proper choice of threshold combined with low noise levels such as those offered by the smoothing filter, would likely outweigh the limited resolution gain of the high resolution filter, although this remains to be verified.

The phenomenon of edge interaction could explain why a relative threshold of 60% was judged optimal by Rothuizen et al. for the thin walled phantom study. By selecting a higher relative threshold, they approximated the absolute threshold corresponding to half the unblurred step more closely.

8.4 Laplacian of a Gaussian operator

The Laplacian of a Gaussian (LOG) operator is a member of a class known as edge detectors. These methods are based on the detection of discontinuities in the grey level profiles found in the vicinity of edges. The formulation of the LOG operator combines a differentiation step (the Laplacian) with (Gaussian) smoothing. An important issue to consider when implementing the LOG operator, is selecting the Gaussian standard deviation. This subject will be considered after having understood the principles underlying edge detectors.

8.4.1 Background

Edge detectors, when based on the step edge model, state that the position of an edge corresponds to extrema of the first derivative or to the zero-crossing of the second derivative in the direction the of gradient (De Michaeli et al., 1989; Clark, 1989; Luncher and Beddoes, 1986; Torre and Poggio, 1986).

Regularization: Edge detectors are ill-defined in the presence of noise, i.e. the errors (noise) in the edge profile are amplified, hindering the detection of maxima or zero-crossings. Since the true solution cannot be obtained from the imperfect (noisy) data, the problem must be regularized. A common regularizing approach is to introduce a compromise between fidelity to the data and fidelity to some a priori knowledge about the solution (Demoment, 1989). In this case, the a priori knowledge is that the solution should be "smooth". Torre and Poggio (1986) proposed two regularization schemes: functional approximation and low pass filtering.

Low pass filtering can be performed by different type of filters. After a rather involved analysis, Torre and Poggio (1986) concluded that bandpass filters, while good regularizers, suffer from (theoretical) infinite support which can lead to implementation problems. On the other hand, support limited filters are only marginally useful in reducing the effect of noise. Minimal uncertainty filters, such as the Gaussian function, offer good regularization and are optimal in the sense that they minimize the spread of the filter in both spatial and frequency domain. Claims of optimality have also been made by Canny (1986) and Shanmugan et al. (1979). However, Torre and Poggio point out that in both cases, the

optimal filter can be approximated by a combination of Gaussian smoothing and differentiation.

A very common approach to edge detection is therefore to smooth the the image with a Gaussian filter of given standard deviation σ and then differentiate. We now turn our attention to how differentiation can be carried out.

Gradient: The gradient $\nabla f(x,y)$ is a first order directional derivative given by:

$$\nabla f(x,y) = \begin{bmatrix} \nabla_x \\ \nabla_y \end{bmatrix} = \begin{bmatrix} \delta f/\delta x \\ \delta f/\delta y \end{bmatrix} = f_x \bar{e}_x + f_y \bar{e}_y \qquad (8.15)$$

Torre and Poggio (1986) mentioned that two direction dependent derivatives are sufficient to detect all edges in an image, a condition satisfied by the gradient. Each derivative, Δx and Δy requires a separate convolution, thereby increasing processing time. Furthermore, because Δx responds more strongly to vertical edges while horizontal boundaries are detected by Δy, the application of each filter separately results in disjointed elements of edgels. By combining the output of both filters, edges appear more complete but are rarely closed. Detection must be followed by a linking procedure, either parallel or sequential, to insure edge continuity. We have found no accounts of parallel linking algorithms in the medical image literature but the work of Liu (1977), Herman and Liu (1979), Artzy (1981) and Udupa (1982) are examples of the sequential boundary tracking.

Laplacian of a Gaussian: The simplest linear, isotropic second derivative operator is the Laplacian:

$$\nabla^2 f(x,y) = \delta^2 f/\delta x^2 + \delta^2 f/\delta y^2 \qquad (8.16)$$

Being isotropic, it produces closed curves, or curves that terminate at the boundary of the image and therefore yields a partioned or segmented image in a single step, a distinct advantage over gradient based methods.

Furthermore, it commutes with the Gaussian smoothing filter, both operations being linear. Both steps can even be combined in a single operation: the Laplacian of a Gaussian filter. Its mathematical formulation is given by:

$$LOG(x,y) = \frac{1}{\pi \sigma_{LOG}^4} \left(\frac{x^2 + y^2}{\sigma_{LOG}^2} - 1\right) e^{\frac{-(x^2 + y^2)}{2\sigma_{LOG}^2}} \qquad (8.17)$$

Its other advantages include its ease of implementation, and its approximation by the difference of two Gaussians (Hildreth, 1983; Bomans et al. 1990). It can also be represented as a product of one dimensional functions, a property that can be used to

decrease the number of operations necessary for convolution (Huertas and Medioni, 1986). Furthermore, by approximating the output of the LOG filter in the vicinity of an edge with a proper function (even linear functions are adequate), the zero-crossing can be localized with sub-pixel accuracy (Huertas and Medioni, 1986).

When implementing the LOG operator, the user should be aware of the following limitations. It is only when edges are straight and (infinitely) long that the zero crossings of the Laplacian and the second derivative in the direction of the gradient coincide. This can be inferred from the following equation (Clark, 1989):

$$\nabla^2 f = \frac{\delta^2 f}{\delta n^2} + |\nabla f| \kappa \tag{8.18}$$

where κ: curvature

$\frac{\delta^2 f}{\delta n^2}$: second derivative in the direction of the gradient

This last term is given by:

$$\frac{\delta^2 f}{\delta n^2} = \frac{f_x^2 f_{xx} + f_x f_y f_{xy} + f_y^2 f_{yy}}{f_x^2 + f_y^2} \tag{8.19}$$

It can be seen from equation (8.18) that the larger the curvature, the more the Laplacian deviates from $\delta^2 f/\delta n^2$ and therefore the more the detected edge will be displaced with respect to the true edge. Berzins (1984) theoretically studied the magnitude of error due to deviation of edge models from the ideal infinite straight edge and concluded that the edge displacement could be much less that the filter standard deviation σ_{LOG} under certain conditions. Concerning edge geometry, these conditions include:

1) the length of the edge and its radius of curvature must be large compared to σ_{LOG}.

2) the distance to the nearest sharp corner must be large compared to θ/σ_{LOG} where θ is the angle of the corner in radians.

Just as a zero crossing of the Laplacian does not always correspond to that of $\delta^2 f/\delta n^2$, a zero crossing of a second derivative does not always coincide with an extrema in the first derivative. Inflection points will be detected by a zero crossing scheme but will not affect the performance of extrema based methods. Therefore, more false edges are to be expected by the former.

Medical imaging literature: The LOG operator was recently used on sets of 3D magnetic resonance images (Kübler and Gerig, 1990; Bomans et al. 1990). Bomans et al. selected

the "optimal" value for σ_{LOG}, i.e. one that sufficiently smooths noise without unduly distorting the edges, on a visual basis. They also used a post-processing step (morphological operators) to relocate edges more accurately.

Based on visual inspection, the authors of both studies concluded that this segmentation method yielded 3D reconstructed images close to anatomical reality. Kübler and Gerig further mentioned that the LOG operator showed significant differences when compared to a region filling algorithm without mentioning which method yielded the most accurate results. Nor did they specify the Gaussian standard deviation of the LOG operator nor the properties used to control the region growing algorithm.

8.4.2 Discussion

Canny (1986) and Bergholm (1987) noted that edge detectors face the conflicting goal of producing low error rates, i.e. edges should not be missed and no false edges detected, while accurately locating the edges. The parameter controlling the balance between detection and localization is filter size: the larger the operator, the more noise is smoothed but the more edges are distorted. This trade-off is governed by the standard deviation of the Gaussian filter.

Lunger and Beddoes (1986) described a procedure for selecting this parameter based on the type of edges, their intensity, the amount of blur and sampling considerations. They also provided a means for estimating the expected error (standard deviation) of the zero crossing about the true edge. However, this study was based on the assumption of white Gaussian noise which is not valid for X-ray CT images and therefore their analysis cannot be used for CT images.

We wish to point out that the choice of σ_{LOG} should take into account not only the amplitude of the noise but also its frequency distribution. Figure 8.3 shows the estimated NPS for the smoothing, head edge enhancement and high resolution reconstruction filters along with the frequency structure of the LOG operator generated for different values of σ_{LOG}. One can only appreciate the similarity between the two entities. Choosing σ_{LOG} such that the maximum of the LOG coincides with the maximum in the NPS, defeats the purpose of smoothing prior to detection since the noise will not be filtered out of the signal (it could even be amplified). With CT images, the problem of selecting a value for σ_{LOG} must therefore not only consider the balance between detection and localization but also take the frequency structure of the noise into consideration. Unfortunately, more work is required to evaluate the interaction between these factors since this problem has never received any attention.

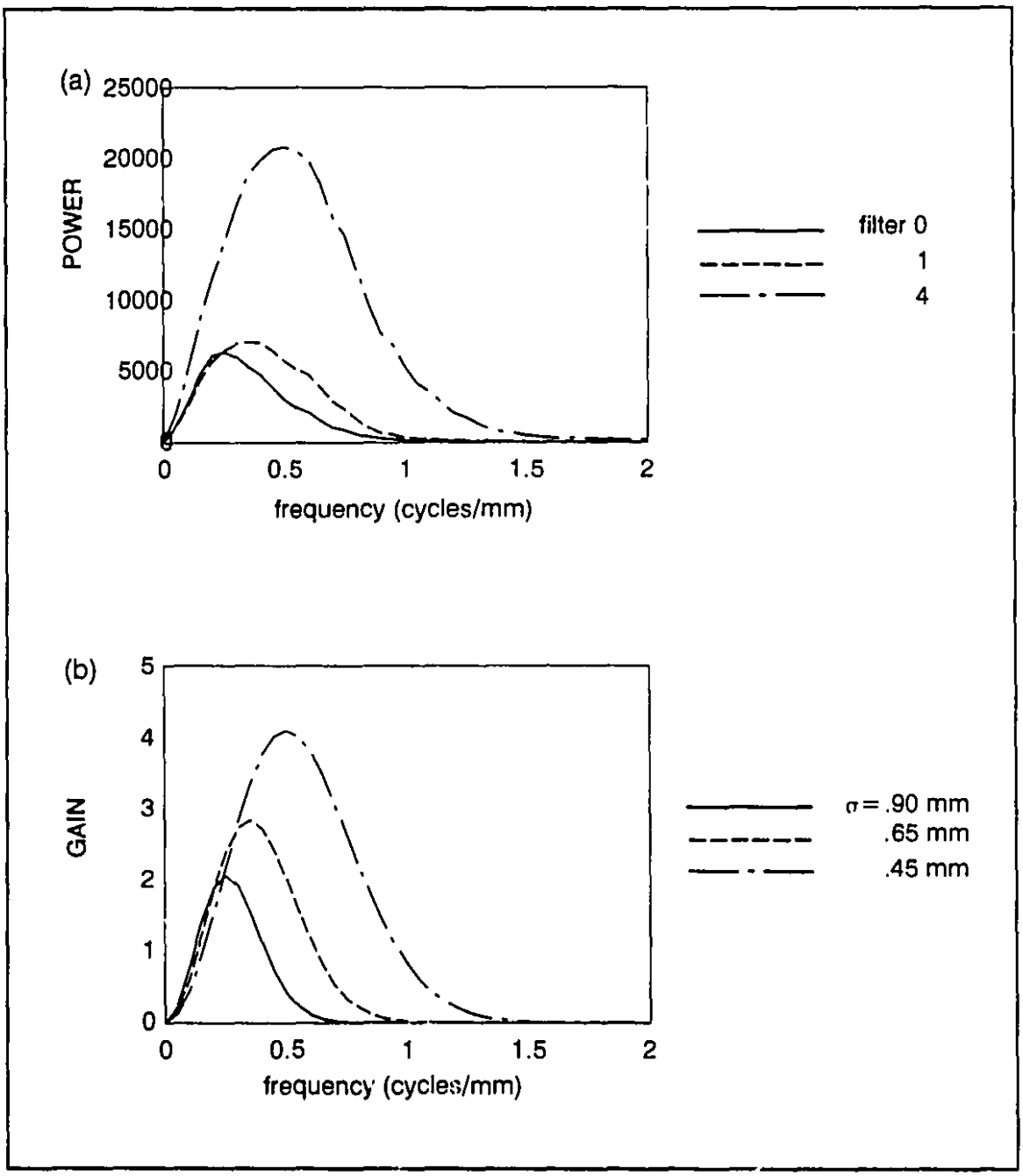

Figure 8.3 Comparison of noise power spectrum and frequency characteristics of LOG operator

Both the NPS of a CT scanner (a) and the MTF of the Laplacian of a Gaussian edge detector (b) exhibits very similar bandpass characteristics. When selecting the smoothing factor of the LOG operator (σ_{LOG}), it is therefore important to take the noise characteristics, which vary with the image reconstruction filter, into account.

The phenomenon of edge interaction, which can effect the performance of the threshold operator, is even more important for the Laplacian of a Gaussian filter. The additional blurring action of the Gaussian low pass filter incorporated in the detection scheme is superimposed on the blur already in the image thereby increasing edge interaction. The user should also keep this limitation in mind when choosing a value of σ_{LOG}.

8.5 Conclusions

Many of the segmentation methods found in the general literature have been used to provide data for the reconstruction of 3D models of the human anatomy. However, when implementing these methods, the characteristics of the imaging system are rarely, if ever, considered. As a result, operator parameters are often chosen empirically, resulting in sub-optimal use and/or misplaced edges.

We took a closer look at two popular segmentation methods, the threshold and Laplacian of a Gaussian operators. In doing so, we explicitly took the shape of the point spread function and noise properties into account. Throughout our analysis, we modelled the interface between adjacent tissues as a step edge. This is a reasonable assumption for segmenting structures of the musculo-skeletal system since tissues are characterized by distinct x-ray attenuation coefficients.

For a one-dimensional isolated edge, and symmetric PSF, we showed that the optimal relative threshold was 50%. This theoretical result substantiates the conclusion of two experimental studies which placed the optimal relative threshold between 45% and 60%.

It is reasonable to assume that the edge location will be preserved at the 50% level in two dimensions, provided that the PSF is axially symmetric, and that the edge be straight or its radius of curvature is (much) larger than the extent of the PSF.

One of the implications of this criterion is that the absolute threshold level will vary depending on the tissues in contact. Therefore, using a single global threshold will lead to erroneous edge location if an object is in contact with more than one tissue type. Furthermore, because the system is shift-variant, the bias introduced by using a single global threshold will depend on the position and orientation of the edge.

An edge can no longer be considered isolated, and the 50% criterion fails, when it interacts with a neighboring edge. This occurs when the width of the double step edge is smaller that the width of the PSF. This distance is approximately equal to twice the full width at half maximum (FWHM) for the Gaussian PSF or twice the half width at first zero

crossing (HWZC) for the damped cosine PSF (i.e. twice the resolution of the imaging system). This distance varies with the filter used to reconstruct the image and with the position and orientation of the edges due to shift-variance.

The size of the LOG operator, which is controlled by the standard deviation of the Gaussian filter, determines the balance between the detection and localization properties of this segmentation method. This approach is valid in the presence of white noise. However, as we pointed out, the frequency structure of the LOG operator and of the noise in CT images are very similar. Failing to recognize this similarity can result in noise amplification, thereby defeating the purpose of smoothing the signal prior to differentiation. One must also keep in mind that the blurring inherent to the imaging system is compounded by the action of the Gaussian smoothing and that the edge interaction distance increases accordingly.

CHAPTER 9
CONCLUSION

9.1 Summary

Limitations of the imaging device, such as blurring patterns, noise characteristics and artefacts, have been largely ignored when applying general image processing techniques to medical images. We believe that by gaining a detailed knowledge of the characteristics of the imaging system, we will be in a better position to determine the limits of the image processing algorithms, and to improve their performance.

The first objective of this work was therefore to develop experimental tools to characterize the imaging system. To realize this goal we:

- estimated the NPS in a variety of imaging conditions,
- developed and evaluated parametric models of the PSF,
- experimentally quantified the shift-variance, using the parametric models and an array of spatially distributed point sources,
- validated the use of point sources, by comparing the non- parametric PSF estimates obtained with this input to those found using a correlation-based estimation method.

The second goal was to investigate ways of using this information to process the images. We:

-developed and evaluated a coordinate transformation for shift-variant image restoration,

-explored the limits of the threshold and Laplacian of a Gaussian segmentation operators, based on the shape of the PSF and the noise properties.

9.2 Original contributions

In the course of the project, we claim the following original contributions.

9.2.1 Parametric models (Chapter 4)

1) We extended the Gaussian model to incorporate three new features:

a) It is non-linear in its parameters. The non-linear formulation minimizes negative biases in shape parameter estimates (p_x, p_y) compared to a linearized model. Furthermore, this approach gives us the opportunity to track the position of an input with sub-pixel accuracy.

b) The model does not assume radial symmetry. The comparison of the shape parameters in two orthogonal directions proved useful in quantifying the anisotropic properties of the PSF.

c) The model takes the average background value into account. Omission of this parameter can lead to positive biases in shape parameter estimates for a negative background while negative biases can be expected when the background is positive. We showed and explained why this effect is worst in the case of positive background.

2) We formulated an entirely new model, the damped cosine function. This model describes the negative tails observed in the PSF produced with the high resolution reconstruction filter. It also explains the shape of the MTF throughout the whole frequency range. We also incorporated the three original features of the Gaussian model to the formulation of the damped cosine model.

9.2.2 Shift-variant study (Chapter 5)

1) We developed and tested a new experimental method to characterize and quantify the shift-variant and anisotropic properties of the PSF.

a) We designed and built a custom phantom consisting of an array of spatially distributed point sources as input.

b) We considered the effect of the image reconstruction filter. We thus experimentally verified the claim that the apodizing filter does not affect the pattern of shift-variance.

c) We also considered the effect of scan time. For the particular scanner used, we observed a large decrease in shift-variance in the tangential direction while the shape of the PSF was not affected in the radial direction.

2) We experimentally verified certain trends predicted by theory. In particular:

a) We confirmed the presence of a rotating blur.

b) We observed and quantified the loss of PSF radial symmetry with the increase of radial distance from the center of the field of view.

c) We observed and quantified the widening of the PSF in the tangential and radial directions.

9.2.3 Correlation based non-parametric identification (Chapter 6)

1) To our knowledge, we are the first to adapt this method for the identification of X-ray CT systems and even to medical imaging systems in general.

a) We designed an input whose auto-correlation function was suitable for the method while being physically realizable. It consisted of a 2D array of pseudo-randomly located holes drilled in radiopaque material.

b) We proceeded to an exhaustive simulation in order to determine the effect of the following parameters:

- hole size
- hole separation
- overall size of input
- pixel size
- sub-pixel translation between input and output images
- rotation between input and output images
- cupping

c) We designed and implemented an algorithm to digitize the input in such a way as to minimize input noise.

2) We developed a procedure to properly register the input and output images in order to optimize, in the informal sense, the identification process. The rotation was evaluated by estimating the orientation of alignment axes with the image raster axes. The capacity of the parametric models to position the input with sub- pixel accuracy was used to evaluate the residual translation.

3) We validated the use of point sources as input for non-parametric estimation by comparing these estimates to those obtained with the correlation based methods.

9.2.4 Coordinate transformation (Chapter 7)

1) We developed and implemented a coordinate transformation for the shift-invariant restoration of CT images. The transformation is based on the experimental results of the shift-variance study.

2) We formulated simple requirements to insure that the cascade of forward and inverse transformation would not introduce artefacts into the image.

3) We developed a quantitative evaluation procedure. This procedure was beneficial in:

a) delimiting the usefulness of the method,

b) detecting a limitation which had not been reported in the literature. Indeed, for the PSF to be truly isotropic in the transformed plane, the function which describes the variation in PSF width in the tangential or angular direction must be constrained to vary in a piecewise constant manner.

9.2.5 Segmentation (Chapter 8)

1) We theoretically showed that for a 1D isolated edge, the optimum relative threshold is 50%. We believe that the notion of 1D edge is valid for 2D edges whose radius of curvature is (much) larger than the width of the PSF.

2) Based on the interaction between neighboring edges, we determined that this 50% criterion fails when the distance between two edges is smaller than twice the resolution of the system.

3) Using these results, we substantiated certain experimental results found in the literature (Rothuizen et al., 1986) but which had not been theoretically justified.

4) We observed that the smoothing parameter of the LOG operator should take the noise frequency distribution as well as the problem of edge interaction into account.

9.2.6 General comments

It should be noted that the numerical values concerning resolution, the amount of shift-variance and the noise characteristics are specific to the scanner on which the experiments were performed. We did show however, that most of the trends were compatible with theory, independently of scanner geometry. It is therefore reasonable to assume that the trends we observed would also be valid for other models of X-ray scanner. Furthermore, all the identification tools we developed are sufficiently general to be used on any X-ray CT unit and even adapted to other medical imaging modalities.

The only restriction placed on the coordinate transformation for the isoplanatic representation of the PSF is that the system exhibit a rotating blur. Most modern X-ray systems, which acquire data over 360°, comply to this requirement. However systems with slow acquisition times, e.g. SPECT scanners, often acquire data over 180° and may not exhibit a rotating blur.

The 50% relative criterion for its part is valid provided that the PSF is axially symmetric. On the other hand, the choice of the Laplacian of a Gaussian smoothing parameter is very application and machine dependent. Indeed, the NPS, which is one of the factors which should govern the choice of this parameter, is greatly influenced by the ρ-filter apodizing function. Since each company designs its own filters, the shape of the NPS, hence the smoothing parameter, will vary depending on the scanner with which the data is acquired and the filter used to reconstruct the image.

9.3 Future work

We mentioned in chapter 1 that we are interested in the design and fabrication of custom-fitted articular resurfacing implants. A flow-chart of the entire project is illustrated in figure 9.1. It is evident from this diagram that the work presented in this thesis represents only a small portion of the efforts required to produce an implant. Indeed, we have only considered the relationship between the first two steps, imaging and segmentation. In the remainder of this section, we will list subjects which are considered for future work.

9.3.1 Image processing

We presented a coordinate transformation permitting the isoplanatic representation of shift-variant images. We mentioned that this method could be used for the restoration of shift-variant images. It still remains to be shown however, if the method improves the restoration itself. It is conceivable that the coordinate transformation could modify the outcome of a particular restoration method. Therefore, it would be important to compare the results of a restoration method implemented with and without the coordinate transformation.

It would also be interesting to evaluate the usefulness of image restoration as a pre-processing step to segmentation. Indeed, restoration decreases the amount of blur. But this improvement is most often realized at the expense of increased noise which may be detrimental to the segmentation operators, and more specifically to edge detectors.

We proposed a relative segmentation criterion based on a 1D step edge model. We mentioned that this criterion was valid as long as the radius of curvature of the edge was (much) larger than the extent of the PSF. The interaction between the 2D edge and PSF will have to be examined more closely in order to specify this condition more accurately.

We also mentioned that the choice of the Laplacian of a Gaussian smoothing parameter should take the shape of the NPS into account. However, more work is required to determine the exact nature of the interaction between the noise characteristics and the performance of the Laplacian of a Gaussian filtering operator.

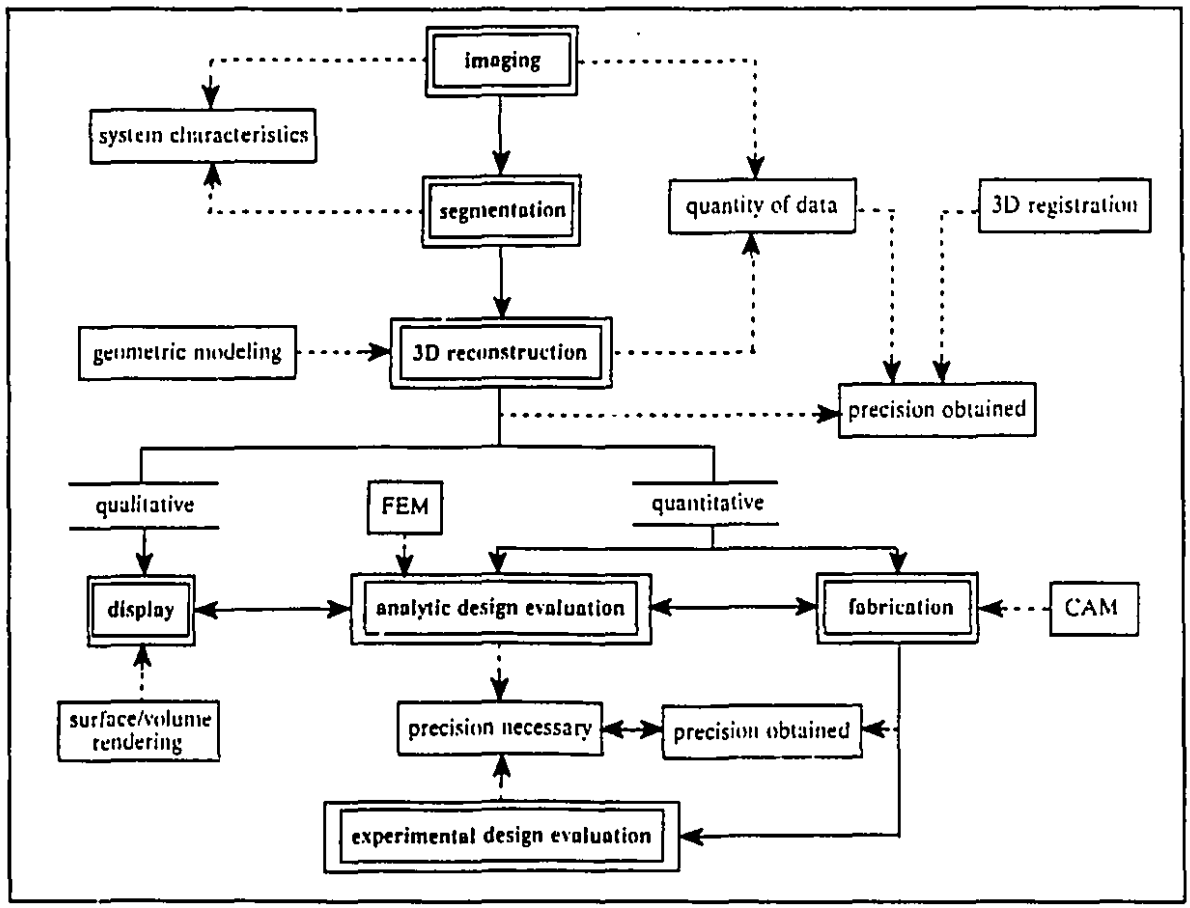

Figure 9.1 Synopsis of long term project

9.3.2 Reconstruction

The 3D geometric reconstruction approach must be adapted to the application. Most algorithms have been devised to display the reconstructed objects on a graphic screen. To increase the speed of display while limiting the amount of memory, surfaces are often approximated by a set of triangular tiles (Batnitzsky, 1981) or the faces of cubic voxels (Herman and Liu, 1977; Artzy et al., 1981). We will not only have to display the geometric information but also use it to generate tools paths for a numerically controlled machine. (This machine will produce the implant, a mold from which the implant will be cast or even a positive for investment casting). New forms of interpolation, better suited to a computer assisted machining environment must be adopted.

An issue which has received little attention is that of the amount of data necessary to build an accurate model. This also brings us to the problem of assessing the accuracy of the model. The box labelled "precision necessary" in figure 9.1 refers to this topic.

Modelling approaches: Inherent to the geometric model is the interpolation method used to represent the surface between sample points. We wish to investigate alternative interpolation functions in the context of kriging. With dual kriging, the interpolation function is a sum of two terms. The choice of the first term, or drift, is arbitrary and represents the expected value, or average behavior, of the variable. The second term relates to the error. It also reflects the spatial correlation that usually exists between the data. Because of this correlation property, kriging often yields superior results when compared to other interpolation techniques. Furthermore, by varying the form of the two terms, different interpolation schemes, such as linear or spline interpolation, can be generated within the same mathematical framework.

Amount of data necessary: The accuracy of the geometric model is expected to increase with the amount of data available. It is current practice in medical 3D reconstruction to scan the joint with the highest axial resolution and sampling possible. But is all this data necessary? Increasing the distance between each image would reduce the amount of data, the examination time is shortened, thus reducing the cost of the examination, the risk of patient movement and total radiation in the case of X-ray CT. Furthermore, the image processing time will also decrease. We are faced with an interesting optimization problem which, to our knowledge, has never been treated.

Sampling theory offers an elegant solution to the problem of determining the minimum quantity of data to represent the bony surfaces since it guarantees that a properly sampled signal ("geometric" model) can be interpolated to yield the continuous signal. The sampling theorem states that a signal must be sampled at a rate greater than or equal to twice the highest frequency contained in the signal. Fourier descriptors could be used to uncover the frequency characteristics of the bone geometry.

Assessment of accuracy: The methods for assessing the accuracy of the reconstruction are scarce and range from visual comparisons (Hemmy and Tessier, 1985), estimation of surface area and object volume (Udupa, 1981), to comparing the distance between anatomical landmarks on the object and a machined replica (Woolson et al., 1986). All these methods are based on global measures and therefore give no information on local variations between the actual and reconstructed surfaces. At the heart of local error assessment is the problem of spatially registering two objects (the reconstructed model and the physical object) in 3D space. Methods to do so include visual inspection (Pietzyk et al., 1990), the use of markers and/or alignment frames, identification of landmarks on

both surfaces matched with least-squared algorithms, and alignment of centroids and principal axes (moment based method) (Vannier and Gayou, 1988). Precise application of markers and frames can be difficult, while anatomical landmarks may not be identifiable on both objects (especially when dealing with smooth articular surfaces) and moment based methods require a priori definition of corresponding subvolumes. Pellizari et al. (1989) devised a general algorithm with the intention of circumventing these shortcomings. However, the surface defined with the highest resolution must be represented in a special format and the method is only applicable to closed surfaces. Methods used in part inspection and robotics are most often defined in 2D or deal with depth projection maps and are inadequate for this problem.

The first step in assessing the accuracy will be to scan limbs with the highest axial sampling rate possible and with different image reconstruction algorithms. The bones will then be stripped of all soft tissues and measured with a system having a better resolution than that of the imaging device. A coordinate measuring machine (CMM) is envisioned for this task. The result of these measurements will be known as the "physical model". The second step consists of developing a general 3D registration algorithm necessary to align the "physical model" and the results of segmentation. Local discrepancies (distance, variations in curvature) can then be measured and used to compare the accuracy of different pre-processing/segmentation/segmentation algorithms.

9.3.3 Fabrication

The choice of fabrication processes used to manufacture "off the shelf" implants is largely motivated by the implant material(s) and desired mechanical properties. We will limit our discussion to metals which offer special challenges where manufacturing processes are concerned. Metals used in orthopaedics for long term applications are either cobalt- or titanium-based alloys. Hot isostatic pressing (HIP) (Chandok and Rizzo, 1981), a derivative of sintering, and isothermal pressing, a forging technique where the metal exhibits (near) superplastic properties (Shepp, 1989), are favoured fabrication techniques. However, a large number of parts must be produced to write off the high costs associated with producing the matrices.

Therefore, these methods could not be used to produce the customized implant directly. However, they could be employed to generate near-form blanks. Two options are then available: either both surfaces (inner and outer) are customized, thereby increasing the finishing time, or only the inner surface is personalized. This last option implies that the blanks will have to be available in different sizes, increasing the cost of producing the matrices.

Customizing the surfaces will involve machining. The shell-like nature of the implant, the high forces and high temperatures associated with conventional (chip removal) machining cobalt and titanium alloys (Wilson, 1984) create a challenging problem. Customizing efforts found in the literature usually involve optimizing hip implant stem geometry where the size and shape of the prosthesis does not create any special machining problems of the sort. Another question to be considered is that of positioning and clamping of the workpiece. Electro-discharge (erosion) machining (EDM) could solve some of the problems foreseen with conventional machining and is considered as an alternative. However, the use of EDM will require additional surface finishing to remove the redeposited layer of molten metal which is detrimental to fatigue properties.

A completely different option consists of investment casting the implant. The problem in this case is producing the thin shelled positives. Stereolithography, which has recently been used to produce patterns and/or prototypes (Jara-Almonte, 1990), is an interesting candidate especially since the data is already available in a slice by slice format However, the problems associated with distortion and the limited accuracy of the system are geometry specific problems that will have to be dealt with. Alternatively, the positives could be machined.

9.3.4 Design evaluation

The precision with which the implant should be made to fit the bone (see figure 9 1, box labelled "precision necessary") must also be determined. Indeed, an imperfect fit will lead to undue stress in both the prosthesis and bone. This problem can be addressed analytically with a finite element analysis. Issues such as material selection and fixation can also be studied with this method. Furthermore, once a prototype has been produced, it can be tested experimentally to uncover problems which could not be simulated analytically

REFERENCES

H.C. Andrews. Two-dimensional transforms. In Topics in Applied Physics, volume 6: Picture Processing and Digital Filtering. 2nd ed. T.S. Huang, ed. Berlin: Springer-Verlag, 1979: 21-68.

E. Artzy, G. Friederer, G.T. Herman. The theory, design, implementation and evaluation of a three-dimensional surface detection algorithm. Computer Graphics and Image Processing, 15, 1981: 1-24.

H.H. Barrett, W. Swindell. Radiological imaging. The theory of image formation, detection, and processing. Volume 2, New York: Academic Press, 1981. pp. 375-445.

D.A. Bassano. Specification and quality assurance for CT scanners, in Medical physics of CT and ultrasound. G.D. Jullerton, J.A. Zagnebski, ed. New York: American Association of Physicists in Medicine, 1980.

R.H.T. Bates and M.J. McDonnell. Image restoration and reconstruction. Oxford: Clarendon Press, 1989.

S. Batnitzky, H.I. Price, P.N. Cook, L.T. Cook, S.J. Dwyer III. Three-dimensional computer reconstruction from surface contours for head CT examinations. J. Computer Assisted Tomography, 5(1), 1981: 60-67.

J.S. Bendat, A.G. Piersol. Engineering applications of correlation and spectral analysis. New York:John Wiley and Sons, 1980.

JS Bendat, AG Piersol. Random data: analysis and measurement procedures. 2nd edition (revised and expanded), New York: John Wiley and Sons, 1986.

F. Bergholm. Edge focusing. IEEE Trans. on Pattern Analysis and Machine Intelligence, 9(6), 1987: 726-741.

V. Berzins. Accuracy of Laplacian edge detectors. Computer Vision, Graphics, and Image Processing, 27, 1984: 195-210.

J. Biemond, R.L. Lagendijk, R.J. Mersereau. Iterative methods for image deblurring. Proceedings of the IEEE, 78(5), 1990.

C.J. Bischof and J.C. Ehrhardt. Modulation transfer function of the EMI CT head scanner. Med. Phys., 4(2), 1977: 163-167.

M. Bomans, K.-H. Höhne, U. Tiede, M. Riemer. 3-D segmentation of MR images of the head for 3-D display. IEEE Trans. on Medical Imaging, 9(2), 1990: 177-183.

G.Borasi, G. Castellani, R. Domenichini, M Franchini, M. Granata, A. Terresin, G. Tosi. Image quality and dose in computerized tomography: evaluation of four CT scanners. Med. Phys. 11(3), 1984: 321-325.

D.P. Boyd, D.L. Parker. Basic principles of computed tomography, in Computed Tomography of the body. A.A. Moss, G. Gamsu, H.K. Genant ed., Philadelphia: W.B. Saunders, 1983.

R.N. Bracewell. Correction for collimator width (restoration) in reconstructive x-ray tomography. JCAT, 1(1), 1977: 6-15.

R.N. Bracewell. The Fourier transform and its applications. 2nd edition, revised, New York: McGraw-Hill, 1986.

R.A. Brooks and G. Di Chiro. Principles of computer assisted tomography (CAT) in radiographic and radioisotopic imaging. Phys. Med. Biol., 21(5), 1971: 689-732.

R.A Brooks, G. Di Chiro. Beam hardening in x-ray reconstructive tomography. Phys. Med. Biol., 21(3), 1976(a): 390-398.

R.A. Brooks and G Di Chiro. Statistical limitations in x-ray reconstructive tomography. Med. Phys., 3(4), 1976(b): 237-240.

S.C. Bushong. Radiologic science for technologists. Physics, biology and protection. 4th ed., St-Louis: C.V. Mosby, 1988: 401-405.

J. Canny. A computational approach to edge detection. IEEE Trans. on Pattern Analysis and Machine Intelligence, 8(6), 1986: 679-698.

V.K. Chandok, F.J. Rizzo. Hot isostatic pressed powder metal titanium implant devices. Titanium Alloys in Surgical Implants. Conference Proceedings, Phoenix, May 11-12, 1981: 33-42.

J.S. Chen and G. Medioni. Detection, localization, and estimation of edges. IEEE Trans. on Pattern Analysis and Machine Intelligence, 11(2), 1989: 191-198.

D.A. Chesler, S.J. Riedere, N.J. Pelc. Noise due to photon counting statistics in computed x-ry tomography. JCAT, 1(1), 1977: 64-74.

K.J. Cios, A. Sarieh. An edge exrtraction technique for noisy images. IEEE Trans. on Biomedical Engineering, 37(5), 1990: 520-524.

C.M. Citrin. High resolution orbital computed tomography. JCAT, 10(5), 1986: 810-816.

J.J. Clark. Authenticating edges produced by zero-crossing algorithms. IEEE Trans. on Pattern Analysis and Machine Intelligence, 11(1), 1989: 43-57.

A.J. Coleman, M. Sinclair. A beam-hardening correction using dual-energy computed tomography. Phys. Med. Biol., 30(11), 1985: 1251-1256.

I.A. Cunningham, A. Fenster. A method for modulation transfer function determination from edge profiles with correction for finite element differentiation. Med. Phys. 14(4), 1987: 533-537.

E. De Micheli, B. Caprile, P. Ottonello, V. Torre. Localization and noise in edge detection. IEEE Trans. on Pattern Analysis and Machine Intelligence, 11(10), 1989: 1106-1117.

G. Demoment. Image reconstruction and restoration: overview of common estimation structures and problems. IEEE Trans. on Acoustics, Speech, and Signal Processing. 37(12), 1989: 2024-2036.

A.P. Dhawan, R.M. Rangayyan, R.Gordon. Image restoration by Wiener deconvolution in limited-view computed tomography. Applied Optics, 24, 1985: 4013-4020.

TD Doukoglou. Non-parametric system identification techniques for numerical deconvolution of scanning laser microscope images. Master's thesis, McGill University, 1989.

R.T. Droege, R.L. Morin. A practical method to measure the MTF of CT scanners. Med. Phys. 9(5), 1982: 758-760.

R.T. Droege, M.S. Rzeszotarski. An MTF method immune to aliasing. Med. Phys. 12(6), 1985: 721-725.

J.C. Ehrhardt. Reduction of aliasing in modulation transfer function measurements. Med. Phys. 13(5), 1986: 658-662.

E.J. Farrell, R.A. Zapulla. Three-dimensional data visualization and biomedical applications. CRC critical reviews in biomedical engineering, 16(4), 1989: 323-363

K. Faulkner and B.M. Moores. Analysis of x-ray computed tomography images using the noise power spectrum. Phys. Med. Biol. 29, 11, 1984: 1343-1352.

J.E. Freund. Statistics. A first course. 3rd ed., Englewood Cliffs: Prentice-Hall, 1981.

K.S. Fu, J.K. Mui. A survey on image segmentation. Pattern Recognition, 13, 1981: 3-16.

M.L. Giger and K. Doi. Investigation of basic imaging properties in digital radiology. I. Modulation transfer function. Med. Phys., 11(3), 1984: 287-295.

S.J. Glick, M.A. King, B.C. Penney. Characterization of the modulation transfer function of discrete filtered backprojection. IEEE Trans. on Medical Imaging, 8(2), 1989: 203-213.

G.H. Glover, R.L. Eisner. Theoretical resolution of computed tomography systems. JCAT, 3(1), 1979: 85-91.

G.H. Glover and R.L. Eisner. Correction to "Theoretical resolution of computed tomography systems". JCAT, 4(1), 1980: 108.

G.H. Glover, N.J. Pelc. Nonlinear partial volume artifacts in x-ray computed tomography. Med. Phys. 7(3), 1980: 238-248.

KR Godfrey. The theory of the correlation method of dynamic analysis and its application to industrial processes and nuclear power plant. Measurement and Control, 2, 1969: T65-T72.

KR Godfrey. Correlation methods. Automatica, 16, 1980: 527-534.

R.C. Gonzalez, P Wintz. Digital image processing. Readings, Mass.: Addison-Wesley, 2nd ed., 1987. 503 p.

D.J. Goodenough, K.E. Weaver, D.O. Davis. Development of a phantom for evaluation and assurance of image quality in CT scanning. Optical Engineering, 16(1), 1977: 52-65.

K.M. Hanson. Detectability in computed tomographic images. Med. Phys., 6(5), 1979: 441-451.

DC Hemmy, PL Tessier. CT of dry skulls with craniofacial deformities: accuracy of three-dimensional reconstruction. Radiology, 157, 1985: 113-116.

G.T. Herman, H.K. Liu. Display of three-dimensional information in computed tomography. JCAT, 1(1), 1979: 155-160.

G.T. Herman. Image reconstruction from projections. New York: Academic Press, 1980.

G.T. Herman. A survey of 3D medical imaging technologies. IEEE Eng. Med. Biol., 9(4), 1990: 15-17.

E.C. Hildreth. The detection of intensity changes by computer and biological vision systems. Computer Vision, Graphics, and Image Processing, 22, 1983: 1-27.

K.W. Hogan and K.A. Hickey. Gamma camera MTFs from edge response function measurements. Med. Phys. 10(3), 1983: 361-364.

T.C. Hon, R.M. Rangayyan, L.J. Hahn, R. Kloiber. Restoration of Gamma camera-based nuclear medicine images. IEEE Trans. on Medical Imaging, 8(4), 1989: 354-363.

A. Huertas and G. Medioni. Detection of intensity changes with subpixel accuracy using Laplacian-Gaussian masks. IEEE Trans. on Pattern Analysis and Machine Intelligence, 8(3), 1986: 651-664.

IW Hunter, RE Kearney. Two-sided linear filter identification. Med. and Biol. Eng. and Comput., 21, 1983: 203-209.

CC Jara-Almonte, A Bagchi, AA Ogale, RL Dooley. Design environment for rapid prototyping. Proceedings of the Winter Annual Conference of the ASME, Dallas, TX, Nov. 25-30, 1990: 31-36.

P.M. Joseph. The influence of gantry geometry on aliasing and other geometry dependent errors. IEEE Trans. on Nuclear Science, 27(3), 1980: 1104-1111.

P.M. Joseph, R.D. Spital, C.D. Stockman. The effects of sampling on CT images. Computerized Tomography, 4, 1980: 189-206.

P.M. Joseph and R.A. Schulz. View sampling requirements in fan beam computed tomography. Med. Phys., 7(6), 1980: 692-702.

P.M. Joseph, R.D. Spital. The exponential edge-gradient effect in x-ray computed tomography. Phys. Med. Biol., 26(3), 1981: 473-487.

P.F. Judy. The line spread function and modulation transfer function of a computed tomography scanner. Med. Phys., 3(4), 1976: 233-236.

A.C. Kak and M Slaney. Principles of computerized tomographic imaging. New York: IEEE Press, 1988. 329 p.

H. Kanomori, N Nakamori, K Inoue, E Takenaka. Effects of scattered x-rays on CT images. Phys. Med. Biol., 30(3), 1985: 239-249.

RE Kearney, IW Hunter. System identification of human joint dynamics. CRC Critical Reviews in Biomedical Engineering, 18(1), 1990: 55-87.

R.G. Keys. Cubic convolution interpolation for digital image processing. IEEE Trans. on Acoustics, Speech, and Signal Processing, 29(6), 1981: 1153-1160.

M.F. Kijewski, P.F. Judy. The effects of misregistration of the projections on the spatial resolution of CT scanners. Med. Phys., 10(2), 1983: 169-175.

M.F. Kijewski and P.F. Judy. The noise power spectrum of CT images. Phys. Med. Biol., 32(5), 1987: 565-575.

M.F. Kijewski and P.F. Judy. Letter to the Editor: Reply to 'Comments on the noise power spectrum of CT images'. Phys. Med. Biol., 1988: 1049-1051.

E. Klotz, W.A. Kalender, T. Sandor. Automated definition and evaluation of anatomical ROI's for bone mineral determination by QCT. IEEE Trans. on Medical Imaging, 8(4), 1989: 371-376.

P.J. Koltai, G.W. Wood. Three dimensional CT reconstruction for the evaluation and surgical planning of facial fractures. Otolaryn-gol. Head Neck Surg., 95, 1986: 10-15.

O. Kübler and G. Gerig. Segmentation and analysis of multidimensional data-sets in medicine. NATO ASI Series, Vol. F 60, 3D Imaging in Medicine, K.-H. Höhne, ed. Berlin: Springer-Verlag, 1990. p. 63-79.

H.K. Liu. Two- and three-dimensional boundary detection. Computer Graphics and Image Processing, 6, 1977: 123-134.

K.W. Logan, K.A. Hickey. Gamma camera MTFs from edge response function measurements. Med. Phys., 10(3), 1983: 361-364.

W.H.H.J. Lunscher and M.P. Beddoes. Optimal edge detector design I: Parameter selection and noise effects. IEEE Trans. on Pattern Analysis and Machine Intelligence, 8(2), 1986: 164-177. (a)

M.T. Madsen. A Method for obtaining an approximate Wiener filter. Med. Phys., 17(1), 1990: 126-130.

E.W. Marchand. Derivation of the point spread function from the line spread function. J. Opt. Soc. Am. 54(7), 1964: 915-919.

E.W. Marchand. From line to point spread function: the general case. J. Opt. Soc. Am. 55(4), 1965: 352-354.

PZ Marmarelis, VZ Marmarelis. Analysis of physiological systems. The white noise approach. New York: Plenum Press, 1978.

E.C. McCullough. Factors affecting the user of quantitative information from a CT scanner. Radiology, 124, 1977: 99-107.

W.J. McIntyre, R.J. Alfidi, J. Haaga, E. Chernak, T.F. Meany. Comparative modulation transfer functions of the EMI and Delta scanners. Radiology, 120, 1976: 189-191.

D. Meagher. Geometric modelling using octree encoding. Computer Graphics and Image Processing, 19, 1982: 129-147.

C.E. Metz, K Doi. Transfer function analysis of radiographic imaging systems. Phys. Med. Biol. 24(6), 1979: 1079-1106.

A. Müller, P. Rüegsegger, P. Seitz. Optimal CT settings for bone evaluations. Phys. Med. Biol., 30(5), 1985: 401-409.

V.S. Nalwa. Edge-detector resolution improvement by image interpolation. IEEE Trans. on Pattern Analysis and Machine Intelligence, 9(3), 1987: 446-451.

V.S. Nalwa, T.O. Binford. On detecting edges. IEEE Trans. on Pattern Analysis and Machine Intelligence, 8(6), 1986: 699-714.

E.L. Nickoloff and R. Riley. Simplified approach for modulation transfer function determination in computed tomography. Med. Phys., 12(4), 1985: 437-442.

J.P. Norton. An introduction to identification. London: Academic Press, 1986.

J.A. Parker, R.V. Kenyon, D.E. Troxel. Comparison of interpolation methods for image resampling. IEEE Trans. on Medical Imaging, 2(1), 1983: 31-39.

CA Pellizari, GTY Chen, DR Spelbring, RR Weichselbaum CT Chen. Accurate three-dimensional registration of CT, PET, and MR images of the brain. J. Comput. Assist. Tomogr., 13, 1989: 20-26.

B.C. Penney, S.J. Glick, M.A. King. Relative importance of the error sources in Wiener restoration of scintigrams. IEEE Trans. on Medical Imaging, 9(1), 1990: 60-70.

T.M. Peters and R.M. Lewitt. Computed tomography with fan beam geometry. JCAT, 1(4), 1977: 429-436.

T.M. Peters. Resolution improvement to C.T. systems using aperture function correction. In Mathematical aspects of computerized tomography. From Lecture notes in medical informatics, volume 8, D.A.B. Lindberg and P.L. Reichertz ed., Berlin: Springer-Verlag, 1981: 241-251.

Philips Medical Systems. Tomoscan CT operator's manual. Release 3.0, 1988.

U Pietrzyk et al. Three-dimensional alignment of functional and morphological tomograms. J. Comput. Assist. Tomogr., 14(1), 1990: 51-59.

S.C. Prasad. Effects of focal spot intensity distribution and collimator width in reconstructive X-ray tomography. Med. Phys., 6(3), 1979: 229-232.

U.V.G. Rao and V.K. Jain. Gaussian and exponential approximation of the modulation transfer function. J. Opt. Soc. Am., 57(9), 1967: 1159-1160.

S. Rathee, Z.J. Koles, T.R. Overton. Modeling X-ray beam profiles in computed tomography (CT). Proceedings of the 17th Canadian Medical and Biological Engineering Conference, Banff, May 1991: 167-168.

M.L. Rhodes. An algorithmic approach to controlling search in three-dimensional image data. Proceedings of SIGGRAPH'79, Chicago, Ill., 1979: 134-142.

J.A. Rice. Mathematical statistics and data analysis. Belmont: Wadsworth and Brooks, 1988.

S.J. Riederer, N.J. Pelc, D.A. Chesler. The noise power spectrum in computed x-ray tomography. Phys. Med. Biol., 23(3), 1978: 446-454.

R.A. Robb, C. Barillot. Interactive display and analysis of 3-D medical images. IEEE Trans. Med. Imag., 8(3), 1989: 217-226.

G.M. Robbins. Image restoration for a class of linear spatially-variant degradations. Pattern Recognition, 2, 1970: 91-103.

G.M. Robbins, and T.S. Huang. Inverse filtering for linear shift-variant imaging systems. Proceedings of the IEEE, 60(7), 1972: 862-872.

A. Rosenfeld and L.S. Davis. Iterative histogram modification. University of Maryland, Computer Science Center, TR-519, April 1977.

A. Rosenfeld and A.C. Kak. Digital picture processing. 2nd ed., New York: Academic Press, 1982.

K. Rossman. Point spread-function, line spread-function and modulation transfer-function. Radiology, 93, 1961: 257-272.

P. Rothuizen, L. van Erning, R. Huiskes. The accuracy of criteria for automatic 3-D graphics reconstruction of bone from computer tomography. Biomechanics: Basic and Applied Research, G. Bergman, R. Kölbel, A. Rohlmann, eds., Selected Proceedings of the Fifth Meeting of the European Society of Biomechanics, Sept. 8-10, Berlin, 1986: 109-114.

Y. Sawagari, T. Soeda, T. Nakamizo. Classical methods and time series estimation. In: Trends and progress in system identification, P. Eykhoff ed., Oxford: Pergamon Press, 1985: 67-102.

A.A. Sawchuk. Space-variant image motion degradation and restoration. Proceedings of the IEEE, 60(7), 1972: 854-861.

A.A. Sawchuk. Space-variant image restoration by coordinate transformations. J. Opt. Soc. Am., 64(2), 1974: 138-144.

A.A. Sawchuk, and M.J. Peyrovian. Restoration of astigmatism and curvature of field. J. Opt. Soc. Am., 65(6), 1975: 712-715.

N.J. Schneiders, S.C. Bushong. Single-step calculation of the MTF from the ERF. Med. Phys. 5(1), 1978: 31-33.

N.J. Schneider and S.C. Bushong. Computer assisted MTF determination in CT. Med. Phys., 7(1), 1980: 76-78.

K.F. Shanmugan, F.M. Dickey, J.A. Green. An optimal frequency domain filter for edge detection in digital pictures. IEEE Trans. on Pattern Analysis and Machine Intelligence, 1, 1979: 37-49.

P.P. Shepp. Le matriçage isotherme. Revue Technique Sulzer, 71(1), 1989: 13-20.

MR Spiegel. Formules et tables de mathematiques. Serie Schaum, Paris: McGraw-Hill Inc., 1974.

H.S. Stiehl. 3D image understanding in radiology. IEEE Eng. in Med. Biol., 9(4), 1990: 24-28.

J.P. Stonestrom, A. Macovski. Scatter considerations in fan beam computerized tomographic systems. IEEE Trans. in Nuclear Science, 23(5), 1976: 1453-1458.

J.P. Stonestrom, R.E. Alvarez, A. Macovski. A framework for spectral artifact corrections in x-ray CT. IEEE Trans. in Biomed. Eng., 28(2), 1981: 128-141.

D.R. Sumner, C.L. Olson, P.M. Freeman, J.J. Lobick, T.P. Andriacchi. Computed tomographic measurement of cortical bone geometry. J. Biomechanics, 22(6/7), 1989: 649-653.

K.D. Toennies, J.K. Udupa, G.T. Herman, I.L. Wornom III, S.R. Buchman. Registration of 3D objects and surfaces. IEEE Computer Graphics and Applications, May 1990: 52-62.

V. Torre and T.A. Poggio. On edge detection. IEEE Trans. on Pattern Analysis and Machine Intelligence, 8(2), 1986: 147-163.

JJ Tuma. Engineering mathematics handbook. New York: McGraw-Hill Book Co., 3rd edition, 1967.

H.P. Tümmler, H. Stallforth, M. Ungethüm. Contour finding of CT-images - An assumption of individually designed implants. Proceedings of the 11th Annual International Conference of the IEEE Engineering in Medicine and Biology Society, Seattle, Nov. 9-12, 1989: 555-556.

J.K. Udupa. Determination of 3-D shape parameters from boundary information. Computer Graphics and Image Processing, 17, 198?. 52-59.

J.K. Udupa, S.N. Srihari, G.T. Herman. Boundary detection in multi-dimensions. IEEE Trans. on Pattern Analysis and Machine Intelligence, 4(1), 1982: 41-50.

M.W. Vannier, J.L. Marsh, J.O. Warren. Three dimensional computer graphics for craniofacial surgical planning and evaluation. Computer Graphics, 17(3), 1983: 263-273.

MW Vannier, DE Gayou. Automated registration of multi-modality images. Radiology, 169(3), 1988: 860-861.

J.G. Verly, R.N. Bracewell. Blurring in tomograms made with x-ray beams of finite width. JCAT, 3(5), 1979: 662-678.

J.G. Verly. X-ray computed tomography in the presence of arbitrary symmetrical focal spot intensity distribution. Med. Phys., 7(1), 1980: 27-34.

J.S. Weszka, R.N. Nagel, A. Rosenfeld. A threshold selection technique. IEEE Trans. Comput., 23, 1974: 1322-1326.

J.S. Weszka, A. Rosenfeld. Threshold selection techniques 5. University of Maryland, Computer Science Center, TR-349, Feb. 1975.

J.S. Weszka. A survey of threshold selection techniques. Computer Graphics and Image Processing, 7, 1978: 259-265.

M Wilson. Machining orthopaedic implants. Manufacturing technology- Research and development. Conference Proceedings, Dublin, March 6- 7, 1984: 17-40.

ST Woolson, P Dev, LL Fellingham, A Vassiliadis. Three-dimensional imaging of bone from computerized tomography. Clin. Orthop. Rel. Res., 202, 1986: 239-248.